# Novel Applications of Semiconductor Disk Lasers
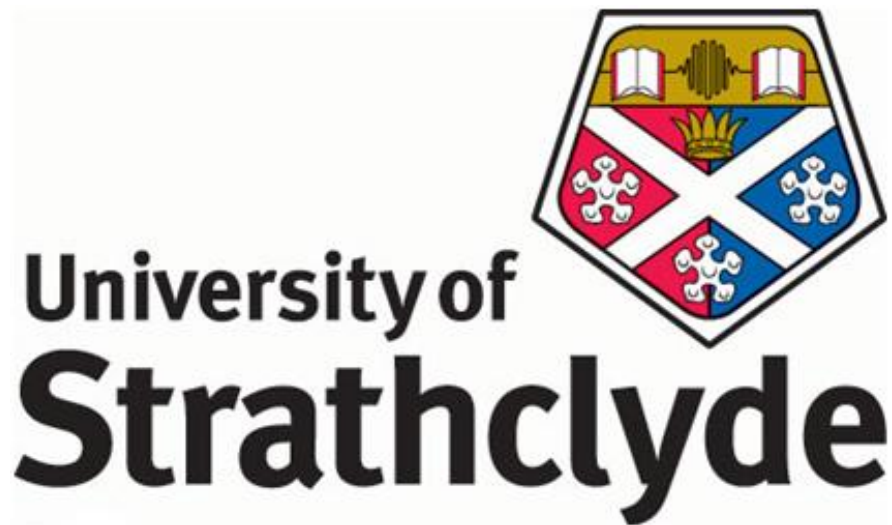
A Thesis Submitted to the Department of Physics
University of Strathclyde
For the Degree of Doctor of Philosophy

By
Sharon Louise Vetter

September 2011

DECLARATION OF AUTHENTICITY AND AUTHOR'S RIGHTS

This thesis is the result of the author's original research. It has been composed by the author and has not been previously submitted for examination, which has led to the award of a degree.

Signed _____

Date _____

In loving memory of my parents

Abstract

Semiconductor disk lasers (SDL) based on the GaInNAs/Ga(N)As material system have been developed for applications requiring emissions within the 1180 nm to 1300 nm wavelength range. The laser design offers an attractive opportunity for the production of high power, near diffraction limited beam quality with broad wavelength tunablility. Two distinctive applications of the SDL have been demonstrated in this thesis; one as an optical excitation source for other laser and amplification systems, and the second towards a compact frequency doubled laser device with yellow/orange emission.

An SDL designed with central wavelength emission at 1220 nm forms the basis of the pump source. In the first instance applied to pump Thulium (Tm^{3+}) and Thulium, Holmium (Tm^{3+}, Ho^{3+}) doped dielectric laser systems for operation ~2 μm, based on host tellurite glasses and tungstate crystal gain media. The SDL was wavelength tuned to coincide with the peak absorption in the materials ~1211 nm, operating with powers in excess of 600 mW. The results for the glass laser obtained up to 60 mW output power at ~1940 nm and ~22% internal slope efficiency, whilst the tungstate crystal achieved 200 mW output at ~2000 nm and ~35% internal slope efficiency. The second pumping application exploits Raman amplification in a single-mode silica fibre of length ~26 km. 4.6 dB Raman gain was obtained using a tunable signal source ranging from 1270 nm to 1320 nm.

Formation of a novel 'microchip' SDL laser design has been proposed, incorporating a nonlinear crystal bonded directly to the SDL device. Fundamental emission of ~1180 nm from the SDL provided frequency doubled ~590 nm output of ~25mW, with ~22 nm wavelength tuning range.

Acknowledgements

I would like to begin by expressing my gratitude to my supervisor Dr. Stephane Calvez, for his encouragement, his inspiration and his tremendous skill at explaining things simply and clearly. I feel very fortunate to have been given the opportunity of pursuing this PhD under his knowledgeable guidance. Thank you!

I have also been privileged to have studied at the Institute of Photonics, with its welcoming and supportive environment due to the staff and students alike. I wish to thank Professor Martin Dawson, Dr. Jennifer Hastie, Dr. Nicolas Laurand, Dr. David Burns, Dr. John-Mark Hopkins, Dr. Patricia Millar, Dr. Benoit Guilhabert, Dr. David Massoubre and Dr. Alan Kemp particularly for their openness and willingness to answer my many questions, leading to some very useful discussions over the years. I feel that everyone I have had the fortune of working with at the Institute has helped me along my PhD journey! In addition, the camaraderie I have experienced with my fellow PhD students has made every day at the Institute a joy! The many social outings and ability to share a laugh with some kindred spirits has certainly made me feel part of a very special group!

On a personal note, I find it difficult to express in words my heartfelt thanks to those closest to me. To my sister Valerie, who has provided consistent positive encouragement and support in so many ways! To my partner Stephen, who has helped me more than he realizes! Thank you both for your patience and understanding, especially during thesis writing when I was prone to periodically disappearing off the radar!

If you can dream - and not make dreams your master,
If you can think - and not make thoughts your aim;
If you can meet with Triumph and Disaster
And treat those two impostors just the same;
If you can bear to hear the truth you've spoken
Twisted by knaves to make a trap for fools,
Or watch the things you gave your life to, broken,
And stoop and build 'em up with worn-out tools:
Excerpt from *If* by Rudyard Kipling

Table of Contents

Table of Contents

Table of Contents

Chapter 1

Introduction

1.1 Motivation

At a pivotal time in 1960, Theodore Maiman operated the first ruby crystal laser [1]. From this early innovation, laser technology now forms the foundation of varied and widespread applications. Today, laser developments range from military and defense applications, global entertainment and computer products, and many vital industrial and retail operations. Laser bar code reading for example, provides the fundamental basis of modern commercial product database management creating key efficiency benefits. Heavy and micro industrial laser applications are now at the forefront of many major manufacturing processes. Advances in medical lasers have created a trend in the uptake of devices designed for surgery and eye treatment. Laser science now forms the foundation of both global telecommunication and information technology, and instrumental in the study of our atmospheric environment and astrophysics research.

In light of these established uses, laser development plays an essential role in the advancement of technical research. Emerging as a competitive laser technology the Semiconductor Disk Laser (SDL) is no exception [2], providing a high brightness laser source with near-diffraction limited beam quality at relatively high output powers, having achieved ~20W single mode output [3] with up to ~60W capability as a green laser [4]. Further, SDLs can be wavelength engineered through their choice of semiconductor gain material [5-7] and use of nonlinear conversion techniques to allow spectral coverage from the UV/visible [7-9] up to the mid-infrared [10-12] and even into the THz region [13, 14].

The main focus of this thesis is the development of dilute nitride SDLs. Ever since its discovery in 1995 by Kondow *et al.* [15, 16], the GaInNAs gain material was found to exhibit very useful traits. By including even small amounts of nitrogen into GaAs has the effect of decreasing the lattice constant of the material and the bandgap,

resulting in longer wavelength emission. It has been noted that the nitrogen content must be kept at a minimum otherwise the material is prone to crystalline defects, with adverse effects on the material quality. The addition of indium increases the lattice constant yet decreases the bandgap. In the formation of a quantum well (QW) where the GaInNAs material is 'sandwiched' between two layers of GaAs with a much larger bandgap, deep wells are created which act to strongly confine the carriers resulting in very good temperature characteristics. In addition, the material can be lattice matched to a GaAs substrate which can utilise high contrast AlGaAs-based Bragg mirrors, having much improved performance over InP-based systems. The designs of the GaInNAs/GaAs SDL devices used throughout this thesis have provided laser output across the spectral range $1150 - 1350$ nm. These wavelengths have potential use in a selection of applications to include gasoline detection [17, 18] and telecommunications [19].

The versatility of SDLs has been demonstrated through their recent use as pump sources for other lasers and amplifiers, which forms an integral part of this thesis. Systems pumped by an SDL include $Tm^{3+}(,Ho^{3+})$-doped glass, crystal and fibre lasers [20], a Cr^{2+}:ZnSe laser [21], a Cr^{2+}:Chalcogenide laser [22], a $KGd(WO_4)_2$ Raman laser [23], a Raman fibre amplifier [24] and a Raman-bismuth fibre amplifier [25]. The ability of the SDL to be wavelength tuned to specified spectral outputs, whilst maintaining high power, single mode operation have made these applications possible.

Another aspect to SDL capability has been the use of nonlinear techniques to obtain laser emission in the visible, as previously mentioned. By targeting the challenging yellow/orange spectral region, this thesis aims to provide a viable alternative to other laser systems. Many different approaches using diode pumped solid-state lasers designed to operate with yellow/orange output are outlined in Table 1.1.

Table 1.1: Developments of Yellow Solid-State Lasers.

Approach	Wavelength	Power	Disadvantages	Reference
Neodymium Dopant				
Nd:YVO$_4$ 1066.7nm + Self-Raman Laser 1178.7nm	589.4nm	151mW (P$_{avg}$)	Complex	[26]
Nd:YVO$_4$ + SFM(equal dual wavelength) + KTP	593nm	410mW	Complex	[27]
Nd:YVO$_4$ + SFM(1060nm+1342nm) + BIBO	593nm	48.5mW	Complex	[28]
Nd:YVO$_4$ + SFM (1064nm+1342nm)	589nm	340mW	Complex	[29]
Nd:YVO$_4$ + SFM(1064nm+1176nm) + LBO	559nm	0.47W	Complex	[30]
Nd:YAG + SFM(1064nm+1319nm) + KTP	589nm	8.1W	Complex	[31, 32]
Nd:Silica Fibre 938nm+ Er/Yb:Fibre 1583nm + PPKTP/PPSLT	589nm	0.5W	Complex	[33]
Nd:YAG 1123nm + SHG (LBO)	561nm	1.2W	Not Tunable	[34]
Dye Laser				
Rhodamine 6G (Pumped by 532nm)	557nm	71µJ	Low Power	[35]

Approach	Wavelength	Power	Disadvantages	Reference
Ytterbium Doped Fibre				
Yb:Fibre 1150nm + PPLN	575nm	40mW	Complex, SHG Crystal Heating	[36]
Yb:Fibre 1160nm Self Heating + PPLN	580nm	860mW	Complex, high thermal sensitivity	[37]
Yb:Fibre 1178nm + Solid-core Photonic Bandgap Fibre+MgO:PPLN	589nm	1.4W	Complex	[38]
Raman Laser				
Nd:YAG 1064nm + LiIO$_3$ Raman Crystal first Stokes 1155nm + LBO	578nm	1.2W (P$_{avg}$)	Thermal lens issues	[39]
Ba(NO$_3$)$_2$ Raman Laser pumped by Frequency Doubled Nd:YAG 532nm	563nm (first stokes), 599nm (second stokes)	25mJ, 32mJ	Complex, dependent upon frequency doubled Nd:YAG system	[40]
Raman fibre 1179nm+ Yb:Fibre 1118nm + MgO:PPLN	589nm	>3W	Complex	[41, 42]
P:Fibre Raman Laser 1178nm pumped by Yb:Fibre 1100nm + LBO	589nm	10W,25W	Complex	[43, 44]
PbWO$_4$ Raman Laser + pumped by Nd:YAG SHG 532nm	558.9nm (first stokes)	1mJ	Complex, low power	[45]
Raman fibre laser 1178nm with Coherent Beam Combination + LBO	589nm	20W, 50W	Complex	[46, 47]

Approach	Wavelength	Power	Disadvantages	Reference
Bismuth Doped Fibre Laser				
Bi:Fibre 1160nm + PPLN	580nm	~200mW	Fibre Operation high thermal sensitivity	[48]
Bi:Fibre 1178nm pumped by Yb:fibre + MgO:PPLN	589nm	125mW	Complex	[49]
Optical Parametric Amplifiers				
Optical Parametric Amplifier – Modelocked Nd:YVO$_4$ laser 1064nm Master Oscillator Power Amplifier (MOPA) + LBO	589nm	4.6W	Complex	[50] [51]
Special Dopants				
Dysprosium doped ZBLAN fibre pumped with Argon ion laser at 457nm	575nm	~10mW	New technology, low output powers	[52]
Dysprosium doped Fluoro-Aluminate Glass Fibre pumped by GaN LD at 398.8nm	575nm	~11mW	New technology, low output powers	[53]

The majority of these approaches centre on neodymium (Nd) doped materials such as yttrium orthovanadate (YVO_4) and yttrium aluminium garnet (YAG). These systems are generally quite complex, needing sum-frequency mixing (SFM) to target the correct visible wavelength, with use of nonlinear crystals such as lithium triborate (LBO), potassium titanyl phosphate (KTP) and bismuth borate (BIBO). Use of second harmonic generation (SHG) and Nd transitions showing lower gain (~1123nm) have also been reported to reach the yellow region [54].

Other approaches have adopted more energy efficient ytterbium (Yb) doped fibres, with a challenge to push the Yb emission to ~1180 nm by employing photonic crystal fibres to suppress gain at 1050 nm or self-heating. Frequency doubling materials used include periodically poled lithium niobate (PPLN) and magnesium oxide doped varieties (MgO:PPLN) along with periodically poled KTP and the relatively new periodically poled stoichiometric lithium tantalite (PPSLT). Alternative to Yb has been use of other dopants such as bismuth (Bi) or frequency shift, using nonlinear conversion based on the Raman effect.

In recent years the attention towards bismuth doped fibres was predominantly focused on the development of optical fibre communications, to target the ~1300 nm low dispersion window of silica fibres [55, 56] and low loss at 1400-1500 nm [57]. The extension into the visible has been promising using a Yb-doped fibre pumping scheme, to produce 1160 nm output from the Bi-doped fibre then frequency doubled using PPLN [49]. However, bismuth is still not thoroughly understood, with ongoing investigations into its performance in relation to other dopant materials in its host matrix.

The SHG Raman shifted (fibre) lasers have achieved the highest yellow (589 nm) output powers at 50W using 3 coherently combined beams from Raman fibre amplifiers, which are then frequency doubled using LBO nonlinear crystal. This however involves a complex array of components, as do the other Raman laser configurations. One exception worth highlighting is the system produced by Macquarie University, consisting of a Nd:YAG laser, intracavity $LiIO_3$ Raman-active crystal and an LBO nonlinear crystal, capable of producing average pulsed yellow

laser output of 1.2W [39]. The significance of their research has been the subsequent commercialisation of a *"Magic Wand Yellow Laser"* through a start-up venture called Lighthouse Technologies for product supply to the medical industry [58].

A minority of approaches to yellow laser production have included a complex system based on an optical parametric amplifier (OPA), a low powered dye laser and use of Dysprosium as a dopant. The development of Dysprosium doped lasers for direct yellow emission has been slow, with very low output (~10mW) powers achieved.

1.2 Background

The development of the Semiconductor Disk Laser, also commonly known as the Vertical-External-Cavity Surface-Emitting Laser (VECSEL), extends back to the mid to late 1990's [59, 60]. The origin of the design exploits the benefits attributed to two preceding laser structures, the Vertical-Cavity Surface-Emitting Laser (VCSEL) and the solid-state optically pumped thin disk laser as illustrated in Figure 1-1. Combined advantages from the two structures provide a laser system which is capable of excellent beam quality, power scalable, with flexible operational wavelength design and compact.
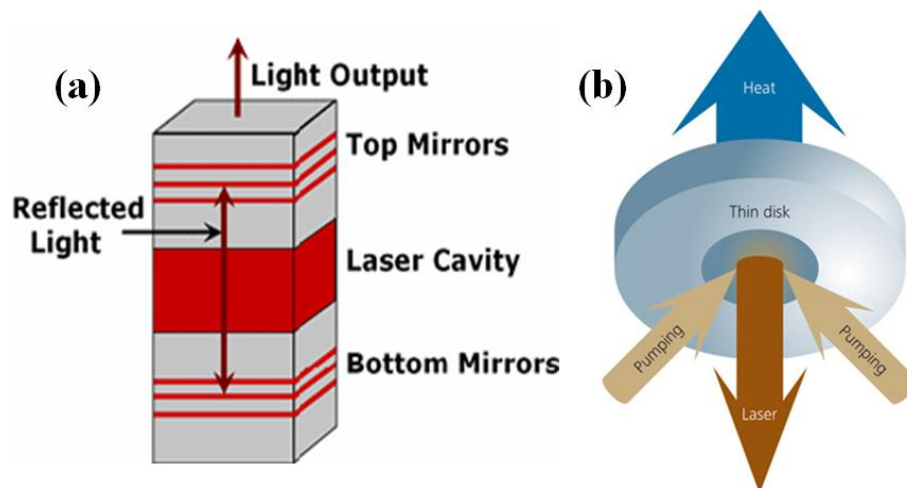
Figure 1-1: Schematic of (a) Vertical-Cavity Surface-Emitting Laser (VCSEL) [61] and (b) solid-state optically pumped thin disk laser[62].

Early SDL systems were based on the InGaAs/GaAs material system, targeting the ~1000 nm wavelength region with output powers >0.5W. Since then wavelength coverage and highest achievable output powers has been extended due to our further understanding of semiconductor material systems and improvements to epitaxial growth techniques. Initially the driving market for their use had been display technology and the field of telecommunications to compete with InP-based platforms. At present there is a much wider scope of applications for SDLs as initially anticipated.

The optically pumped SDL is generally of the form shown in Figure 1-2, which demonstrates the external cavity formed between the epitaxial grown semiconductor chip and the external mirror. Further benefits to this architecture over its predecessor the VCSEL, lie in its functionality to include intracavity elements such as filters, saturable absorbers and nonlinear elements to allow single frequency, mode-locking and frequency doubling, without impinging on beam quality and high output power capability.
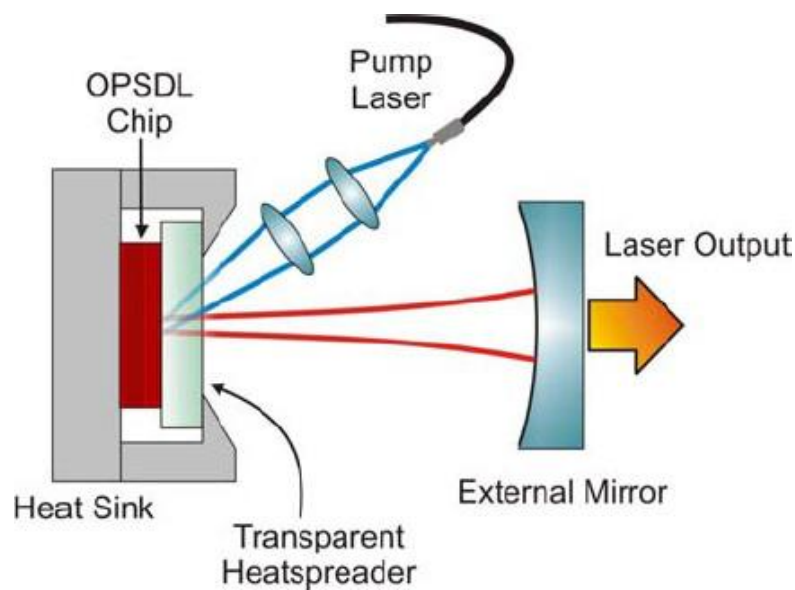
Figure 1-2: General form of an optically pumped Semiconductor Disk Laser (OPSDL) [63].

By analogy to doped-dielectric *microchip* lasers [64], a variation on the above design eliminates the air-gap formed between the OPSDL chip/heatspreader and the external

mirror. Instead the cavity may be composed entirely of a solid medium, such as that of the transparent heatspreader, forming the basis of a quasi-monolithic or *microchip* cavity configuration [65]. Successful demonstrations based on this plano-concave cavity design have been realised by Laurand *et al.* [66], depositing mirror coated microlenses onto the surface of the heatspreader, creating very compact laser devices as illustrated in Figure 1-3.
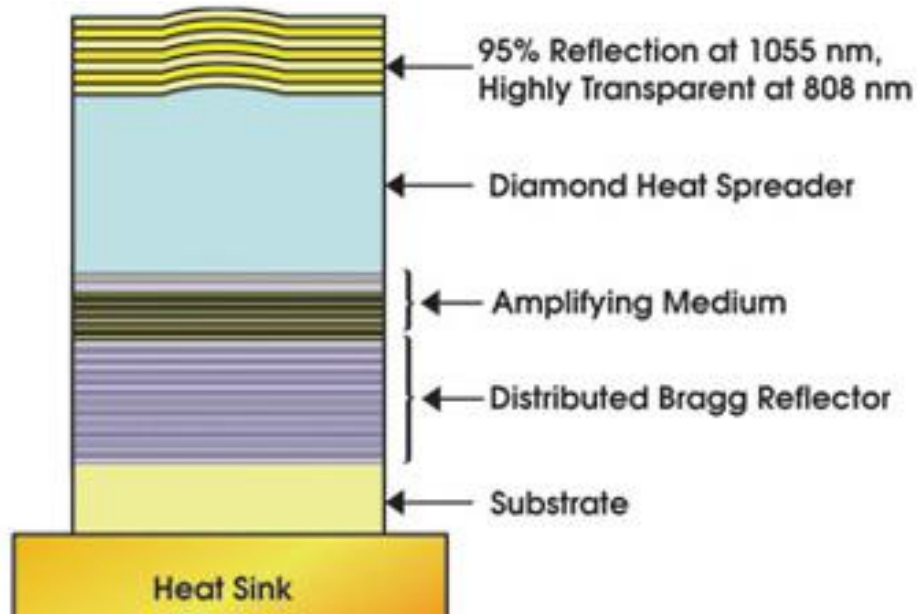
Figure 1-3: Illustration of plano-concave microchip SDL design [67].

In the realm of microchip visible lasers, developments exploiting more traditional doped-dielectrics as a gain medium and a frequency doubling crystal, have lead the way in intracavity frequency doubled laser design as illustrated in Figure 1-4, producing blue, red and green laser outputs [68-70].

9
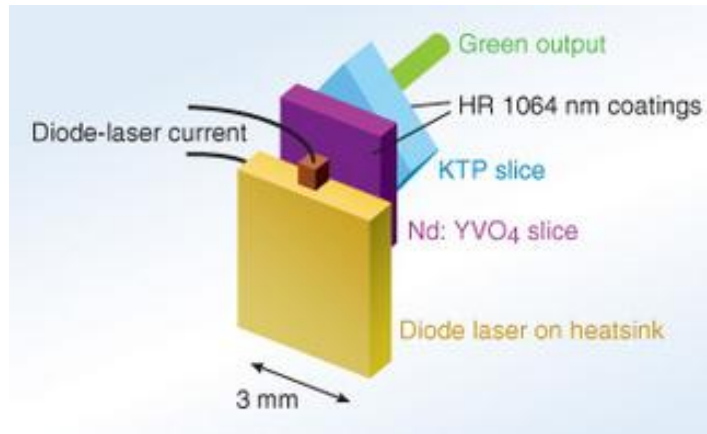
Figure 1-4: Diode pumped solid-state laser (DPSS) comprising Nd:YVO$_4$ gain material, with KTP doubling crystal to produce green (532nm) laser output [71].

A simpler version of a visible microchip laser with yellow emission was reported by Burns *et al.* [72]. It uses a diode laser to pump a Yb-doped crystal that also acts as a frequency doubler, Yb:YAB, referred as a microchip self-frequency doubled laser, as shown in Figure 1-5.
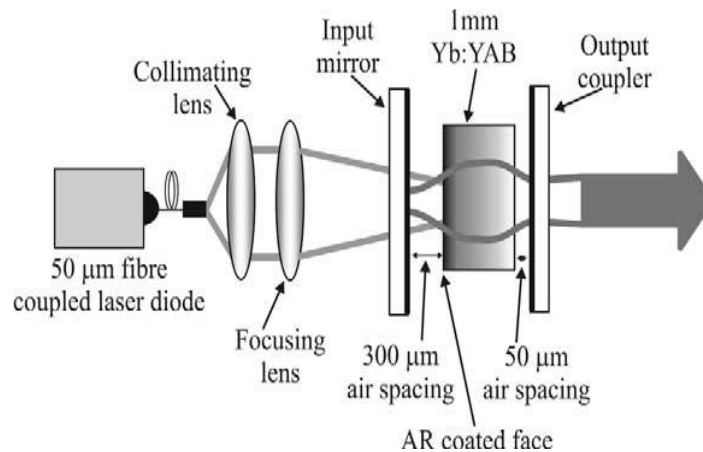
Figure 1-5: Schematic of diode pumped Yb:YAB self-frequency doubled laser developed by Burns et al [72].

This laser serves its purpose as a compact method to produce ~1mW of yellow laser light. However, the multimode low output power with added complexity of temperature tuning the material, paves the way for improved laser systems to be explored such as ones based on SDLs as attempted in this thesis.

10

In this respect, the pre-requisite to frequency doubled yellow-red emission is the generation of high brightness output in the 1150 – 1320 nm region. The wavelength operation of an SDL device is determined primarily by choice of semiconductor materials. A '*world map*' was developed in the 1970's [73] to provide a visual comparison of the various semiconductor material systems with respect to their band gap energy and crystal lattice parameter. This figure was developed based upon semi-empirical data gathered from a variety of research groups examining the properties of semiconductor alloys. Figure 1-6 is a variation of the *world map* highlighting the design wavelength region of interest for this thesis, 1.18 μm to 1.35 μm including the quaternaries GaInNAs lattice matched to GaAs, and both InGaAsP and AlInGaAs lattice matched to InP. In order to obtain good quality material growth, it is advantageous for all alloys to have a very similar lattice constant to the substrate. Therefore the lattice matched material should be close to or along the corresponding vertical solid-black lines, shown in Figure 1-6.
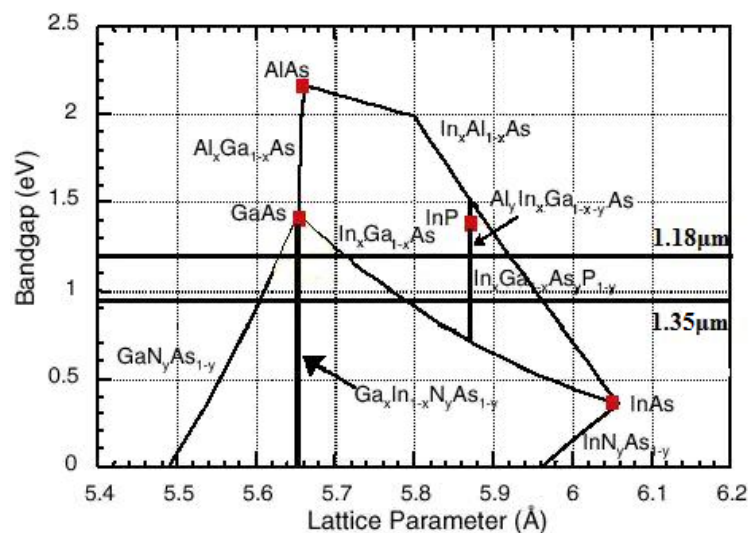
Figure 1-6: Binary, ternary and quaternary semiconductor material systems with respect to their bandgap energy and crystal lattice parameter. Indicated is the wavelength region 1.18 μm to 1.35 μm [74].

Earlier SDL designs used GaAs QWs for 840 nm emission [75, 76], and InGaAs QWs for 920 nm [77], ~960 nm [3, 78], ~980 nm [79, 80], ~1000 nm [60, 81, 82], ~1060 nm [83-85] and 1175 nm [86] emissions. These structures were all lattice matched to a GaAs substrate operating at their fundamental wavelength. SDLs implementing InGaAsP and AlInGaAs gain materials lattice matched to InP have

been demonstrated, with operation at 1310 nm [87], 1550 nm [87, 88], and 1549 nm [89]. The emergence of GaInNAs has enabled the lattice matching capability to GaAs whilst potentially accessing wavelengths between 1150 – 1500 nm.

Sophisticated growth techniques such as that of Molecular Beam Epitaxy (MBE), allows compound semiconductors to be grown at atomic scales. The significance of this allows us to create periodic potentials within the crystalline structure with dimensions equating to the de Broglie wavelengths of electrons and holes. At the core of SDL operation is the quantum well, with the emission wavelength as a consequence of the bandgap of the material as demonstrated in Figure 1-7. The dispersion in the crystalline semiconductor material describes the occupation of the carriers (electrons and holes) along the same energy band with a continuous distribution of energies, but has a different wavevector. Further details of the conditions governing the emission are provided in Chapter 2, Section 2.2.2.
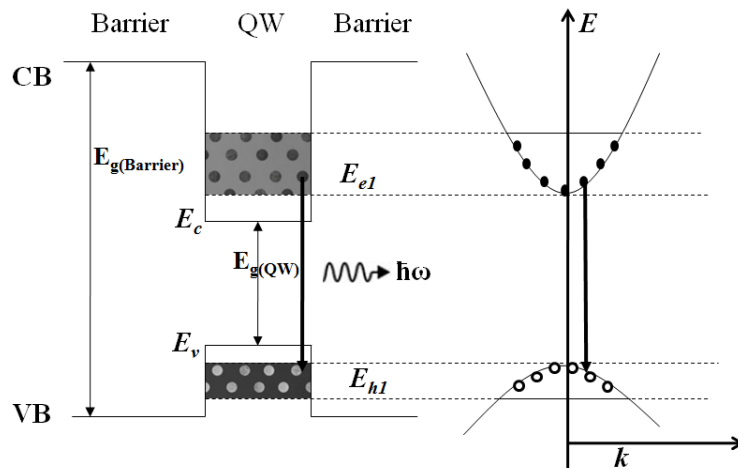
Figure 1-7: Quantum well structure showing the energies E_c and E_v of the conduction band (CB) and valence band (VB) edges respectively, and the bandgaps of the barrier $E_{g(Barrier)}$ and QW $E_{g(QW)}$ with photon emission $\hbar\omega$ from $e1$-$h1$ transitions between the quantized energy bands within the well, and the reciprocal energy dispersion in k-space.

In the case of InGaAs/GaAs QWs, the bandgap performance has been well documented [90-94], but in order to reach longer wavelengths higher concentrations of indium are needed. Unfortunately the wavelength operation is limited to <1.2 μm due to catastrophic structural collapse at high concentrations.

12

Evolution in growth of this material leads to the formation of coherently strained islands, or quantum dots (QD) in order to alleviate the strain. This self-assembly of QDs is better known as Stranski-Krastanow growth [95, 96], which has enabled the production of alternative laser structures at operational wavelengths up to 1.3 μm on GaAs substrates [97]. Through continual improvements to growth and design criteria, the QD is fast becoming a rival technology to that of QWs. Devices exploiting this technology have employed techniques such as dots-in-a-well (DWELL) to maximise gain in the structure [98], as well as multiple stacks of QDs to ensure dislocation free growth [99]. Good performance SDLs exploiting QD active regions have been demonstrated in the time frame of this PhD [100-103].

As an alternative to InGaAs QDs, the addition of nitrogen has been shown to enable long wavelength (1.2 − 1.5 μm) emission [15, 104] and serves as the basis for the gain of the SDLs studied in this thesis. Indeed, the unique III-V quaternary material GaInNAs has sparked a great deal of interest, since this material possesses some interesting traits. Nitrogen inclusion into GaAs has been known to exhibit a large bandgap bowing, referring to the curves generated between constituent semiconductor alloy materials as shown in Figure 1-6, whilst red-shifting the energy [105]. Yet it has been proposed that the distribution of nitrogen atoms into the host material GaInAs is random throughout the structure [106, 107] with the formation of cluster states in the conduction band. In addition the introduction of nitrogen has been interpreted as an impurity which manifests as a deep level defect within the material [108-110]. These explain in part the behaviour of this material, particularly its large bandgap dependence on nitrogen concentration and large effective mass, with weaker bandgap dispersion and therefore temperature insensitivity. The semi-empirical Band Anti-Crossing (BAC) method has been developed to describe the interaction between the localised states of the nitrogen with the host matrix GaInAs delocalised states [111-113].

The relationship between the two interacting energy states can be described using the two-state eigenvalue problem [111], as shown in Equation (1.1.1). The perturbed energy of the conduction band is associated with the nitrogen impurity E_N in relation to the energy of the GaInAs host matrix E_M.

$$\begin{vmatrix} E - E_M & V_{MN} \\ V_{MN} & E - E_N \end{vmatrix} \qquad (1.1.1)$$

The parameter V_{MN} is the interaction between the two states. This relationship in terms of the molar fraction of nitrogen is given in Equation (1.1.2) [112] with C_{NM} as the semiconductor matrix constant and y the nitrogen concentration.

$$V_{NM} = C_{NM}\sqrt{y} \qquad (1.1.2)$$

The BAC model formulates a split in the conduction band as shown in Figure 1-8, producing two sub-bands E_+ and E_- [111] as expressed in Equation (1.1.3).

$$E_{\pm} = \frac{\left((E_N + E_M) \pm \sqrt{(E_N - E_M)^2 + 4V_{MN}^2} \right)}{2} \qquad (1.1.3)$$

Extensive studies of this material system by Skierbiszewski *et al.* [114, 115] have found typical values of $C_{NM} \approx 2.7eV$ and $E_N \approx 1.65eV$.
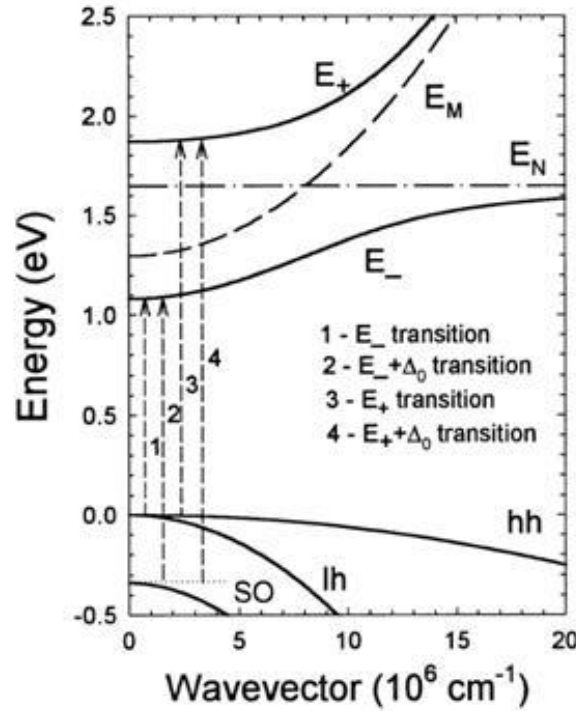
Figure 1-8: Energy band splitting into E_+ and E_- bands, indicating the N impurity level energy band E_N and host energy level E_M. The transitions between the light/heavy hole and spin-orbital split-off valence bands in relation to the E_+ and E_- bands are shown. [112]

These results have been verified using pressure experiments [111, 116], such that the nitrogen impurity level reduces the pressure coefficient of the conduction band, into the two sub-bands E_+ and E_-. The lower sub-band, E_- facilitates a reduction in the bandgap, whilst the E_+ transition from the valence band results in a high energy edge [117]. Similarly the affect on the electron effective mass is shown in Equation (1.1.4) [114], which is dependent upon the nitrogen composition, y and m_M is the electron effective mass of the matrix material. Experimental results indicate a large effective mass.

$$\frac{1}{m_\pm^*} = \frac{1}{2m_M}\left[1 \pm \frac{(E_M-E_N)}{\sqrt{(E_M-E_N)^2+4yC_{NM}^2}}\right] \qquad (1.1.4)$$

Further use of the BAC model has been incorporated into the gain section within Chapter 2.

The significance of the GaInNAs material system has the potential to rival InP-based systems for telecoms applications, but also due to its fast absorption recovery it has been useful as a saturable absorber for modelocking solid-state lasers [118-120] and as a modulator device [121-123] due to its large quantum confined Stark effect (QCSE). Importantly, its use as a gain element for SDLs [124, 125] forms the vital component to this PhD research work.

1.3 Thesis Scope

This thesis has been organised into two segments. The first of which discusses the design, fabrication and performance related aspects of GaInNAs/GaAs based SDL devices extending across Chapters 2, 3 and 4. The second segment is applications based, providing experimental results of the SDL used as a pump source in Chapter 5 and frequency doubled in Chapter 6.

Chapter 2 delves into the structural design of SDLs, with particular emphasis given to each of the main sections of the device; the Distributed Bragg Reflector mirror, the gain region, the confinement window and finally the cap layer. MBE growth has

been used to produce the semiconductor wafers which have been implemented as SDL devices. The growth of dilute nitride materials has some associated challenges which shall be explained.

Chapter 3 reflects the importance of thermal management necessary for successful operation of SDLs, providing an initial synopsis of progress made in this area. Building on previous knowledge, simulation work shall be presented to compare the thermal performance of devices based on their optical pumping regime (front or end pumped) using different configurations of diamond heatspreader within the structure and thin disk structures. Another examination focuses on the material systems, in order to put into perspective the thermal response of GaInNAs compared to InP-based active regions. The final section describes the construction of the laser, providing details of the bonding to the diamond heatspreader and subsequent mounting onto the water cooled copper heatsink.

Chapter 4 presents the characterisation and performance related results for a selection of SDL devices. The reflectivity and photoluminescence are measured to relate the output to design expectations. Laser performance is then presented for a set of devices with emission wavelengths spanning the $1180 - 1320$ nm range. The experimental results are also used to confirm the simulation work performed in Chapter 3 on the thermal resistance.

Chapter 5 is the first of two application-based chapters, demonstrating the use of an SDL as an excitation source. In the first instance, an SDL designed for operation ~1220 nm was used to pump Tm^{3+}(,Ho^{3+})-doped glass and crystal lasers. In addition a 1220 nm SDL was used as the pump source for Raman amplification in a silica fibre.

Chapter 6 explores the design of a frequency doubled microchip SDL with yellow laser output ~590 nm. An initial survey of the last 12 years of frequency-doubled SDLs demonstrates the attractiveness of this type of laser for emission in the UV/Visible. The design aspects of a microchip frequency doubled SDL are explored, highlighting cavity configurations and the device thermal response. Experimental

results shall be presented for a double-bonded SDL, to include the nonlinear crystal-diamond heatspreader-SDL chip as a step towards the microchip configuration.

Chapter 7 provides a final summary of this thesis and makes suggestions for further development work which was not undertaken during this PhD.

References

[1]   T. H. Maiman, "Stimulated Optical Radiation in Ruby," *Nature,* vol. 187, pp. 493-494, (1960).

[2]   Solus-Technologies Ltd. Available: http://www.solus-technologies.com/

[3]   B. Rudin, A. Rutz, M. Hoffmann, D. J. H. C. Maas, A.-R. Bellancourt, E. Gini, T. Südmeyer and U. Keller, "Highly efficient optically pumped vertical-emitting semiconductor laser with more than 20 W average output power in a fundamental transverse mode," *Optics Letters,* vol. 33, pp. 2719-2721, (2008).

[4]   J. Chilla, Q.-Z. Shu, H. Zhou, E. Weiss, M. Reed and L. Spinelli, "Recent advances in optically pumped semiconductor lasers," *Proceedings of SPIE Solid State Lasers XVI: Technology and Devices,* vol. 6451, (2007).

[5]   A. C. Tropper and S. Hoogland, "Extended cavity surface-emitting semiconductor lasers," *Progress in Quantum Electronics,* vol. 30, pp. 1-43, (2006).

[6]   N. Schulz, J.-M. Hopkins, M. Rattunde, D. Burns and J. Wagner, "High-brightness long-wavelength semiconductor disk lasers," *Laser & Photonics Reviews,* vol. 2, pp. 160-181, (2008).

[7]   S. Calvez, J. E. Hastie, M. Guina, O. G. Okhotnikov and M. D. Dawson, "Semiconductor disk lasers for the generation of visible and ultraviolet radiation," *Laser & Photonics Reviews,* vol. 3, pp. 407 - 434, (2009).

[8]   M. D. Dawson, "Visible and Ultraviolet Semiconductor Disk Lasers," in *The European Conference on Lasers and Electro-Optics (CLEO/Europe)*, Munich, Germany, p. CB1_1, (2009).

[9]   D. J. Stothard, J.-M. Hopkins, D. Burns and M. H. Dunn,"Stable, continuous-wave, intracavity, optical parametric oscillator pumped by a semiconductor disk laser (VECSEL)," *Optics Express,* vol. 17, pp. 10648-10658, (2009).

[10]   N. Hempler, J.-M. Hopkins, M. Rattunde, B. Rösener, R. Moser, C. Manz, K. Köhler, J. Wagner and D. Burns, "Tuning and brightness optimization of high-performance GaSb-based semiconductor disk lasers from 1.86 to 2.80üm," in *The European Conference on Lasers and Electro-Optics (CLEO/Europe)*, Munich, Germany, p. CB7_3, (2009).

[11]   M. Rahim, M. Arnold, F. Felder, K. Behfar and H. Zogg, "Midinfrared lead-chalcogenide vertical external cavity surface emitting laser with 5 μm wavelength," *Applied Physics Letters,* vol. 91, pp. 151102-151102-3, (2007).

[12]   M. Rahim, A. Khiar, F. Felder, M. Fill and H. Zogg, "4.5 um wavelength vertical external cavity surface emitting laser operating above room temperature," *Applied Physics Letters,* vol. 94, pp. 201112-3, (2009).

[13]   J. V. Moloney, M. Scheller, J. M. Yarborough, S. W. Koch, M. Koch and M. Fallahi, "Compact, high-power, roomtemperature, narrow-line terahertz source". *SPIE Newsroom*, (2011), Available: http://spie.org/documents/Newsroom/Imported/003523/003523_10.pdf

[14]   R. Gebs, P. Klopp, G. Klatt, T. Dekorsy, U. Griebner and A. Bartels, "Time-domain terahertz spectroscopy based on asynchronous optical sampling with femtosecond semiconductor disk laser," *Electronics Letters,* vol. 46, pp. 75-77, (2010).

[15]   M. Kondow, K. Uomi, A. Niwa, T. Kitatani, S. Watahiki and Y. Yazawa, "GaInNAs: A Novel Material for Long-Wavelength-Range Laser Diodes with Excellent High-Temperature Performance," *Japanese Journal of Applied Physics,* vol. 35, pp. 1273 - 1275, (1996).

[16]   M. Kondow, T. Kitatani, S. Nakatsuka, M. C. Larson, K. Nakahara, Y. Yazawa, M. Okai and K. Uomi, "GaInNAs: A Novel Material for Long-Wavelength Semiconductor Lasers," *IEEE Journal of Selected Topics in Quantum Electronics,* vol. 3, pp. 719 - 730, (1997).

[17]   Y. Y. Voronov, V. G. Muradov and D. G. Sannikov,"Absorption Spectra of Gasolines in the Region 1090–1220 nm," *Journal of Applied Spectroscopy,* vol. 70, pp. 628-631, (2003).

[18]   V. G. Muradov and D. G. Sannikov, "Study of Absorption Spectra of Gasolines and Other Hydrocarbon Mixtures in the Second Overtone Region of the CH_3, CH_2, CH Groups," *Journal of Applied Spectroscopy,* vol. 72, pp. 174 - 179, (2007).

[19]   Y.-S. Su, C.-F. Lin, D.-K. Yu and B.-R. Wu, "Semiconductor lasers tunable from 1.3 um to 1.54 um for optical communication," *Proceedings of SPIE: WDM and Photonic Switching Devices for Network Applications III,* vol. 4653, pp. 96 - 104, (2002).

[20]   S. L. Vetter, L. J. McKnight, S. Calvez, M. D. Dawson, F. Fusari, A. A. Lagatsky, W. Sibbett, C. T. A. Brown, V.-M. Korpijärvi, M. D. Guina, B. Richards, G. Jose and A. Jha, "GaInNAs semiconductor disk lasers as pump sources for Tm3+ (,Ho3+)-doped glass, crystal and fibre lasers " in *Proceedings of SPIE Solid State Lasers XVIII: Technology and Devices*, vol. 7193, pp. 719317-719317-11, (2009).

[21]   N. Hempler, J.-M. Hopkins, B. Rösener, M. Rattunde, J. Wagner, V. V. Fedorov, I. S. Moskalev, S. B. Mirov and D. Burns, "Semiconductor disk laser pumped Cr^{2+}:ZnSe lasers," *Optics Express,* vol. 17, pp. 18136-18141, (2009).

[22]   N. Hempler, J.-M. Hopkins, B. Rösener, N. Schulz, M. Rattunde, J. Wagner, U. N. Roy, A. Burger and D. Burns, "Semiconductor Disk Laser Pumped Cr^{2+}:Chalcogenide Lasers," in *Conference on Lasers and Electro-optics/ Quantum Electronics and Laser Science Conference and Photonics Applications Systems Technologies* San Jose, CA, USA, p. CFW2, (2008).

[23]   D. C. Parrotta, W. Lubeigt, A. J. Kemp, D. Burns, M. D. Dawson and J. E. Hastie, "Continuous-wave Raman laser pumped within a semiconductor disk laser cavity," *Optics Letters,* vol. 36, pp. 1083-1085, (2011).

[24]   A. Chamorovskiy, J. Rautiainen, A. Rantamäki and O. G. Okhotnikov, "Low-noise Raman fiber amplifier pumped by semiconductor disk laser," *Optics Express,* vol. 19, pp. 6414-6419, (2011).

[25]   A. Chamorovskiy, J. Rautiainen, A. Rantamäki, K. M. Golant and O. G. Okhotnikov,"1.3 μm Raman-bismuth fiber amplifier pumped by semiconductor disk laser," *Optics Express,* vol. 19, pp. 6433-6438, (2011).

[26]   X.-Y. Liu, Bo Zhang, C.-P. Wang, S. Li, F. Su and P. Jia, "Diode-Pumped Intracavity Frequency-Doubled Nd:YVO$_4$ Self-Raman Yellow Laser," *Acta Photonica Sinica,* vol. 36, pp. 1777 - 1780, (2007).

[27]   J. Zhang, J. Wang, P. Su, L. Han and G. Xiong, "Theoretical and Experimental Study of LD Pumped Nd:YVO$_4$ Yellow Laser with Sum-Frequency Generation," *Acta Photonica Sinica,* vol. 12, (2008).

[28]   T.-H. Liu, H. Tan, L. L. Gao, B. Wang and M. Jie, "Intracavity Sum-frequency Mixing with BIBO in 593 nm Laser," *Acta Photonica Sinica,* vol. 36, pp. 1195 - 1197, (2007).

[29]   Y.-F. Chen and S. W. Tsai, "Diode-pumped -switched Nd:YVO4 yellow laser with intracavity sum-frequency mixing," *Optics Letters,* vol. 27, pp. 397-399, (2002).

[30]   A. Kananovich, A. Demidovich, M. Danailov, A. Grabtchikov and V. Orlovich, "All-solid-state quasi-CW yellow laser with intracavity self-Raman conversion and sum frequency generation," *Laser Physics Letters,* vol. 7, pp. 573 - 578, (2010).

[31]   Y.-F. Lu, Y. Bo, S.-Y. Xie, Q.-J. Peng, D.-F. Cui and Z.-Y. Xu, "An 8.1 W diode pumped solid-state quasi-continuous-wave yellow laser at 589 nm by intracavity sum-frequency mixing generation," *Optics Communications,* vol. 281, pp. 5596-5600, (2008).

[32]   A. Geng, Y. Bo, X. Yang, H. Li, Z. Sun, Q. Peng, X. Wang, G. Wang, D. Cui and Z. Xu, "Intracavity sum-frequency generation of 3.23 W continuous-wave yellow light in an Nd:YAG laser," *Optics Communications,* vol. 255, pp. 248-252, (2005).

[33]   D. M. Pennington, J. W. Dawson, A. Drobshoff, Z. Liao, S. Payne, D. Bonaccini, W. Hackenberg and L. Taylor, "Compact fiber laser approach to 589 nm laser guide stars," in *Conference on Lasers and Electro-Optics/International Quantum Electronics Conference and Photonic Applications Systems Technologies*, San Francisco, CA, USA, p. CFD1, (2004).

[34]   Y. Yao, Q. Zheng, D. P. Qu, K. Zhou, Y. Liu and L. Zhao, "All-solid-state continuous-wave frequency-doubled Nd:YAG/LBO laser with 1.2 W output power at 561 nm," *Laser Physics Letters,* vol. 7, pp. 112 - 115, (2010).

[35]   H. Watanabe, T. Omatsu and M. Tateda, "Efficient self-pumped phase conjugation with a loop geometry in a Rhodamine-6G solid dye laser amplifier," *Optics Express,* vol. 11, pp. 176-180, (2003).

[36]   S. Sinha, C. Langrock, M. J. Digonnet, M. M. Fejer and R. L. Byer, "Efficient yellow-light generation by frequency doubling a narrow-linewidth 1150 nm ytterbium fiber oscillator," *Optics Letters,* vol. 31, pp. 347-349, (2006).

[37]   V. V. Dvoyrin, V. M. Mashinsky, O. I. Medvedkov and E. M. Dianov, "Yellow Frequency-Doubled Self-Heated Yb Fiber Laser," in *Conference on Lasers and Electro-Optics/Quantum Electronics and Laser Science Conference and Photonic Applications Systems Technologies*, San Jose, CA, USA, p. CWB5, (2008).

[38]   H. Maruyama, A. Shirakawa, K. i. Ueda, C. B. Olausson, J. K. Lyngse and J. Broeng, "1178 nm all Yb-fiber laser source power-scaled by solid-core photonic bandgap fiber for 589nm generation," in *European Conference on Lasers and Electro-Optics 2009 and the European Quantum Electronics Conference. CLEO Europe - EQEC 2009*, pp. 1-1, (2009).

[39]   H. M. Pask and J. A. Piper, "Efficient all-solid-state yellow laser source producing 1.2-W average power," *Optics Letters,* vol. 24, pp. 1490-1492, (1999).

[40]   C. He and T. H. Chyba, "Solid-state barium nitrate Raman laser in the visible region," *Optics Communications,* vol. 135, pp. 273-278, (1997).

[41]   D. Georgiev, V. P. Gapontsev, A. G. Dronov, M. Y. Vyatkin, A. B. Rulkov, S. V. Popov and J. R. Taylor,"Watts-level frequency doubling of a narrow line linearly polarized Raman fiber laser to 589nm," *Optics Express,* vol. 13, pp. 6772-6776, (2005).

[42]   S. V. Popov, A. B. Rulkov, J. R. Taylor, A. G. Dronov, M. Y. Vyatkin, D. Georgiev and V. P. Gapontsev, "3W CW Generation at 589nm with Narrow Line Linearly Polarized Raman Fibre Laser," in *Advanced Solid-State Photonics*, Incline Village, NV, USA, p. MC4, (2006).

[43]   Y. Feng, S. Huang, A. Shirakawa and K.-i. Ueda, "589 nm Light Source Based on Raman Fiber Laser," *Japanese Journal of Applied Physics,* vol. 43, pp. L722 - L724, (2004).

[44]   Y. Feng, L. R. Taylor and D. B. Calia, "25 W Raman-fiber-amplifier-based 589 nm laser for laser guide star," *Optics Express,* vol. 17, pp. 19021-19026, (2009).

[45]   A. A. Kaminskii, C. L. McCray, H. R. Lee, S. W. Lee, D. A. Temple, T. H. Chyba, W. D. Marsh, J. C. Barnes, A. N. Annanenkov, V. D. Legun, H. J. Eichler, G. M. A. Gad and K. Ueda, "High efficiency nanosecond Raman lasers based on tetragonal $PbWO_4$ crystals," *Optics Communications,* vol. 183, pp. 277-287, (2000).

[46]   L. Taylor, A. Friedenauer, V. Protopopov, Y. Feng, D. Bonaccini Calia, V. Karpov, W. Hackenberg, R. Holzlohner, W. Clements, M. Hager, F. Lison and W. Kaenders, "20 W at 589 nm via frequency doubling of coherently beam combined 2-MHz 1178-nm CW signals amplified in Raman PM fiber amplifiers," in *European Conference on Lasers and Electro-Optics 2009 and the European Quantum Electronics Conference. CLEO Europe - EQEC 2009,* pp. 1-1, (2009).

[47]   L. R. Taylor, Y. Feng and D. B. Calia, "50W CW visible laser source at 589nm obtained via frequency doubling of three coherently combined narrow-band Raman fibre amplifiers," *Optics Express,* vol. 18, pp. 8540-8555, (2010).

[48]   E. M. Dianov, A. V. Shubin, M. A. Melkumov, O. I. Medvedkov and I. A. Bufetov, "High-power cw bismuth-fiber lasers," *Journal of Optical Society of America B,* vol. 24, pp. 1749-1755, (2007).

[49]   A. B. Rulkov, A. A. Ferin, S. V. Popov, J. R. Taylor, I. Razdobreev, L. Bigot and G. Bouwmans, "Narrow-line, 1178nm CW bismuth-doped fiber laser with 6.4W output for direct frequency doubling," *Optics Express,* vol. 15, pp. 5473-5476, (2007).

[50]   B. Luther-Davies, V. Kolev and M. Duering, "A Simple Scalable Solid-State 589nm Laser Guide Star Source Based on Optical Parametric Amplifiers," in *Conference on Lasers and Electro-Optics/Quantum Electronics and Laser Science Conference and Photonic Applications Systems Technologies*, Baltimore, Maryland, USA, p. CWB2, (2007).

[51]   M. Duering, V. Kolev and B. Luther-Davies, "Generation of tuneable 589nm radiation as a Na guide star source using an optical parametric amplifier," *Optics Express,* vol. 17, pp. 437-446, (2009).

[52]   J. Limpert, H. Zellmer, P. Riedel, G. Maze and A. Tunnermann, "Laser oscillation in yellow and blue spectral range in Dy^{3+}:ZBLAN," *Electronics Letters,* vol. 36, pp. 1386 - 1387, (2000).

[53]   Y. Fujimoto, O. Ishii and M. Yamazaki, "Yellow laser oscillation in Dy^{3+}-doped waterproof fluoro-aluminate glass fibre pumped by 398.8 nm GaN laser diodes," *Electronics Letters,* vol. 46, pp. 586-587, (2010).

[54]   X. Guo, M. Chen, G. Li, B. Zhang, J. Yang, Z. Zhang and Y. Wang, "Diode-pumped 1123-nm Nd:YAG laser," *Chinese Optics Letters,* vol. 2, pp. 402-404, (2004).

[55]   E. M. Dianov, S. V. Firstov, V. F. Khopin, A. N. Guryanov and I. A. Bufetov, "Bi-doped fibre lasers and amplifiers emitting in a spectral region of 1.3 μm," *Quantum Electronics,* vol. 38, pp. 615 - 617, (2008).

[56]   E. M. Dianov, M. A. Mel'kumov, A. V. Shubin, S. V. Firstov, V. F. Khopin, A. N. Gur'yanov and I. A. Bufetov,"Bismuth-doped fibre amplifier for the range 1300 — 1340 nm," *Quantum Electronics,* vol. 39, p. 1099, (2009).

[57]   V. V. Dvoirin, V. M. Mashinskii, O. I. Medvedkov, A. A. Umnikov, A. N. Gur'yanov and E. M. Dianov, "Bismuth-doped telecommunication fibres for lasers and amplifiers in the 1400–1500-nm region," *Quantum Electronics,* vol. 39, p. 583, (2009).

[58]   Macquarie University. Available: http://www.researchactive.mq.edu.au/showitem.asp?ItemID=508

[59]   A. Mooradian and M. E. Kuznetsov, "High Brightness, Vertical Cavity Semiconductor Lasers," US Patent, (1995).

[60]   M. Kuznetsov, F. Hakimi, R. Sprague and A. Mooradian, "High-power (>0.5 W CW) diode-pumped vertical-external-cavity surface-emitting semiconductor lasers with circular TEM_{00} beams," *IEEE Photonics Technology Letters,* vol. 9, pp. 1063-1065, (1997).

[61]   Olson-Technology Inc. Available: http://www.olson-technology.com/mr_fiber/glossary-uv.htm

[62]   Jenoptik AG. Available: http://www.jenoptik.com/Internet_EN_Scheibenlaser_Technologie

[63]   M. Rattunde, B. Rösener, N. Schulz, C. Manz, J.-M. Hopkins, D. Burns and J. Wagner, "Two-micron semiconductor disk lasers achieve higher powers". *Lasers & Sources*, (2008).

[64]   J. J. Zayhowski and A. Mooradian, "Single-frequency microchip Nd lasers," *Optics Letters,* vol. 14, pp. 24-26, (1989).

[65]   J. E. Hastie, J.-M. Hopkins, C. W. Jeon, S. Calvez, D. Burns, M. D. Dawson, R. Abram, E. Riis, A. I. Ferguson, W. J. Alford, T. D. Raymond and A. A. Allerman, "Microchip vertical external cavity surface-emitting lasers," in *The*

16th Annual Meeting of the IEEE Lasers and Electro-Optics Society, LEOS 2003, pp. 507-508 vol.2, (2003).

[66]   N. Laurand, C. L. Lee, E. Gu, J. E. Hastie, S. Calvez and M. D. Dawson, "Microlensed microchip VECSEL," *Optics Express,* vol. 15, pp. 9341-9346, (2007).

[67]   Photonics   Spectra,   Available: http://www.photonics.com/Article.aspx?AID=30698

[68]   D. G. Matthews, R. S. Conroy, B. D. Sinclair and N. MacKinnon, "Blue microchip laser fabricated from Nd:YAG and KNbO$_3$," *Optics Letters,* vol. 21, pp. 198-200, (1996).

[69]   R. S. Conroy, A. J. Kemp, G. J. Friel and B. D. Sinclair, "Microchip Nd:vanadate lasers at 1342 and 671nm," *Optics Letters,* vol. 22, pp. 1781-1783, (1997).

[70]   B. D. Sinclair, "Frequency-doubled microchip lasers," *Optical Materials,* vol. 11, pp. 217-233, (1999).

[71]   St Andrews University Microchip Laser Research Group. Available: http://www.st-andrews.ac.uk/~bds2/mchip.html

[72]   P. A. Burns, J. M. Dawes, P. Dekker, J. A. Piper, J. Li and J. Wang, "Coupled-cavity, single-frequency, tunable cw Yb:YAB yellow microchip laser," *Optics Communications,* vol. 207, pp. 315 -320, (2002).

[73]   A. I. Alferov, "Nobel Lecture: The double heterostructure concept and its applications in physics, electronics, and technology," *Reviews of Modern Physics,* vol. 73, pp. 767 - 782, (2001).

[74]   J. S. Harris Jr., "GaInNAs long-wavelength lasers: progress and challenges," *Semiconductor Science and Technology,* vol. 17, p. 880, (2002).

[75]   M. A. Holm, D. Burns, P. Cusumano, A. I. Ferguson and M. D. Dawson, "High-Power Diode-Pumped AlGaAs Surface-Emitting Laser," *Applied Optics,* vol. 38, pp. 5781-5784, (1999).

[76]   M. A. Holm, D. Burns, A. I. Ferguson and M. D. Dawson, "Actively stabilized single-frequency vertical-external-cavity AlGaAs laser," *IEEE Photonics Technology Letters,* vol. 11, pp. 1551-1553, (1999).

[77]   K. Ki-Sung, Y. Jaeryung, K. Gibum, L. Sangmoon, C. Soohaeng, K. Junyoun, K. Taek and P. Yongjo, "920-nm Vertical-External-Cavity Surface-Emitting Lasers With a Slope Efficiency of 58% at Room Temperature," *IEEE Photonics Technology Letters,* vol. 19, pp. 1655-1657, (2007).

[78]   L. Fan, M. Fallahi, J. Hader, A. R. Zakharian, J. V. Moloney, J. T. Murray, R. Bedford, W. Stolz and S. W. Koch, "Multichip vertical-external-cavity surface-emitting lasers: a coherent power scaling scheme," *Optics Letters,* vol. 31, pp. 3612-3614, (2006).

[79]   W. J. Alford, T. D. Raymond and A. A. Allerman, "High power and good beam quality at 980 nm from a vertical external-cavity surface-emitting laser," *Journal of the Optical Society of America B,* vol. 19, pp. 663-666, (2002).

[80]   L. Fan, M. Fallahi, A. R. Zakharian, J. Hader, J. V. Moloney, R. Bedford, J. T. Murray, W. Stolz and S. W. Koch, "Extended Tunability in a Two-Chip VECSEL," *IEEE Photonics Technology Letters,* vol. 19, pp. 544-546, (2007).

[81]   S. Lutgen, T. Albrecht, P. Brick, W. Reill, J. Luft and W. Spath, "8-W high-efficiency continuous-wave semiconductor disk laser at 1000 nm," *Applied Physics Letters,* vol. 82, pp. 3620-3622, (2003).

[82]   M. Kuznetsov, F. Hakimi, R. Sprague and A. Mooradian, "Design and characteristics of high-power (0.5-W CW) diode-pumped vertical-external-cavity surface-emitting semiconductor lasers with circular TEM_{00} beams," *IEEE Journal of Selected Topics in Quantum Electronics,* vol. 5, pp. 561-573, (1999).

[83]   A. Harkonen, S. Suomalainen, E. Saarinen, L. Orsila, R. Koskinen, O. Okhotnikov, S. Calvez and M. Dawson, "4 W single-transverse mode VECSEL utilising intra-cavity diamond heat spreader," *Electronics Letters,* vol. 42, pp. 693-694, (2006).

[84]   E. J. Saarinen, A. Härkönen, S. Suomalainen and O. G. Okhotnikov, "Power scalable semiconductor disk laser using multiple gain cavity," *Optics Express,* vol. 14, pp. 12868-12871, (2006).

[85]   K. S. Kim, J. R. Yoo, S. M. Lee, S. J. Lim, J. Y. Kim, J. H. Lee, S. H. Cho, T. Kim and Y. J. Park, "Highly efficient InGaAs QW vertical external cavity surface emitting lasers emitting at 1060 nm," *Journal of Crystal Growth,* vol. 287, pp. 629-632, (2006).

[86]   M. Fallahi, L. Fan, Y. Kaneda, C. Hessenius, J. Hader, H. Li, J. V. Moloney, B. Kunert, W. Stolz, S. W. Koch, J. Murray and R. Bedford, "5-W Yellow Laser by Intracavity Frequency Doubling of High-Power Vertical-External-Cavity Surface-Emitting Laser," *IEEE Photonics Technology Letters,* vol. 20, pp. 1700 - 1702, (2008).

[87]   A. Sirbu, A. Mereuta, J. Rautiainen, J. Lyytikainen, A. Caliman, O. Okhotnikov and E. Kapon, "High power vertical external cavity surface-emitting lasers (VECSELs) emitting in 1310 nm and 1550 nm bands," in *IEEE LEOS Annual Meeting Conference Proceedings, LEOS '09.*, pp. 835-836, (2009).

[88]   C. Symonds, I. Sagnes, J. L. Oudar, S. Bouchoule, A. Garnache, J. Berggren and M. Strassner, "Room temperature CW lasing operation of monolithically grown 1.55 μm vertical external cavity surface emitting laser," *Optics Communications,* vol. 230, pp. 419-423, (2004).

[89]   H. Lindberg, A. Larsson and M. Strassner, "Single-frequency operation of a high-power, long-wavelength semiconductor disk laser," *Optics Letters,* vol. 30, pp. 2260-2262, (2005).

[90]   J. J. Coleman, "Strained-Layer InGaAs Quantum-Well Heterostructure Lasers," *IEEE Journal on Selected Topics in Quantum Electronics,* vol. 6, pp. 1008 - 1013, (2000).

[91]   H.-P. D. Yang, I.-L. Chen, C.-H. Lee, C.-H. Chiou, T.-D. Lee, I.-C. Hsu, F.-I. Lai, G. Lin, H.-C. Kuo and J. Y. Chi, "Highly Strained InGaAs/GaAs Quantum Well Vertical-Cavity Surface-Emitting Lasers," *Japanese Journal of Applied Physics,* vol. 46, pp. L509-L511, (2007).

[92]   L. Fan, C. Hessenius, M. Fallahi, J. Hader, H. Li, J. V. Moloney, W. Stolz, S. W. Koch., J. T. Murray and R. Bedford, "Highly strained InGaAs/GaAs multiwatt vertical-external-cavity surface-emitting laser emitting around 1170 nm," *Applied Physics Letters,* vol. 91, pp. 131114-1 - 131114-3, (2007).

23

[93] A. Tropper, S. Hoogland, A. Garnache, K. G. Wilcox, Z. Mihoubi, S. Elsmere and A. Quarterman, "Spectrotemporal Gain Bandwidth Measurement in an InGaAs/GaAsP Quantum Well Vertical-External-Cavity Surface-Emitting Semiconductor Laser," in *Conference on Lasers and Electro-Optics/Quantum Electronics and Laser Science Conference and Photonic Applications Systems Technologies*, San Jose, CA, USA, p. CWD6, (2008).

[94] M. A. Holm, D. Burns, A. I. Ferguson and M. D. Dawson, "Single-frequency second-harmonic generation in a vertical external-cavity semiconductor laser," in *Conference on Lasers and Electro-Optics,(CLEO 2000),* pp. 440-441, (2000).

[95] I. N. Stranski and L. Krastanow, "Zur Theorie der orientierten Ausscheidung von Ionenkristallen aufeinander," *Monatshefte für Chemie / Chemical Monthly,* vol. 71, pp. 351-364, (1937).

[96] T. Walther, A. G. Cullis, D. J. Norris and M. Hopkinson, "Nature of the Stranski-Krastanow Transition during Epitaxy of InGaAs on GaAs," *Physical Review Letters,* vol. 86, p. 2381, (2001).

[97] P. Bhattacharya and Z. Mi, "Quantum-Dot Optoelectronic Devices," *Proceedings of the IEEE,* vol. 95, pp. 1723-1740, (2007).

[98] D. L. Huffaker, G. Park, Z. Zou, O. B. Shchekin and D. G. Deppe, "1.3 μm room-temperature GaAs-based quantum-dot laser," *Applied Physics Letters,* vol. 73, p. 2564, (1998).

[99] H. Y. Liu, I. R. Sellers, T. J. Badcock, D. J. Mowbray, M. S. Skolnick, K. M. Groom, M. Gutiérrez, M. Hopkinson, J. S. Ng, J. P. R. David and R. Beanland, "Improved performance of 1.3μm multilayer InAs quantum-dot lasers using a high-growth-temperature GaAs spacer layer," *Applied Physics Letters,* vol. 85, (2004).

[100] P. J. Schlosser, J. E. Hastie, S. Calvez, A. B. Krysa and M. D. Dawson, "InP/AlGaInP quantum dot semiconductor disk lasers for CW TEM$_{00}$ emission at 716 - 755 nm," *Optics Express,* vol. 17, pp. 21782-21787, (2009).

[101] M. Butkus, K. G. Wilcox, J. Rautiainen, O. G. Okhotnikov, S. S. Mikhrin, I. L. Krestnikov, A. R. Kovsh, M. Hoffmann, T. Südmeyer, U. Keller and E. U. Rafailov,"High-power quantum-dot-based semiconductor disk laser," *Optics Letters,* vol. 34, pp. 1672-1674, (2009).

[102] T. D. Germann, A. Strittmatter, U. W. Pohl, D. Bimberg, J. Rautiainen, M. Guina and O. G. Okhotnikov,"Quantum-dot semiconductor disk lasers," *Journal of Crystal Growth,* vol. 310, pp. 5182-5186, (2008).

[103] J. Rautiainen, I. Krestnikov, M. Butkus, E. U. Rafailov and O. G. Okhotnikov, "Optically pumped semiconductor quantum dot disk laser operating at 1180 nm," *Optics Letters,* vol. 35, pp. 694-696, (2010).

[104] S. Sato and S. Satoh, "1.21 μm Continuous-Wave Operation of Highly Strained GaInAs Quantum Well Lasers on GaAs Substrates," *Japanese Journal of Applied Physics,* vol. 38, pp. L990-L992, (1999).

[105] M. Weyers, M. Sato and H. Ando,"Red shift of photoluminescence and absorption in dilute GaAsN alloy layers," *Japanese Journal of Applied Physics,* vol. 31, pp. L853 - L855, (1992).

[106] P. R. C. Kent and A. Zunger,"Theory of electronic structure evolution in GaAsN and GaPN alloys," *Physical Review B,* vol. 64, p. 115208, (2001).

[107] A. Al-Yacoub and L. Bellaiche, "Quantum mechanical effects in (Ga,In)(As,N) alloys," *Physical Review B,* vol. 62, p. 10847, (2000).

[108] P. Vogl, "Predictions of Deep-Impurity-Level Energies in Semiconductors," Chapter 2, pp. 101 - 155 in *Advances in Electronics and Electron Physics* vol. 62, P. W. Hawkes, Editor, Academic Press Inc., (1984).

[109] P. Krispin, S. G. Spruytte, J. S. Harris and K. H. Ploog, "Deep-level defects in MBE-grown Ga(As,N) layers," *Physica B: Condensed Matter,* vol. 308-310, pp. 870-873, (2001).

[110] H. P. Hjalmarson, P. Vogl, D. J. Wolford and J. D. Dow, "Theory of Substitutional Deep Traps in Covalent Semiconductors," *Physical Review Letters,* vol. 44, p. 810, (1980).

[111] W. Shan, W. Walukiewicz, J. W. Ager, E. E. Haller, J. F. Geisz, D. J. Friedman, J. M. Olson and S. R. Kurtz, "Band Anticrossing in GaInNAs Alloys," *Physical Review Letters,* vol. 82, p. 1221, (1999).

[112] W. Shan, W. Walukiewicz, K. M. Yu, J. W. Ager III, E. E. Haller, J. F. Geisz, D. J. Friedman, J. M. Olson, S. R. Kurtz, H. P. Xin and C. W. Tu, "Band Anticrossing in III–N–V Alloys," *physica status solidi (b),* vol. 223, pp. 75-85, (2001).

[113] M. Hetterich, A. Grau, A. Egorov, Yu and H. Riechert, "Boundary conditions for the electron wavefunction in GaInNAs-based quantum wells and modelling of the temperature-dependent bandgap," *Journal of Physics: Condensed Matter,* vol. 16, pp. S3151 - S3159, (2004).

[114] C. Skierbiszewski, "Experimental studies of the conduction-band structure of GaInNAs alloys," *Semiconductor Science and Technology,* vol. 17, p. 803, (2002).

[115] C. Skierbiszewski, P. Perlin, P. Wisniewski, T. Suski, J. F. Geisz, K. Hingerl, W. Jantsch, D. E. Mars and W. Walukiewicz, "Band structure and optical properties of $In_yGa_{1-y}As_{1-x}N_x$ alloys," *Physical Review B,* vol. 65, p. 035207, (2001).

[116] X. Liu, M.-E. Pistol, L. Samuelson, S. Schwetlick and W. Seifert, "Nitrogen pair luminescence in GaAs," *Applied Physics Letters,* vol. 56, p. 1451, (1990).

[117] Q. X. Zhao, S. M. Wang, Y. Q. Wei, M. Sadeghi, A. Larsson and M. Willander, "Radiative recombination of localized excitons and mobility edge excitons in GaInNAs/GaAs quantum wells with strong carrier localization," *Physics Letters A,* vol. 341, pp. 297-302, (2005).

[118] H. D. Sun, G. J. Valentine, R. Macaluso, S. Calvez, D. Burns, M. D. Dawson, T. Jouhti and M. Pessa, "Low-loss 1.3-μm GaInNAs saturable Bragg reflector for high-power picosecond neodymium laser," *Optics Letters,* vol. 27, pp. 2124 - (2002).

[119] A. McWilliam, A. A. Lagatsky, C. G. Leburn, P. Fischer, C. T. A. Brown, G. J. Valentine, A. J. Kemp, S. Calvez, D. Burns, M. D. Dawson, M. Pessa and W. Sibbett, "Low-loss GaInNAs saturable Bragg reflector for mode-locking of a femtosecond Cr^{4+} : forsterite-laser," *IEEE Photonics Technology Letters,* vol. 17, pp. 2292-2294, (2005).

[120] S. Calvez, J.-M. Hopkins, S. A. Smith, A. H. Clark, R. Macaluso, H. D. Sun, M. D. Dawson, T. Jouhti, M. Pessa, K. Gundogdu, K. C. Hall and T. F. Boggess, "GaInNAs/GaAs Bragg-mirror-based structures for novel 1.3μm

device applications," *Journal of Crystal Growth,* vol. 268, pp. 457 - 465, (2004).

[121] V. Lordi, H. B. Yuen, S. R. Bank and J. S. Harris, "Quantum-confined Stark effect of GaInNAs(Sb) quantum wells at 1300–1600nm," *Applied Physics Letters,* vol. 85, p. 902, (2004).

[122] Y. S. Jalili, P. N. Stavrinou, J. S. Roberts and G. Parry, "Electro-absorption and electro-refraction in InGaAsN quantum well structures," *Electronics Letters,* vol. 38, pp. 343-344, (2002).

[123] T. Fujisawa, M. Arai and F. Kano, "Many-body design of highly strained GaInNAs electroabsorption modulators on GaInAs ternary substrates," *Journal of Applied Physics,* vol. 107, pp. 093107-093107-7, (2010).

[124] H. Lindberg, M. Sadeghi, M. Westlund, S. Wang, A. Larsson, M. Strassner and S. Marcinkevicius, "Mode locking a 1550 nm semiconductor disk laser by using a GaInNAs saturable absorber," *Optics Letters,* vol. 30, pp. 2793-2795, (2005).

[125] A. Sirbu, E. Saarinen, J. Rautiainen, J. Puustinen, A. Mereuta, J. Lyytikainen, L. Toikkanen, J. Nikkinen, A. Caliman, V. Iakovlev, O. Okhotnikov and E. Kapon, "Wafer-fused 1310 nm and 1550 nm mode-locked semiconductor disk lasers," in *12th International Conference on Transparent Optical Networks (ICTON),* pp. 1-4, (2010).

Chapter 2

Laser Design and Wafer Growth

2.1 Introduction

This chapter predominantly captures the design aspects of Semiconductor Disk Lasers (SDL). The four main regions of the SDL structure are the cap, confinement window, the gain section and the Distributed Bragg Reflector (DBR) mirror. Each in turn shall be explained, offering justification for the material choice and design approaches where appropriate. The individual SDL structures which were used in this thesis are specified along with their associated design wavelengths, material system and partner Universities supplying the wafers.

For completeness, the Molecular Beam Epitaxial (MBE) growth shall be briefly described, including the growth processes and specific challenges associated with nitrogen inclusion.

2.2 SDL Structural Design

It must be stated that all structures used for characterisation and in subsequent experiments were designed by Dr. Stephane Calvez at the Institute of Photonics. Figure 2-1 illustrates the main sections concerning the design of SDLs. Focus is given to each of the sections as they are grown onto the substrate from the mirror to the cap layer, to describe their purpose and mode of operation.
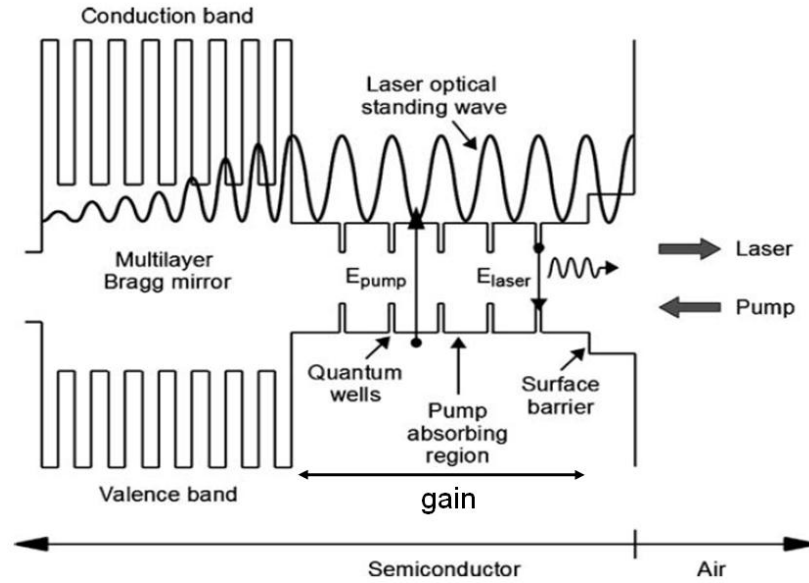
Figure 2-1: General structure of an SDL including the Bragg mirror, active region containing the quantum wells and the surface barrier comprising the confinement window and cap [1].

2.2.1 The Distributed Bragg Reflector

The mirror section consists of a Distributed Bragg Reflector (DBR) with its principle operation based on layers of materials with contrasting high refractive index (n_{high}) and low refractive index (n_{low}). The Bragg mirror operates through the constructive interference caused by Fresnel reflections at the interface of the material pair. The reflection from low to high refractive index material experiences no phase change, whilst the opposite presents a 180° phase shift. The overall result, after reflections from *N* pairs of the material, is the recombination of the in-phase light at the surface. It aims to achieve maximum reflectivity at the designed operational wavelength, or Bragg wavelength λ_B. The expression for the thickness of each of the DBR layers is represented in Equation (2.1.1), where $n(\lambda_B)$ is the refractive index of the layer at the design wavelength.

$$t = \frac{\lambda_B}{4n(\lambda_B)} \tag{2.1.1}$$

The mirror can be modeled using the principles of the propagation of the beam through a periodically stratified medium or thin film approximation, as presented in Born and Wolf [2]. The matrix evaluation of a layer is expressed in Equation (2.1.2).

$$M_{layer} = \begin{bmatrix} \cos \beta & -\frac{i}{n_l} \sin \beta \\ -\frac{i}{n_l} \sin \beta & \cos \beta \end{bmatrix} = \begin{bmatrix} M_{00} & M_{01} \\ M_{10} & M_{11} \end{bmatrix} \qquad (2.1.2)$$

The dispersion in the material is represented in Equation (2.1.3), with n_l representing the refractive index of the layer and the λ is the design wavelength passing through the layer of thickness t.

$$\beta = \frac{2\pi}{\lambda} n_l t \qquad (2.1.3)$$

Solving for the reflectivity of the system employs Equation (2.1.4), substituting in the corresponding matrix elements from Equation (2.1.2) with $p_1 = n_{top}$ or n_1 corresponding to the top layer or internal first layer in the pair, and $p_2 = n_{substrate}$ or n_2 corresponding to the substrate or internal last layer in the pair as appropriate.

$$r = \frac{(M_{00} + M_{01} \cdot p_2) p_1 - (M_{10} + M_{11} \cdot p_2)}{(M_{00} + M_{01} \cdot p_2) p_1 + (M_{10} + M_{11} \cdot p_2)} \qquad (2.1.4)$$

In terms of r in Equation (2.1.4) the reflectance of the system $R = |r|^2$. The overall DBR reflectivity of the system can be shown to be given by Equation (2.1.5) [1, 3], to factor in the incident $n_{incident}$ or top surface refractive index and the exit n_{exit} or substrate refractive index, in combination with the internal refractive index contrast.

$$R_{DBR} = \left(\frac{1 - qp^{2N}}{1 + qp^{2N}} \right)^2 \qquad (2.1.5)$$

In this equation the variables $p = \frac{n_{low}}{n_{high}}$ and $q = \frac{n_{incident}}{n_{exit}}$.

The range of wavelengths over which the DBR operates is called the bandwidth or stopband and is represented in Equation (2.1.6).

$$\Delta\lambda_{DBR} = \frac{4\lambda_{centre}}{\pi} arcsin \left(\frac{1-q}{1+q} \right) \qquad (2.1.6)$$

The wavelength λ_{centre} is the central wavelength of the stopband.

Figure 2-2 is the reflectivity spectrum for an 1180 nm designed structure, consisting of 25 pairs of GaAs, with n=3.466 (n_{high}) and AlAs n=2.937 (n_{low}). This structure has a top confinement window of Al$_{0.3}$GaAs, ($n_{incident}$=2.938) and a GaAs substrate (n_{exit}).
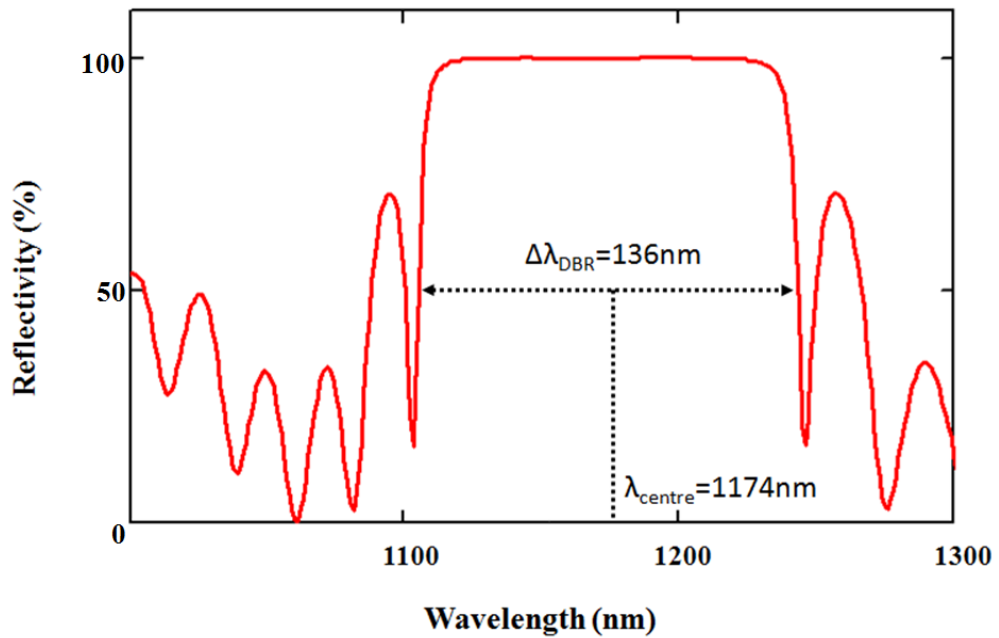

Figure 2-2: Reflectivity of sample *AsN2592* designed for 1180 nm with 25 pairs AlAs/GaAs.

Increasing the number of mirror pairs in the structure increases the reflectivity. This is demonstrated in Figure 2-3, showing the reflectivity increase from ~80% at 5 pairs to ~100% with 25 pairs.

30
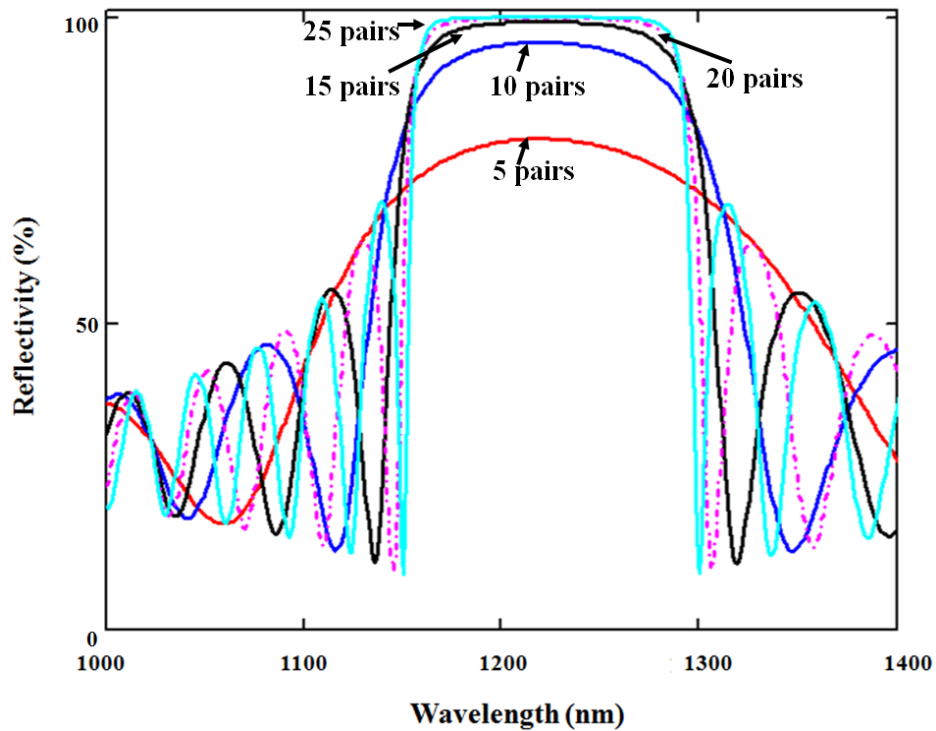
Figure 2-3: AlAs/GaAs DBR stack with increasing mirror pairs from 5 to 25 (λ_B=1220nm).

In Figure 2-4 the curves of AlAs/GaAs, AlAs/AlGaAs and InGaAsP/InP material systems are compared for reflectivity with respect to the number of mirror pairs. The higher the refractive index contrast and a smaller *p* value, the fewer the number of mirror pairs required to reach ~100% reflectivity. Such a large number of pairs would not be considered acceptable for three main reasons. Firstly, the excessive thickness of the DBR can potentially degrade performance of the device due to thermal conductivity issues making it difficult for heat removal from the active region. Secondly, more material resources would be required for larger quantities of layers. Finally, the growth conditions must be very carefully controlled to prevent structural defects caused by strain from materials not precisely lattice matched to the substrate.
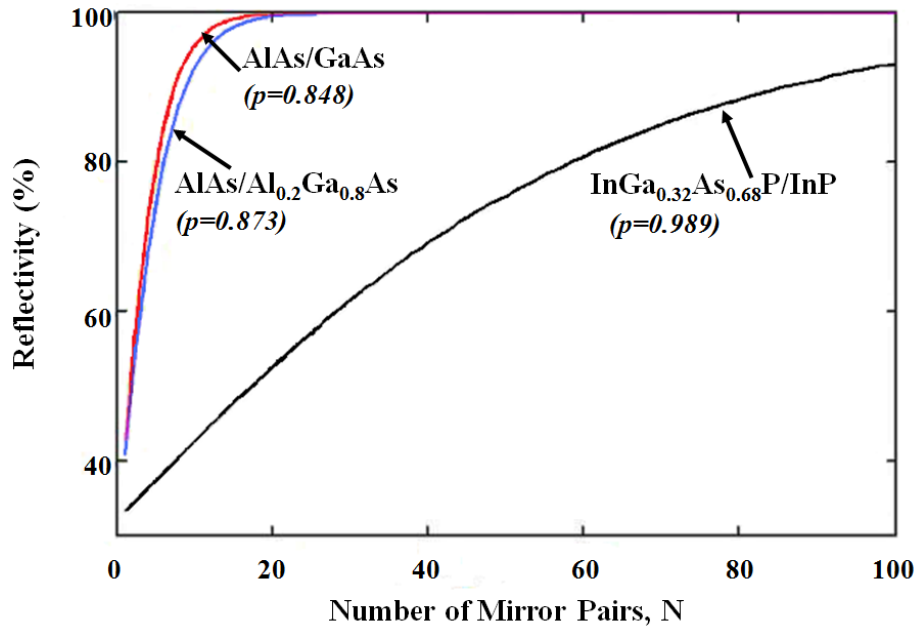
Figure 2-4: Reflectivity with respect to the number of mirror pairs for AlAs/GaAs (*red*), AlAs/AlGaAs (*blue*) and InGaAsP/InP (*black*) having a bandgap energy $E_g=0.91$ eV [4] (λ_B=1300nm).

Another important design criterion to consider is the refractive index contrast, $\Delta n=n_{high}-n_{low}$, of the DBR material stack. This can be quite significant since it contributes to higher reflectivity as well as increasing the bandwidth or stopband. In Table 2.1 three material systems are compared, all at the design wavelength of 1300nm. In this example it is clear that AlAs/GaAs has the highest refractive index contrast, and is therefore considered the best choice for DBR material.

Table 2.1: DBR material systems with λ_B= 1300nm.

DBR Material System	Refractive Indices, n	Δn
AlAs/GaAs	2.925/3.45	0.525
AlAs/Al$_{0.2}$Ga$_{0.8}$As	2.925/3.352	0.427
In$_{0.68}$Ga$_{0.32}$As$_{0.68}$P$_{0.32}$/InP	3.604/3.643	0.039

Furthermore, Figure 2-5 shows the reflectivity profiles of AlAs/GaAs, AlAs/AlGaAs and InGaAsP/InP at 1300nm.
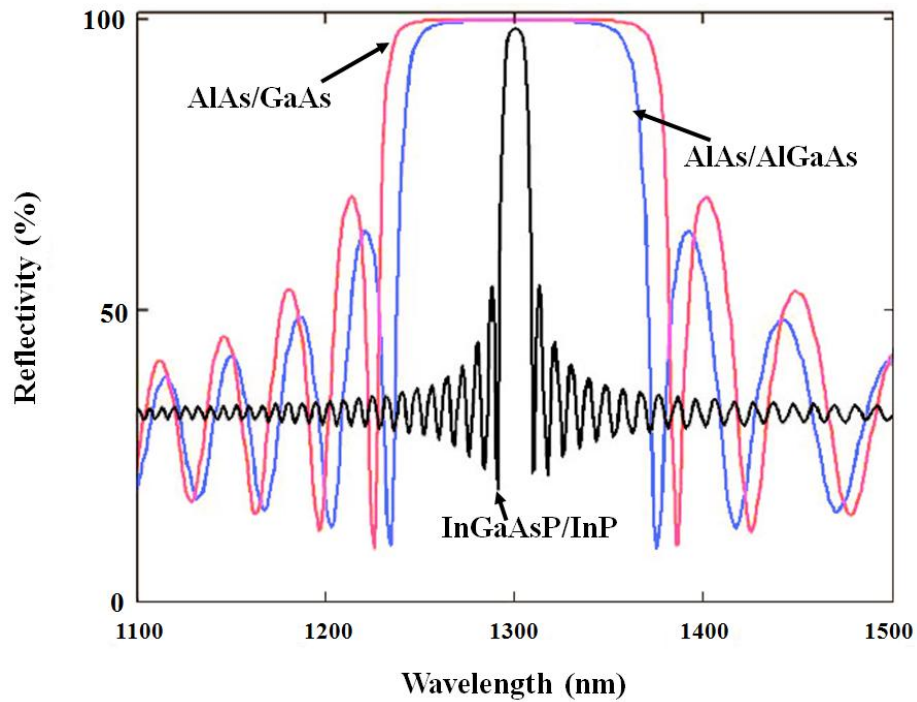
Figure 2-5: Reflectivity profiles of 25 mirror pairs DBR stack of AlAs/GaAs *(red)*, AlAs/AlGaAs *(blue)* and 150 mirror pairs of InGaAsP/InP *(black)*with λ_B=1300nm.

In Table 2.2 there is a clear distinction between the much lower stopband value using 150 mirror pairs for InGaAsP/InP compared with those of both AlAs/GaAs and AlAs/AlGaAs using only 25 pairs.

Table 2.2: Comparison of DBR material systems stopband, number of mirror pairs and corresponding reflectivity (λ_B= 1300nm).

DBR Material System	Stopband	Number of Mirror Pairs	Reflectivity, R
AlAs/GaAs	153.9 nm	25	100%
AlAs/Al$_{0.2}$Ga$_{0.8}$As	130.7 nm	25	99.9%
In$_{0.68}$Ga$_{0.32}$As$_{0.68}$P$_{0.32}$/InP	16.8 nm	150	98.23%

Ideally the DBR material would be lattice matched to the substrate. However, alternative arrangements have involved wafer fusion techniques [5, 6], metamorphic growth [7] and deposition of dielectric mirrors [8, 9]. Wafer fusion allows a

GaAs/AlAs DBR to be included into an SDL structure by bonding directly to an InAlGaAs active region. The drawbacks to this technique include the potential of interface degradation as well as it being a more complicated and costly process. The metamorphic growth of GaAs/AlAs directly onto InP layers causes strain due to the large lattice mismatch, thereby a propensity for dislocations. The deposition of dielectric mirrors, in the context of integration with the growth of the laser structure, has been used as the top mirror of a VCSEL. Examples of such dielectric mirrors include Si/Al_2O_3 onto a GaInAsP/InP VCSEL [8] and MgF/ZnSe/MgF/Au onto a InGaAs/GaAs VCSEL [9]. In the context of SDLs (VECSELs), dielectric mirror coatings have been deposited onto a diamond heatspreader in order to miniaturise the cavity [10, 11]. However, to date no dielectric mirrors have been integrated into the SDL structural design.

In summary, the choice of material for the DBR adheres to a high index contrast to reach a reflectivity ~100% employing the least number of mirror pairs to achieve the desired result. It is thus an advantage using AlAs/GaAs DBRs in these lasers, which can be lattice matched to a GaAs substrate, which is also compatible with the choice of gain material GaInNAs.

2.2.2 The Gain Region

The most important section of the SDL is the gain section, consisting mainly of GaInNAs QWs with GaAs barriers. The intricacy and crucial design of this region elicits further expansion, to discover how the various parameters contribute as a whole to the success of the device. To start with the source of gain provided by the QWs shall be explored with particular emphasis on the nitride material system, which highlights the strain effects associated within the heterostructure. Next we turn our attention to the resonant periodic gain (RPG) design and QW distribution within this region. In addition the optical pumping arrangement impacts significantly on the design, in terms of wavelength and excitation region targeted (in-well or in-barrier). Finally, uses of modeling techniques have provided a means to anticipate the overall device performance.

2.2.2.1 Quantum Wells

The basis by which gain can be achieved has been formulated on the quantum confinement of carriers within a potential well, or quantum well (QW). The well thickness becomes comparable to the *de Broglie* wavelength of the carriers (electrons and holes) forcing them to occupy discrete energy levels called energy sub-bands within the well, as illustrated in Figure 2-6.
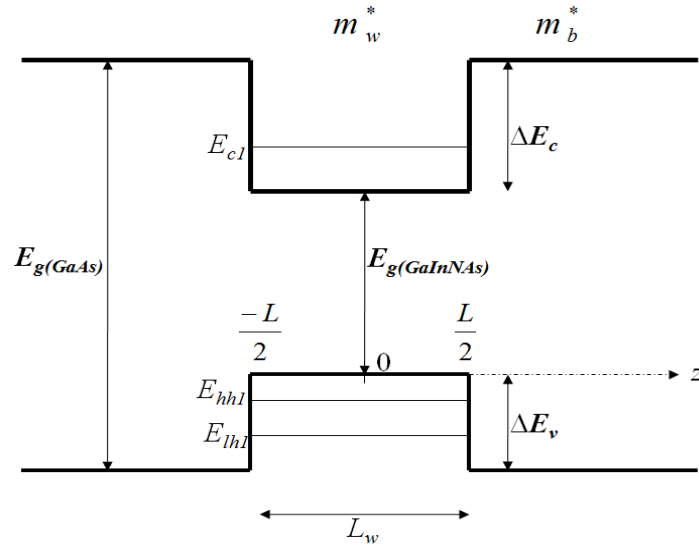
Figure 2-6: GaInNAs QW of width L_w with GaAs barriers, indicating the bandgap energies $E_{g(GaAs)}$ and $E_{g(GaInNAs)}$, effective masses in the well m_w* and the barrier m_b*, the differences in conduction band edge ΔE_c and valence band ΔE_v, with the subband energy levels E_{c1}, E_{hh1}, and E_{lh1} (where *c=conduction band, hh= heavy hole* and *lh=light hole*).

The quantized energy of the system must satisfy the time independent Schrodinger equation as presented in Equation (2.1.7) [12], where $\hbar = \dfrac{h}{2\pi}$, the potential barriers of the well are *V(z)*, the wave function is *φ(z)* and *m** is the effective mass in the well (m_w) or barrier (m_b).

$$E\varphi(z) = \left[-\frac{\hbar^2}{2m^*}\frac{d^2}{dz^2} + V(z)\right]\varphi(z) \qquad (2.1.7)$$

However, the inclusion of nitrogen induces a conduction band splitting as described in Chapter 1, thereby altering the potential barrier of the well. Based on formulations

from Hetterich *et al.* [13], there is an energy dispersion associated with the host matrix material E_M with an additional energy-dependent contribution due to the interaction with the nitrogen states $\frac{V_{NM}^2(z)}{E - E_N(z)}$, as given in Equation (2.1.8)

$$E\varphi(z) = \left[-\frac{\hbar^2}{2m^*}\frac{d^2}{dz^2} + \left(E_M(z) + \frac{V_{NM}^2(z)}{E - E_N(z)} \right) \right] \varphi(z) \tag{2.1.8}$$

The solutions of the wave function for the bound states are of the form provided in Equation (2.1.9), given that the states in the well occur where |z|=L/2 and in the barrier, |z|<L/2.

$$\varphi(z) = \begin{cases} Ae^{(ikz)} + Be^{(-ikz)}, & |z| = \frac{L}{2} \\ Ce^{(\kappa z)} + De^{(-\kappa z)}, & |z| < \frac{L}{2} \end{cases} \tag{2.1.9}$$

The expressions for *k*, referring to the well and κ for the barrier are provided in Equations (2.2.0) and (2.2.1).

$$k = \sqrt{\frac{2m_w^*}{\hbar^2}\left[E - E_{M(w)} + \frac{V_{NM(w)}^2}{E_{N(w)} - E} \right]} \tag{2.2.0}$$

$$\kappa = \sqrt{\frac{2m_b^*}{\hbar^2}\left[E - E_{M(b)} + \frac{V_{NM(b)}^2}{E_{N(b)} - E} \right]} \tag{2.2.1}$$

The eigenstates of the system, referring to even and odd wavefunctions, can be solved using Equations (2.2.2) (*even*) and (2.2.3) (*odd*).

$$\cos\left(\frac{kL_w}{2}\right) - \frac{m_b^* k}{m_w^* \kappa} \sin\left(\frac{kL_w}{2}\right) = 0 \tag{2.2.2}$$

$$\cos\left(\frac{kL_w}{2}\right) + \frac{m_w^* \kappa}{m_b^* k} \sin\left(\frac{kL_w}{2}\right) = 0 \tag{2.2.3}$$

Using the methodology set out by Chuang [12], to obtain the eigenenergy *E* for an even solution to the wavefunction, we substitute Equations (2.2.0) and (2.2.1) into the general form $\frac{m_b k}{m_w \kappa} \tan k \frac{L_w}{2} = 0$ to obtain Equation (2.2.4).

$$\frac{m_b^*\left(\frac{2m_w^*}{\hbar^2}\left[E-E_{M(w)}+\frac{V_{NM(w)}^2}{E_{N(w)}-E}\right]\right)^{1/2}}{m_w^*\left(\frac{2m_b^*}{\hbar^2}\left[E-E_{M(b)}+\frac{V_{NM(b)}^2}{E_{N(b)}-E}\right]\right)^{1/2}}\tan\left(\left(\frac{2m_w^*}{\hbar^2}\left[E-E_{M(w)}+\frac{V_{NM(w)}^2}{E_{N(w)}-E}\right]\right)^{1/2}\frac{L_w}{2}\right)=0 \qquad (2.2.4)$$

The transition energy, can thus be formulated using solutions for the eigenenergies E_{c1} and E_{hh1} (E_{lh1}), and the bandgap energy E_g of the QW material, which in this case is GaInNAs. Therefore, with optical emission occurring from transitions between the lowest energy states in the conduction band, E_{c1} to the highest level in the valence band of heavy-holes E_{hh1} the transition energy is given in Equation (2.2.5).

$$E_{C-HH} = E_{g(GaInNAs)} + E_{c1} + E_{hh1} \qquad (2.2.5)$$

Through substitution of the appropriate effective masses, relating to either the electrons in the conduction band m_e^* or those in the heavy-hole m_{hh}^* (light-hole m_{lh}^*) band, the eigenenergies can be solved. Ultimately, gain has been achieved through satisfying the Bernard-Duraffourg condition [14] $E_c - E_v = \hbar\omega$ where the emission $\hbar\omega$ results from the population inversion between the conduction and valence bands.

The material composition greatly influences the bandgap energy, with alterations to the conduction (valence) band edge. In order to demonstrate the effect the inclusion of nitrogen has on the bandgap and indeed the transition energy, two QW material systems have been compared. Figure 2-7 shows the transition energy curves for $In_{0.33}GaAs/GaAs$, $In_{0.33}GaN_{0.007}As/GaAs$ and $In_{0.38}GaAs/GaAs$. These indicate that even with a 0.7% concentration of nitrogen the transition energy was significantly reduced, providing an emission wavelength of 1220 nm (1.016eV) using a QW width of ~7 nm. Additionally, higher concentrations of indium are needed to obtain emission at 1220 nm, however this introduces higher strain effects as will be discussed in the next section and further in Section 2.5 with regards to MBE growth, thus making GaInNAs QWs a more viable option.
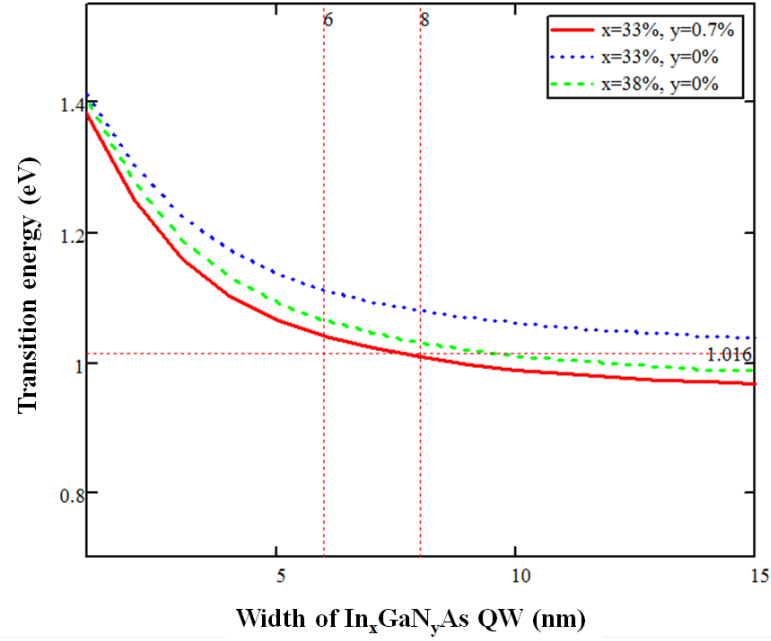
Figure 2-7: Transition energy over a range of QW lengths, to compare GaIn$_{0.33}$N$_{0.007}$As (*solid red*), In$_{0.33}$GaAs (*dashed blue*) and In$_{0.38}$GaAs (*dashed green*). The marker line is the emission energy 1.016 eV (1220 nm).

In this thesis the focus has been on GaInNAs/GaAs QW based devices for operation in the 1150 nm to 1350 nm emission region. Alternative material systems could be used such as InGaAsP/InP or AlInGaAs/InP for operation in the 1200 nm to 1360 nm region. The main advantage of the studied alloy lies in its more favourable confinement and effective mass. Considering that the electron thermionic emission lifetime τ_ε from a QW is given in Equation (2.2.6) [15, 16] where k_B is Boltzmann's constant, there is an interdependency between the depth of the QW ΔE_c and the electron effective mass m_e^*. Therefore high electron escape rates have an effect upon the carrier recombination, producing photon emission.

$$\tau_\varepsilon = \sqrt{\frac{2\pi m_e^* L_w^2}{k_B T}} \, exp\left[\frac{k_B T}{\Delta E_c}\right] \qquad (2.2.6)$$

In Table 2.3, the differences between material systems GaInNAs/GaAs, GaInPAs/InP and AlInGaAs/InP have been compared at 1300 nm operation, regarding their conduction band offsets, electron effective masses and electron thermionic emission lifetimes at 300K. These results highlight the distinction of GaInNAs for more effective carrier confinement, with a larger offset and lower

38

thermionic emission lifetime. Similarly the nitrogen induced enhancement of the effective mass along with smaller emission lifetime, suggests that this material would offer a slight advantage over its InGaAs counterpart for emission at 1150 nm to 1200 nm.

Table 2.3: A comparison of conduction band offsets, electron effective masses and thermionic emission lifetimes for material systems; GaInNAs/GaAs, GaInPAs/InP, AlInGaAs/InP at 1300 nm operation [17] and GaInNAs/GaAs and InGaAs/GaAs at 1200 nm operation.

Material System	Conduction band offset, ΔE_c	Electron Effective mass, m_e^*	Thermionic emission lifetime, τ_ε
1300 nm Operation			
$GaIn_{0.38}N_{0.01}As/GaAs$	406meV	$0.053m_0$	38 ns
$Ga_{0.2}In_{0.8}P_{0.3}As/ Ga_{0.9}In_{0.1}P_{0.8}As/InP$	100meV	$0.047m_0$	0.009 ns
$(Al_{0.3}Ga_{0.7})_{0.4}In_{0.6}As/(Al_{0.7}Ga_{0.3})_{0.5}In_{0.5}As/ Al_{0.5}In_{0.5}As/InP$	310meV	$0.041m_0$	16 ns
1200 nm Operation			
$GaIn_{0.33}N_{0.007}As/GaAs$	375meV	$0.053m_0$	34 ns
$In_{0.43}GaAs/GaAs$	306meV	$0.047m_0$	14 ns

2.2.2.2 Strain Effects in GaInNAs Quantum Wells

The main levels of strain inherent in any semiconductor material system consist of *internal* and *external* strain. The mere fact that alloys, such as GaInNAs, consist of elements with varying atomic sizes implies that a certain amount of internal strain exists within the material structure [18]. The careful control of growth temperatures and fluctuations of the elemental mole fractions such as indium and nitrogen [19] make it possible to produce good quality quaternary materials, which shall be discussed further in Section 2.5.

The main focus here shall be on the influence of external or epitaxial strain, caused by the structured layering of semiconductor materials with different crystalline lattice constants. Figure 2-8 (a) illustrates two forms of strain experienced by the material,

compressive (positive) which occurs when the lattice constant of the substrate is smaller than the deposited material, and *tensile (negative)* which is the opposite [20].
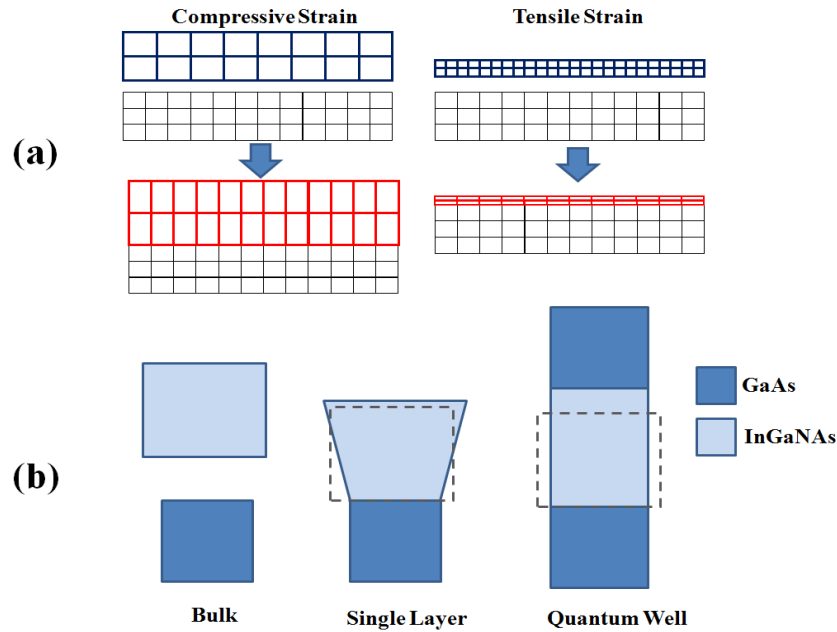

Figure 2-8: (a) Illustration of compressive and tensile strain due to materials with different lattice constants. (b) Comparison of bulk materials with that of a single layer and quantum well with subsequent strain in the material [21].

The epitaxial growth of a QW, which is surrounded by material with a different lattice constant, is demonstrated in Figure 2-8 (b). This aims to show the behaviour of the material for a compressively strained system, in which the material experiences in-plane biaxial strain due to the deformation of the lattice of the material in order to match the lattice of the substrate. The misfit between the two material systems was described by Coleman [21] as $f = \dfrac{\Delta a}{a_{alloy}}$ with the expression used to calculate strain given in Equation (2.2.7).

$$\varepsilon = \frac{a_{alloy} - a_{sub}}{a_{sub}} \tag{2.2.7}$$

Using this evaluation, Figure 2-9 shows ~2% compressive strain experienced by the $In_{0.3}GaN_{0.01}As/GaAs$ material system which is predominantly caused by the presence of indium, with a much larger atomic size compared to the other elements in the crystalline material lattice.
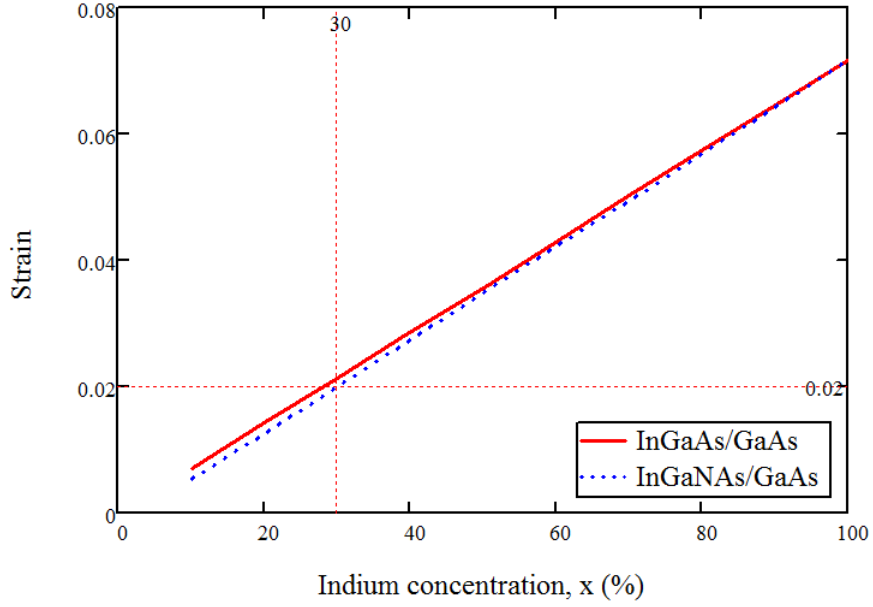
Figure 2-9: The compressive strain experienced in an In$_x$GaAs/GaAs material system compared to that of In$_x$GaN$_{0.01}$As/GaAs with increasing indium concentrations.

Experimental studies have shown that in InGaAs/GaAs multilayers, indium concentrations below ~30%, misfit dislocations are prevalent, while above 30% threading dislocations have been observed [22]. Therefore, using the critical layer thickness h_c evaluation proposed by *Matthews and Blakeslee* [21, 23], a limit on the material thickness to accommodate misfit dislocations can be determined. The expression in Equation (2.2.8), draws on the elasticity constants of the material denoted by C_{11} and C_{12}, and used to evaluate Poisson's Ratio $v=C_{12}/C_{11}+C_{12}$.

$$h_c = \frac{a_{alloy}}{\kappa\sqrt{2}\pi f} \frac{1-0.25v}{1+v}\left(ln\frac{h_c\sqrt{2}}{a_{alloy}}+1\right) \qquad (2.2.8)$$

In this equation, a_{alloy} is the lattice constant of the alloy as before, with $\kappa = 1$ for a strained layer superlattice and f represents the misfit between materials. In setting the layer thickness of an In$_x$Ga$_{1-x}$As QW to equal the critical thickness, $L_z=h_c$, the wavelength relationship to the optical emission energy in $\lambda(x,L_z)=hc/E(x,L_z)$ can be compared to that of a bulk strained system, as shown in Figure 2-10. This evaluation by Coleman provides a clear indication that InGaAs/GaAs QW devices are limited to below ~1.2 µm operation.
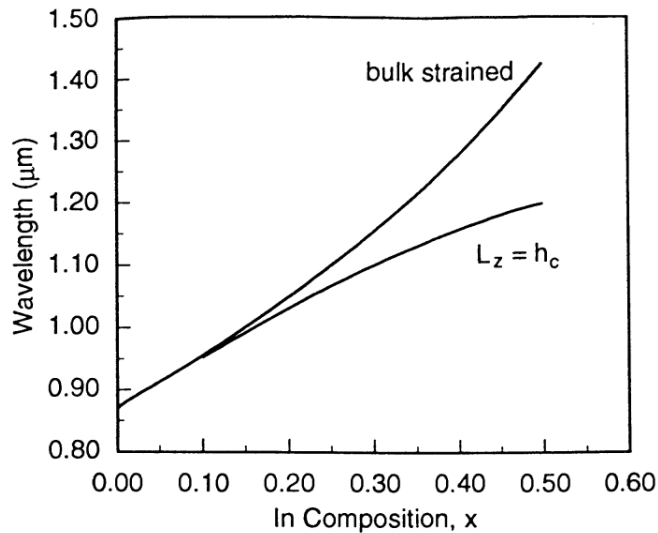
Figure 2-10: Wavelength ranges possible for In$_x$GaAs/GaAs QWs, where the QW thickness is set to the critical thickness, compared with bulk strained QW [21].

Figure 2-11 shows a critical thickness limit for In$_{0.3}$GaAs/GaAs of ~5-6 nm but for In$_{0.3}$GaN$_{0.01}$As/GaAs this is extended to ~7-8 nm. Steep decreases in these limits are observed above ~30% indium, due to the propensity for dislocations.
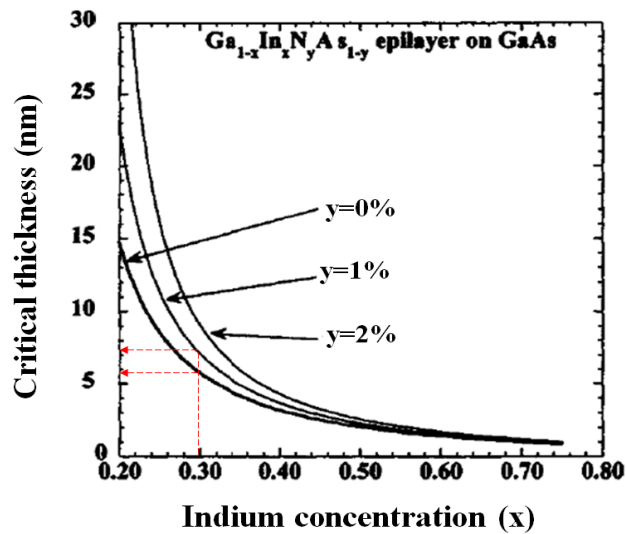
Figure 2-11: Critical thickness for In$_x$Ga$_{1-x}$N$_y$As$_{1-y}$/GaAs, with comparison made between nitrogen inclusion of 0%, 1% and 2% [24].

The effect of material strain has a profound impact on the heavy-hole and light-hole energy bands, as shown in Figure 2-12, resulting in subsequent alteration to the transition energy of the system and effective heavy-hole (light-hole) masses.

42
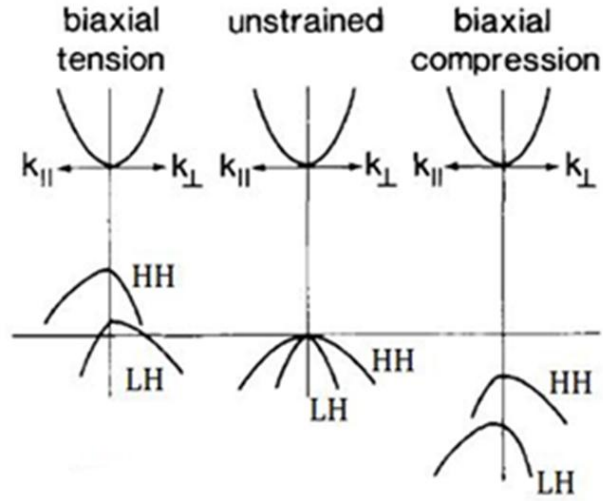
Figure 2-12: Effects of strain on the band structure of a zinc-blende crystal, indicating the heavy-hole (HH) and light-hole (LH) valence band degeneracy [25].

The effects of strain have been observed to lower the threshold pump power [26]. The reason for this relates to the degeneracy of the valence band with a reduction in the heavy-hole (light-hole) effective mass and subsequent changes to the density of states.

The degeneracy of the sub-bands has been reflected in the shear and hydrostatic deformation potentials of the QW layer. The elasticity constants of the material, C_{11} and C_{12}, are used to evaluate the tetragonal distortion of the GaInNAs layer with the split of the valence band under shear strain effects. The displacement due to strain for the heavy-hole (hh) is given in Equation (2.2.9) whilst for the light-hole (lh) in Equation (2.3.0) [27, 28].

$$\delta E_{hh} = 2a_v \left(1 - \frac{C_{12}}{C_{11}}\right)\varepsilon + b\left(1 + \frac{2C_{12}}{C_{11}}\right)\varepsilon \qquad (2.2.9)$$

$$\delta E_{lh} = 2a_v \left(1 - \frac{C_{12}}{C_{11}}\right)\varepsilon - b\left(1 + \frac{2C_{12}}{C_{11}}\right)\varepsilon \qquad (2.3.0)$$

The shear deformation potential of the valence band is b with hydrostatic deformation potential a_v. The shift in the conduction band energy due to strain is

given in Equation (2.3.1), where a_c is the hydrostatic deformation potential of the conduction band[1].

$$\delta E_c = 2a_c \left(1 - \frac{C_{12}}{C_{11}}\right)\varepsilon \qquad (2.3.1)$$

Factoring in these strain effects imposed on a $GaIn_xN_yAs/GaAs$ QW material system with In_x and N_y concentrations, the expression for the transition energy between the conduction band and heavy-hole band is provided in Equation (2.3.2). The expression for the transition with the light-hole band would replace the last term with δE_{lh} respectively.

$$E_{c-hh} = E_g(x,y) + \delta E_c(x,y) - \delta E_{hh}(x,y) \qquad (2.3.2)$$

In Figure 2-13, the transition energy with the corresponding critical thickness for the material provides an indication that with low concentrations of nitrogen the transition energy can extend to higher wavelengths, as demonstrated in Figure 2-7 for 1220 nm (1.016eV). However, with higher concentrations of indium such as x=35% this limits the QW critical thickness.
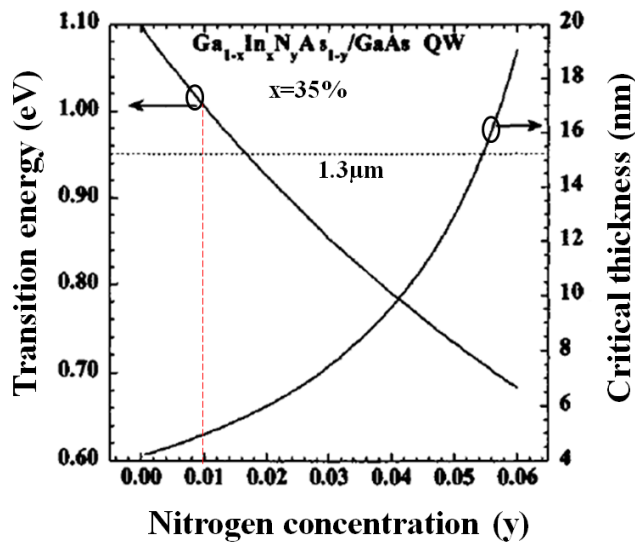
**Figure 2-13: Transition energies and critical thicknesses for a GaIn$_{0.35}$N$_y$As/GaAs QW across a range of nitrogen concentrations *(y)* [24]. Indicated is 1.3 μm emission and *y=1%*.**

---

[1] The hydrostatic deformation potentials a_v, a_c in Equations (2.2.9), (2.3.0) and (2.3.1) should not be mistaken for the lattice parameters a_{sub} or a_{alloy} for the strain in Equation (2.2.7).

A method which is widely used to compensate for material strain is to incorporate *strain compensating layers* (SCL) within the structure, which have opposite strain to that of the QW material. Using the *zero-stress* method developed by Ekins-Daukes *et al.* [29] the elastic stiffness coefficient A of the material is expressed in Equation (2.3.3), which can be substituted for $A_{InGaNAs}$ and A_{GaNAs} for the QW and SCL respectively. This material system has been implemented for a 10 QW InGaNAs structure, where the compressively strained QW has been grown with tensile strained SCL of GaNAs.

$$A = C_{11} + C_{12} - \frac{2C_{12}^2}{C_{11}} \qquad (2.3.3)$$

The average in-plane stress X due to the strain imposed by the layering of the two material systems can be expressed in Equation (2.3.4), with the thicknesses t, lattice constants a, strain ε and elastic stiffness coefficients A all denoted by the appropriate material, *InGaNAs* and *GaNAs*.

$$X = \frac{2}{t_{GaNAs}+t_{InGaNAs}}\left(t_{GaNAs}A_{GaNAs}\varepsilon_{GaNAs} + t_{InGaNAs}A_{InGaNAs}\varepsilon_{InGaNAs}\frac{a_{GaNAs}}{a_{InGaNAs}}\right)$$

$$(2.3.4)$$

Therefore for strain balancing, the strain compensating layer thickness is found when X=0, as is illustrated in Figure 2-14. In this example, for the material system $In_{0.33}GaN_{0.007}As/GaN_{0.015}As/GaAs$ the strain compensating layer thickness is ~45 nm.
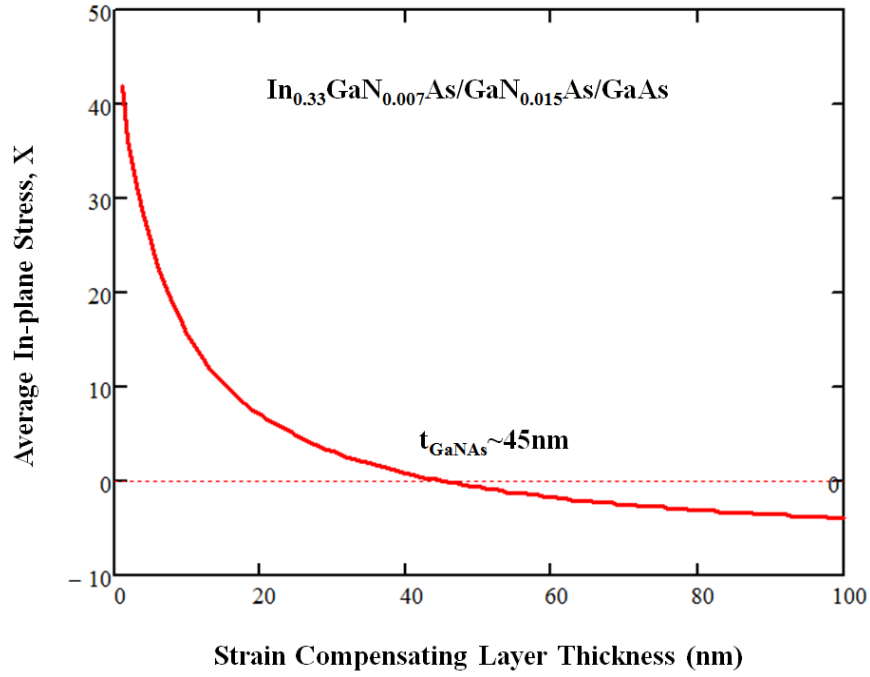
Figure 2-14: Average in-plane stress for a biaxially strained material system with respect to the compensating layer thickness.

In realistic terms moderately strained samples are necessary to benefit from their reduced thresholds and higher output power characteristics [26], likewise the critical thickness constraints limit the thicknesses of the epitaxial layers. The total strain of the system from Figure 2-14, calculated using $\varepsilon_{total} = \frac{t_{InGaNAs}\varepsilon_{InGaNAs} + t_{GaNAs}\varepsilon_{GaNAs}}{t_{InGaNAs} + t_{GaNAs}}$ for SCL thicknesses of 4 nm on either side of a 7 nm QW provides an acceptable ~0.9% strain.

2.2.2.3 Resonant Periodic Gain and QW Distribution

The design of an SDL has within its structure, the gain region embedded between the DBR mirror and the top surface, in which the semiconductor/air interface creates a subcavity. This subcavity acts as a Fabry-Perot etalon, forming the basis of the resonance effect. In order to maximise the effective gain, the QWs are positioned to coincide with the resonance peaks (anti-nodes), resulting in an intensity build-up in the subcavity. To achieve this, QWs are spatially located at half wavelength intervals, with the length of the active region designed to be an integer number of

half wavelengths, $L = \frac{m\lambda}{2}$. An example of a resonant cavity design is provided by Garnache et al [30] in Figure 2-15, using 7 nm thick $In_{0.2}Ga_{0.8}As$ MQWs and 10 nm thick GaAs barriers, designed for 980 nm operation.
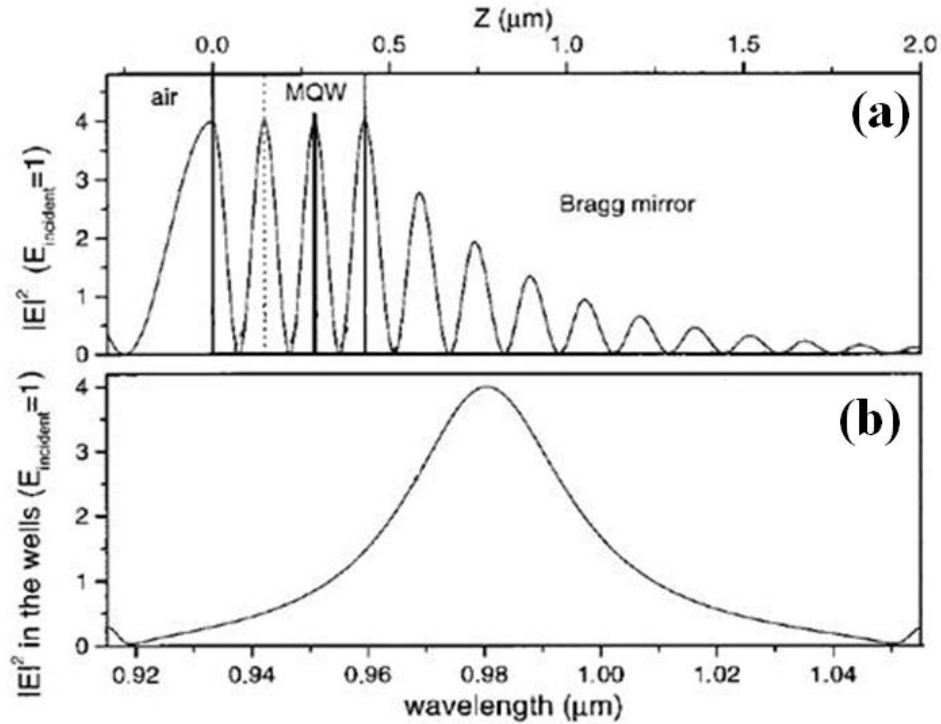
Figure 2-15: The |E|² field (with incident E-field normalised to 1) through the SDL structure (a) and in the QWs (b), showing an intensity peak at the design wavelength of 980 nm [30].

The periodicity of the placement of the QWs is thus correlated to the optical standing wave in the subcavity. This results in a directional dependent, and wavelength selective gain medium. The effective gain for the resonant mode is enhanced over other longitudinal modes having the effect of reducing the laser threshold. It is reasonable to infer that less laser pump power is required to reach threshold when higher effective gain is attained in the active region. By design the RPG wavelength aims to coincide with the QW emission.

A consequence of placing the QWs at the anti-nodes is a strong dependence upon the frequency of the optical field in the subcavity. This highlights the temperature sensitivity of the device, since an increase in temperature shifts the location of the

anti-nodes away from the QWs, resulting in a reduction in gain and inefficiency. Figure 2-16 provides an indication that the rates for the shift due to temperature are different, with 0.1 nm/K for the RPG compared to 0.3 nm/K in the case of the QW peak emission. Included is the observed PL, which gives an indication of the performance of the SDL. The design must therefore take into consideration this 'gain offset' with respect to temperature sensitivity, in order to achieve high output powers. A further discussion on thermal management of SDL devices shall be provided in Chapter 3.
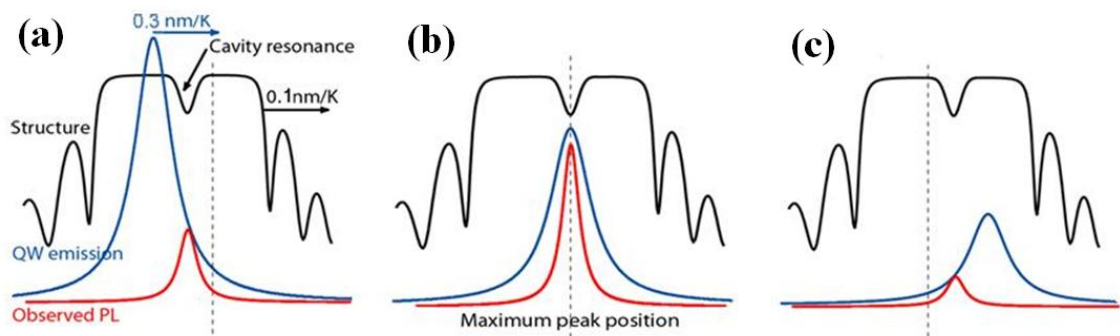
Figure 2-16: (a) Shift rates of the RPG cavity resonance compared with QW emission, indicating also the observed PL, (b) the maximum PL intensity at the optimal operating temperature, when the RPG cavity resonance and QW emission are aligned, and (c) the rapid decrease in PL and QW emission as the mismatch increases.

In contrast the anti-resonant design indicated in Figure 2-17 from Garnache *et al.* [30], has shortened the window layer having an impact on the optical field intensity inside the active region subcavity. The length of the cavity has now changed to be a multiple of the quarter wavelength. In this way the resonance effects are no longer prominent. Figure 2-17 (b) shows a minimum of the E-field in the wells at the design wavelength with peaks occurring at the half wavelength positions, where the resonance condition for the subcavity is fulfilled. The threshold for such an anti-resonant device is higher due to the low peak field intensity available at the position of the QWs.
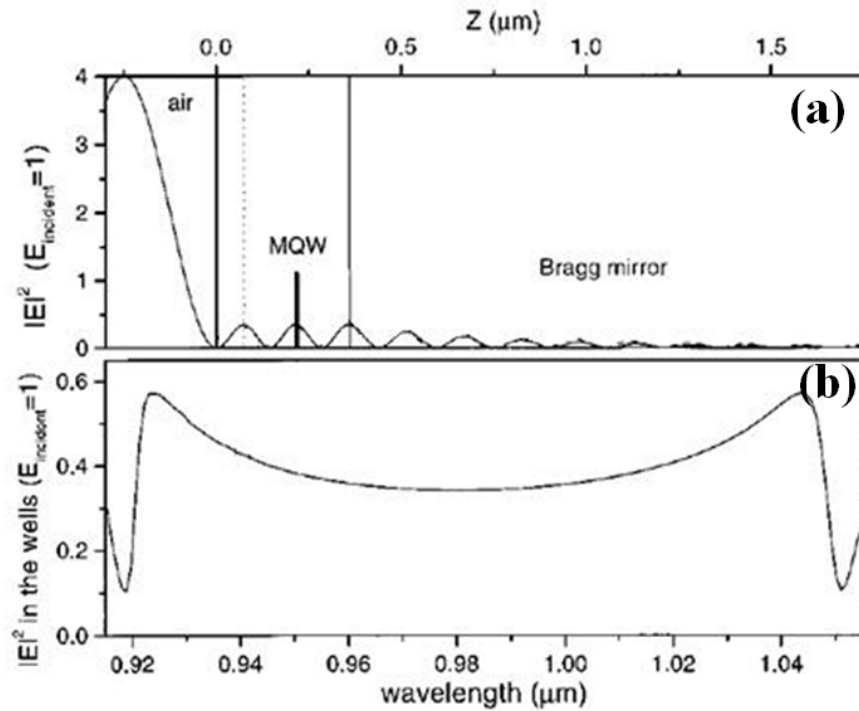
Figure 2-17: (a) The |E|^2 field (with the incident E-field normalised to 1) along the SDL device for an anti-resonant design, and (b) the |E|^2 field in the wells is a minimum at the design wavelength 980 nm [30].

The designs adopted for the SDLs used in this research have implemented resonant RPG structures. In Figure 2-18 the Scanning Electron Microscope image of the MBE grown *AsN2527* structure is shown, included with the resonant design of the 1220 nm device. For this device the length of the gain region is 5λ, with the QWs positioned at the anti-nodes of the optical field intensity. The performance results for this particular SDL are provided in Chapter 4.
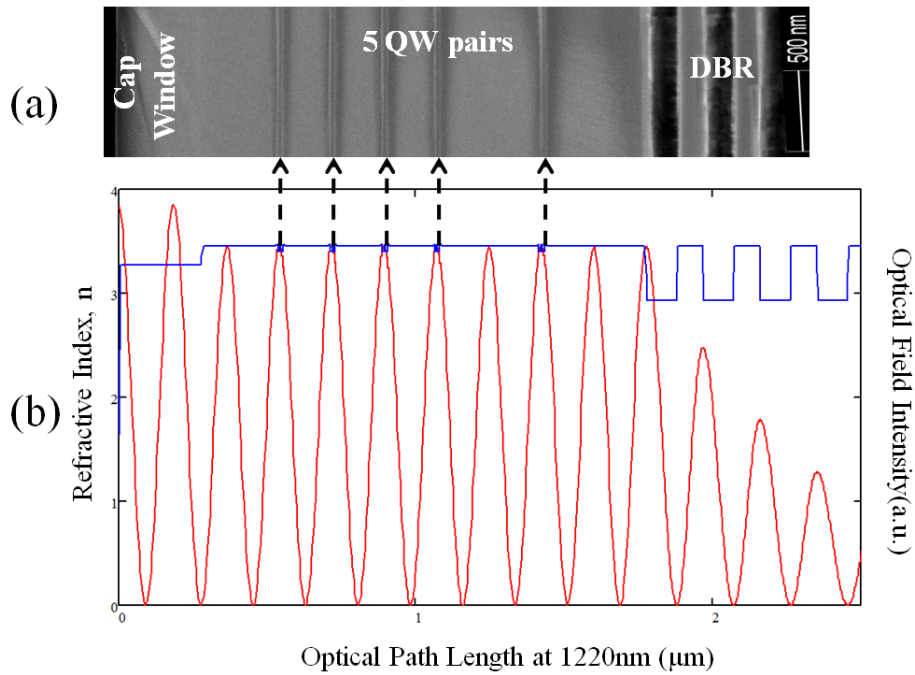
Figure 2-18: (a) The SEM image of *AsN2527* 1220 nm structure to align with (b) the design profile of the same structure with the refractive index of the layers *(blue)* and the optical field intensity *(red)* illustrating the QW positioned at the anti-nodes of the field intensity.

The main benefit of an anti-resonant device has been its capability to tune across a wider wavelength range, whilst raising the threshold and lowering the gain. However, the influence of a resonant subcavity acts to narrow the gain bandwidth, with previous attempts to design an anti-resonant subcavity resulting in lower gain [31]. Borgentum *et al.* [32] have attempted to maximise on the benefits afforded the anti-resonant gain design, whilst extending tunability by creating an anti-resonant subcavity. Their design included an additional anti-resonant structure next to the air interface, thereby obtaining an anti-resonant wavelength at 980 nm and peak resonant wavelengths at 960 nm and 1000 nm, extending the wavelength tuning range across 43 nm.

2.2.2.4 Optical Pumping

The key aspect to optical pumping is absorption by the material of the incident radiation, as this process facilitates gain in the system. The choice of pump wavelength depends upon the pump regime employed, referring to *barrier pumping* and *in-well pumping* as illustrated in Figure 2-19. It is important to distinguish

between these two [33]. Barrier pumping targets the barrier or spacer layer adjacent to the QW, requiring the pump energy to be greater than the bandgap energy of this layer. The carriers created within the barrier decay rapidly to the energy levels in the QWs which have a smaller energy bandgap than the barrier and are also thinner to aid carrier confinement. Alternatively the in-well pumping case excites electrons directly in the QW, and the pump photon energy chosen must be lower than the barrier bandgap but greater than that of the QW [34, 35].
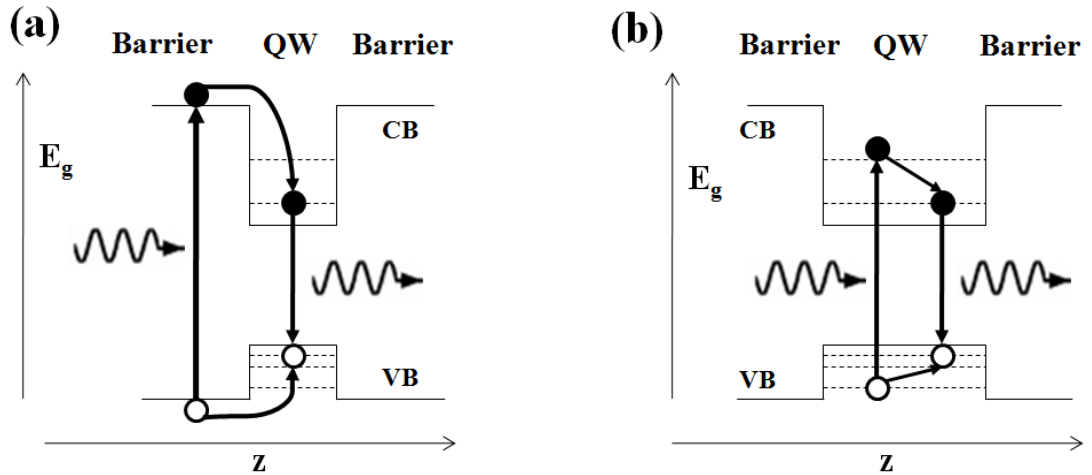
Figure 2-19: Comparison of (a) barrier pumping regime and (b) in-well pumping.

Throughout this thesis, the SDL designs have incorporated in-barrier pumping, using GaAs for the barrier material. The benefits to barrier pumping include insensitivity to the chosen pump wavelength, as long as it is greater than the barrier bandgap, whilst employing higher pump photon absorption due to the longer lengths of the material, enabling lower pump thresholds. However, the difference between the pump and output laser photon energies, known as the quantum defect ($q=hv_{pump}-hv_{laser}$) can contribute to thermal increases within the gain region.

In order to provide efficient single-pass pump absorption, the overall barrier thickness is chosen so that a large fraction of the incoming pump is absorbed. In Equation (2.3.5) [36] the absorption length, L is related to the absorption coefficient of the material in accordance with the optical pumping wavelength $\alpha(\lambda)$ and $\varkappa_{abs}$ which is the absorption fraction P_{abs}/P_{in} of the material.

$$L = -\frac{1}{\alpha(\lambda)}\ln\left(1 - \varkappa_{abs}\right) \qquad (2.3.5)$$

In order to demonstrate the relative insensitivity to pump wavelength, Figure 2-20 presents evaluations for some expected fractions of pump absorption from 40% up to 95%. The pump wavelengths from 750 nm to 830 nm show a small deviation in the required absorption lengths.
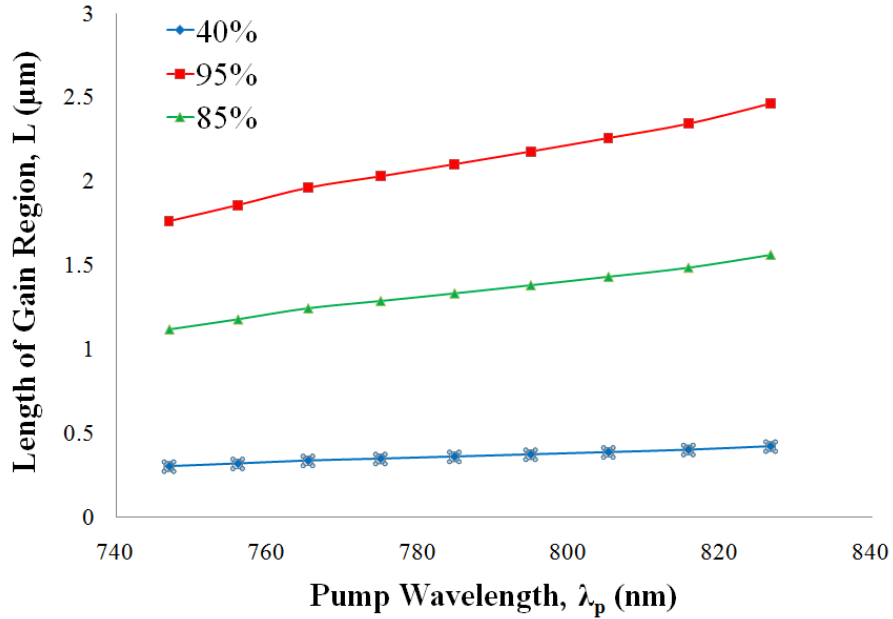
Figure 2-20: Length of the gain region across a range of pump wavelengths, for expected pump absorptions of 40%, 85% and 95%.

As described in the previous section, in order to extract maximum gain, the positioning of the wells in conjunction with the length of the gain region facilitate the success of the RPG structure. Using an 808 nm pump and GaAs barrier material with an absorption coefficient of *~13x10³ cm⁻¹* at that wavelength [37], assuming 85% pump absorption leads to a length *L≈1.4 μm.* In the case of an SDL designed to operate at 1220 nm, satisfying the RPG criteria of an integer number of half wavelengths, the length would therefore be *L=8λ/2n.*

The delivery of the pump beam uses optical elements to focus onto the device. With such a short cavity length L_{cavity} (< 2 μm) the beam does not get the opportunity to experience any significant divergence over this distance, so the cavity behaves like a

planar absorber, in this respect simplifying requirement on beam quality and optical delivery.

2.2.2.5 Laser Performance Modeling

In order to predict the performance of the laser design, modeling techniques based on those developed by Kuznetsov [38] were performed. These were adapted for the GaInNAs/GaAs material system, under the same assumptions that no thermal effects were incorporated into the model.

An important aspect pertaining to the design of the gain region, is the significance of the number of QWs. The previous demonstration of a resonant periodic gain structure has shown the impact that the active region length and placement of the QWs has in maximising gain of the device. However, it is essential to understand what constitutes the optimal number of QWs for the device and examine any limiting factors.

The aim of any such laser device is to achieve maximum output power. The output is therefore interlinked with the amount of gain from the QWs. It is thus a foregone conclusion that the higher the number of QWs, the more gain available to produce a high power laser. The threshold pump power, above which the gain exceeds the losses in the laser cavity, aims to be kept low. The relationship that the threshold pump power P_{th} has in relation to the number of QWs N_w is shown in Equation (2.3.6).

$$P_{th} = N_{th} \frac{h\nu_p(N_w L_w A_p)}{\eta_{abs}\tau(N)}$$ (2.3.6)

In this equation, the length of the QW L_w, pump spot area A_p, the energy of the pump photons $h\nu_p$, the absorption efficiency η_{abs} and the threshold carrier lifetime $\tau(N)$ have an impact on the threshold power.

$$\frac{1}{\tau(N)} = A + BN + CN^2$$ (2.3.7)

The threshold carrier density N_{th} is shown in Equation (2.3.8), where N_0 is the transparency carrier density, the mirror reflectivity's are R_1, R_2 the cavity round-trip loss is T_{loss}, the confinement factor Γ and gain coefficient is g_0.

$$N_{th} = N_0 (R_1 R_2 T_{loss})^{-(2\Gamma g_0 N_w L_w)^{-1}} \tag{2.3.8}$$

Table 2.4 provides a summary of the values used in the models.

Table 2.4: Parameters used in the model calculations.

Parameter	Description	Value	Units
λ_p	Pump Wavelength	808	nm
λ_l	Laser Wavelength	1220	nm
d_{pump}	Pump spot diameter	100	μm
L_w	Quantum Well Thickness	7	nm
R_1	On-wafer mirror reflectivity	0.999	
g_0	Material gain coefficient	2243[39]	cm^{-1}
N_0	Transparency carrier density	2.5x10^{18}[40]	cm^{-3}
T_{loss}	Round-trip loss transmission factor	0.99 [38]	
Γ	RPG longitudinal confinement factor	2 [38]	
η_{abs}	Pump absorption efficiency	0.85 [38]	
A	Monomolecular recombination coefficient	1x10^8[41]	s^{-1}
B	Bimolecular recombination coefficient	1x10^{-10}[41]	cm^{3}s^{-1}
C	Auger recombination coefficient	4x10^{-29}[41]	cm^{6}s^{-1}

The simulation results of the threshold pump power as a function of the number of QWs is shown in Figure 2-21 for an GaInNAs/GaAs SDL designed to operate at 1220 μm. The curves are over a range of output coupler mirror reflectivity, R_2 in Equation (2.3.8). These simulations show the lower the output coupling, the lower the threshold pump power and fewer numbers of QWs are required.
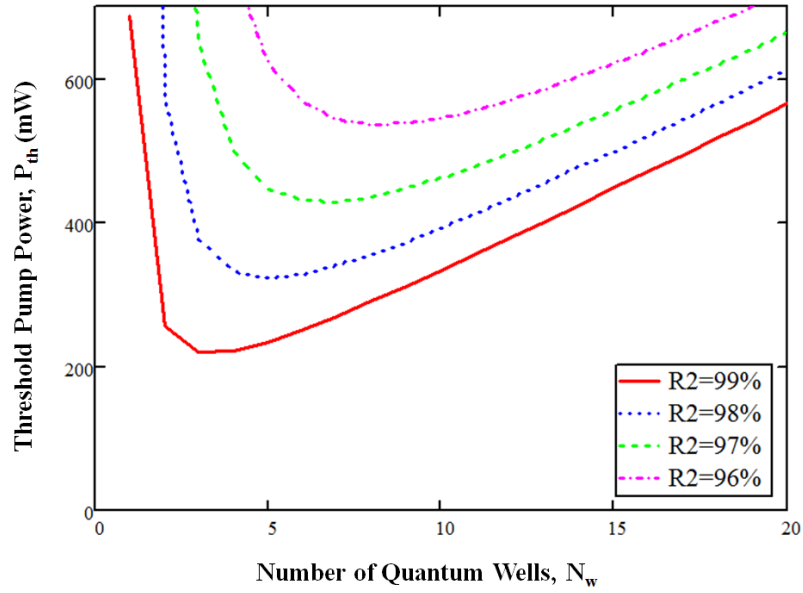
Figure 2-21: Threshold pump power with respect to Number of QWs for output coupler reflectivity values of 99%, 98%, 97% and 96%.

The output power of the SDL can be evaluated using Equation (2.3.9), where P_p is the pump power and η_{diff} is the differential efficiency, which can also be referred to as the slope efficiency η_{slope} as shown in Equation (2.5.5) in Section 2.4.6.

$$P_{laser} = (P_p - P_{th})\eta_{diff} \tag{2.3.9}$$

The relationship that output power P_{laser} has to the number of QWs is shown in Equation (2.4.0), for the carrier density N below threshold and its dependency upon the pump power P_p.

$$N = \frac{\eta_{abs}P_p}{h\nu_p(N_wL_wA_p)}\tau(N) \tag{2.4.0}$$

The results of laser output power, using pump powers of 1.8 W, are shown in Figure 2-22, again over a range of output coupler reflectivity. These curves indicate that the higher the output coupling (96%), the higher the output powers achievable, yet more QWs are required to provide a higher level of gain to counter the increased loss introduced into the cavity.
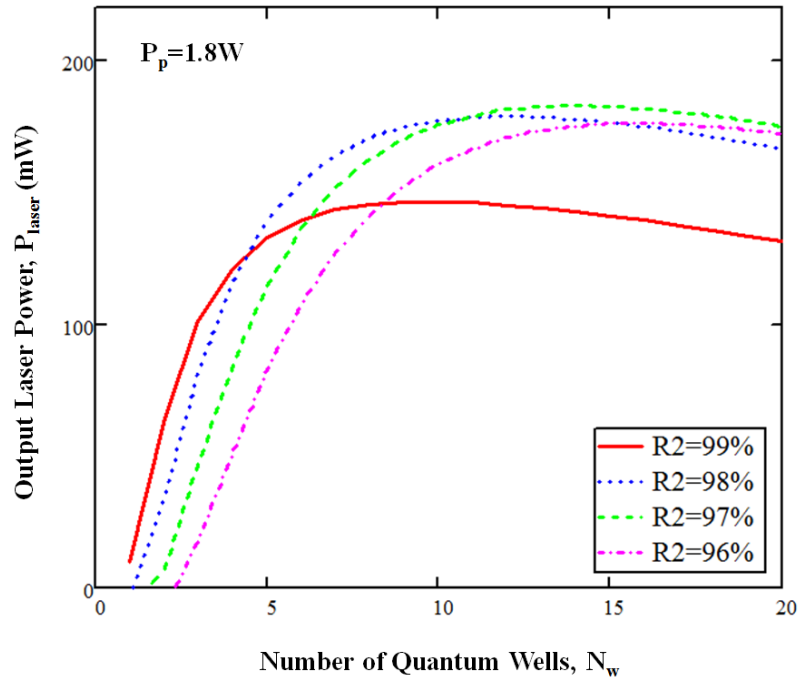
Figure 2-22: Output laser power as a function of the number of QWs over output coupler reflectivity 99%, 98%, 97% and 96%.

These results have highlighted the trade-off between the numbers of QWs required to reach high output powers with reasonably low pump thresholds. The optimum number of QWs typically falls between 5 and 15, to provide a good level of flexibility for output coupler reflectivity powers. Too high a number and the constraints due to strain on the material system can contribute towards device failure.

2.2.3 The Confinement Window

The Al_xGaAs carrier confinement window layer is sandwiched between the cap and the gain section. This region has a relatively large bandgap ~1.957eV [42], to provide strong carrier confinement in the gain region to prevent carriers escaping to the surface to recombine non-radiatively. The thickness of this layer is typically~$\frac{3\lambda}{4n}$, and is chosen to be transparent at both the pump and operational wavelength of the SDL.

Due consideration has been given to the layer thickness, in fulfillment of its role within the overall SDL structure. It needs to be thin enough for high thermal

conductivity, so it does not hinder the heat transfer through to the heatspreader. Further details of this shall be explored in Chapter 3, using simulations of these SDL devices and the thermal management techniques. In addition, the layer needs to be thick enough with a high barrier, to prevent carrier surface recombination which is similar to that presented in Section 2.2.2.1 for carrier confinement in QWs.

The barrier ΔE_c in the case of $Al_{0.3}GaAs/GaAs$ is sufficiently large at ~372meV to produce a thermionic emission lifetime ~0.4µs, using Equation (2.2.6), modified for this material system and the thickness of the gain section instead of a QW. Focusing on the tunneling of particles to the surface, an evaluation was made based on the expression in Equation (2.4.1), [43] where h is Planck's constant, the thickness of the gain region t_{gain} is ~1.5µm, the effective masses in the bulk of the gain region uses m_{GaAs}, and in the window m_{AlGaAs}.

$$\frac{1}{\tau_{tunnel}} = \frac{h}{4t_{gain}^2 m_{GaAs}^*} exp - \left[\frac{4\pi t_{window}\sqrt{2m_{AlGaAs}\Delta E_c)}}{h} \right]^{-1} \qquad (2.4.1)$$

The carrier tunneling lifetime dependence upon the thickness of the barrier is shown in Figure 2-23 with the lifetime increasing the thicker the confinement window.
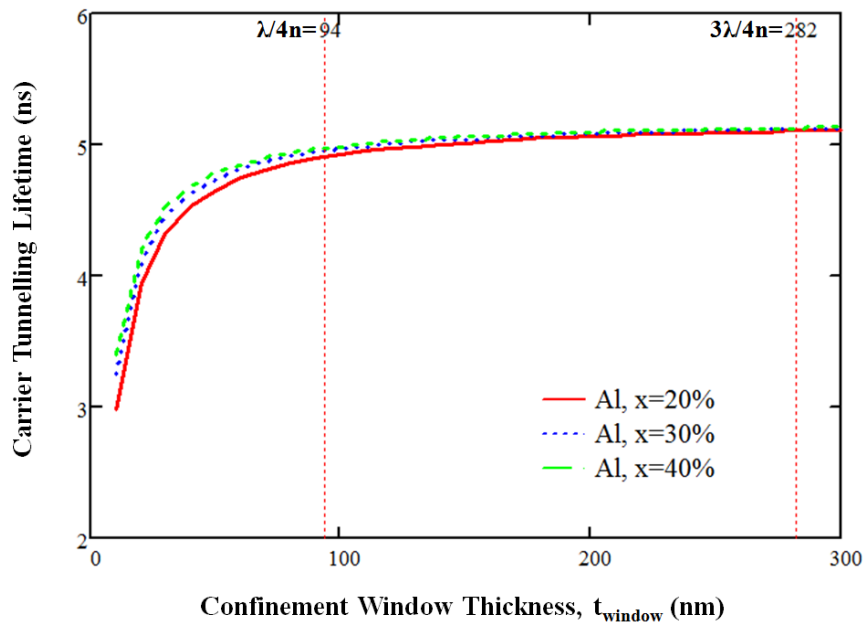
Figure 2-23: Tunneling rate of carriers from the gain region into the confinement window, as a function of the barrier thickness.

The thickness of this section more than adequately prevents tunneling of carriers to the surface, with a $\sim\frac{3\lambda}{4n}$ ($\approx$282 nm) dimension of Al$_{0.3}$GaAs for an SDL operating at 1220 nm, as indicated in Figure 2-23.

2.2.4 The Cap

The purpose of the cap layer is to prohibit the oxidation of the underlying AlGaAs window layer through exposure to the environment. Structures throughout this work have the cap layer consisting of GaAs with a thickness of between 10-20 nm. An example is shown in Figure 2-24 of a structure which has experienced the effects from oxidation, having areas near the centre and edges of the wafer corroded. A probable cause for the oxidation effects is the thin growth of the GaAs cap layer in conjunction with incorrect storage of the wafer, allowing prolonged exposure to the environment. It may be considered that long term storage should use a nitrogen rich environmental cupboard.
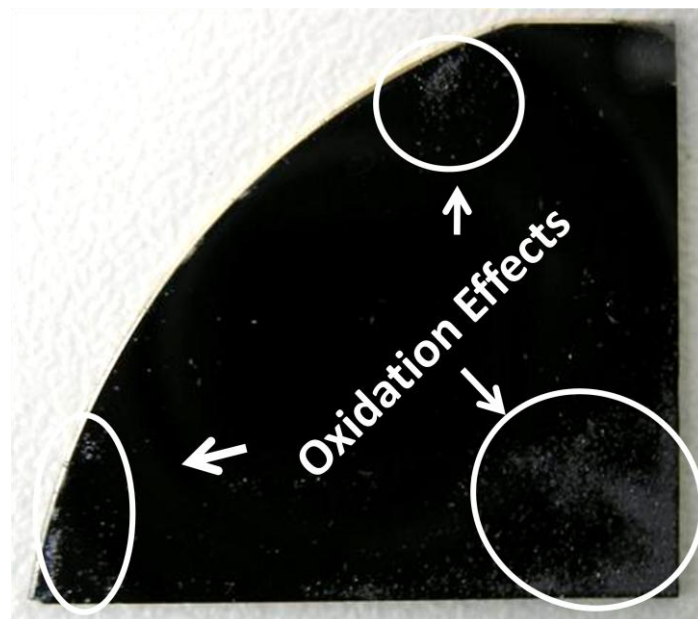
Figure 2-24: Samsung sample _K732_ 1047nm indicating the result of oxidation on the surface of the semiconductor wafer.

A suggested alternative to GaAs would be the use of InGaP, an example of which has been used in the growth of a 980nm InGaAs/GaAs SDL [44]. This material system does not suffer from oxidation degradation, and may also serve as a confinement window.

2.3 Devices Emitting in the Range 1180nm to 1300nm

In Table 2.5 a synopsis of the MBE grown structures is provided. These have been studied and subsequently applied as pump sources and also frequency doubled, details of which are provided in upcoming Chapters. The structures are categorised by the technical institutions producing the MBE grown wafers, and listed according to their design wavelengths. The numbers of QWs for the samples produced at ORC, Tampere University of Technology and at Stanford University adhere to ~8-10, which provides wider scope to use higher output coupler transmissions as described in Section 2.3.3. However, the samples grown at Sheffield University examine the least amount of QWs ~4-8, at the operational limit.

Table 2.5: Comparision of GaIn(N)As Structure Designs.

Design λ	ID Code	No of QWs	QW Distribution	Gain
ORC, Tampere University of Technology				
1180nm	AsN2596	10	2 QWs along 5 anti-nodes	$GaIn_{0.29}N_{0.011}As/GaN_{0.011}As/GaAs$
1200nm	AsN2592	8	2 QWs along 4 anti-nodes	$GaIn_{0.29}N_{0.011}As/GaN_{0.011}As/GaAs$
1220nm	AsN2527	10	2 QWs along 5 anti-nodes	$GaIn_{0.33}N_{0.007}As/GaN_{0.01}As/GaAs$
1230nm	AsN2084	10	2 QWs along 5 anti-nodes	$GaIn_{0.38}N_{0.01}As/GaAs$
1240nm	AsN2809	10	2 QWs along 5 anti-nodes	$GaIn_{0.38}N_{0.01}As/GaAs$
1300nm	AsN660	10	2 QWs along 5 anti-nodes	$GaIn_{0.37}N_{0.012}As/GaAs$
Sheffield University				
1200nm	Vn1381	4	1 QW along 4 anti-nodes	$GaIn_{0.38}As/GaAs$
1200nm	Vn1399	8	1 QW along 8 anti-nodes	$GaIn_{0.38}As/GaAs$
1200nm	Vn1534	4	1 QW along 4 anti-nodes	$GaIn_{0.33}N_{0.01}As/GaAs$
1200nm	Vn1536	8	1 QW along 8 anti-nodes	$GaIn_{0.33}N_{0.01}As/GaAs$
1200nm	Vn1567	6	1 QW along 6 anti-nodes	$GaIn_{0.33}N_{0.01}As/GaAs$
Stanford University				
1300nm	-----	10	2 QWs along 5 anti-nodes	$Ga_{0.67}In_{0.33}N_{0.019}As/GaAs$

Furthermore, the samples supplied from Sheffield University include those with GaInAs gain material, for operation at 1200 nm. These wafers were used as a

comparison with GaInNAs/GaAs structures designed to operate at the same wavelength. Previously in Section 2.2.2.1, Figure 2-7 provides the transition curves for similar designs, highlighting the need for indium concentrations ~38% in order for the device to reach ~1200 nm operating wavelengths with QW thicknesses of 8 nm. Such high concentrations of indium provide a considerable challenge for the MBE growth. In contrast, GaInNAs/GaAs, with 1% nitrogen inclusion and 33% indium has allowed the QW thickness to be reduced to ~5-7 nm. The characterisation results presented in Chapter 4, shall provide further details of the photoluminescence performance and quality of growth intrinsic to these structures.

2.4 Wafer Growth

The fabrication of the SDL is critical to laser performance, relying on high quality growth to minimise defects and any potential contributions to losses in the device.

2.4.1 Molecular Beam Epitaxial Wafer Fabrication

Molecular Beam Epitaxy builds up epitaxial layers on a molecular scale of the constituent elements in an ultrahigh vacuum chamber to form a semiconductor wafer. The growth of semiconductor material has been achieved through two main methods, the aforementioned MBE and Metalorganic Chemical Vapour Deposition (MOCVD). The MOCVD process uses a thermo-chemical decomposition of the constituent chemicals, and leaves a solid residue of the required material onto the heated substrate surface. MBE is the preferred growth method for the GaInNAs structures used in this research due to the sufficiently high quality wafers fabricated in this manner, having obtained good laser results. Added to this has been the collaborative work between the Institute of Photonics and the growth facilities at partner Universities.

In simplistic terms MBE is a vacuum evaporation process. The chamber, as illustrated in Figure 2-25 and pictured in Figure 2-26, is held under high vacuum $<10^{-10}$ Torr pressure with the heated substrate (GaAs) at the centre usually kept at between 450°C-650°C during growth. It is worth noting that the DBR section for all

devices have been grown at 580°C-600°C. The effusion cells contain the ultrapure elements such as gallium, arsenic and indium, which are heated to evaporation. The control of the amount of each element is performed using shutters. The molecular beam of these elements travels towards the substrate where they combine to form an epitaxial film. The epitaxial growth occurs as the elements are free to move on the surface of the wafer until they align to correct positions in the crystal lattice to bond. Growth rates can typically be between 0.5-2μm per hour, thus an SDL device which is ~6000 nm thick in general takes ~10 hours to grow.

The monitoring of the growth process uses Reflection High Energy Electron Diffraction (RHEED) [45]. The method characterises the surface growth of the wafer by firing electrons from the RHEED gun at a small angle onto the surface, then a pattern is formed at the detector or RHEED screen to indicate the formation of each monolayer.
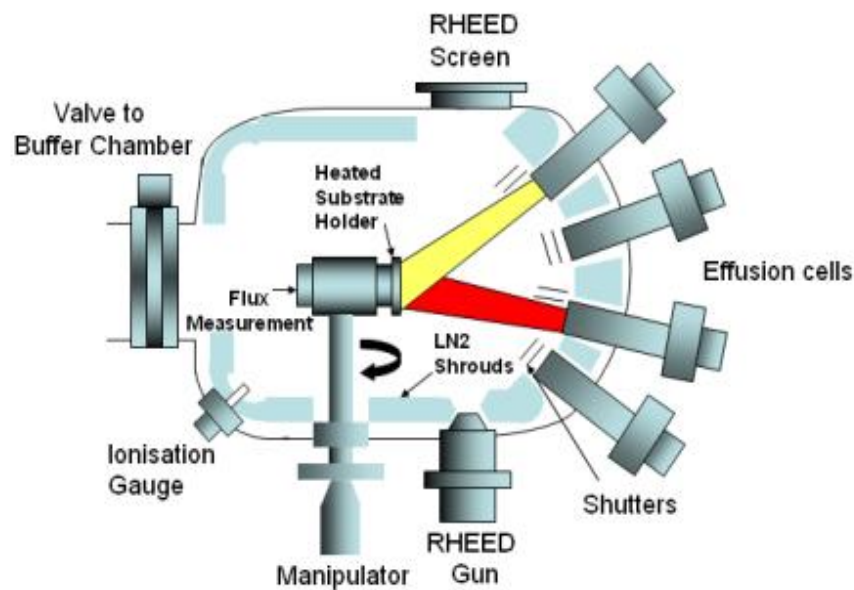
Figure 2-25: Schematic of the MBE chamber.
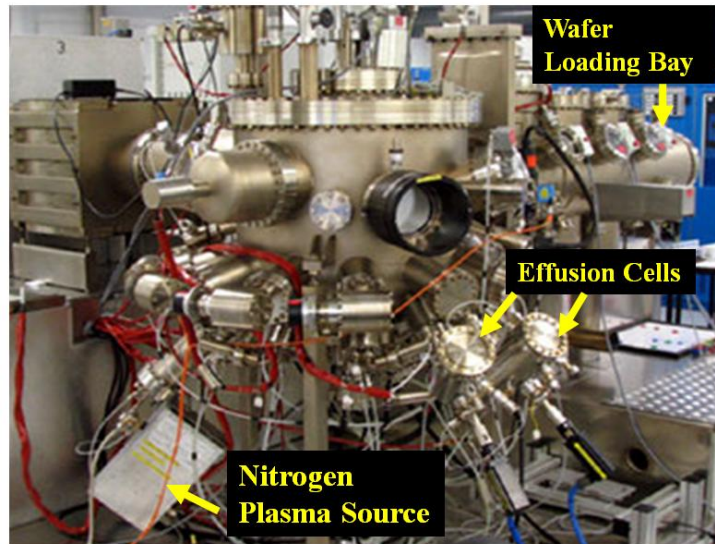
Figure 2-26: MBE machine at Sheffield University (*photo courtesy of Sheffield University*).

During growth, every effort must be made to avoid contaminants, since even the smallest amount can play a large part in rendering a device unusable. An example might be traces of organic material left by a fingerprint during the handling of the chamber components. This emphasises the importance of procedures to mitigate against these type of risks.

In the fabrication of a GaInNAs/GaAs SDL the growth involving the gallium, indium and arsenic elements follows a fairly standard technique for semiconductor device production. The gallium and indium both are added to effusion cells, which consist of a crucible, heating elements with heat shielding, a water or liquid nitrogen cooling system, and shutters. Gallium readily forms bonds with arsenic to form GaAs, whereby indium positions itself along the crystalline lattice, filling vacancies at arsenic anti-sites. The effect of indium upon the overall growth structure causes compressive strain to the system, owing to the larger size of the atoms. Due to the chemical nature of arsenic, a modified effusion cell called a *cracker cell* is required to transform the element from a solid to a gas phase at ~615°C, a process known as sublimation. The careful control of the temperature and pressure inside the cell allows the evaporation phase to form As_4 molecules which are thermally *cracked* at

900°C to form As_2. These As_2 molecules are more useful as they are more rapidly incorporated into the crystalline structure than As_4 molecules [46].

The more complicated element incorporated into the growth of these devices is nitrogen. Only a small amount is needed in the crystalline formation of GaInNAs, to achieve the desired effect of reduced energy gap and better confinement of electrons. Nitrogen is a group V element like arsenic, but has a smaller atomic size. With integration into the crystal structure the lattice constant is decreased, resulting in tensile strain. The incorporation of both nitrogen and indium thus balances the two opposing effects of strain, tensile and compressive. The chemical properties of nitrogen show that the molecule N_2 forms a strong, stable triple bond. As a consequence, the process needed for epitaxial growth requires an RF plasma cracking cell to break the bonds to produce atomic nitrogen. The nitrogen is ignited inside a small chamber in the cell forming plasma, which is held at high pressure inside the cell. There is some nitrogen that recombines when entering the growth chamber, but some still remains dissociated to form bonds at the wafer surface. Unfortunately, molecules of nitrogen are incorporated into the growth and can form deep level defects [47]. Furthermore, crystalline defects can also occur by medium energy nitrogen ions impacting the crystal surface [48]. It is possible to reduce some of these defects by using ion deflecting plates [49, 50], which are placed in front of the nitrogen plasma source thereby deflecting the high-energy charged species from reaching the sample at the expense of being able to reach high nitrogen concentrations. Careful control of the cell operating conditions is needed to ensure a low flux of undesirable nitrogen elements.

Adverse device performance caused by some of these defects during crystal growth can be improved through the process of Rapid Thermal Annealing.

2.4.2 Effects of Rapid Thermal Annealing

The process of Rapid Thermal Annealing (RTA) employs two methods, *in situ* and *post-growth*. The difference between these two methods lies in where the annealing takes place, since in situ annealing occurs within the growth chamber whilst post-

growth places the as grown semiconductor wafer into an external furnace. The latter technique allows the wafer to be divided up, thus providing an opportunity to assess optimal annealing temperatures and times.

The annealing temperatures vary, but does not exceed 900°C as this has an effect upon the crystalline structure with out-gassing of the arsenide and consequently degrades the structural quality [51]. Likewise the annealing time varies but typically is between 1-5 minutes. A careful balance must be maintained between annealing time and temperature, although it is the temperature that is most critical in this process.

The various defects caused by electron [52] and hole traps [18] inherent to the growth of dilute nitride structures have been identified by many groups studying this material system. An observed enhancement of indium segregation due to the inclusion of nitrogen during growth [53] is another defect. In addition, defects are present from strain relaxation with hardening of the lattice due to *Ga-N* bonds and dislocation pinning at nitrogen atoms [54]. Many of these defects can be negated by RTA. One such defect is the removal of the interstitial nitrogen through RTA [55].

An undeniable consequence of RTA has been an increase in photoluminescence (PL) spectra as illustrated in Figure 2-34, with an $In_{0.31}Ga_{0.69}As_{0.982}N_{0.018}$/GaAsN QW structure. This improvement is limited however by the annealing temperature. At high temperatures the indium experiences out-diffusion from the QW [56] and the PL intensity can be reduced as can be seen at 800°C in Figure 2-27. The samples grown for the purposes of this research have employed the RTA technique to enhance the PL intensity and improve laser efficiency.
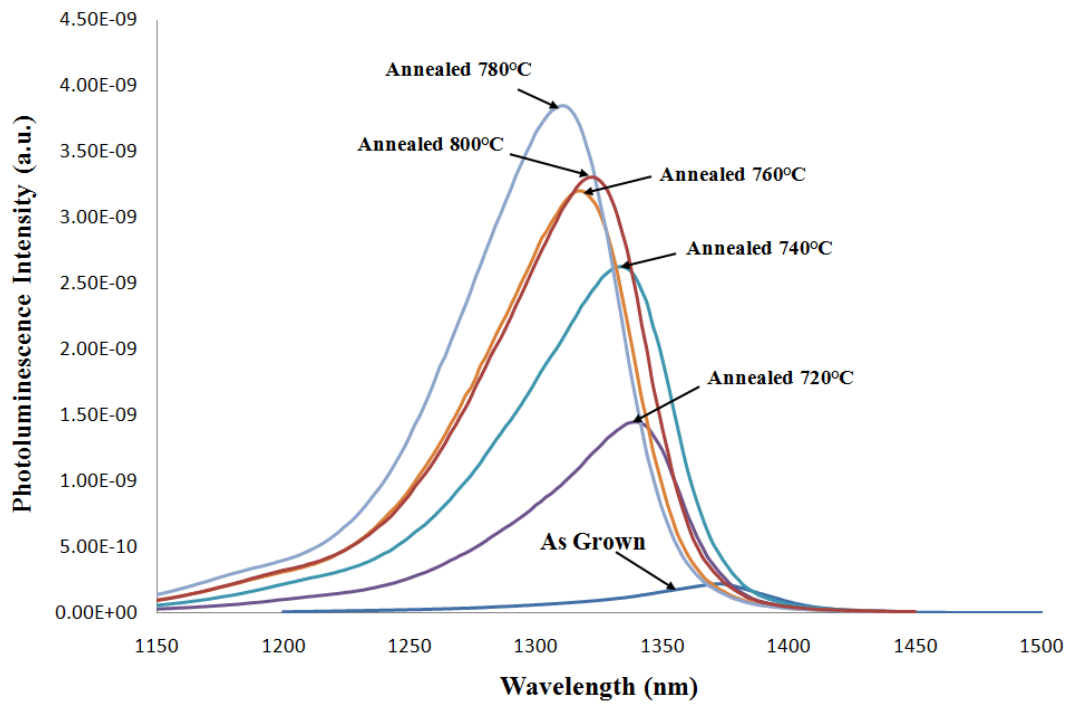
Figure 2-27: Photoluminescence spectra from $In_{0.31}Ga_{0.69}As_{0.982}N_{0.018}$/GaAsN QW structure, showing the increased PL intensity compared to the as grown sample with increasing RTA temperature.

In addition to improvements to PL intensity, a blue-shifting of the spectra is observed in Figure 2-19, with the sample experiencing a ~20nm blue-shift. Many different causes have been proposed for this phenomenon. One such cause is the *In/N* inter-diffusion in the QW resulting in composition homogenisation [57] and another proposes a change in *Ga-N* bond lengths during the annealing process [58]. The effects causing this blueshift have been linked to temperature dependence. Different effects are present at high temperatures as opposed to those at low temperatures. For example at low temperature RTA, there has been proposed a bonding reconfiguration between *N-Ga* and *N-In* [59] whilst at high temperatures inter-diffusion processes dominate [60, 61]. It is unsure whether there is one definitive reason to explain the observed blue shift in the PL, but perhaps all of these hypotheses contribute to this effect. However, from a design point of view blue-shifting effects are undesirable when targeting GaInNAs SDL devices for longer wavelengths.

The results obtained regarding PL measurements for the dilute nitrides used for this work is shown in Chapter 4.

2.5 Conclusions

The multifaceted design concepts of SDL devices have been explored in this chapter, with emphasis on the unique advantages in using dilute nitride gain material. The requirement for nitrogen to have lower temperature growth conditions results in a variety of unwanted effects such as nitrogen clustering and introducing deep level defects into the material. A method by which to remedy some of these issues was to perform RTA on the wafer samples resulting in a notable *blue-shift* response of the photoluminescence output. An important feature of the SDL is its high thermal sensitivity during operation. Thermal management techniques to ensure the best possible output characteristics shall be discussed in the next chapter.

References

[1]   M. Kuznetsov, "VECSEL Semiconductor Lasers: A Path to High-Power, Quality Beam and UV to IR Wavelength by Design", Chapter 1, pp. 1-71, O. G. Okhotnikov, Editor, *Semiconductor Disk Lasers Physics and Technology*. Wiley-VCH, (2010).

[2]   M. Born and E. Wolf, "Propagation in a stratified medium. Theory of dielectric films," in *Principles of Optics: Electromagnetic theory of propagation interference and diffraction of light*, Seventh Edition, Cambridge University Press, pp. 54-74, (1999).

[3]   D. I. Babic, and S. W. Corzine, "Analytic expressions for the reflection delay, penetration depth, and absorptance of quarter-wave dielectric mirrors," *IEEE Journal of Quantum Electronics,* vol. 28, pp. 514-524, (1992).

[4]   Y. Yamazoe, T. Nishino, Y. Hamakawa and T. Kariya, "Bandgap Energy of InGaAsP Quaternary Alloy," *Japanese Journal of Applied Physics,* vol. 19, pp. 1473 - 1479, (1980).

[5]   J. Rautiainen, J. Lyytikäinen, A. Sirbu, A. Mereuta, A. Caliman, E. Kapon and O. G. Okhotnikov, "2.6 W optically-pumped semiconductor disk laser operating at 1.57 um using wafer fusion," *Optics Express,* vol. 16, pp. 21881-21886, (2008).

[6]   O. G. Okhotnikov, "Tailoring the wavelength of semiconductor disk lasers," in *Vertical External Cavity Surface Emitting Lasers (VECSELs)*, San Francisco, California, USA, pp. 79190U-17, (2011).

[7]   J.-P. Tourrenc, S. Bouchoule, A. Khadour, J.-C. Harmand, A. Miard, J. Decobert, N. Lagay, X. Lafosse, I. Sagnes, L. Leroy and J.-L. Oudar, "Thermal optimization of 1.55 μm OP-VECSEL with hybrid metal–metamorphic mirror for single-mode high power operation," *Optical and Quantum Electronics,* vol. 40, pp. 155-165, (2008).

[8]   S. Uchiyama and S. Kashiwa, "GaInAsP/InP SBH surface emitting laser with Si/Al$_2$O$_3$ mirror," *Electronics Letters,* vol. 31, pp. 1449 - 1451, (1995).

[9]   M. R. McDaniel, D. L. Huffaker and D. G. Deppe, "Hybrid dielectric/metal reflector for low threshold vertical-cavity surface-emitting lasers," *Electronics Letters,* vol. 33, pp. 1704-1705, (1997).

[10]   J. E. Hastie, J.-M. Hopkins, C. W. Jeon, S. Calvez, D. Burns, M. D. Dawson, R. Abram, E. Riis, A. I. Ferguson, W. J. Alford, T. D. Raymond and A. A. Allerman, "Microchip vertical external cavity surface-emitting lasers," in *The 16th Annual Meeting of the IEEE Lasers and Electro-Optics Society, 2003. LEOS 2003.*, pp. 507-508 vol.2, (2003).

[11]   S. A. Smith, J.-M. Hopkins, J. E. Hastie, D. Burns, S. Calvez, M. D. Dawson, T. Jouhti, J. Kontinnen and M. Pessa, "Diamond-microchip GaInNAs vertical external-cavity surface-emitting laser operating CW at 1315nm," *Electronics Letters,* vol. 40, pp. 935-936, (2004).

[12]   S. L. Chuang, "Basic Quantum Mechanics," Chapter 3, pp. 77 - 112, in *Physics of Photonic Devices*, Second edition Hoboken, New Jersey: John Wiley & Sons, Inc, (2009).

[13]   M. Hetterich, M. D. Dawson, A. Egorov, Yu, D. Bernklau and H. Riechert, "Electronic states and band alignment in GaInNAs/GaAs quantum-well structures with low nitrogen content," *Applied Physics Letters,* vol. 76, pp. 1030-1032, (2000).

[14]   M. G. A. Bernard and G. Duraffourg, "Laser Conditions in Semiconductors," *physica status solidi (b),* vol. 1, pp. 699-703, (1961).

[15]   H. Schneider and K. v. Klitzing, "Thermionic emission and Gaussian transport of holes in a GaAs/Al$_x$Ga$_{1-x}$As multiple-quantum-well structure," *Physical Review B,* vol. 38, pp. 6160 - 6165, (1988).

[16]   R. Nagarajan and J. E. Bowers, "High-Speed Lasers," Chapter 3, pp. 177 - 290, in *Semiconductor Lasers I: Fundamentals*, E. Kapon, Editor, San Diego: Academic Press, (1999).

[17]   M. Kondow, "GaInNAs Long-Wavelength Lasers for 1.3-μm-Range Applications," Chapter 11, pp. 331 - 360, in *Optoelectronic Properties of Semiconductors and Superlattices: Physics and Applications of Dilute Nitrides.* vol. 21, I. A. Buyanova and W. M. Chen, Editors, New York: Taylor & Francis Books, Inc., (2005).

[18]   A. B. Chen, A. Sher and M. A. Berding, "Semiconductor alloy theory: Internal strain energy and bulk modulus," *Physical Review B,* vol. 37, p. 6285, (1988).

[19]   J.-M. Chauveau, A. Trampert, K. H. Ploog, M.-A. Pinault and E. Tournie, "Interplay between the growth temperature, microstructure, and optical properties of GaInNAs quantum wells," *Applied Physics Letters,* vol. 82, pp. 3451-3453, (2003).

[20]   S. L. Chuang, "Theory of Electronic Band Structures in Semiconductors,"Chapter 4, pp. 113 - 178, in *Physics of Photonic Devices*, Second edition Hoboken, New Jersey: John Wiley & Sons, Inc, (2009).

[21]   J. J. Coleman, "Strained Layer Quantum Well Heterostructure Lasers," Chapter 8, pp. 367 - 407 in *Quantum Well Lasers*, P. S. Zory Jr., Editor, San Diego: Academic Press Limited, (1993).

[22]   J. J. Katcki, J. Ratajczak, J. Adamczewska, F. Phillipp, N. Y. Jin-Phillipp, K. Reginski and M. Bugajski, "Formation of Dislocations in InGaAs/GaAs Heterostructures," *Physica status solidi (a),* vol. 171, pp. 275 - 282, (1999).

[23]   J. W. Matthews and A. E. Blakeslee,"Defects in epitaxial multilayers: I. Misfit dislocations," *Journal of Crystal Growth,* vol. 27, pp. 118-125, (1974).

[24]   Q. X. Zhao, S. M. Wang, M. Sadeghi, A. Larsson, M. Willander and J. H. Yang, "Effects of nitrogen incorporation on the properties of GaInNAs/GaAs quantum well structures," *Japanese Journal of Applied Physics,* vol. 97, pp. 073714-1 - 073714-6, (2005).

[25]   R. M. Kolbas, N. G. Anderson, W. D. Laidig, Y. Sin, Y. C. Lo, K. Y. Hsieh and Y. J. Yang, "Strained-layer InGaAs-GaAs-AlGaAs photopumped and current injection lasers," *IEEE Journal of Quantum Electronics,* vol. 24, pp. 1605-1613, (1988).

[26]   K. S. Kim, J. R. Yoo, S. M. Lee, S. J. Lim, J. Y. Kim, J. H. Lee, S. H. Cho, T. Kim and Y. J. Park, "Highly efficient InGaAs QW vertical external cavity surface emitting lasers emitting at 1060 nm," *Journal of Crystal Growth,* vol. 287, pp. 629-632, (2006).

[27]   B. Gonul, E. Bakır and K. Koksal, "Analysis of the band alignment of highly strained indium-rich GaInNAs QWs on InP substrates," *Semiconductor Science and Technology,* vol. 21, pp. 876 - 880, (2006).

[28]   A. Gavini and M. Cardona, "Modulated Piezoreflectance in Semiconductors," *Physical Review B,* vol. 1, p. 672, (1970).

[29]   N. J. Ekins-Daukes, K. Kawaguchi and J. Zhang, "Strain-Balanced Criteria for Multiple Quantum Well Structures and Its Signature in X-ray Rocking Curves," *Crystal Growth & Design,* vol. 2, pp. 287-292, (2002).

[30]   A. Garnache, A. A. Kachanov, F. Stoeckel and R. Houdré, "Diode-pumped broadband vertical-external-cavity surface-emitting semiconductor laser applied to high-sensitivity intracavity absorption spectroscopy," *Journal of the Optical Society of America B,* vol. 17, pp. 1589-1598, (2000).

[31]   J.-Y. Kim, S. Cho, J. Lee, G. B. Kim, S.-J. Lim, J. Yoo, K.-S. Kim, S.-M. Lee, J. Shim, T. Kim and Y. Park, "A Measurement of Modal Gain Profile and Its Effect on the Lasing Performance in Vertical-External-Cavity Surface-Emitting Lasers," *IEEE Photonics Technology Letters,* vol. 18, pp. 2496-2498, (2006).

[32]   C. Borgentun, J. Bengtsson, A. Larsson, F. Demaria, A. Hein and P. Unger, "Optimization of a Broadband Gain Element for a Widely Tunable High-Power Semiconductor Disk Laser," *Photonics Technology Letters, IEEE,* vol. 22, pp. 978-980, (2010).

[33]   J. Wagner, N. Schulz, M. Rattunde, C. Ritzenthaler, C. Manz, C. Wild and K. Köhler, "Barrier- and in-well pumped GaSb-based 2.3 μm VECSEL," *Physica status solidi (c),* vol. 4, pp. 1597 - 1600, (2007).

[34]   M. Schmid, S. Benchabane, F. Torabi-Goudarzi, R. Abram, A. I. Ferguson and E. Riis,"Optical in-well pumping of a vertical-external-cavity surface-emitting laser," *Applied Physics Letters,* vol. 84, pp. 4860 - 4862, (2004).

[35]   S.-S. Beyertt, M. Zorn, T. Kübler, H. Wenzel, M. Weyers, A. Giesen, G. Tränkle and U. Brauch, "Optical In-Well Pumping of a Semiconductor Disk Laser With High Optical Efficiency," *IEEE Journal of Quantum Electronics,* vol. 41, pp. 1439 - 1449, (2005).

[36]   R. Ramaswami, K. N. Sivarajan and G. H. Sasaki, "Detectors," Chapter 3, pp. 198 - 203 in *Optical Networks: A Practical Perspective*, Third edition Burlington: Elsevier, (2010).

[37]   Brigham Young University, Department of Electrical and Chemical Engineering. Available: http://www.cleanroom.byu.edu/OpticalCalc.phtml

[38]   M. Kuznetsov, F. Hakimi, R. Sprague and A. Mooradian, "Design and characteristics of high-power (0.5-W CW) diode-pumped vertical-external-cavity surface-emitting semiconductor lasers with circular TEM_{00} beams," *IEEE Journal of Selected Topics in Quantum Electronics,* vol. 5, pp. 561-573, (1999).

[39]   M. Kondow, T. Kitatani, S. Nakatsuka, M. C. Larson, K. Nakahara, Y. Yazawa, M. Okai and K. Uomi, "GaInNAs: A Novel Material for Long-Wavelength Semiconductor Lasers," *IEEE Journal of Selected Topics in Quantum Electronics,* vol. 3, pp. 719 - 730, (1997).

[40]   D. Alexandropoulos and M. J. Adams, "Assessment of GaInNAs as a potential laser material," *IEE Proceedings in Optoelectronics,* vol. 150, pp. 40-44, (2003).

[41]   G. Knowles, R. Fehse, S. Tomic, S. J. Sweeney, T. E. Sale, A. R. Adams, E. P. O'Reilly, G. Steinle and H. Riechert, "Investigation of 1.3-um GaInNAs vertical-cavity surface-emitting lasers (VCSELs) using temperature, high-pressure, and modeling techniques," *IEEE Journal of Selected Topics in Quantum Electronics,* vol. 9, pp. 1202-1208, (2003).

[42]   T. Westgaard, Q. X. Zhao, B. O. Fimland, K. Johannessen and L. Johnsen, "Optical properties of excitons in $GaAs/Al_{0.3}Ga_{0.7}As$ symmetric double quantum wells," *Physical Review B,* vol. 45, p. 1784, (1992).

[43]   A. M. Fox, D. A. B. Miller, G. Livescu, J. E. Cunningham and W. Y. Jan, "Quantum well carrier sweep out: relation to electroabsorption and exciton saturation," *IEEE Journal of Quantum Electronics,* vol. 27, pp. 2281-2295, (1991).

[44]   W. J. Alford, T. D. Raymond and A. A. Allerman, "High power and good beam quality at 980 nm from a vertical external-cavity surface-emitting laser," *Journal of the Optical Society of America B,* vol. 19, pp. 663-666, (2002).

[45]   H. A. Atwater, C. C. Ahn, S. S. Wong, G. He, H. Yoshino and S. Nikzad, "Energy-Filtered RHEED and REELS for In Situ Real Time Analysis During Film Growth," *Surface Review and Letters,* vol. 4, pp. 525 - 534, (1997).

[46]   J. C. Garcia, C. Neri and J. Massies, "A comparative study of the interaction kinetics of As2 and As4 molecules with Ga-rich GaAs (001) surfaces," *Journal of Crystal Growth,* vol. 98, pp. 511-518, (1989).

[47]   A. S. Rutz, "GaInNAs SESAMs and VECSELs at 1.3 and 1.5 um wavelength," PhD, ETH, Zurich, (2008).

[48]   M. A. Wistey, S. R. Bank, H. B. Yuen, B. Hopil and J. S. Harris, Jr., "Nitrogen plasma optimization for high-quality dilute nitrides," *Journal of Crystal Growth,* vol. 278, pp. 229-233, (2005).

[49]   S. R. Bank, M. A. Wistey, H. B. Yuen, V. Lordi, V. F. Gambin and J. S. Harris, Jr., "Effects of antimony and ion damage on carrier localization in molecular-beam-epitaxy-grown GaInNAs," pp. 1320-1323, (2005).

[50] D. B. Jackrel, S. R. Bank, H. B. Yuen, M. A. Wistey, J. S. Harris, Jr., A. J. Ptak, S. W. Johnston, D. J. Friedman and S. R. Kurtz, "Dilute nitride GaInNAs and GaInNAsSb solar cells by molecular beam epitaxy," *Journal of Applied Physics,* vol. 101, pp. 114916-8, (2007).

[51] S. Govindaraju, J. Reifsnider, M. Oye and A. Holmes, "Time and temperature dependence on rapid thermal annealing of molecular beam epitaxy grown $Ga_{0.8}In_{0.2}N_{0.01}As_{0.99}$ quantum wells analyzed using photoluminescence," *Journal of Electronic Materials,* vol. 32, pp. 29-33, (2003).

[52] S. O. Kasap and P. Capper, P., Editors *Springer handbook of electronic and photonic materials* Optoelectronic Devices and Materials. Wurzburg: Springer, (2006).

[53] E. Luna, A. Trampert, E.-M. Pavelescu and M. Pessa, "Nitrogen-enhanced indium segregation in (Ga,In)(N,As)/GaAs multiple quantum wells grown by molecular-beam epitaxy," *New Journal of Physics,* vol. 9, p. 405, (2007).

[54] E. C. Young, A. N. Koveshnikov, S. Tixier, K. L. Kavanagh and T. Tiedje, "Strain relaxation by <100> misfit dislocations in dilute nitride $In_xGa_{1-x}As_{1-y}N_y$/GaAs quantum well," *Physica status solidi (a),* vol. 202, pp. 2849 - 2857, (2005).

[55] S. G. Spruytte, C. W. Coldren, J. S. Harris, W. Wampler, P. Krispin, K. Ploog and M. C. Larson,"Incorporation of nitrogen in nitride-arsenides: Origin of improved luminescence efficiency after anneal," *Journal of Applied Physics,* vol. 89, pp. 61 - 68, (2001).

[56] G. Mussler, J. M. Chauveau, A. Trampert, M. Ramsteiner, L. Däweritz and K. H. Ploog,"Nitrogen-dependent optimum annealing temperature of Ga(As,N)," *Journal of Crystal Growth,* vol. 267, pp. 60-66, (2004).

[57] L. Grenouillet, C. Bru-Chevallier, G. Guillot, P. Gilet, P. Ballet, P. Duvaut, G. Rolland and A. Million, "Rapid thermal annealing in GaN_xAs_{1-x}/GaAs structures: Effect of nitrogen reorganization on optical properties," *Journal of Applied Physics,* vol. 91, pp. 71-73, (2002).

[58] T. Kitatani, M. Kondow and M. Kudo,"Transition of Infrared Absorption Peaks in Thermally Annealed GaInNAs," *Japanese Journal of Applied Physics,* vol. 40, pp. L750 - L752, (2001).

[59] V. Dixit, H. F. Liu and N. Xiang, "Study of thermal-anneal-induced rearrangement of N-bonding configurations in GaInNAs/GaAs quantum well," *Advanced Materials Research,* vol. 31, pp. 209 - 211, (2008).

[60] M. Hugues, B. Damilano, J. M. Chauveau, J. Y. Duboz and J. Massies, "Blue-shift mechanisms in annealed (Ga,In)(N,As)/GaAs quantum wells," *Physical Review B,* vol. 75, p. 045313, (2007).

[61] V. Liverini, A. Rutz, U. Keller and S. Schön, "Effects of rapid thermal annealing conditions on GaInNAs band gap blueshift and photoluminescence intensity," *Journal of Applied Physics,* vol. 99, p. 113103, (2006).

Chapter 3

Thermal Management

3.1 Introduction

Effective thermal management ranks high in the design and development of lasers which is why this chapter is dedicated to exploring this issue, specifically applied to SDLs. The inherent thermal sensitivity of these devices and drive for power scalability has created a host of studies dedicated to this topic. Section 3.2 shall provide a review of some previous evaluations, targeting thermal management techniques and recommendations to achieve high laser output. Further, Section 3.3 presents the foundations on which the thermal models are based, with use in subsequent sections.

As a continuation of previous studies, Section 3.4 focuses on the specific characteristics attributed to the GaInNAs/Ga(N)As material system, along with other epitaxial layers included in these devices. This helps to construct the picture of the mechanisms involved in heat development and dissipation, and consequently identify areas of improvement to the overall device performance. The valuable simulation software tool in the form of COMSOL Multiphysics^{TM} has been employed to evaluate the thermal response of the SDL under various conditions and design configurations. The optical pumping regime, referring to front and end pumped devices shall be explored in Section 3.5. In this study, simulations based on device designs implemented by other groups shall be looked at, along with proposed use of the heatspreader in structures intended to maximise heat extraction.

Finally, the construction of the SDL device shall be presented in Section 3.6 using the commonly used bonding technique of the semiconductor chip to the heatspreader and mounting onto a copper heatsink.

3.2 Review of SDL Thermal Management

There has been considerable interest in the thermal management of SDLs, and understandably so, considering the high thermal sensitivity attributed to the QW gain structure of these devices. In the gain region of an optically pumped SDL the thermal load increases per absorbed pump photon with the increasing pump rate.

In an SDL, the fundamental relationship between the gain with carrier population and lifetime rates $\tau(N)$ is given in Equation (3.1.1) [1]. In this expression the transparency carrier density is N_0 and g_0 is the semiconductor material gain parameter, with the absorption efficiency in the material η_{abs}, number of QWs N_w and their lengths L_w. The thermal load is dependent upon the incident pump beam, such that the expression includes the pump power P_p, energy $h\upsilon_p$ and pump spot area A_p.

$$g = g_0 ln \left(\frac{\eta_{abs} P_p}{h\upsilon_p (N_w L_w A_p)} \frac{\tau(N)}{N_0} \right) \qquad (3.1.1)$$

It is therefore reasonable to infer that with gain rising sub-linearly with the carrier population and the carrier lifetime decreasing, the carriers are unable to remain in the upper state long enough to facilitate recombination. There reaches a point when the diminished gain falls below the cavity losses and the laser switches off. In addition, the subcavity resonant periodic gain structure is also influenced by temperature increases as described in Chapter 2, Section 2.2.2.3.

These thermal effects have a profound influence on device performance. For example, in the case of the confinement of carriers in the QWs, the thermionic escape into the barriers impacts upon the internal quantum efficiency of the device. Further, the requirement for an even distribution of carriers between the wells is necessary, otherwise the carrier concentrations may vary significantly between the top and bottom QW, impairing the overall gain and efficiency. There is also an observed red-shift to longer wavelengths of the semiconductor bandgap with increased temperature which is different to the shift rate of the resonant periodic gain, resulting in spectral misalignment and contributing to thermal rollover. The control of the design parameters is not a trivial matter, as was highlighted by Schulz

et al [2], where the simultaneous control of the gain offset, output coupler transmission, and number of QWs is necessary to optimise the device.

Thermal evaluations of SDL devices have been well documented, with some leading investigations performed at the Institute of Photonics. There are two main methods employed in device thermal management. The first of which has been thinning or removal of the semiconductor chip substrate to aid in heat removal from the back of the structure also referred to as *thin disk*. The second was the use of a highly conductive platelet attached to the front of the structure (confinement window), commonly termed as an *intracavity heatspreader*. Key topics in this area include comparisons made between the aforementioned thin disk devices and heatspreaders, the best material choices of an intracavity heatspreader and thermal lensing effects in SDLs.

Early investigations performed by Hastie *et al.* [3] had used silicon carbide and sapphire as heatspreader materials resulting in output powers ~100mW for both. The thermal conductivity value for silicon carbide is $k_{SiC}=0.49W/(mmK)$ and for sapphire $k_{Sapphire}=0.044W/(mmK)$. Further improvements were found using the more thermally conductive silicon carbide in an 850 nm GaAs/AlGaAs SDL achieving >0.5W [4]. As a progression towards the most effective heatspreader material Kemp *et al.* [5] examined the use of diamond with thermal conductivity $k_{diamond}=2W/(mmK)$, such as that used in a ~1.3μm GaInNAs/GaAs SDL [6], in comparison with silicon carbide and sapphire, as well as the thin disk approach. In a similar study Giet *et al.* [7] corroborates the previous analysis, showing that overall the heatspreader was superior to the thin disk, with higher output powers, better efficiency and lower thermal resistance, with improved results using diamond compared to those of silicon carbide. Parallel investigations performed by Lindberg *et al.* [8] had focused on InP-based SDLs for operation at long wavelengths. Their results comparing substrate thinning with the heatspreader approach, found an overwhelming benefit to the heatspreader with preference given to diamond use compared with silicon. In more recent modeling evaluations performed on an InGaAs SDL, Zhang *et al.* [9] proposed the partial removal of the substrate was sufficient to reduce heat in the device with diamond again preferred over silicon carbide. However, as a cost saving

alternative silicon carbide would suffice. Having established diamond as the frontrunner in heatspreader material choice, performance related evaluations were used to test the limits on SDL devices.

Maclean *et al.* [10] had used modeling techniques in combination with experimental results to examine the output powers and efficiencies, using diamond heatspreader and thin disk devices across a range of pump spot sizes. Results have highlighted the limitations to power scaling through non-axial heat flow in the heatspreader, which in turn increases the temperature in the gain region with increasing pump spot size, as shown in Figure 3-1. This further limits the device efficiency, which was consistent with the theoretical model of reduced quantum efficiency at higher temperatures and carrier densities.
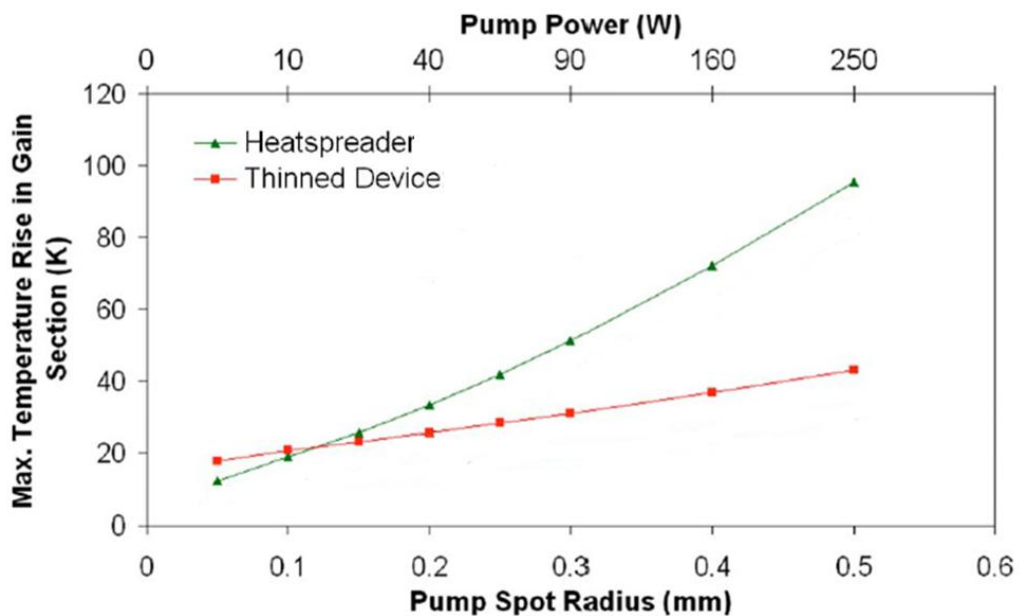

Figure 3-1: Graph of temperature rises in the gain section employing the thin disk (*thinned device*) or heatspreader thermal management techniques, for increasing pump spot radii at constant power intensity of 32 W/cm^2 [10].

Thermal lensing in an SDL has been explored by Kemp *et al.* [11], in light of the response by doped-dielectric lasers using a microchip design. Successful operation of such lasers has been largely attributed to thermal lensing, due to the self-alignment capability brought about from the thermo-optic coefficient $\left(\frac{dn}{dT}\right)$ of the material. The thermal expansion alters the refractive index of the material, thereby altering the

focal length within the 3D gain medium. Applying this analysis to the SDL in similar microchip geometry has provided an indication that due to the near-planar absorption region, thermal lensing has not been found to contribute significantly to device performance. Generally the inclusion of the diamond heatspreader has provided a superior thermal environment with improved beam quality, thus reducing the impact of thermal lensing [11]. Through the development of microlensed microchip SDLs by Laurand *et al.* [12, 13], more detailed investigations were possible to determine thermal lensing effects on a much smaller scaled device. Their findings provide further evidence that thermal lensing is not a major contributor to the laser cavity design, in terms of influencing the focal length of the microlens formed on top of the diamond heatspreader. Using a similar strategy, Chapter 6 delves into the effects of thermal lensing on the design of a frequency doubled microchip SDL. These investigations are worthwhile to fully explore the impact of heating effects on the device performance, but also in light of corresponding results obtained by Laurain et al [14]. Their high outputs using no intracavity elements in a plane-plane cavity design has been largely attributed to the thermal lensing within the optically pumped SDL, justifying that thermal lensing should not be completely ruled out during design considerations.

The following sections shall explore the performance of the SDL device using simulations and material evaluations.

3.3 Thermal Model Foundations

The models used here originate from those developed by Kemp *et al.* [5] and Lindberg *et al.* [8]. In real systems the complex layering of the semiconductor material through a range of scales (*nanometers, microns, millimeters*) requires more computer processing power than is available for this project, in order to mesh all the resolvable points for detailed simulations. Therefore, a more simplistic model is used in which the composite materials have been blocked together, each representing the main regions, such as the diamond heatspreader, the confinement window, the active region, the DBR and the substrate. A general configuration to illustrate these main

regions is given in Figure 3-2 assuming axial symmetry in the device; however it will be evident in later sections that the orientation and components may alter in accordance with pumping configuration and device specifications. Included within these models is indium foil, which is typically used in a real device, to aid conduction of heat away from the sample.
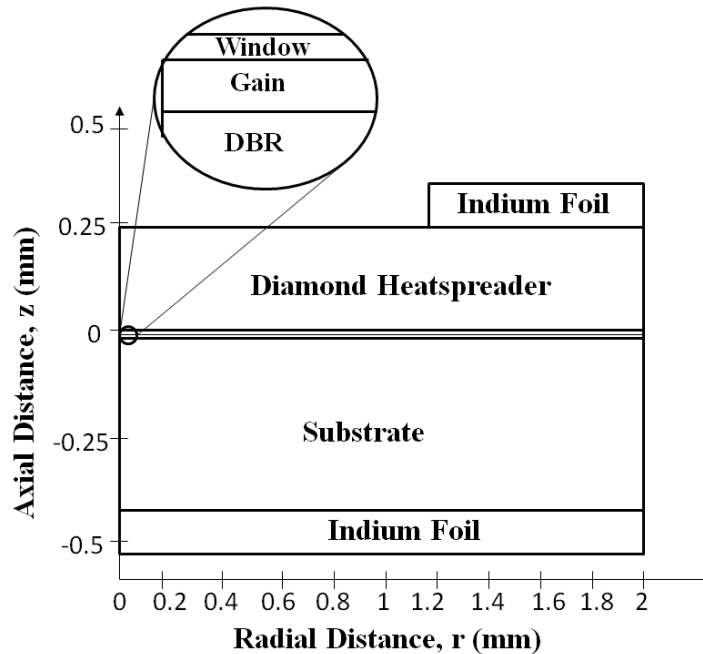

Figure 3-2: Diagram of thermal model system, including the window, gain and DBR, with the diamond heatspreader adjacent to the confinement window and the substrate under the DBR mirror, with indium foil at the intermediate layer to the submount.

Heat conduction plays a central role in these models. COMSOL Multiphysics™ software was used to solve the standard heat equation, expressed in Equation (3.1.2), where k denotes the conductivity, ∇T is the temperature gradient and Q is the total thermal load density in the material [15]. The minus sign ensures that the heat flow is down the temperature gradient, i.e. from high to low temperature regions.

$$-\nabla(k.\nabla T) = Q \qquad (3.1.2)$$

As heat builds up, effective heat removal towards the heatsink and heatspreader are vital to cool the device and maintain high levels of operation. In these structures, with composite layers of semiconductor materials, the transfer of heat across boundaries adheres to the conservation of energy, as given in Equation (3.1.3) with

76

heat flow related to the difference in thermal conductivities and temperature gradients between the two adjacent materials $k_1 \nabla T_1$ and $k_2 \nabla T_2$.

$$n(k_1 \nabla T_1 - k_2 \nabla T_2) = 0 \qquad (3.1.3)$$

The management of calculations governing thermal conductivity in regions such as the DBR, based on superlattices, is accounted for in the axial k_z and radial k_r directions. Equations (3.1.4) and (3.1.5) include summations of each of the epitaxial layers, where the thickness of the *ith* layer is denoted t_i and material conductivity k_i.

$$k_z = \frac{\sum_i t_i}{\sum_i \left(\frac{t_i}{k_i}\right)} \qquad (3.1.4)$$

$$k_r = \frac{\sum_i t_i k_i}{\sum_i t_i} \qquad (3.1.5)$$

In a similar manner, the composite absorption coefficient α is calculated using the expression given in Equation (3.1.6), where α_i is the absorption coefficient of the epitaxial layer *i*.

$$\alpha = \frac{\sum_i \alpha_i t_i}{\sum_i t_i} \qquad (3.1.6)$$

The thermal resistance of the device is the average temperature rise in terms of absorbed power in the axial *z* and radial *r* directions within the pumped volume V_p.

$$R_{th} = \frac{\iiint_{V_p} (T - T_0) P(r,z) dV}{\eta \left[\iiint_{V_p} P(r,z) dV \right]^2} \qquad (3.1.7)$$

The orientation of the device design, used for simulation purposes, must be factored into the calculations governing the heat loads in the regions. In the case of front pumping, the pump beam is incident onto the top of the structure at the confinement window. Here the heat load Q_{gain} within the gain section is given by the relationship in Equation (3.1.8) based on co-ordinates in the axial (z) and radial (r) directions. The definitions for the variables used in the equation are provided in Table 3.1.

$$Q_{gain}(r,z) = \frac{2\alpha_{gain}}{\pi\omega_p^2}P_{abs}exp\left(\frac{-2r^2}{\omega_p^2}\right)exp\left(-\alpha_{gain}(z_{window}-z)\right) \quad (3.1.8)$$

The expression describing the heat load in the DBR region Q_{DBR} is given in Equation (3.1.9).

$$Q_{DBR}(r,z) = \frac{2\alpha_{DBR}}{\pi\omega_p^2}P_{abs}exp\left(\frac{-2r^2}{\omega_p^2}\right)exp\left(-\alpha_{gain}z_{gain}\right)exp\left(-\alpha_{DBR}(z_{window}-z_{gain}-z)\right) \quad (3.1.9)$$

When the device has been orientated for back or end pumping, the pump beam is incident onto the DBR, and the heat load in the DBR section has been set to 0. The expression for Q_{gain} is now changed in line with the appropriate co-ordinates as given in Equation (3.2.0).

$$Q_{gain}(r,z) = \frac{2\alpha_{gain}}{\pi\omega_p^2}P_{abs}exp\left(\frac{-2r^2}{\omega_p^2}\right)exp\left(\alpha_{gain}(z_{DBR}+z)\right) \quad (3.2.0)$$

Table 3.1: Typical parameters used in thermal simulations.

Symbol	Definition	Value
z_{window}	Window thickness	2.48×10^{-4} mm
z_{gain}	Gain region thickness	9.361×10^{-4} mm
z_{DBR}	DBR thickness	4.741×10^{-3} mm
z_{sub}	Substrate thickness	0.35 mm
z_{dia}	Diamond heatspreader thickness	0.25 mm
k_{window}	Window thermal conductivity	0.012 W/(mm.K)
k_{active}	Active region thermal conductivity	0.044 W/(mm.K)[16]
k_{DBRz}	DBR axial thermal conductivity	0.0612 W/(mm.K)[17, 18]
k_{DBRr}	DBR radial thermal conductivity	0.0697 W/(mm.K)[17, 18]
k_{sub}	Substrate thermal conductivity	0.044 W/(mm.K)[16]
k_{dia}	Diamond heatspreader thermal conductivity	2 W/(mm.K)[19]
k_{indium}	Indium foil thermal conductivity	0.082 W/(mm.K)
ω_p	Pump spot radius	0.05mm
α_{gain}	Pump absorption coefficient in the gain	1430 mm^{-1}
P_{abs}	Absorbed power contributing to heat	5 W
T_{sub}	Substrate temperature	0°C

The average temperature T_{avg} across the gain region is calculated according to Equation (3.2.1), where a high concentration of heat has been generated. The temperature is based on the integral over the volume V_{gain} of the pumped region.

$$T_{avg} = \int \frac{2Texp\left(\frac{-2r^2}{\omega_p^2}\right)}{\pi z_{gain}\omega_p^2} dV_{gain} \qquad (3.2.1)$$

The following section examines the gain materials in the SDL devices used throughout this thesis.

3.4 Thermal Response of the Material System: GaInNAs/Ga(N)As

Fundamental values often listed regarding the thermal properties of materials include specific heat capacity, thermal expansion and conductivity (resistance). In the case of SDLs, the heat generation and dissipation are at the core of power scalability. Referring to the heat capacity is useful to describe the diffusivity of the material, conversely the thermal expansion can influence the thermal lensing associated with the device, as described previously. The pertinent values used here to describe the SDL thermal response during operation, are conductivity and the all important optical absorption coefficient.

It is evident that there is a symbiotic relationship between the thermal loads and the absorbed pump radiation, therefore it can be categorised as one of the main contributors to heat generation within the gain region. Focusing on the SDL designs using the GaInNAs/GaNAs/GaAs gain material system, as described in detail within Chapter 2, the absorption coefficients of each of the materials has been measured. Calculations are based on those given by Chuang [20] with the absorption as a function of the pump energy $\alpha(\hbar\omega)$ given in Equation (3.2.2).

$$\alpha(\hbar\omega) = C_0 \frac{2}{V}\sum_k |\hat{e} \cdot \boldsymbol{p}_{cv}|^2 \, \delta(\mathrm{E_c} - \mathrm{E_v} - \hbar\omega)(\mathrm{f_v(k)} - \mathrm{f_c(k)}) \qquad (3.2.2)$$

$$\text{with} \quad C_0 = \frac{\pi e^2}{n_r c \varepsilon_0 m_0^2 \omega} \;, E_c = E_g + \frac{\hbar^2 k^2}{2m_e^*}, \; E_v = -\frac{\hbar^2 k^2}{2m_h^*} \qquad (3.2.3)$$

$$\text{and} \quad f_v(k) = \frac{1}{1+e^{(E_v(k)-F_v)/k_B T}} \,, f_c(k) = \frac{1}{1+e^{(E_c(k)-F_c)/k_B T}} \qquad (3.2.4)$$

The material bandgap is given as E_g, with the relative effective mass m_r^* found from the relationship $\frac{1}{m_r^*} = \frac{1}{m_e^*} + \frac{1}{m_h^*}$ in which m_e^* is the effective *electron* mass and m_h^* is the effective *hole* mass. The expression for C_0 is provided in Equation (3.2.3) where the material refractive index is n_r, free space permittivity ε_0, speed of light c, electronic charge e, free electron rest mass m_0 and angular frequency ω. The expressions in Equation (3.2.4) refer to the Fermi-Dirac distributions of electrons in the conduction band f_c and valence band f_v respectively.

In the case of bulk material, the momentum matrix element $|\hat{e} \cdot \boldsymbol{p}_{cv}|^2 = M_b^2$ is further evaluated in Equation (3.2.5) where Δ is the slit off energy in the valence band.

$$M_b^2 = \left(\frac{m_0^2}{m_e^*} - 1\right) \frac{m_0 E_g (E_g + \Delta)}{6\left(E_g + \frac{2}{3}\Delta\right)} \qquad (3.2.5)$$

In the case of a quantum well however, the optical matrix elements are modified in accordance with the polarisation components. In the case of TE polarisation, the upward transition from the heavy-hole band to conduction band is provided in Equation (3.2.6).

$$|\hat{e} \cdot \boldsymbol{p}_{cv}|^2 = \langle |\hat{e} \cdot M_{c-hh}|^2 \rangle = \langle |\hat{x} \cdot M_{c-hh}|^2 \rangle = \frac{3}{2} M_b^2 \qquad (3.2.6)$$

Figure 3-3 shows the absorption response of materials within the gain region of the SDL, with GaAs as the barrier, GaNAs strain compensating layers (SCL) and GaInNAs QWs. The evaluations for the barrier material have been based on bulk material due to the thicker barriers or spacer layers; however both the GaNAs and GaInNAs were treated as QWs in the TE polarisation case.
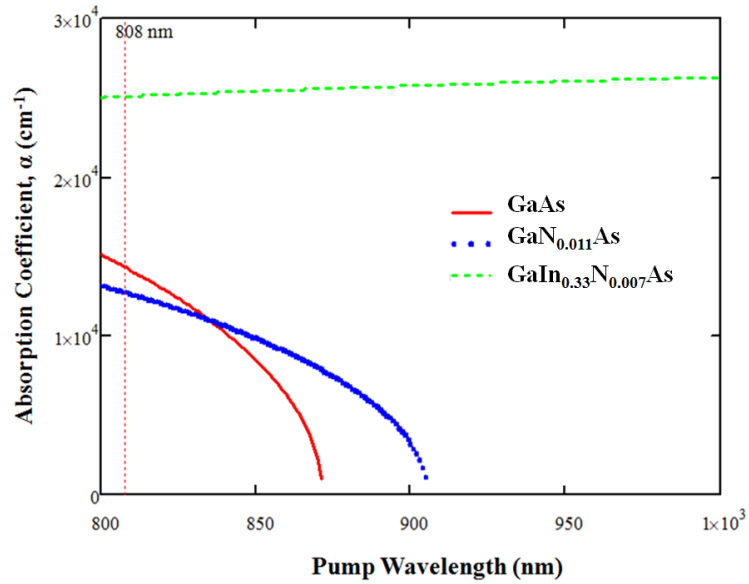
Figure 3-3: Absorption coefficients for GaAs, GaNAs and GaInNAs over a range of pump wavelengths.

The results obtained for a pump at 808 nm were 14266 cm^{-1} for GaAs, 12696 cm^{-1} for GaN$_{0.011}$As and 25079 cm^{-1} for GaIn$_{0.33}$N$_{0.007}$As. The use of barrier pumping provides adequate absorption in the longer GaAs regions, with slightly lower absorption in the thin SCLs. The flat response of the GaInNAs QW absorption is due to the much lower bandgap energy, allowing higher absorption across a wider range of pump wavelengths. In the context of modeling of these devices, the absorption in the gain region uses that of GaAs due to the larger volume of material compared with such thin layers of ~7 nm GaInNAs QWs and ~4 nm GaNAs SCLs, as indicated in Figure 3-4.
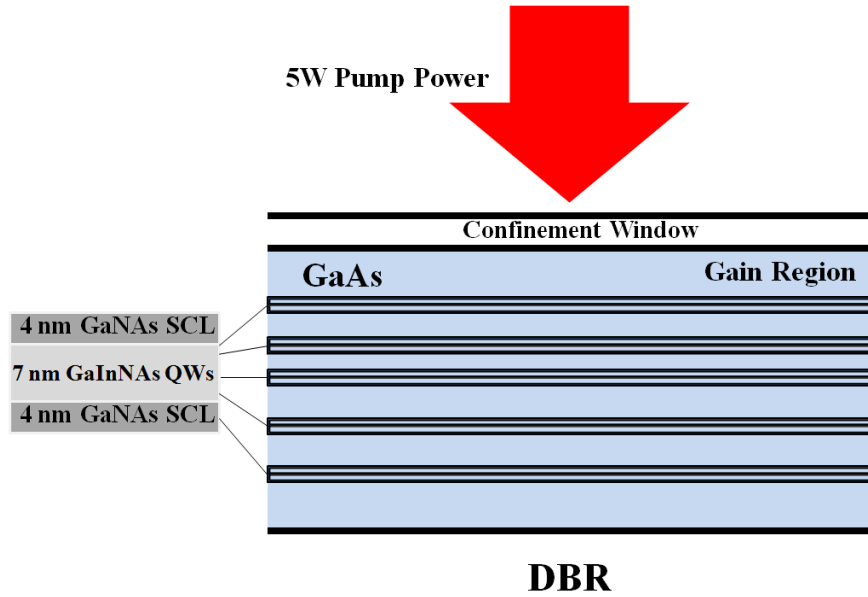
Figure 3-4: Schematic of pumping with 5W pump power, incident onto the confinement window and absorbed in the gain region, predominantly composed of GaAs absorption/spacer layers with 7 nm GaInNAs QWs and 4 nm GaNAs SCLs.

As a whole, the amount of pump power absorbed by the system is influenced by mechanisms intrinsic to the material and pumping regime. In general, these are recognised as the fraction of pump power that contributes to heating $\eta_q = 1 - \frac{\lambda_p}{\lambda_l}$, based on the discrepancy between the pump and laser wavelengths, as well as intrinsic η_i properties to the material as given in Equation (3.2.7). Amongst these intrinsic effects are Auger and defect related recombination processes [21].

$$P_{abs} = \eta_q \eta_i P_p \qquad (3.2.7)$$

Turning now to heat dissipation away from the areas of high thermal loads, we concentrate on the conductivity characteristics of the materials. The materials of particular interest used in the design of the SDLs listed in Chapter 2, Section 2.4, include Al_xGaAs for the confinement window, $In_xGa_{1-x}N_yAs_{1-y}/Ga(N)As$ gain material and the AlAs/GaAs DBR. The position of the confinement window, adjacent to the gain region where the majority of heat is generated, requires adequate thermal conductivity and diffusion. Likewise high conductivity from the DBR aids heat removal from the back of the structure to the heatsink. Figure 3-5 presents a graphic of the simulation results generated by COMSOL software using a $GaIn_{0.033}N_{0.007}As/GaN_{0.011}As/GaAs$ structure design for operation at 1220 nm, with

82

an $Al_{0.3}GaAs$ window and AlAs/GaAs DBR. The heat flux lines are visible in the figure, with heat conduction away from the highest concentration of heat in the gain region towards the heatsink.
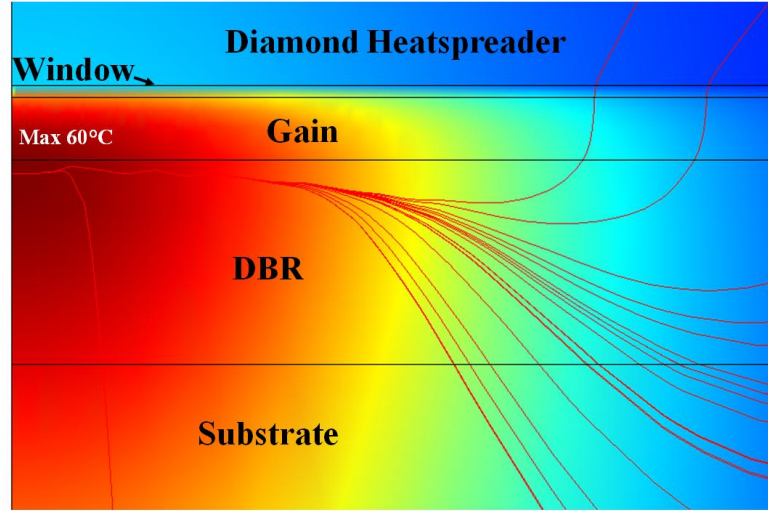

Figure 3-5: COMSOL Muliphysics^{TM} plot showing the simulation results for a GaIn$_{0.33}$N$_{0.007}$As/GaN$_{0.011}$As/GaAs SDL designed for 1220 nm operation, using AlAs/GaAs DBR and Al$_{0.3}$GaAs confinement window. (*Darkest red region corresponds to maximum heat graduating to darker blue areas of lowest temperature.*)

The conductivity calculations for ternary and quaternary material systems have been based on those developed by Adachi [22] and Nakwaski [23]. In Equation (3.2.8) the inverse resistivity values R are used to calculate the thermal conductivity κ for the ternary material Al$_x$GaAs.

$$\kappa(x) = (xR_{AlAs} + (1-x)R_{GaAs} + x(1-x)C_{AlGa})^{-1} \qquad (3.2.8)$$

The expression in Equation (3.2.9) was used to calculate thermal conductivity κ for the quaternary material In$_x$GaN$_y$As.

$$\kappa(x,y) = (xR_{InAs} + (1-x)[(1-y)R_{GaAs} + yR_{GaN}] + x(1-x)[yC_{GaIn} + (1-y)C_{NAs}])^{-1}$$
$$(3.2.9)$$

The parameters used in the above equations are provided in Table 3.2.

Table 3.2: Resistivity R_{AB} values of III-V materials used in calculations with alloy disorder parameters C_{AB} [22].

Material Parameters	Value
Resistivity	
R_{AlAs}	1.10 (cmK/W)
R_{GaAs}	2.22 (cmK/W)
R_{InAs}	3.3 (cmK/W)
R_{GaN}	0.51 (cmK/W)
Disorder Parameters	
C_{AlGa}	32 (cmK/W)
C_{GaIn}	72 (cmK/W)
C_{NAs}	12 (cmK/W)

The InGaAsP/InP material systems for 1300 nm telecoms applications are widely used and these devices add an interesting contrast to the studied InGaNAs/GaAs SDLs. In Figure 3-6 InGaAsP has a comparatively low thermal conductivity to that of InGaNAs, with a steep increase as the material approaches InP having a conductivity value κ_{InP}=0.68 W/cmK. The InGaNAs thermal conductivity curve has been generated starting with a high indium concentration, $In_{0.49}GaAs$ with progressive increases in nitrogen concentrations and decreased indium, ending with $In_{0.09}GaN_{0.015}As$.

In the case of a DBR designed for 1300 nm operation consisting of the $In_{0.68}Ga_{0.32}As_{0.68}P_{0.32}$/InP material system, low thermal conductivity prevents effective heat flow from the active region through to the heatsink. This further highlights the effectiveness of AlAs/GaAs DBRs, having thermal conductivities κ_{AlAs}=0.91 W/cmK and κ_{GaAs}=0.44 W/cmK respectively.
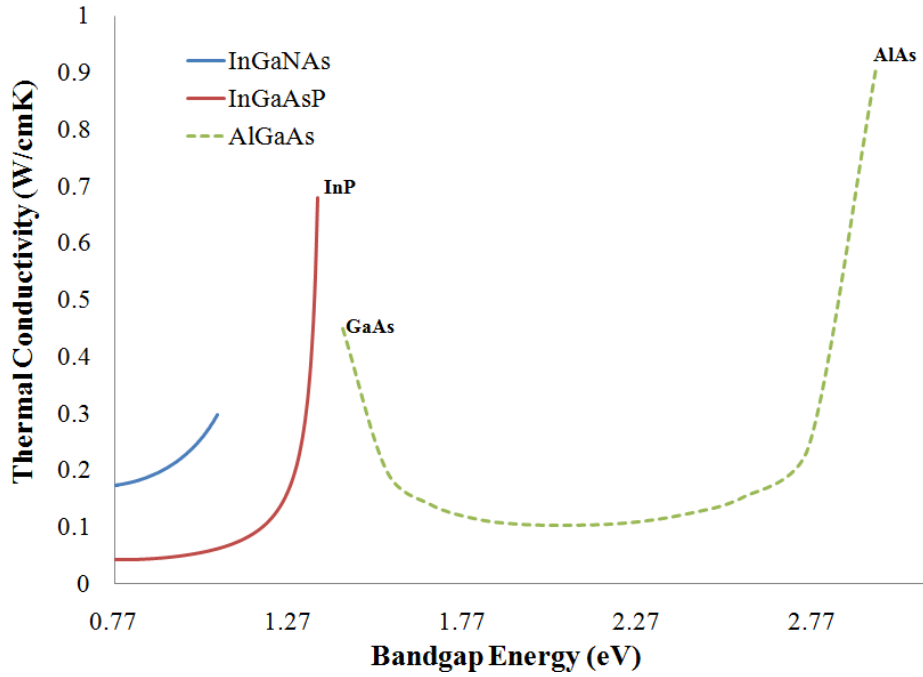
Figure 3-6: Thermal conductivity comparing materials systems InGaNAs, InGaAsP and AlGaAs.

The thermal diffusivity, defined as the relationship between the thermal conductivity κ and the specific heat capacity C_p of the material at constant pressure, is given in Equation (3.3.0) [22].

$$D = \frac{\kappa}{C_p g} \tag{3.3.0}$$

The inverse diffusivity profiles of the Al_xGaAs material compared with $(GaAs)_x(InP)_{1-x}$ are shown in Figure 3-7, in terms of crystal density g of the material. Due to the inverse relationship, the larger bowing of GaAsInP shows lower diffusion compared with AlGaAs. Therefore, the AlAs/GaAs material shows superior performance to InGaAsP/InP, further confounded by the thinner DBR due to fewer material pairs to improve heat removal as explained in Chapter 2.
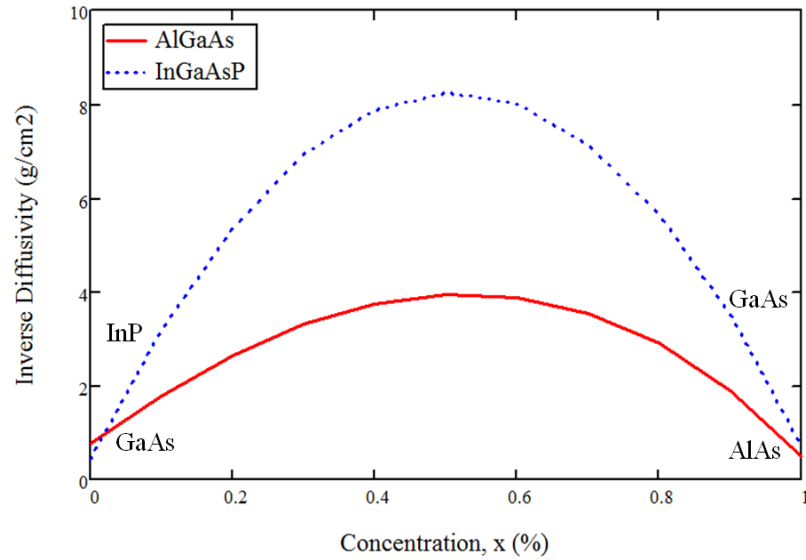
Figure 3-7: Inverse thermal diffusivity of Al$_x$GaAs (*red solid*) compared with (GaAs)$_x$(InP)$_{1-x}$ (*blue dashed*), with the extreme ends of the curve corresponding to GaAs/AlAs and InP/GaAs respectively [22].

To summarise the distinctive materials used in the design of SDL devices studied throughout this thesis, Table 3.3 indicates some material properties relevant to thermal performance.

Table 3.3: Material parameters of SDL devices.

Material	Specific Heat Capacity, C$_p$	Thermal conductivity, κ	Optical Absorption Coefficient, α (808nm)
Confinement Window			
Al$_{0.3}$GaAs	0.3596 (J/g K) [24]	0.116(W/mmK)	-
Gain Region			
GaAs	0.35 (J/g K) [25]	0.44(W/mmK)	14266 (cm^{-1})
GaN$_{0.011}$As	0.32 (J/g K) [26]	0.429(W/mmK)	12696 (cm^{-1})
GaIn$_{0.33}$N$_{0.007}$As	0.34 (J/g K) [22]	0.188(W/mmK)	25079 (cm^{-1})
DBR			
AlAs	0.452 (J/g K) [25]	0.909(W/mmK)	20424 (cm^{-1})
GaAs	0.35 (J/g K) [25]	0.44(W/mmK)	14266 (cm^{-1})
Thermal Management Components (HS/TD)			
Diamond	0.5169 (J/g K)	2 (W/mmK)	-
Solder (Sn-9Zn)	0.252 (J/g K) [27]	0.0573(W/mmK)	-

A comparison of GaInNAs devices studied at the Institute of Photonics, along with alternative SDLs based on InGaAsP gain system was performed in order to determine whether GaInNAs devices would also benefit from advantageous heat dissipation properties. Further motivating the use of this material system for operation in the 1150 – 1600 nm region. An analysis was performed comparing SDL designs based on InGaNAs and InP material systems, for operation across a range of wavelengths as shown in Figure 3-8. The results clearly indicate a distinction between the low thermal resistance (<5K/W) obtained for devices using a heatspreader (HS) compared with thin disk (TD) devices. In addition there was high thermal impedance associated with devices including solder, having a 3 µm thickness and conductivity of 0.0573 W/mmK.
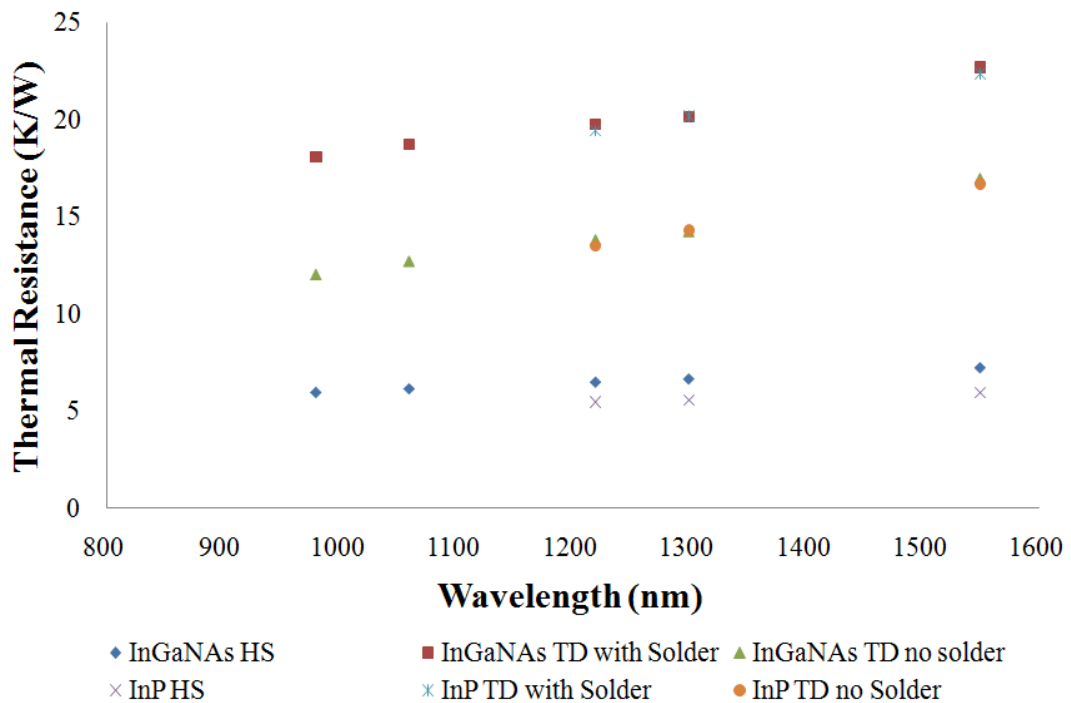

Figure 3-8: Thermal resistance of InGaNAs and InP-based SDL devices, designed across a range of operational wavelengths implementing a heatspreader (HS), thin disk (TD) with solder and without solder, using a pump spot radius of 50 µm.

The COMSOL simulation tool was further used to compare different pump configurations.

3.5 Thermal Response to Pumping Regime

The thermal performance of SDL devices has been explored in this section, for different design architectures using both front and end pumping regimes. For comparative purposes all SDL device designs in this study have used the InGaAs/GaAs material system designed for 1060 nm operation using an excitation wavelength of 808 nm.

3.5.1 Pumping Architectures
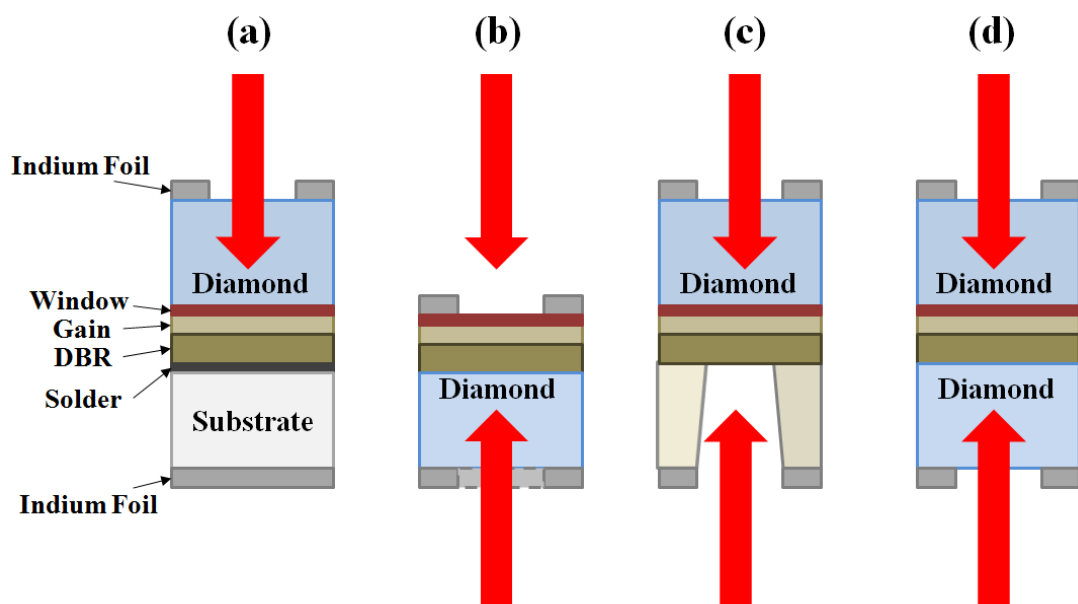
Figure 3-9: (a) Front pumped device employing a diamond heatspreader and soldered onto the substrate, (b) thin disk device front or end pumped, (c) thin disk device with the substrate which can be partially removed (*end pumped via hole*) or fully removed (*front pumped*) and (d) thin disk device 'sandwiched' between diamond heatspreaders front or end pumped [28].

Figure 3.9 is a schematic of the variation of pumping regimes discussed in this section. At one end of the thermal spectrum, the highest expected thermal loads in the device would occur when *no* thermal management techniques have been employed. Focusing on Figure 3-9 (a), a device *without* the presence of the diamond heatspreader and solder results in a maximum temperature rise of ~127°C, with P_{abs}=4.95W using a pump spot radius ω_p of 50 μm.

As a comparison, certain circumstances dictate that a wafer fusion technique is chosen. An example of which is provided by Lyytikäinen *et al.* [29] for an AlGaInP/InP based SDL designed at 1.3 µm operation fused with an AlGaAs/GaAs DBR grown onto a GaAs substrate. This aims to capitalise on the advantages afforded AlGaAs mirrors, of high reflective power using fewer number of mirror pairs whilst reaching the operating wavelength of 1.3 µm, as outlined in Chapter 2. Wafer fusion involves the device soldered onto a substrate, as shown in Figure 3-9 (a) which includes a 3 µm thick layer of AuSn solder between the DBR and substrate, resulting in a maximum temperature rise of ~182°C. This result is in agreement with those presented in Figure 3-8, showing the high thermal impedance caused by the solder, resulting in much higher temperatures within the active region.

The thin disk configuration, through the removal of the substrate, is illustrated in Figure 3-9 (b). The front pumping configuration has been demonstrated by Moloney *et al.* [30] with simulation results yielding an unexpectedly high ~170°C, implying high thermal impedance associated with the DBR. An end pumping regime has the intended advantage of avoiding angled pumping, with its elliptical shaped pump spot incident onto the semiconductor chip contributing to lower beam quality. Kuznetsov *et al.* [1] had provided some means to compensate for this elliptical spot through use of various lenses. However, devices implementing end pumping with the laser and pump beam all in the same plane, have been realised by Samsung [31, 32]. Their SDL devices were based on the InGaAs/GaAsP/GaAs material system, achieving ~9W CW at 1080 nm with operation in the TEM_{00} Gaussian mode. The experimental setup is shown in Figure 3-10, where the diamond heatspreader has been bonded to the back of the thin disk device. An extension to this end pumping configuration has incorporated frequency doubling, to produce green and blue laser outputs [33]. These results help to strengthen the argument towards microchip designs for frequency doubled SDLs, such as those explored in Chapter 6, to allow pumping along the same plane as the laser output.
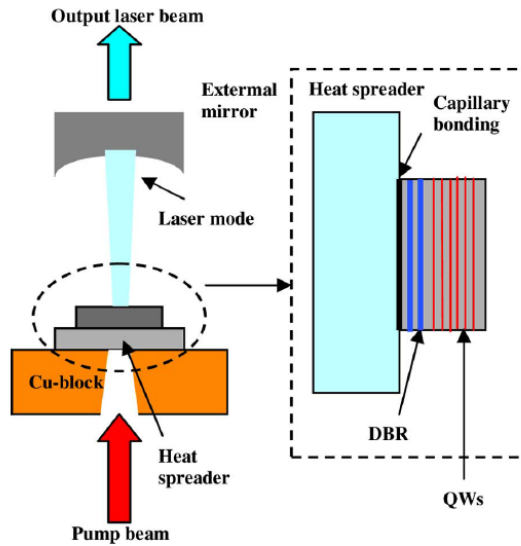
Figure 3-10: Design of an end pumped SDL as used by Lee et al [32] to achieve 9.1W CW power.

The simulation performed to identify the thermal response of Samsung's system, is shown in Figure 3-11. The maximum temperature rise in the device of ~23°C was obtained using a pump spot size of 150 μm, as used in the experiment. However using a smaller pump radius such as 50 μm, used throughout this set of simulations, dramatically increases this maximum temperature to ~145°C.
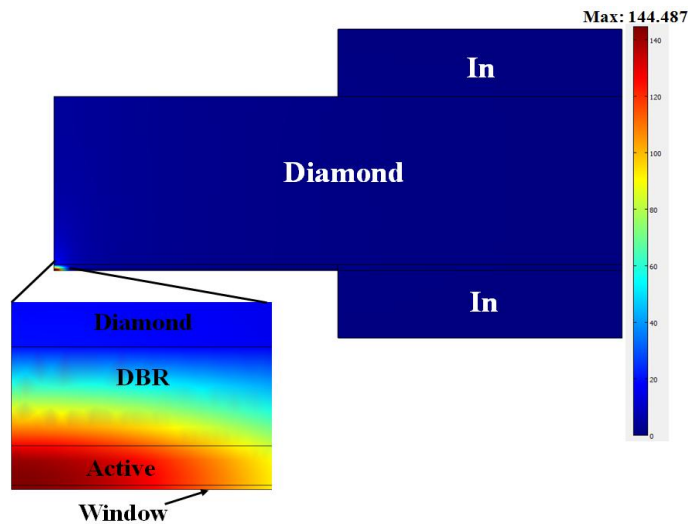

Figure 3-11: End pumped simulation with the diamond bonded onto the back of the thin disk SDL.

Further devices based on end pumping architectures were developed by Kim *et al.* [34] to study the effects that the location of the heatspreader has on its performance. The two devices compared were that of the heatspreader bonded to the back of the chip, such as that shown in Figure 3-10 and Figure 3-9 (b), and another with the heatspreader bonded to the top as in Figure 3-9 (c). They found differences in absorption efficiencies between the two systems and speculate that thermal lens effects are a factor of the pump beam focusing.

The most commonly used pumping configuration adopted in SDL operation is that of front pumping using a heatspreader, however combining the heatspreader with the thin disk is illustrated in Figure 3-9 (c). In this way, heat extraction from the active region has only the window layer as a barrier to the heatspreader, which proves more efficient than extraction through the DBR which is much thicker, as demonstrated previously. Results here provide a maximum temperature rise of 58°C. By comparison, end pumping of the device through a 'hole' made in the substrate has resulted in maximum temperatures of 85°C.

Finally, capitalising on the successful use of the diamond heatspreader was developed one step further, taking the thin disk device and sandwich it between two heatspreaders as shown in Figure 3-9 (d). The simulated results in the front pumping regime gave a maximum temperature rise of ~41°C, as opposed to ~51°C using end pumping. The challenges in implementing such a device lie in the processing of the thin disk material for double bonding. Extreme care would be necessary not to damage the material on such thin scales. It remains to be seen if it could withstand the bonding methods, unless improvements to the technique allow for more efficient means of execution with minimal material handling.

3.5.2 Results and Recommendations for Best Performance

The designs presented in the previous section form the basis of thermal resistance calculations. These were performed for increasing pump spot sizes, from 50 μm to 500 μm $1/e^2$ radius of the Gaussian beam pump profile, as given in Figure 3-12. This is an extension of the study performed by Maclean *et al.* [10], as shown in Figure 3-

1. Understandably the HS-TD-HS 'sandwich' arrangement has the least thermal resistance, with the heatspreader acting on the top and bottom as the most effective means of heat removal from the active area. However in all other cases there is a limit to the pump spot size, above which the TD approach has an improved thermal resistance response.
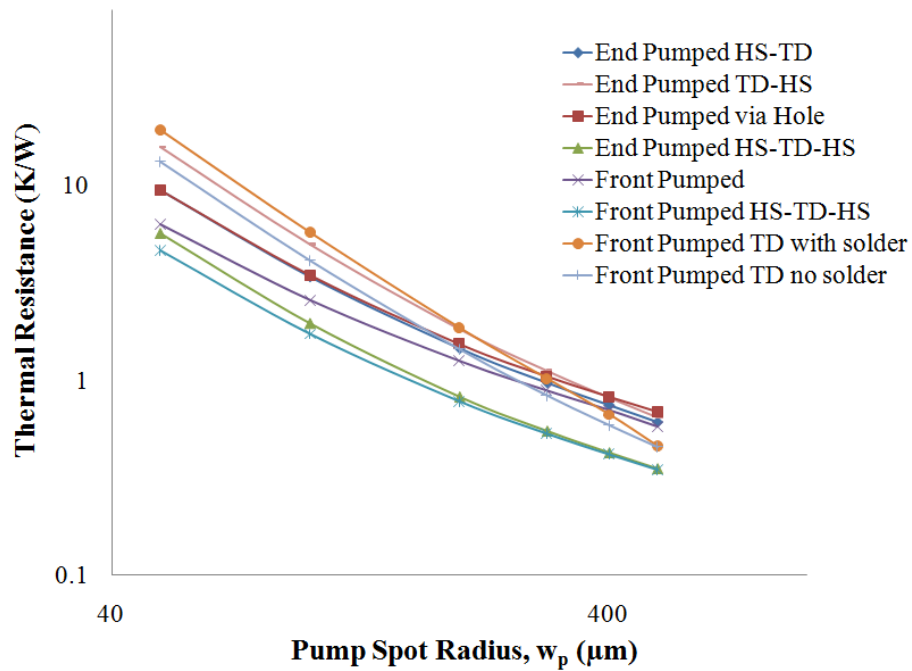

Figure 3-12: Pump-dependent average thermal resistances for both front and end pumped architectures, using InGaAs/GaAs 1060 nm designed devices with the diamond heatspreader (HS) and /or thin disk (TD) approaches.

The results for the soldered TD encountered lower thermal resistance for pump spot radii $>\sim 260 - 320$ μm due to the solder acting to raise the thermal impedance. The direct TD device has a lower thermal resistance for spot radii $>\sim 150 - 280$μm as given in Table 3.4.

Table 3.4: Crossover points of the pump spot radii, above these values the TD approach is favoured over the HS.

Pumping Regime	Direct TD	Soldered TD
Back Pumped via Hole	152μm	258μm
Back Pumped	184μm	310μm
Front Pumped	279μm	320μm

92

There are similarities to the thermal resistance responses to the front pumping regimes compared with end pumping, with the exception of the TD-HS configuration given in Figure 3-14. This emphasises the importance of the location of the HS, given the chosen pumping architecture. The end pumping with the HS bonded to the TD gives an indication as to the higher thermal impedance of the DBR, compared with HS bonding to the top of the device.

The double bond configuration has not been implemented at time of writing this thesis, but has the best potential performance for thermal extraction. Further investigations may be warranted into the feasibility of such a device and possible improvements in terms of power scaling.

3.6 Heatspreader Bonding and Heatsink Mounting of an SDL

In light of the preceding evaluations regarding thermal management, the SDLs used throughout the experimental work for this project have employed the heatspreader approach. The semiconductor wafer sample was bonded to the diamond heatspreader and mounted onto a copper heatsink.

Investigations by Millar *et al.* [35] contrasting natural and synthetic diamond materials as a heatspreader, have emphasised the polarisation attributes similar to those introduced by Van Loon *et al.* [36]. The synthetic diamond was found to exhibit low birefringence, enabling lower losses in polarisation selective cavities. These results are particularly relevant for frequency doubling of an SDL, with use of an intracavity nonlinear crystal such as was demonstrated by Maclean *et al.* [37] and also in Chapter 6 of this thesis, for a microchip frequency doubled SDL. It must also be pointed out that the intracavity diamond heatspreader has been discovered to act as an intracavity etalon. This limits wavelength selection when using a birefringent filter, where the wavelength peaks are determined by the etalon mode spacing. Further demonstrations of this shall be given in Chapter 4, showing stepped tunablility of the GaInNAs-based SDL devices. A solution to obtain continuous

tuning has been given by Maclean *et al.* [37] through use of a wedged anti-reflection coated heatspreader.

The semiconductor wafer produced from the MBE fabrication has typical dimensions of 100 mm in diameter. A smaller segment must be chosen for bonding and subsequent mounting, with dimensions typically ~5 mm^2 taken from the wafer. This was achieved by cleaving a small sample with these dimensions, selected from near the centre of the wafer where usually more uniform growth occurs. In practice variations across the wafer have been found to result in a change in wavelength output and laser performance. The variations of growth result in changes to the epitaxial layer thicknesses which in turn affects the length of the gain region of the structure impacting upon the micro-cavity resonance and gain offset as described in Chapter 2, Section 2.3.2.

The first stage of the bonding process involves cleaning the surfaces of the diamond heatspreader and semiconductor chip. This was achieved by administering a few drops of Acetone onto a piece of lens tissue, then gently wiping once across the surfaces. The same procedure was then performed using Methanol. For all SDL devices this cleaning technique was adopted. Since this time, advances have been made to improve the prospects of consistently achieving successful bonds. Investigations have focused on the properties of the diamond, particularly the *lipophilic* characteristic whereby greasy or oily films readily collect on the surface in conjunction with the *hydrophobic* quality which repels water. This understanding has channeled efforts into using alternative cleaning agents, to avoid the lipophilic response. A group in Heriot-Watt University has therefore proposed using acid to clean the diamond surface, which immediately can be bonded to the semiconductor chip.

However, the bonding of the two surfaces in reference to this work uses the established practice of liquid capillary bonding [38] between the diamond and the chip. This technique exploits the Van der Waals forces experienced by the two surfaces during the expulsion of the liquid joining them. The bonding is dependent

upon the hydrostatic pressure P from the liquid surface tension coefficient α and the gap formed between the two surfaces Δ, illustrated in Figure 3-13.

$$P = \frac{2\alpha}{\Delta} \qquad\qquad (3.3.1)$$
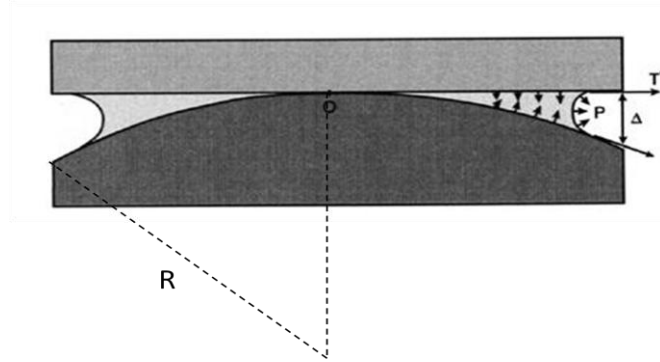
Figure 3-13: Illustration of forces due to stress exerted between two surfaces T' and the hydrostatic pressure P during liquid capillary bonding [38], with the radius of curvature R of the material.

The required strength of the liquid surface tension to bond the surfaces must be greater than the relationship in Equation (3.3.2) to the Young's modulus of the material E, the thickness dimension of the wafer d and the radius of curvature R of the material.

$$\alpha > \frac{Ed^3}{32R^2} \qquad\qquad (3.3.2)$$

Ideally both surfaces should be flat; however there can often be a slight curvature to one, or both of the surfaces. The suitability of either DI water with a surface tension of 72.8 dyn/cm or methanol with 22.5 dyn/cm can be established along with an acceptable thickness d of the sample by using the condition from Equation (3.3.2). The evaluation of the semiconductor chip used the Young's Modulus value for the GaAs substrate material, $E_{GaAs}=8.53x10\text{-}11\ dyn/cm$, due to the larger proportion of material in relation to the epitaxial structure grown on top. The value for $\Delta=0.25\mu m$ was provided by the supplier. Using the relationship for $R \approx \frac{L^2}{8\Delta}$ in this evaluation, Figure 3-14 presents the graphical results for the surface tension of the semiconductor chip for three cleaved lengths L of the material, 3 mm, 4 mm and 5 mm, with the diamond heatspreader of lengths 3 mm and 5 mm. It is apparent from

this graph that cleaved samples that have a length of 3 mm, and material thickness >340 μm will not bond using methanol, likewise if the sample is 4 mm and >500 μm. However, DI water has bonding capability up to a material thickness of ~500 μm for all lengths.

In the context of the thin disk 'sandwich' configuration indicated in Figure 3-9 (d), the best opportunity for success would be the employment of large diamond lengths ≥ 5 mm matched by the same dimension of semiconductor chip. Additionally, both DI water and methanol act as suitable solutions to facilitate capillary bonding.
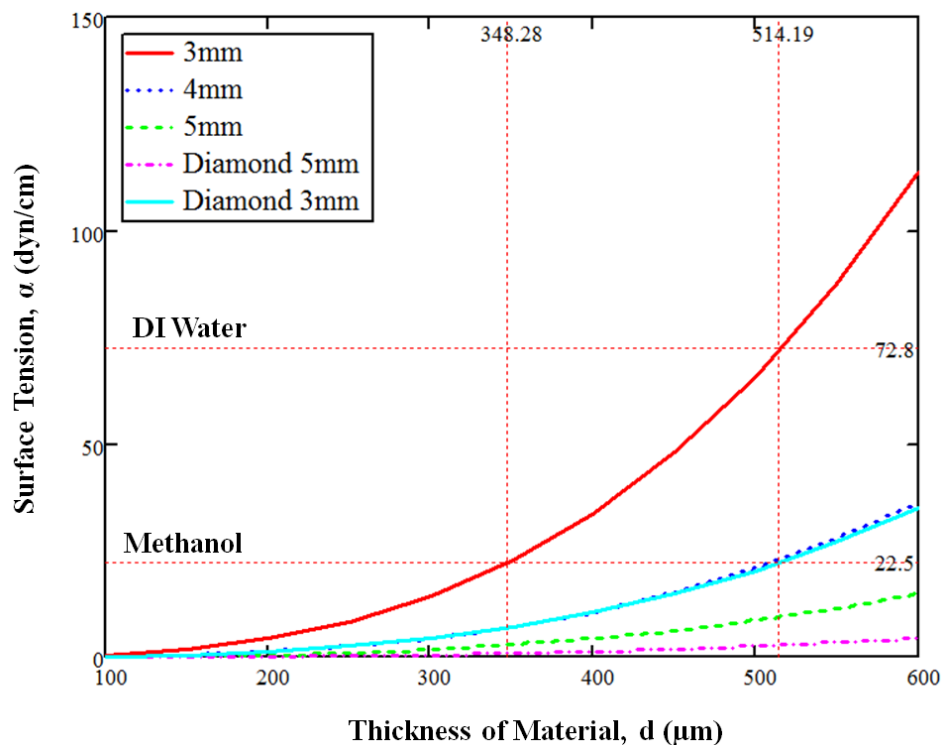
Figure 3-14: The surface tension of GaAs based material across a range of thicknesses, for lengths *L=3mm,4mm and 5mm* and of diamond heatspreader having length of 3mm and 5mm. Indicated are the surface tension values for DI water (*72.8dyn/cm*) and Methanol (*22.5 dyn/cm*).

Evidence of differences in surface flatness have appeared as partial bonds, as shown in Figure 3-15, clearly indicating the bonded area as a solid dark section with fringes appearing in the un-bonded area. It is likely that the diamond curvature effects, in combination with its smaller dimensions, may be a result of this partial bond.
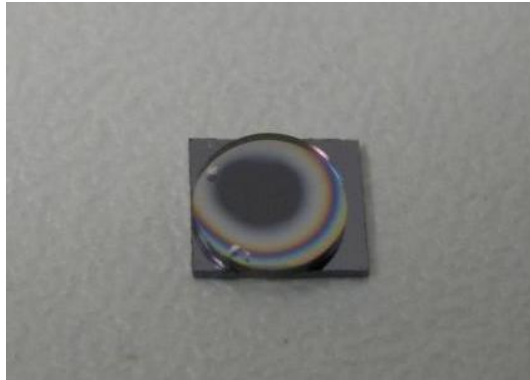
Figure 3-15: 1180 nm Sample *AnN2596* bonded to CVD synthetic diamond.

The bonded sample was mounted onto a backplane cooled copper heatsink, designed for water cooling. In order to aid heat conduction away from the back and partial front of the sample, a ~0.1 mm thick piece of indium foil was placed between the sample and the copper mount. Figure 3-16 illustrates a cross-section of the mounted sample with a picture in the laboratory provided in Figure 3-17.
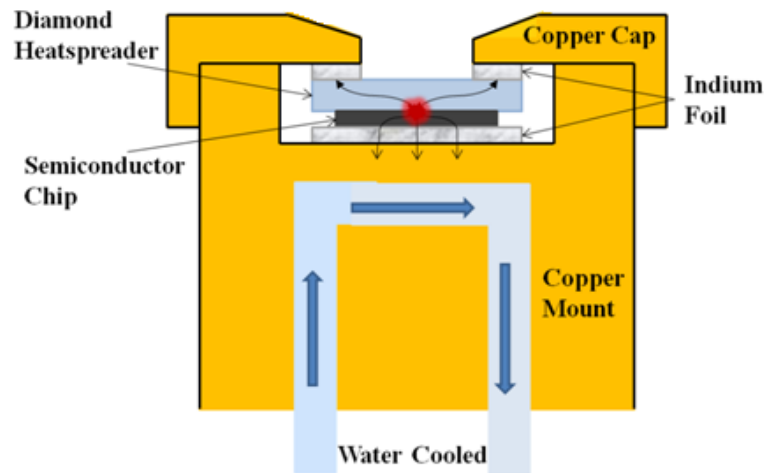
Figure 3-16: Schematic of the water cooled copper heatsink, with the diamond bonded semiconductor chip and indium foil.
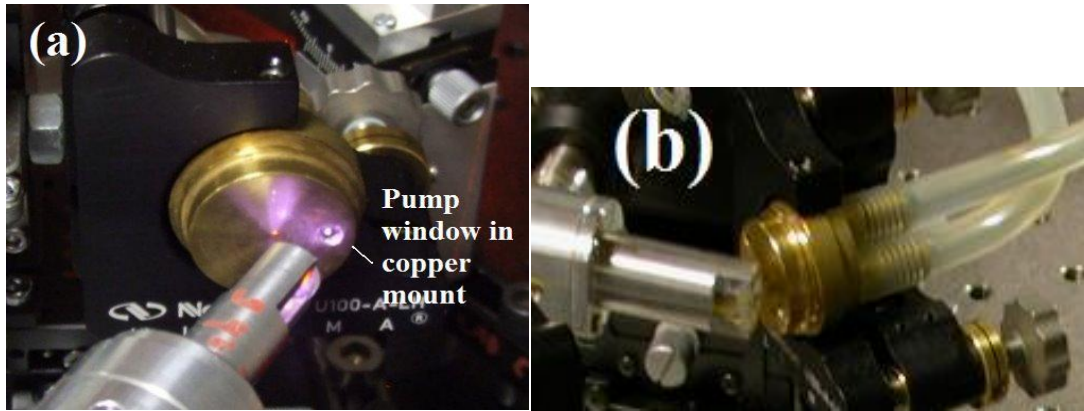
Figure 3-17: (a) Front view of copper mount of the SDL indicating the pump window cut into the cap of the mount. (b) Side view of the mount to show the connection to the water cooling pvc tubing.

The water cooling temperature was generally kept at ~10°C during operation, as this was sufficient to aid thermal management whilst avoiding condensation appearing on the device. Every effort was given to ensure that the temperature and humidity in the laboratory was kept above the dew point, since condensation disrupts operation through the presence of water droplets on the surface of the heatspreader. In addition, the bond may be compromised leading to device failure.

Periodic monitoring of the mounted sample was carried out throughout experimental work, in particular a visual check on the integrity of the bond. Included in the maintenance of the mounted sample was the cleaning of the diamond heatspreader surface, and all mirror surfaces, to ensure that performance was not impeded by any dust build-up on the bonded sample.

3.7 Conclusions

The aim of this chapter has been to explain the practical implications of thermal management of devices. Justification for use of GaInNAs based SDLs has been given, operating at wavelengths 1180 nm to 1300 nm over equivalent InP-based devices. The pumping regime employed has demonstrated a marginal improvement using front pumping compared with end pumping, due to the thermal impedance of the DBR resulting in elevated device temperatures. Overwhelming evidence point towards incorporation of the TD sandwiched between two heatspreaders

configuration, achieving the lowest thermal response. This provides a possible future development, on the condition that the integrity of the device remains intact following substrate removal and bonding procedures. The next chapter shall present the performance results of GaInNAs/Ga(N)As SDL devices, implementing the heatspreader thermal management technique alongside the water cooled copper heatsink.

References

[1]   M. Kuznetsov, F. Hakimi, R. Sprague and A. Mooradian, "Design and characteristics of high-power (0.5-W CW) diode-pumped vertical-external-cavity surface-emitting semiconductor lasers with circular TEM_{00} beams," *IEEE Journal of Selected Topics in Quantum Electronics,* vol. 5, pp. 561-573, (1999).

[2]   N. Schulz, M. Rattunde, C. Ritzenthaler, B. Rosener, C. Manz, K. Kohler and J. Wagner, "Effect of the Cavity Resonance-Gain Offset on the Output Power Characteristics of GaSb-Based VECSELs," *IEEE Photonics Technology Letters,* vol. 19, pp. 1741-1743, (2007).

[3]   J. E. Hastie, C. W. Jeon, J.-M. Hopkins, D. Burns and M. D. Dawson, "Thermal management of AlGaAs VECSELs using intracavity sapphire and silicon carbide heatspreaders " presented at the International Quantum Electronics Conference/ Conference on Lasers, Applications, and Technologies Moscow, Russia, (2002).

[4]   J. E. Hastie, J.-M. Hopkins, S. Calvez, C. W. Jeon, D. Burns, R. Abram, E. Riis, A. I. Ferguson and M. D. Dawson, "0.5-W single transverse-mode operation of an 850-nm diode-pumped surface-emitting semiconductor laser," *IEEE Photonics Technology Letters,* vol. 15, pp. 894-896, (2003).

[5]   A. J. Kemp, G. J. Valentine, J.-M. Hopkins, J. E. Hastie, S. A. Smith, S. Calvez, M. D. Dawson and D. Burns, "Thermal management in vertical-external-cavity surface-emitting lasers: finite-element analysis of a heatspreader approach," *IEEE Journal of Quantum Electronics,* vol. 41, pp. 148-155, (2005).

[6]   J.-M. Hopkins, S. A. Smith, C. W. Jeon, H. D. Sun, D. Burns, S. Calvez, M. D. Dawson, T. Jouhti and M. Pessa, "0.6 W CW GaInNAs vertical external-cavity surface emitting laser operating at 1.32 um," *Electronics Letters,* vol. 40, pp. 30-31, (2004).

[7]   S. Giet, A. J. Kemp, D. Burns, S. Calvez, M. D. Dawson, S. Suomalainen, A. Harkonen, M. Guina, O. Okhotnikov and M. Pessa, "Comparison of thermal management techniques for semiconductor disk lasers," *Proceedings of the SPIE Solid State Lasers XVII: Technology and Devices,* vol. 6871, pp. 687115-687115-10, (2008).

[8]   H. Lindberg, M. Strassner, E. Gerster, J. Bengtsson and A. Larsson, "Thermal management of optically pumped long-wavelength InP-based semiconductor

disk lasers," *IEEE Journal of Selected Topics in Quantum Electronics,* vol. 11, pp. 1126-1134, (2005).

[9]   P. Zhang, Y.-R. Song, X.-P. Zhang, T.-L. Dai, Y.-P. Liang and S.-Q. Fan, "Numerical analysis of thermal effects in InGaAs system vertical-external-cavity surface-emitting laser," *Optical Review,* vol. 18, pp. 317-323, (2011).

[10]   A. J. Maclean, R. B. Birch, P. W. Roth, A. J. Kemp and D. Burns, "Limits on efficiency and power scaling in semiconductor disk lasers with diamond heatspreaders," *Journal of Optical Society of America B,* vol. 26, (2009).

[11]   A. J. Kemp, A. J. Maclean, J. E. Hastie, S. A. Smith, J.-M. Hopkins, S. Calvez, G. J. Valentine, M. D. Dawson and D. Burns, "Thermal lensing, thermal management and transverse mode control in microchip VECSELs," *Applied Physics B: Lasers and Optics,* vol. 83, pp. 189-194, (2006).

[12]   N. Laurand, C. L. Lee, E. Gu, J. E. Hastie, S. Calvez and M. D. Dawson, "Microlensed microchip VECSEL," *Optics Express,* vol. 15, pp. 9341-9346, (2007).

[13]   N. Laurand, C.-L. Lee, E. Gu, J. E. Hastie, A. J. Kemp, S. Calvez and M. D. Dawson, "Array-Format Microchip Semiconductor Disk Lasers," *IEEE Journal of Quantum Electronics,* vol. 44, pp. 1096-1103, (2008).

[14]   A. Laurain, M. Myara, G. Beaudoin, I. Sagnes and A. Garnache, "Multiwatt–power highly–coherent compact single–frequency tunable Vertical–External–Cavity–Surface–Emitting–Semiconductor–Laser," *Optics Express,* vol. 18, pp. 14627 - 14636, (2010).

[15]   A. J. Kemp, J. M. Hopkins, A. J. Maclean, N. Schulz, M. Rattunde, J. Wagner and D. Burns, "Thermal Management in 2.3-um Semiconductor Disk Lasers: A Finite Element Analysis," *IEEE Journal of Quantum Electronics,* vol. 44, pp. 125-135, (2008).

[16]   S. Adachi, "GaAs, AlAs, and $Al_xGa_{1-x}As$: Material parameters for use in research and device applications," *Journal of Applied Physics,* vol. 58, (1985).

[17]   S. Calvez, J. E. Hastie, A. J. Kemp, N. Laurand and M. D. Dawson, "Thermal Management, Structure Design, and Integration Considerations for VECSELs," Chapter 2, pp. 73 - 117 in *Semiconductor Disk Lasers: Physics and Technology*, O. G. Okhotnikov, Editor, Wiley-VCH (2010).

[18]   J. Rautiainen, A. Härkönen, V. M. Korpijärvi, P. Tuomisto, M. Guina and O. G. Okhotnikov, "2.7 W tunable orange-red GaInNAs semiconductor disk laser," *Optics Express,* vol. 15, pp. 18345-18350, (2007).

[19]   element6.   Available: http://www.e6.com/en/education/materialsresourcecentre/materialsproperties/thepropertiesofcvddiamond/

[20]   S. L. Chuang, "Optical Processes in Semiconductors," Chapter 9, pp. 347 - 409 in *Physics of Photonics Devices*, Second edition John Wiley & Sons, Inc, (2009).

[21]   R. Fehse, S. Tomic´, A. R. Adams, S. J. Sweeney, E. P. O'Reilly, A. Andreev and H. Riechert, "A Quantitative Study of Radiative, Auger, and Defect Related Recombination Processes in 1.3-um GaInNAs-Based Quantum-Well Laser," *IEEE Journal of Selected Topics in Quantum Electronics,* vol. 8, pp. 801 - 810, (2002).

[22] S. Adachi, "Thermal Properties," Chapter 2, pp. 45 - 76 in *Properties of Semiconductor Alloys: Group-IV, III-V and II-VI Semiconductors*, P. Capper, S. Kasap and A. Willoughby, Editors, John Wiley & Sons, Ltd, (2009).

[23] W. Nakwaski, "Thermal conductivity of binary, ternary, and quaternary III-V compounds," *Journal of Applied Physics,* vol. 64, pp. 159 - 166, (1988).

[24] S. Adachi, Editor, *Properties of aluminium gallium arsenide*. INSPEC, The Institute of Electrical Engineers, (1993).

[25] M. J. Weber, Editor, *Handbook of Optical Materials*. CRC Press, (2003).

[26] Y. Zhao, G. Chen, S. Wang and S. F. Yoon, "Thermal characterization of gallium arsenic nitride epilayer on gallium arsenide substrate using pulsed photothermal reflectance technique," *Thin Solid Films,* vol. 450, pp. 352-356, (2004).

[27] Y. K. Wu, K. L. Lin and B. Salam, "Specific Heat Capacities of Sn-Zn-Based Solders and Sn-Ag-Cu Solders Measured Using Differential Scanning Calorimetry," *Journal of Electronic Materials,* vol. 38, pp. 227-230, (2009).

[28] S. L. Vetter, S. Calvez and A. J. Kemp, "Thermal management of near-infrared semiconductor disk lasers with AlGaAs mirrors and lattice (mis)-matched active regions," *IEEE Journal of Quantum Electronics,* In publication, (2011).

[29] J. Lyytikäinen, J. Rautiainen, L. Toikkanen, A. Sirbu, A. Mereuta, A. Caliman, E. Kapon and O. G. Okhotnikov, "1.3-µm optically-pumped semiconductor disk laser by wafer fusion," *Optics Express,* vol. 17, pp. 9047-9052, (2009).

[30] J. V. Moloney, A. R. Zakharian, J. Hader and S. W. Koch,"Designing New Classes of High Power, High Brightness VECSELs," *Proceedings of SPIE* vol. 5990, pp. 599003-1 - 599003-8, (2005).

[31] T. Kim, J. Lee, S. Lee, J. Yoo, K. Kim, J. Kim, S. Cho, S. Lim, G. Kim and Y. Park, "End-pumped vertical external cavity surface emitting laser," in *Vertical-Cavity Surface-Emitting Lasers X*, San Jose, CA, USA, pp. 61320D-1 - 61320D-5, (2006).

[32] J. H. Lee, J. Y. Kim, S. M. Lee, J. R. Yoo, K. S. Kim, S. H. Cho, S. J. Lim, G. B. Kim, S. M. Hwang, T. Kim and Y. J. Park, "9.1-W High-Efficient Continuous-Wave End-Pumped Vertical-External-Cavity Surface-Emitting Semiconductor Laser," *IEEE Photonics Technology Letters,* vol. 18, pp. 2117-2119, (2006).

[33] G. B. Kim, J.-Y. Kim, J. Lee, J. Yoo, K.-S. Kim, S.-M. Lee, S. Cho, S.-J. Lim, T. Kim and Y. J. Park, "End-pumped green and blue vertical external cavity surface emitting laser devices," *Applied Physics Letters,* vol. 89, pp. 181106-181106-3, (2006).

[34] J.-Y. Kim, J. Lee, G. B. Kim, S. Cho, J. Yoo, K.-S. Kim, S.-J. Lim, S.-M. Lee, T. Kim and Y. Park, "Effect of Heat Spreader Location on Lasing Properties of End-Pumped Vertical-External-Cavity Surface-Emitting Lasers," *Japanese Journal of Applied Physics,* vol. 46, pp. 5157 - 5159, (2007).

[35] P. Millar, R. B. Birch, A. J. Kemp and D. Burns, "Synthetic Diamond for Intracavity Thermal Management in Compact Solid-State Lasers," *IEEE Journal of Quantum Electronics,* vol. 44, pp. 709-717, (2008).

[36]   F. van Loon, A. J. Kemp, A. J. Maclean, S. Calvez, J.-M. Hopkins, J. E. Hastie, M. D. Dawson and D. Burns, "Intracavity diamond heatspreaders in lasers: the effects of birefringence," *Optics Express,* vol. 14, pp. 9250-9260, (2006).

[37]   A. J. Maclean, A. J. Kemp, S. Calvez, J.-Y. Kim, T. Kim, M. D. Dawson and D. Burns, "Continuous Tuning and Efficient Intracavity Second-Harmonic Generation in a Semiconductor Disk Laser With an Intracavity Diamond Heatspreader," *IEEE Journal of Quantum Electronics,* vol. 44, pp. 216-225, (2008).

[38]   Z. L. Liau, "Semiconductor wafer bonding via liquid capillarity," *Applied Physics Letters,* vol. 77, pp. 651 - 653, (2000).

Chapter 4

SDL Characterisation and Performance

4.1 Introduction

Previous chapters have explored the design parameters of SDLs, with thermal management considerations and performance expectations of GaInNAs devices. This chapter shall present the characterisation and performance results of physical devices, based on the previous design criteria.

Methods evaluating the integrity of the design include *photoluminescence* and *reflectivity* measurements, with Scanning Electron Microscopy (SEM) employed as a means to visually inspect the samples. The photoluminescence (PL) measurement obtains the excitation output of the MBE grown material. The intensity of the PL reflects the quality of the growth. Obtaining sufficiently high intensity profiles provides a reasonable expectation that the material will perform well when implemented into an SDL device. In addition, the output wavelength establishes the efficacy of design for target wavelengths expected. The reflectivity results show the overall reflectance power of the DBR at the design wavelength, with insight into the effects of the sub-cavity resonance. Further, SEM is a useful technique to examine the structure of the devices.

The laser cavity configuration plays a key role in the performance output. Due consideration has been given to achieve mode matching within the cavity in order to attain the best possible output powers and beam quality. The method by which beam quality is measured employs a scanning detector, capturing the beam profile along its propagation. This is known as an M^2 measurement, allowing the beam divergence to be compared with that of an ideal Gaussian beam with an $M^2 \approx 1$.

Wavelength tuning using an intracavity birefringent filter was used to establish the extent of wavelength coverage of these GaInNAs/GaAs SDL devices. Furthermore the filter enabled spectral narrowing, which has been practical for the use of SDLs as an excitation source for other systems, as described in Chapter 5.

The final section of this chapter applies the evaluation techniques for power transfers and wavelength tuning, to obtain the thermal resistance of an 1190 nm SDL. Thermal simulations, similar to those presented in Chapter 3, provide a means to test the accuracy of simulation to empirical results.

4.2 Characterisation

The proceeding fabrication methods, as described in Chapter 2, result in a semiconductor wafer that was characterised to assess the performance according to its design parameters. The methods employed for characterisation measurements encompass Reflectivity, Photoluminescence and SEM.

4.2.1 Reflectivity Measurements

The characterisation measurements of Reflectivity used the experimental setup illustrated in Figure 4-1. The sample was illuminated with a white light source in the form of a tungsten/halogen lamp providing a broad spectral range from ~360nm to ~2500nm. The reflectivity response of the sample was captured by the spectrometer and measured using Spectramax^{TM} software, the same as was used for PL measurements.
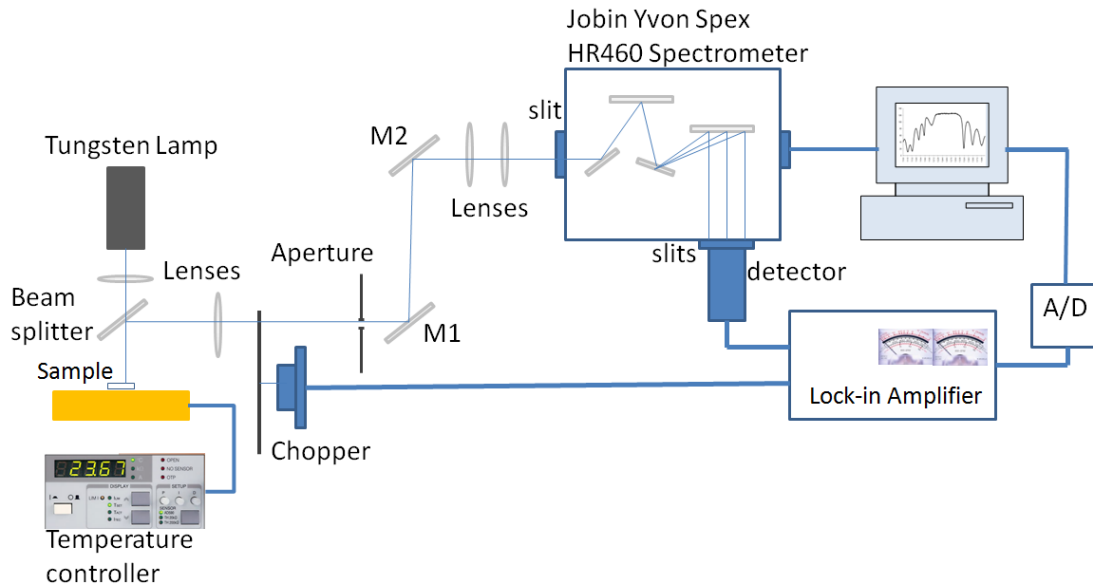
Figure 4-1: Reflectivity experimental setup.

An initial calibration measurement was obtained using a plane mirror that was placed adjacent to the sample. The mount was then moved to illuminate the semiconductor material to perform a reading. It is worth noting that there were small variations in height between the plane mirror and the sample, which introduces an approximate 1% error into the results. Using the Spectramax^{TM} software the recorded results subtracted the initial reference signal from the mirror calibration measurement to obtain the final signal.

The analysis of the reflectivity response highlights two important features, as indicated in Figure 4-2 for the 1220 nm *AsN2527* sample measured at room temperature, ~20°C. The first of which is the stop band, providing data on the refractive index contrast of the DBR material stack. The wider the stop band indicates a high index contrast in the DBR as described in Chapter 2, Section 2.3.1.4. In this sample the stop band is ~135 nm and centre wavelength 1248 nm for the material system, based on 30 pairs of AlAs/GaAs. Using the equations from Section 2.3.1.4 the variable $q = \frac{n_{incident}}{n_{exit}} = 0.997$, which results in an overall reflectivity $R_{DBR}=99.98\%$. The second feature highlighted in Figure 4-2 is the dip in the reflectivity spectrum which is due to the sub-cavity resonance. Using a Mathcad^{TM}

programme developed by Dr. S. Calvez, to calculate the reflectivity of this system, the results are in keeping with the experimental results obtained. The surface PL measurement coincides with the location of the subcavity resonance.
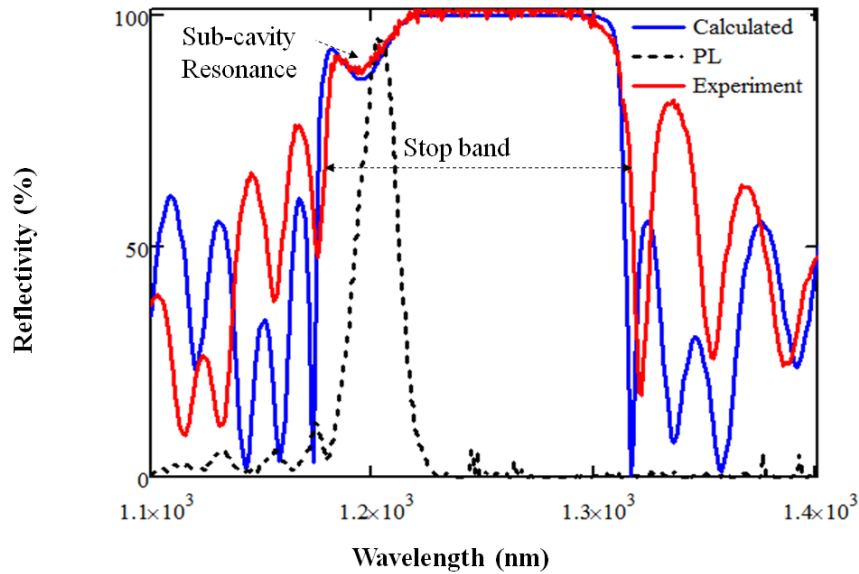

Figure 4-2: Reflectivity measured at 20°C of sample *AsN2527* (*red*), indicating the stopband and sub-cavity resonance dip, compared with the calculated reflectivity of a 10 QW 1220 nm SDL is included (*blue*). Included is PL spectra at 20°C (*black dashed line*).

4.2.2 Photoluminescence Measurements

Two different types of Photoluminescence (PL) measurements were carried out on a 1220 nm designed SDL chip, *edge* and *surface* PL. Edge PL was a means to characterise the emission of the active region within the structure, without the modification associated with the subcavity resonance. The surface PL measurement examines the entire structure, including these resonance effects.

4.2.2.1 Edge PL

The edge PL measurements were performed by focusing a 670 nm excitation laser at the cleaved edge of the sample. The emission was captured by the Jobin Yvon HR460 Spectrometer and analysed using Spectamax™ commercial software. Figure 4-3 is an illustration of the experimental set-up to perform edge PL. Included is the temperature controller, allowing the sample to be heated to assess the QW

106

performance across a range of temperatures. The structure under examination was a 10 QW GaInNAs/GaNAs/GaAs active region designed for operation at ~1220 nm. The GaInNAs QWs were 7 nm thick with 4 nm GaNAs strain compensating layers on either side of the QW. All spectra were measured under the same slit width and time constants, with a resolution of 1 nm.
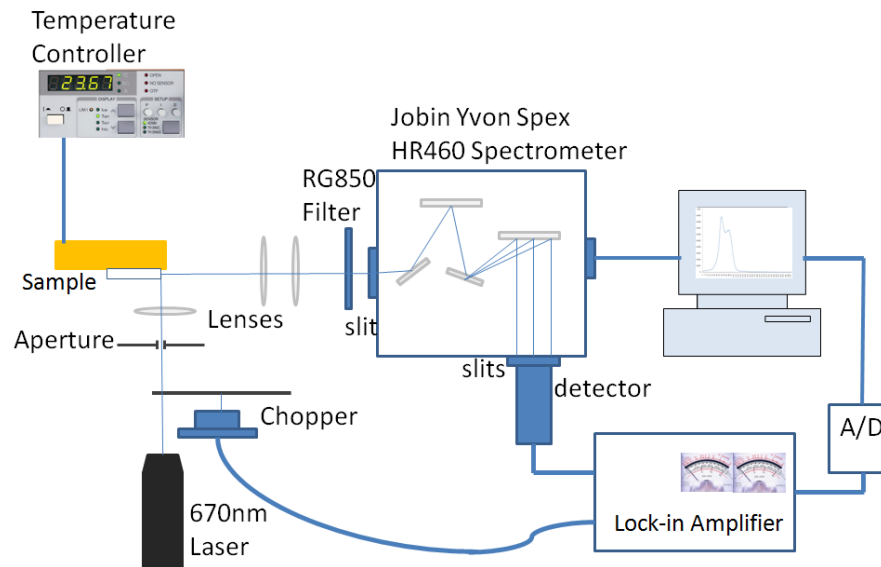

Figure 4-3: Edge PL measurement setup.
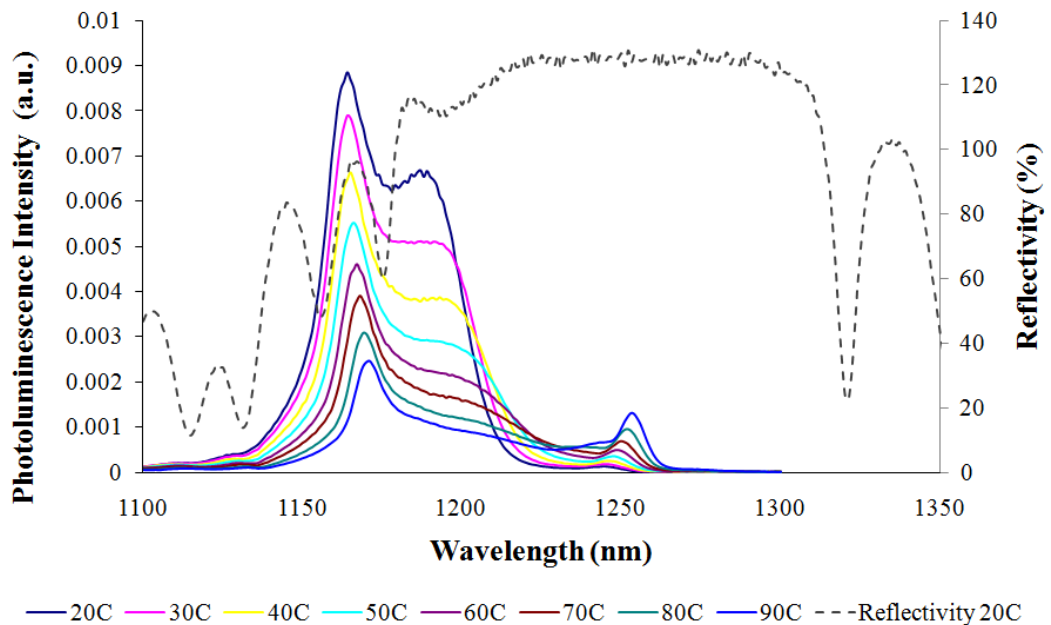
Figure 4-4: Edge PL for *AsN2527* 1220 nm sample, from 20°C to 90°C, with an included Reflectivity spectrum measurement at 20°C.

There were three noticeable features in the spectra results shown in Figure 4-4. The first shows three wavelength regions with peak PL intensities; ~1164 nm (1.066eV), ~1186 nm (1.046eV) and ~1252 nm (0.991eV). Studies performed by Fan *et al.* [1] have found that the transition energy in a GaInNAs QW decreases with increasing bowing parameter and tensile strain effect. However, using the equations presented in Chapter 2 for a strained 7 nm $GaIn_{0.3}N_{0.007}As/GaAs$ QW, gave a calculated result of 1.045eV which is in close agreement with the peak found at ~1186 nm in the experimental results. This PL peak also shows close alignment with the subcavity resonance dip in the Reflectivity spectrum measured at a corresponding temperature of 20°C. The PL peak at ~1164 nm may be attributed to the edge of the DBR structure.

The second feature relates to the changing intensities of the PL peaks. A steady decrease was found for peaks around the 1160-1190 nm regions, with a broadening of the ~1190 nm peak. This relates to thermal broadening and thermal quenching of the system as described by Sun *et al.* [2] for nonradiative recombination of delocalised carriers at higher temperatures in GaInNAs/GaAs QW systems. However, the PL peak at ~1250 nm increases with increasing temperature. This can be explained by a subcavity resonance effect due to the angle of the excitation beam not precisely targeting the active region within the structure. The increase in temperature is enhancing the subcavity resonance by increasing the interaction between the excitonic emission and cavity mode, whilst shifting the PL output to higher wavelengths. In Figure 4-5 the edge PL is compared with the surface PL at the two extremes of temperature, showing that the surface PL occurs between the edge PL emission peaks and the subcavity resonance.
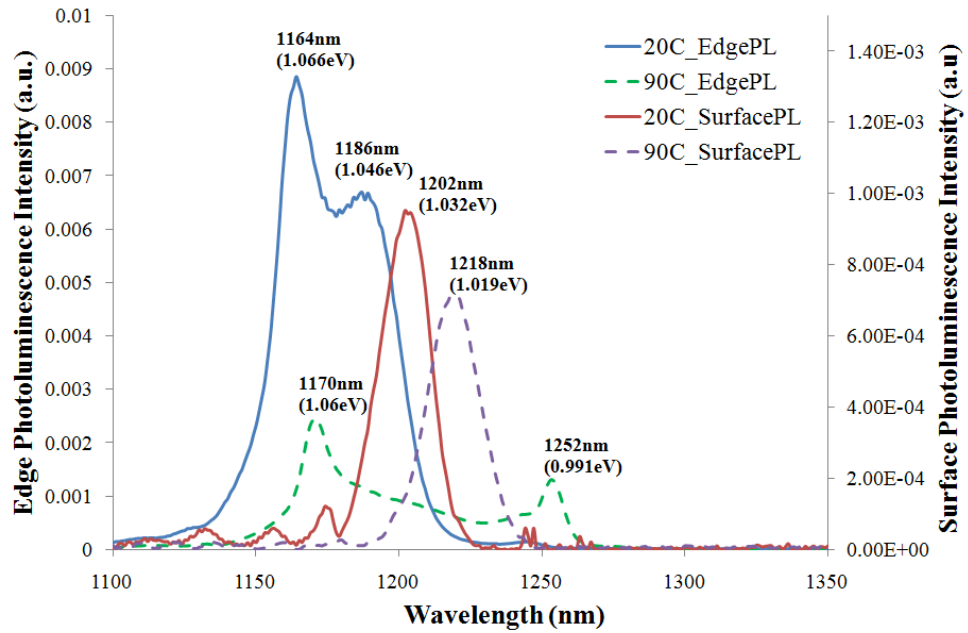
Figure 4-5: Comparison of Edge and Surface PL for measurements taken at 20°C and 90°C, indicated are the intensity peak wavelengths.

The third feature is a red shifting of the PL with increasing temperatures. This is in accordance with the bandgap shift in semiconductor materials as recognised by Varshni [3].

4.2.2.2 Surface PL

The experimental setup to perform surface PL is shown in Figure 4-6, using the same 670 nm excitation laser as for Edge PL. As mentioned the output has been influenced by the sub-cavity resonance due to the excitation field passing through all epitaxial layers from the top surface. The resonantly designed device exhibits pump absorption from the 670 nm source in line with the condition that E_p (1.852 eV) > $E_{g(GaAs)}$ (1.424 eV) > $E_{g(GaInN0.01As)}$ (1.214 eV), the pump energy is greater than both the bandgap of the GaAs barriers and GaInNAs QWs. The subcavity resonance contributes to a peak around that wavelength.
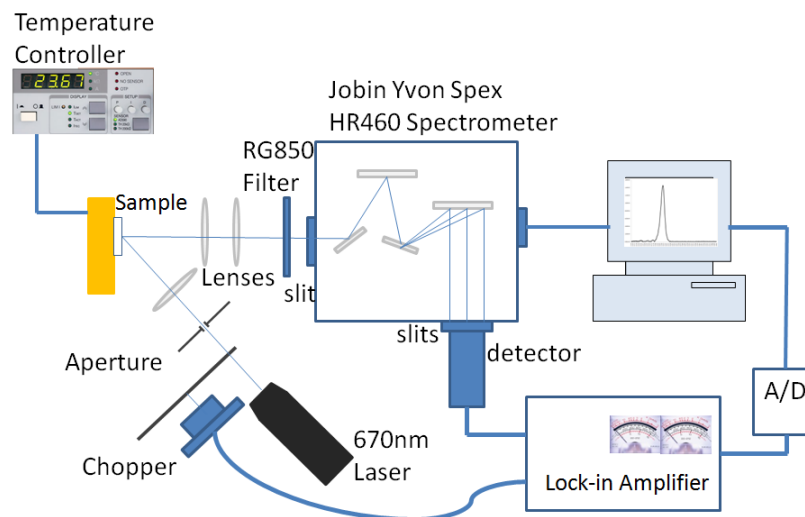
Figure 4-6: Photoluminescence experimental setup.

The sample was mounted with a Peltier cooler and temperature controller, as shown in Figure 4-6. The thermal variation effects of the device were measured, to gauge the device response during operation in an optical pumping regime. Ideally the resonant periodic gain wavelength matches the QW gain spectrum; however thermal variations exist causing a mismatch as discussed in Chapters 2 and 3. PL measurement results from the 1220nm designed *AsN2527* sample is shown in Figure 4-7, over a temperature range from 20°C to 100°C.
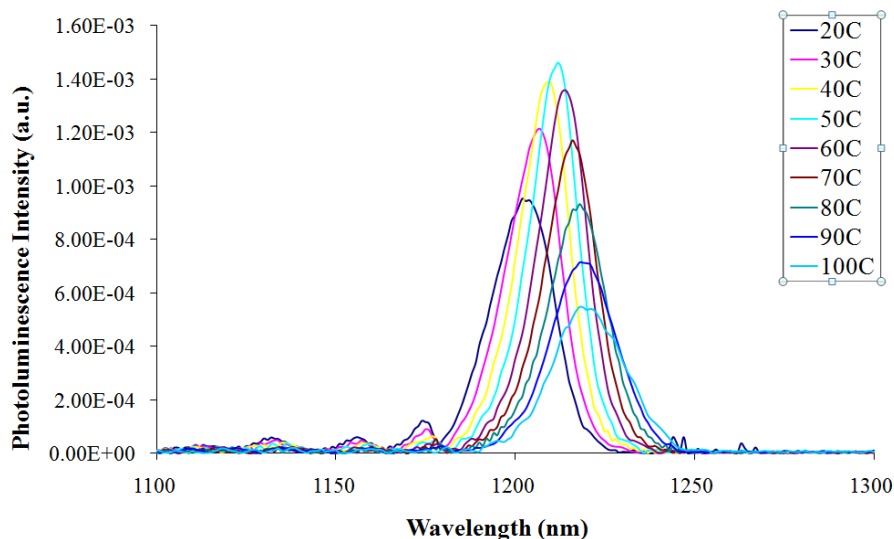
Figure 4-7: Photoluminescence results for sample *AsN2527* designed with 1220 nm output, over a range of temperatures.

To accompany Figure 4-7, the PL peak intensity variation curve is presented in Figure 4-8, with the peak at 50°C corresponding to the alignment of the peak RPG subcavity resonance and the QW emission, indicating an optimum chip operating temperature. The curve representative of the wavelength shift with increasing temperature in Figure 4-8, has two different $\Delta\lambda/\Delta T$ regions. The reason for these different shift rates is due to the influence of the gain bandwidth on the PL and subcavity resonance. This corroborates earlier observations [4], with broader bandwidth the PL is influenced by the subcavity resonance, however with narrow bandwidth the QW gain is more dominant. The results are therefore expected to be roughly between ~0.1 nm/°C and ~0.3 nm/°C inferred from Figure 2-16, Chapter 2, Section 2.3.2.2. The experimental data here presents 0.5 nm/°C $\leq$ 30°C and 0.2 nm/°C $\geq$ 40°C.
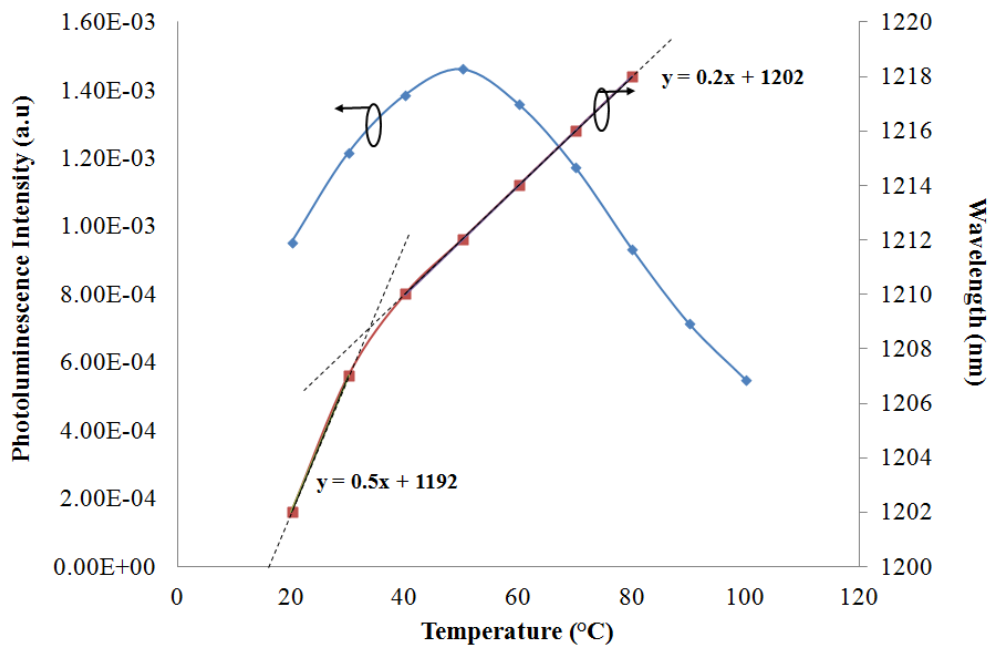
Figure 4-8: PL intensity and wavelength shift with respect to increasing temperature.

The PL intensity profile also provides an indication of the effectiveness of the wafer for use in an SDL. This latter point was particularly highlighted during the characterisation of a batch of wafers grown with different design specifications, comparing 4, 6 and 8 QWs and QW gain materials GaInAs and GaInNAs. The wafers exhibiting the highest PL intensities were capable of providing laser output, as opposed to those with extremely weak PL, which failed as SDL devices.
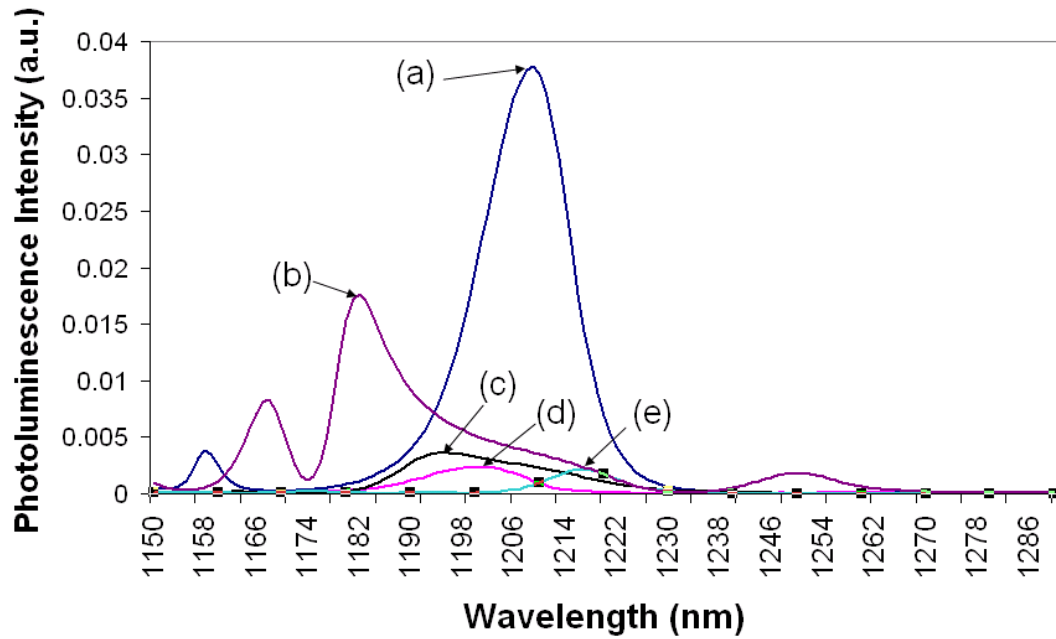
Figure 4-9: Photoluminescence intensity profiles comparing 5 different structures; (a) 4QW GaInAs *Vn1381*, (b) 6QW GaInNAs *Vn1567*, (c) 4QW GaInNAs *Vn1534*, (d) 8QW GaInAs *Vn1399* and (e) 8QW GaInNAs *Vn1536*.

Figure 4-9 illustrates the PL intensities for the series of wafers from the same supplier, using the same MBE machine. In this analysis sample *Vn1381*, PL plot (a) in Figure 4-9, exhibiting the highest intensity profile was the only sample from that batch that was implemented in an SDL. It was short lived as a device; however it invited an investigation into the cause of device failure. The evidence was revealed through SEM images of each of the wafers.

4.2.3 Scanning Electron Microscopy (SEM)

The Scanning Electron Microscope at the Strathclyde University Physics Department was used with courtesy of Professor Robert Martin and Dr. Paul Edwards.

The PL spectrum responses shown in Figure 4-9 in the previous section correspond to the SEM images obtained for each the devices in Figure 4-10 from (a) to (e), respectively. The most successful growth appears in Figure 4-10 (a) for sample *Vn1381* of a 4 QW GaInAs/GaAs wafer which delivered a device with the highest

PL peak response. Within the DBR section of the SEM images, the dark regions correspond to *AlAs* material whilst the lighter regions are *GaAs*.

Examination of the other samples revealed some interesting features which may contribute to the weak PL performance. In Figure 4-10 (b) the 6 QW GaInNAs/GaAs structure exhibits noticeable *voids* or sections of no contact between layers and along the plane of growth. These are prevalent in the DBR section, which implies that the AlAs/GaAs MBE growth using these elements had encountered some issue during the process. The 4 QW GaInNAs/GaAs structure in Figure 4-10 (c) shows a different feature, which may be dislocations due to stresses in the material although the cleaving of the sample may have not been optimal. The DBR stack does not appear as uniform as samples shown in (a), (b) and (d). The AlAs/GaAs material stack lacks cohesion, which makes it appear 'brittle'. In Figure 4-10 (d), again the cleaving of the sample may be in question due to the diagonal markings between the 8 QW GaInAs/GaAs materials. Yet these markings may also be a consequence of uneven MBE growth of the GaAs barriers, which might explain the low peak PL for this sample. Finally, the 8 QW GaInNAs/GaAs sample in Figure 4-8 (e) shows the same occurrence of voids in the DBR structure, with what appear to be *islands* or quantum dots (QD) which have formed around the QWs. Uneven growth patterns of the barrier material are visible for the two QWs above the DBR section. Similar to the sample shown in (c), the DBR section in this sample also appears to lack cohesion with large voids along the growth plane. The results from these SEM images were provided to the MBE grower in order to identify the cause of these growth anomalies and improve the quality for future wafer growth.
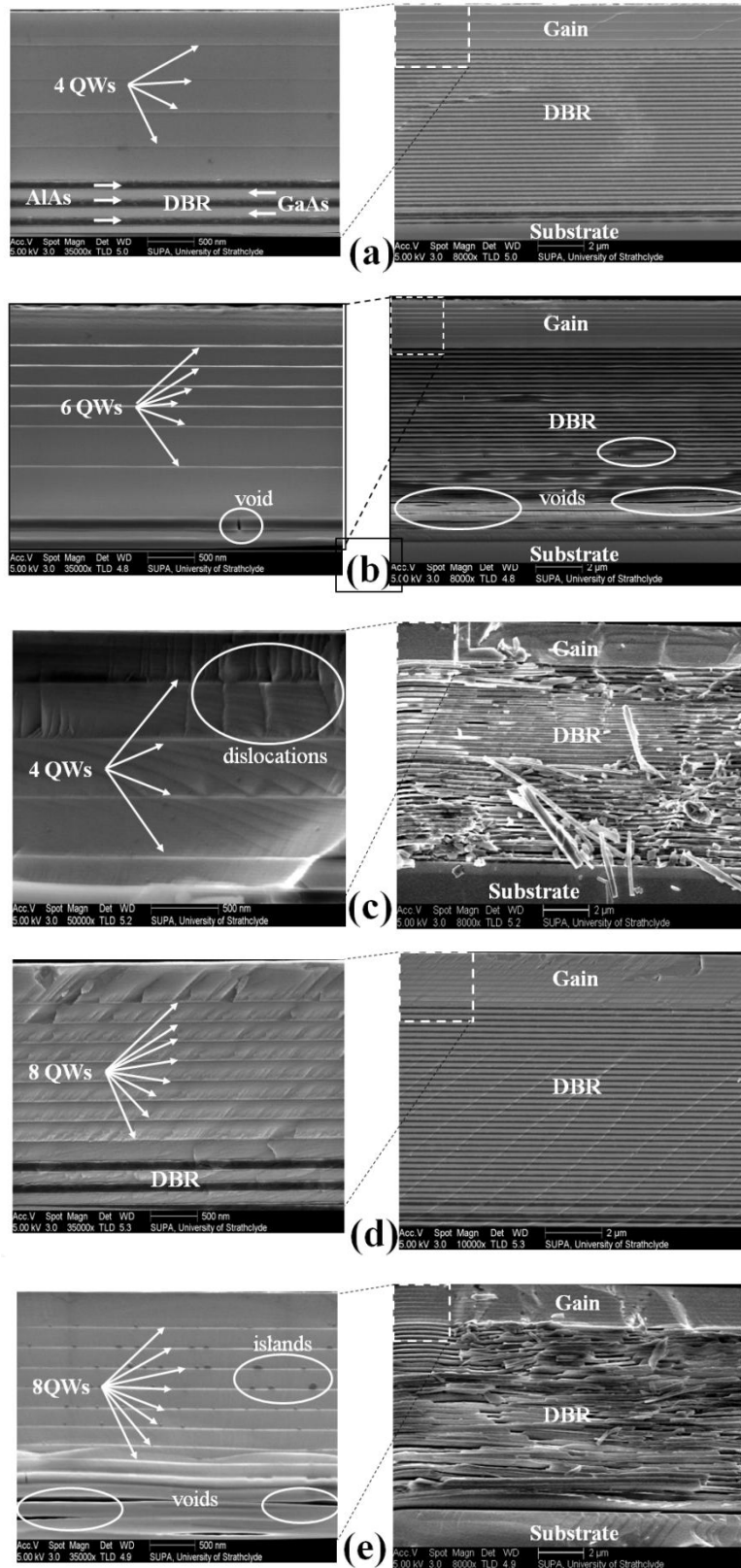
Figure 4-10: SEM images of (a) 4 QW GaInAs/GaAs *Vn1381*, (b) 6 QW GaInNAs/GaAs *Vn1567*, (c) 4 QW GaInNAs/GaAs *Vn1534*, (d) 8 QW GaInAs/GaAs *Vn1399* and (e) 8 QW GaInNAs/GaAs *Vn1536*.

It must be noted that the majority of devices that were MBE grown and implemented for use in this thesis were of a high quality, which is reflected in laser performance.

4.3 Laser Performance

In this section, experimental techniques to provide a measure of the highest achievable output powers, the beam profile and extent of spectral coverage were performed. The initial laser cavity design has a major influence upon this performance, thus due consideration has been given to mode matching.

4.3.1 Mode Matching

In the set up of the SDL and alignment of the cavity, the aim is to attain an optimal configuration. One of the methods to achieve this aim is to employ the *mode matching* technique, due to its impact on the overall efficiency, beam quality and potential output powers achievable. The objective of mode matching is to maximise the extraction of gain from the pumped semiconductor chip. The management of these is possible through the choice of pump delivery optics to achieve an effective pump spot area on the semiconductor chip, and the laser cavity design to modify the mode area. This is significant, because if the pump spot size is larger than the mode size there will be gain available for higher order modes to oscillate thus reducing the beam quality. In the case of a smaller pump spot size and larger fundamental cavity mode, it will experience loss at the edges and be less efficient. The selection of the pump spot size should take into consideration the thermal variations within the semiconductor material, causing fluctuations in the cavity mode size with an effect on the threshold pump powers needed for excitation.

The length of the gain section in the SDL chip has such small dimensions ($L_{cavity} < 2$ μm) that it can be considered a planar absorber, as mentioned previously in Chapter 2, Section 2.2.2.4. In light of this, mode-matching is in a single plane which is advantageous for consideration of pump geometric multiplexing. This technique was demonstrated by Fan et al [5, 6] in solid-state laser systems in which multiple diode pump lasers were used to increase the available pump power delivered to the gain

medium. Therefore in the case of an SDL, the focusing of the multiple pump beams is onto a planar gain region, reducing the three-dimensional overlap required when focusing into a gain crystal.

A software tool used during this project to aid with the cavity design was Winlase[TM]. The software provided a means to simulate the cavity performance using various optics and under specific performance constraints, to create a visual interpretation of the beam profile within the laser cavity. This is based on implementing *ABCD* matrix evaluations for all cavity components. A summary of the optical elements with the corresponding *2x2 ABCD* matrix is provided in Table 4.1.

Table 4.1: Optical elements and the ABCD matrix equivalent [7].

Optical Element	ABCD Matrix
Propagation through a medium having index-of-refraction *n* and length *d*	$\begin{bmatrix} 1 & d/n \\ 0 & 1 \end{bmatrix}$
Refraction at a spherical boundary of radius *R*, entering a medium of index n_2 from a medium of index n_1. *R* is positive if the center of curvature lies in the positive direction of ray propagation.	$\begin{bmatrix} 1 & 0 \\ -\dfrac{n_2 - n_1}{n_2 R} & \dfrac{n_1}{n_2} \end{bmatrix}$
Transmission through a thin lens of focal length *f*	$\begin{bmatrix} 1 & 0 \\ -1/f & 1 \end{bmatrix}$
Reflection from a spherical mirror having radius *R*. *R* is positive if the center of curvature lies in the positive direction of incident ray propagation.	$\begin{bmatrix} 1 & 0 \\ 2/R & 1 \end{bmatrix}$

ABCD simulations use the convention of calculating components as they are encountered within the cavity. Figure 4-11 shows a Winlase[TM] plot of the evolution of the beam width within the SDL three mirror cavity, with the SDL chip on the left followed by the curved folding mirror in the middle and finally the output coupler mirror on the far right. The distances are *D1=54 mm* from the SDL to the folding mirror *M1* at a 5° angle to the output coupler, with a Radius of Curvature *(ROC)=-100mm*, and a distance *D2=200 mm* between the folding mirror and the plane output coupler mirror *M2*. The result of this simulation provides a measure of ~52 μm mode radius incident on the SDL gain chip. The stability of the laser cavity adheres to the condition as set out in Hunziker *et al.* [8] using the *g* parameters for $g_1 g_2 = \frac{1}{2}$ where

the parameters are related to the mode radii on the semiconductor material w_1 and on the output coupler mirror w_2 shown in Equation (4.1.1).

$$g_1 = \pm\frac{1}{\sqrt{2}}\frac{w_2}{w_1}, \text{ and } g_2 = \pm\frac{1}{\sqrt{2}}\frac{w_1}{w_2}$$

(4.1.1)

Using this criteria and the mode sizes calculated for the cavity in Figure 4-11 has $w_1=52\mu m$ and $w_2=320\mu m$, providing a product of $g_1g_2=0.5$ indicating a stable cavity.
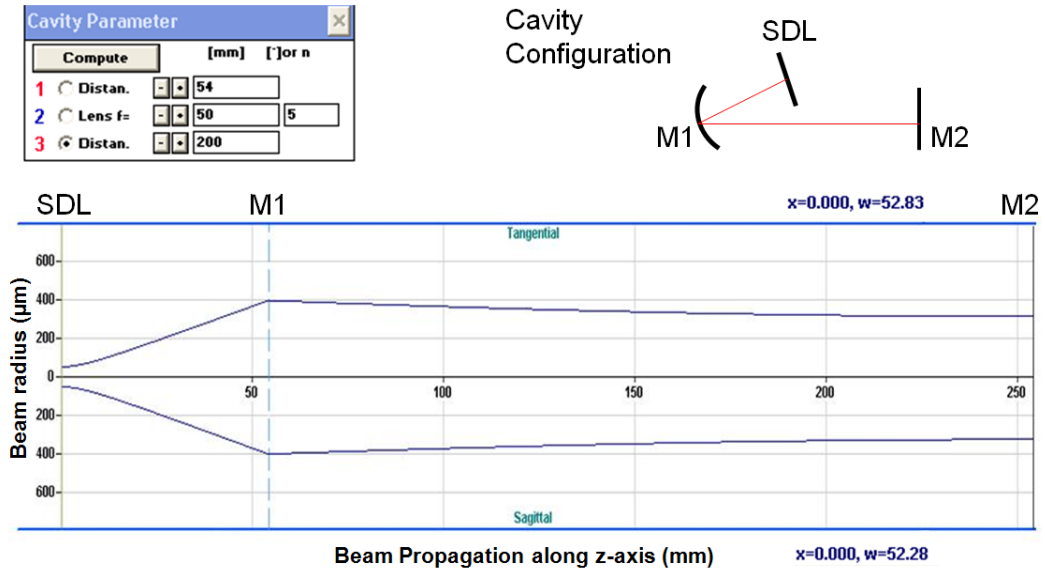
Figure 4-11: Winlase^{TM} simulation of a cavity designed for 1220nm operation, indicated are the locations of the *SDL* chip, folding mirror *M1* and output coupler mirror *M2* as shown in the cavity configuration.

The method in which mode matching can be achieved is through varying the distances *D1* and *D2*, and changing the radius of curvature R_c of the folding mirror in order to match the pump spot size on the semiconductor chip. The pump radiation was delivered through a 100 μm core fibre, with the spot size on the chip determined by the focusing optics. Equation (4.1.2) provides a means to calculate the mode radius w_1 on the chip, based upon the laser operating wavelength λ_{laser}, the cavity length L_c and the radius of curvature of the mirror R_c [9].

$$w_1^2 = \frac{4\lambda_{laser}L_c}{\pi}\sqrt{\frac{(R_c-L_c)}{L_c}}$$

(4.1.2)

The simulation results, using this equation are shown in Figure 4-12.
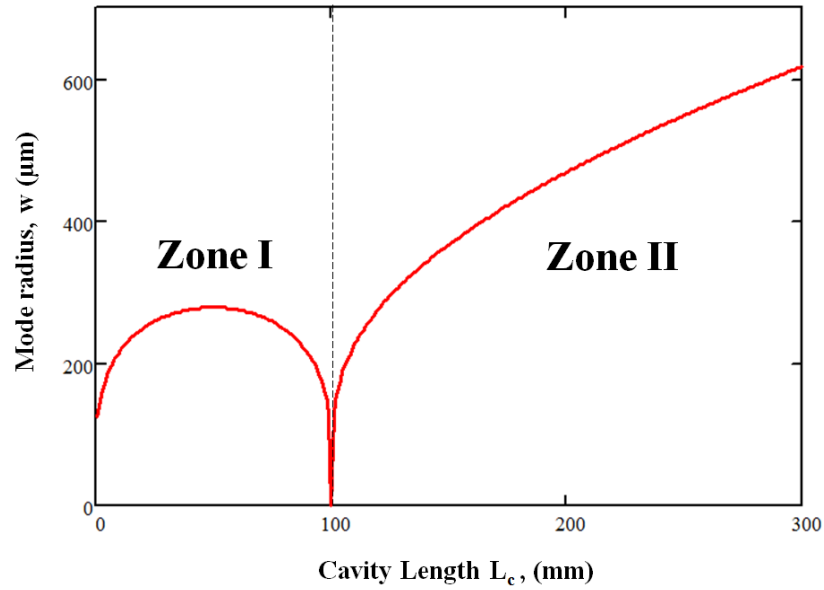
Figure 4-12: Mathcad^{TM} simulation of the mode radius w over a range of cavity lengths L_c, using a folding mirror radius of curvature $R_c = 100$ mm.

The two stability zones in Figure 4-12 correspond to the full width stability ranges in the expressions shown in Equation (4.1.3) [8], where z_1 is the Rayleigh range with d_1 and d_2 the intracavity distances.

$$\Delta d_1^{fw} = 2z_1, \quad \text{and} \quad \Delta d_2^{fw} = \frac{2d_1^2}{z_1} \qquad (4.1.3)$$

For the SDL with an operating wavelength $\lambda=1.22\mu m$, and intracavity distances $d_1=200mm$, $d_2=54mm$ and the mode radii $w_1=320\mu m$ and $w_2=52\mu m$, therefore $\Delta d_2^{fw} = 303mm$. The full width stability range for Δd_1^{fw} is dependent upon the Rayleigh range of the beam from the folding mirror within the cavity.

4.3.2 Power Transfer

The power scaling of SDLs has been one of the main attributes used to benchmark these devices. High output powers imply a good quality device, in terms of growth, optimised design and effective thermal management. The data presented for the devices here have all used three mirror cavity configurations, as shown in Figure 4-13. The output coupler was a dichroic mirror, selected to have transmission powers

for High Reflectance (HR) at the design wavelength, through to a 1%, 2% and in some cases >3% transmission powers.
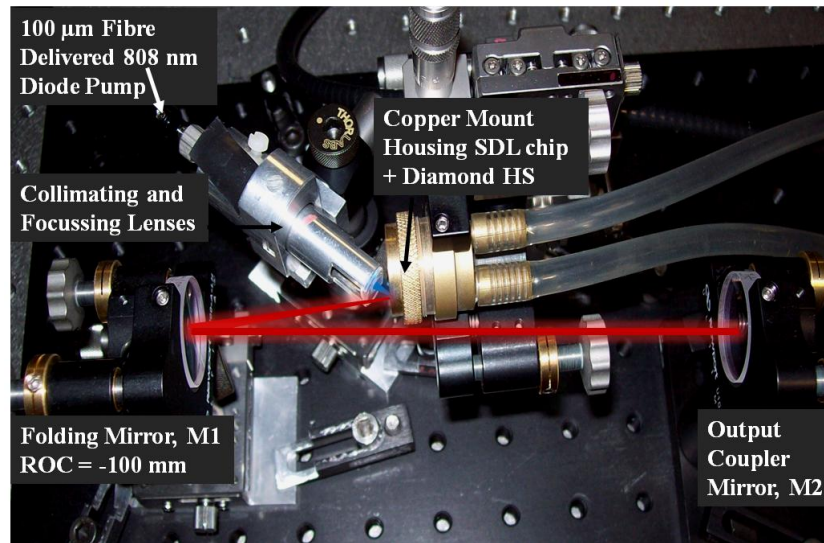
Figure 4-13: SDL in a three-mirror cavity configuration showing the beam path *(red)*, the laser cavity is formed between the SDL, M1 and M2.

The output power was measured against increasing input powers, resulting in the power transfer curves as shown in Figure 4-14, for a 1220 nm designed SDL.
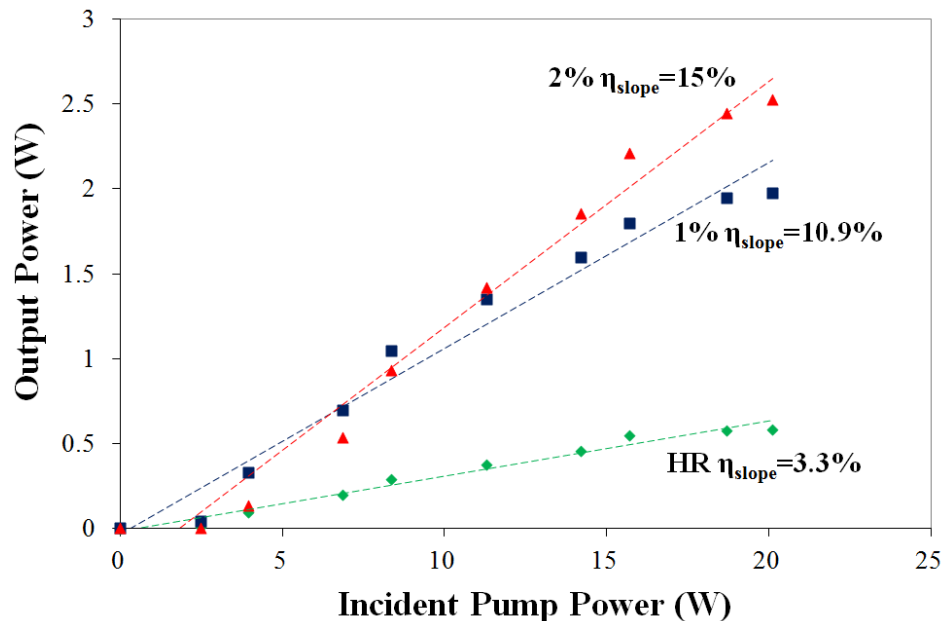
Figure 4-14: Power transfer curves of *AsN2527* 1220nm SDL with Output Couplers (OC) High Reflectance (HR), 1% and 2% transmissions.

Figure 4-15 summarises the best performance obtained with all GaInNAs based SDL devices that were characterised during this research work.
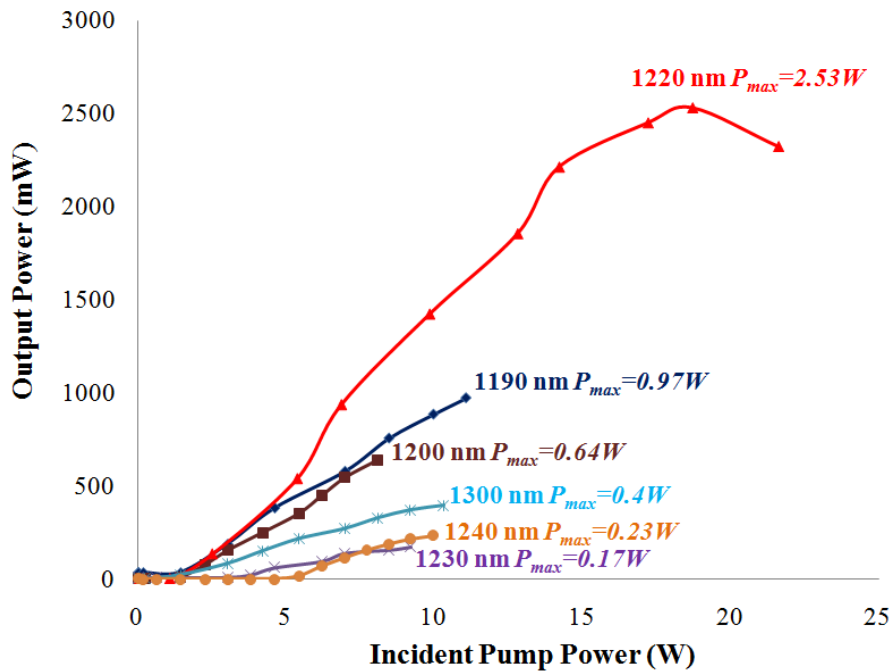
Figure 4-15: Highest achieved power transfer curves for all devices measured, indicating the device design wavelengths.

An overall assessment of the maximum powers achieved for each of the devices is shown in Figure 4-16, with inclusion of the maximum slope efficiencies. There is a division between the performances of devices operating at wavelengths between 1180 nm − 1220 nm indicated in area *A* compared with 1230 nm − 1300 nm in area *B*.
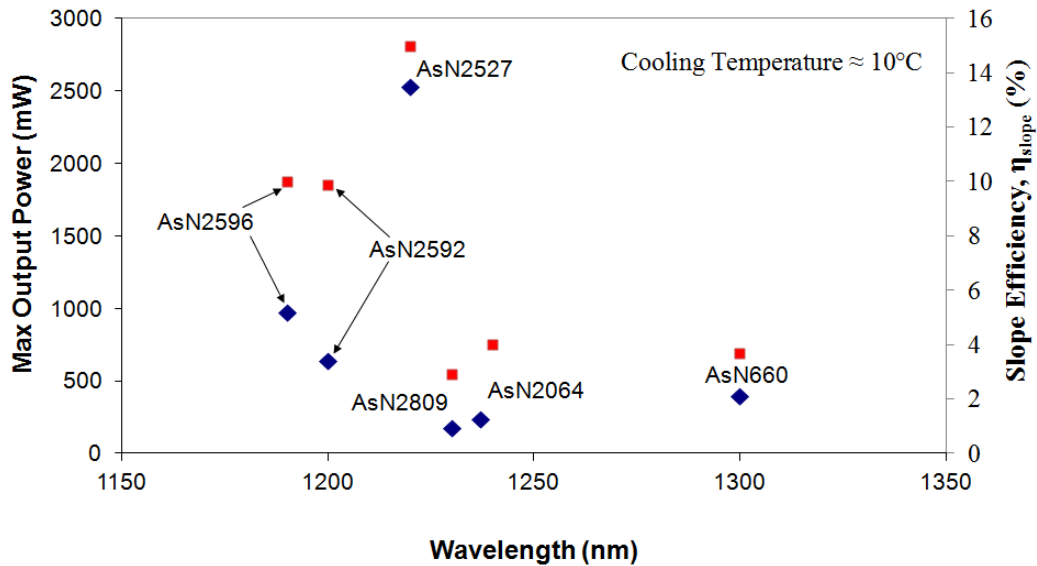
Figure 4-16: Comparison of maximum output powers (*blue diamond*) and slope efficiencies (*red squares*) for all samples.

Contributing factors which may have influenced the laser performance include the quantum efficiency as well as the strain effects of the material system. It is noticeable that the quantum efficiency ($\eta_q = \lambda_{pump}/\lambda_{laser}$) using 808 nm diode pump lasers is slightly higher in the *A* devices with values of 68%-66%, but ranging between 65%-62% in the *B* laser devices. This is a reasonable expectation, however it highlights the pump laser design considerations needed for devices which operate further into the infrared emission in order to maximise the quantum efficiency [10]. Furthermore the region *A* devices have included strain compensating layers of GaNAs as part of the active region design compared to those of *B* which have none. The high level of performance attributed to the 1220 nm device might account for the amount of nitrogen in the GaInNAs QW, which is much lower at ~0.6-0.7% compared to the other devices. This provides some correlation between performance and the nitrogen content, indicating that low concentrations of nitrogen in the material enables a lower probability of quantum defects such as those described in Chapter 2 in Section 2.5.

The results in Figure 4-17 provides the threshold pump powers and slope efficiencies for the 1220 nm device using different output coupler transmission powers. It is evident that increasing the output coupler transmission tends to a higher slope

efficiency and output power. Meanwhile the threshold pump power shows an initial increase.
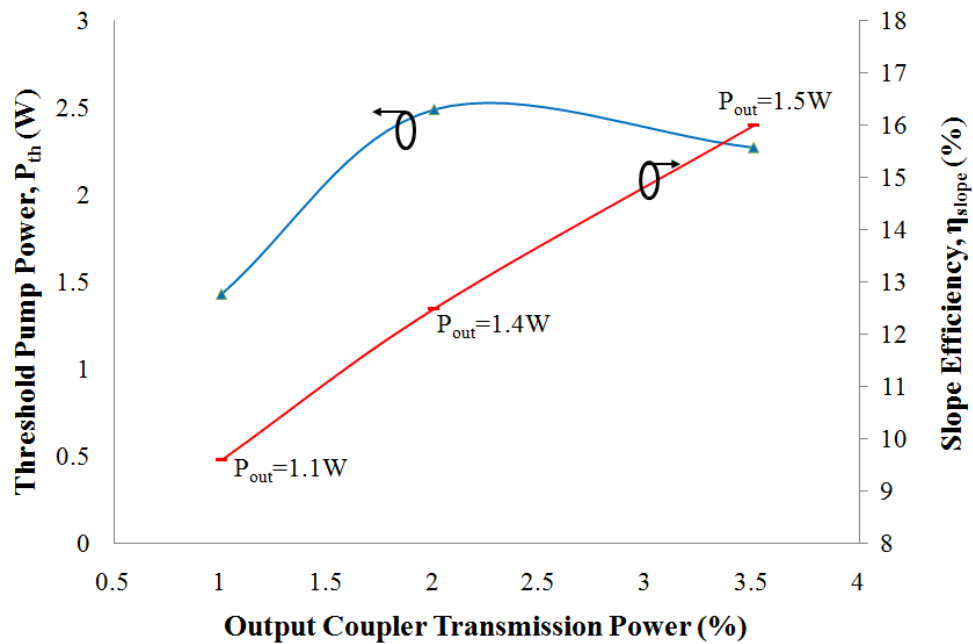
Figure 4-17: Threshold pump powers (*blue*) and slope efficiencies (*red*) across a range of output couplers T=1%, 2% and 3.5% for sample *AsN2527* 1220 nm.

The analysis of pump threshold and slope efficiency has been extended across a range of cooling temperatures from 5°C to 45°C, using the *AsN2592* 1200 nm SDL. Figure 4-18 shows that increasing the temperature results in ~50% decrease in slope efficiency with ~20% increase in threshold pump power. The slope efficiency at device cooling temperatures ≤20°C experience higher efficiencies with a more gradual drop-off rate compared with those >20°C. This further verifies how significant the thermal effects are in relation to SDL performance.
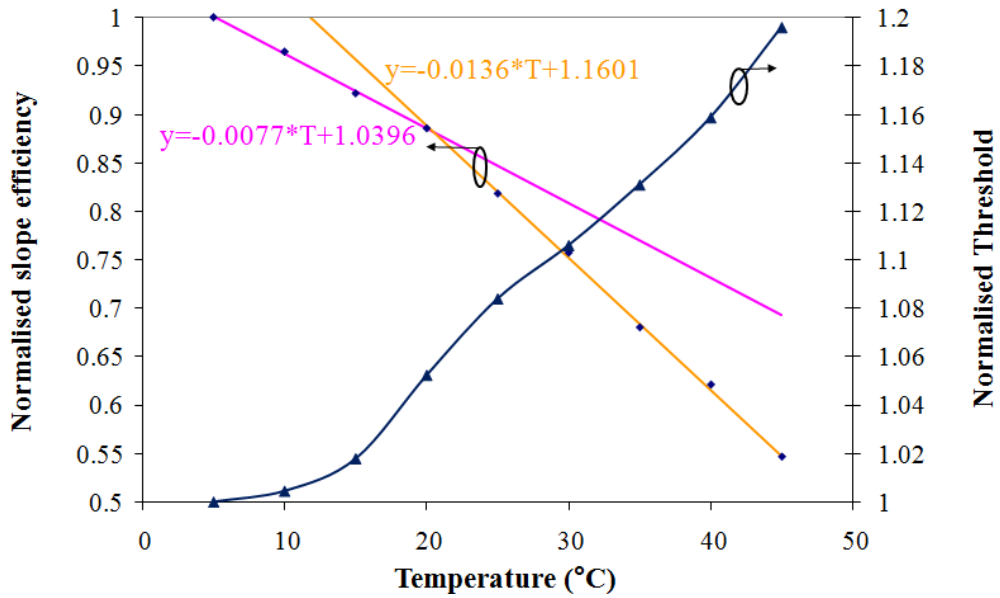
Figure 4-18: Normalised slope efficiency and threshold pump powers over a range of temperatures for the AsN2592 1200 nm device [11].

The two devices which exhibited the best performance in terms of output powers and slope efficiency were *AsN2527 1220 nm* and *AsN2596 1180(1190) nm*. These were chosen for use as pump sources, as described in Chapter 5 and also for frequency doubling in Chapter 6.

4.3.3 Beam Profile Measurements

The beam quality of a laser has been quantified using a benchmark called the *M^2 measurement*. This refers to the Beam Parameter Product (BPP) which is a ratio of the beam divergence measurement in comparison to a diffraction-limited Gaussian beam, at the design wavelength. A desirable M^2 value is ~1, which indicates a beam on a par with the ideal Gaussian beam profile.

M^2 measurements were performed using a BeamMaster scanning detector, which operates by alignment of the detector head with the SDL output beam and sliding the detector along its propagation direction. The BeamMaster scans the beam and captures its sagittal and tangential aspects. The profile was then shown using the computer software, as illustrated in Figure 4-19.
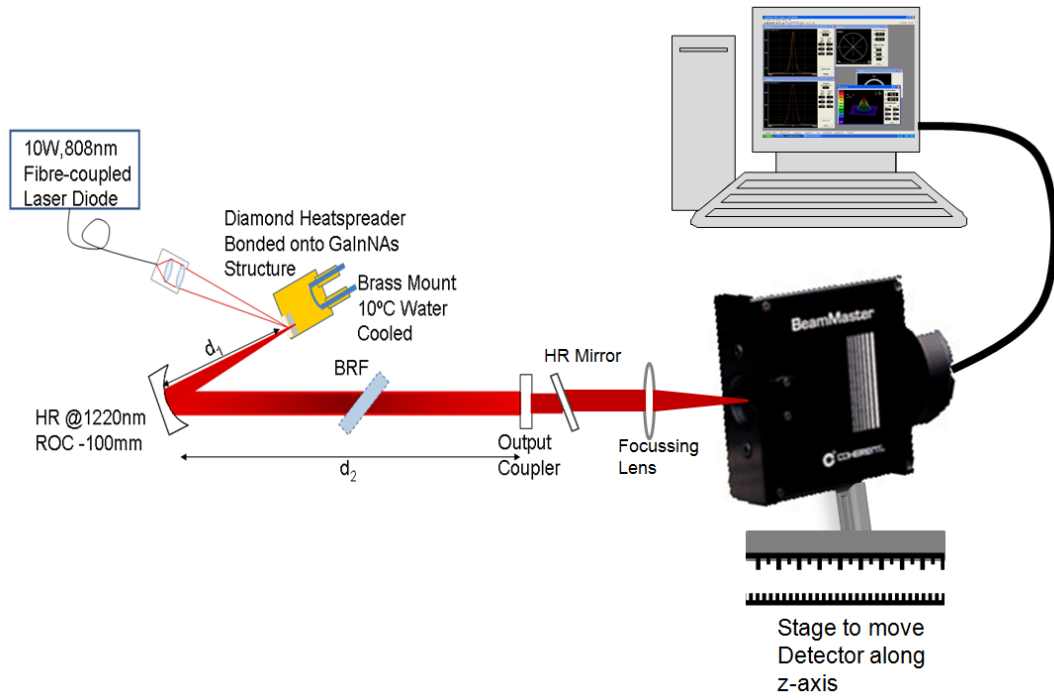
Figure 4-19: Schematic of M² measurement apparatus using the BeamMaster scanning detector.

The SDL used for these measurements was a 1220 nm device, with cavity dimensions *d1 = 58 mm* to the folding mirror with *ROC = -100 mm*, and *d2 = 403 mm* to the output coupler with 2% transmission power. The maximum output power of the SDL was 760 mW, but to prevent damage to the detector a HR mirror was placed before the focusing lens. The tolerance for the detector was <10 mW of input beam power.

The beam waist as a function of the spatial component along the z-axis, can be evaluated using Equation (4.1.4) [12, 13].

$$w(z) = w_0 \sqrt{1 + (M^2 \frac{z}{z_R})^2} \qquad (4.1.4)$$

The Rayleigh range, $z_R = \frac{\pi w_0^2}{\lambda}$ and the half-angle of the Gaussian beam is $\theta = M^2 \frac{\lambda}{\pi w_0}$. Through the collection of data captured by the BeamMaster computer programme, the *1/e²* radius Gaussian beam values are recorded, and used as *w(z)* in

Equation (4.1.3). The results are shown in Figure 4-20; including the tangential, sagittal and ideal Gaussian beam curves, with a 10% error incumbent on these figures. The error associated with these types of measurements stem from the precision of alignment at the centre of the detector head. Any deviation consequently affects the beam shape and may not follow perfectly along the central axis of the beam.
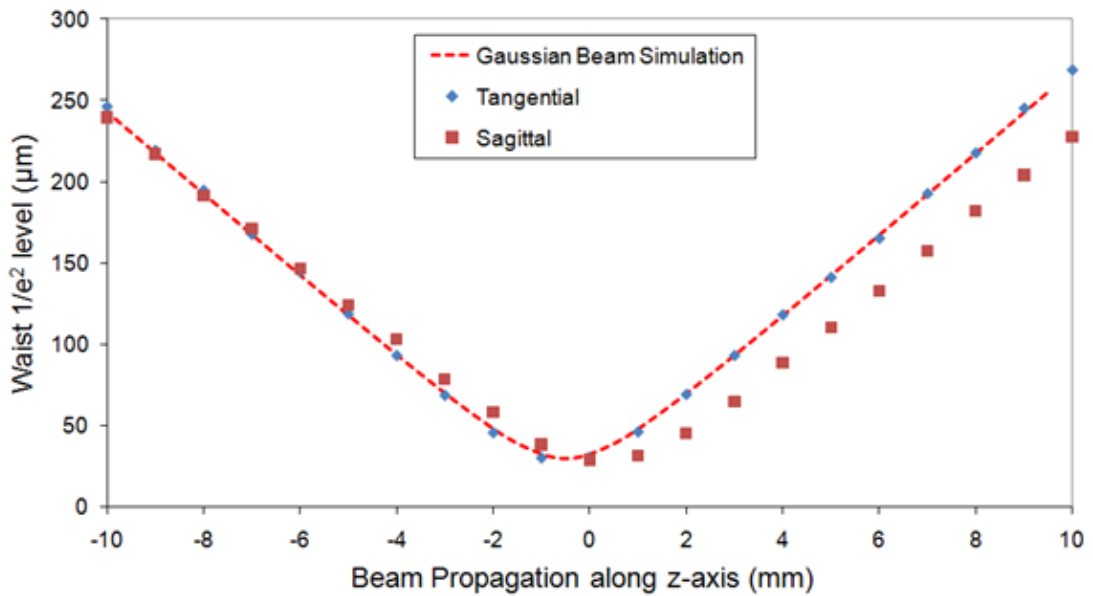
Figure 4-20: Beam profile plots for the tangential $M^2 \approx 2$ and sagittal $M^2 \approx 1.7$, compared with the Gaussian beam.

These results achieved an M^2, tangential = 1.97 and sagittal = 1.71. This SDL was subsequently used as a pump source for a thulium-doped glass laser, as described in Chapter 5.

4.3.4 Wavelength Tuning Ranges

Wavelength tuning and in particular the ability to select a specific wavelength are an important function in SDL operation. The tuning ranges give an indication of the gain bandwidth of the material, based on design and material constraints. The wavelength selection of the device gives functionality to target specific absorption or excitation spectral regions in other material systems. Specific examples of this are

presented in Chapter 5, using a wavelength selected SDL to pump a thulium-doped glass laser system.

Wavelength tuning techniques include the use of prisms, gratings, intra-cavity etalons and birefringent filters. For the work presented in this thesis, a birefringent filter (BRF) was employed for wavelength selection. The material of the filter was composed of crystalline quartz, used for its birefringent (uniaxial) crystal properties, and mounted intracavity at Brewster's angle. The thickness and orientation of the BRF provide the mechanism to allow one frequency within the gain curve of the laser to be chosen. It is that frequency that suffers minimum loss since its polarisation is unaffected, while all other frequencies are suppressed. By changing the orientation of the filter the frequency experiencing minimum loss is altered, thereby tuning the filter.

The two important attributes of the filter include wavelength selectivity and its free spectral range (FSR) capability. The geometry of the filter is key in the selection process, and Figure 4-21 represents the path of the refracted incident beam as it passes through the filter.
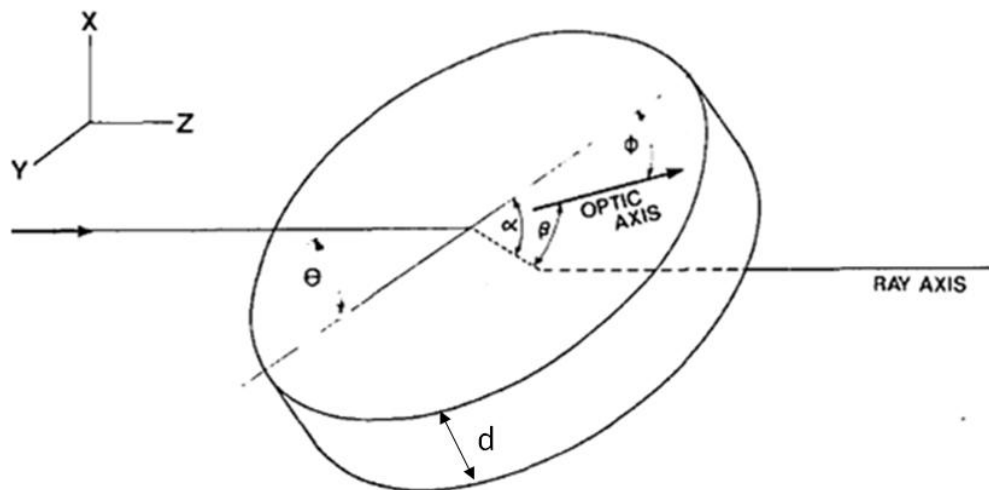
Figure 4-21: Birefringent filter illustration to show the angular dependence of the incident beam though the filter with thickness d, at an incident angle θ, rotation angle ϕ, angle between the refracted ray and the optic axis β, and the angle between the refracted ray and the plate angle α [14].

Using the evaluations presented by Zhu [15] the birefringent filter selectivity is represented by the single pass transmittance of the filter $|T|$ expressed in Equation (4.1.5), with the condition that the internal angle α=45°.

$$T(\lambda, d, \phi) = \left| \frac{(1+q^2)\cos\delta \pm \sqrt{(1+q^2)^2 \cos^2\delta - 4q^2}}{2} \right| \qquad (4.1.5)$$

The transmission factor of the filter $q = \frac{2n}{(1+n^2)}$ and the phase of the beam is expressed in Equation (4.1.6), as a function of the wavelength λ, the thickness of the filter d and the tuning angle φ, in which the polar angle β changes with tuning such that $\beta(\varphi)=arccos(Cos\varphi Cos\theta)$. The birefringence of the filter $\Delta n = n_e - n_o$.

$$\delta(\lambda, d, \phi) = \frac{-\pi \Delta n d \sin^2(\beta(\varphi))}{\lambda \sin\theta} \qquad (4.1.6)$$

The transmission of the 4 mm thick filter for five different tuning angles is shown in Figure 4-22, providing a wavelength coverage capability of ~42 nm, peak-to-peak at each angle.
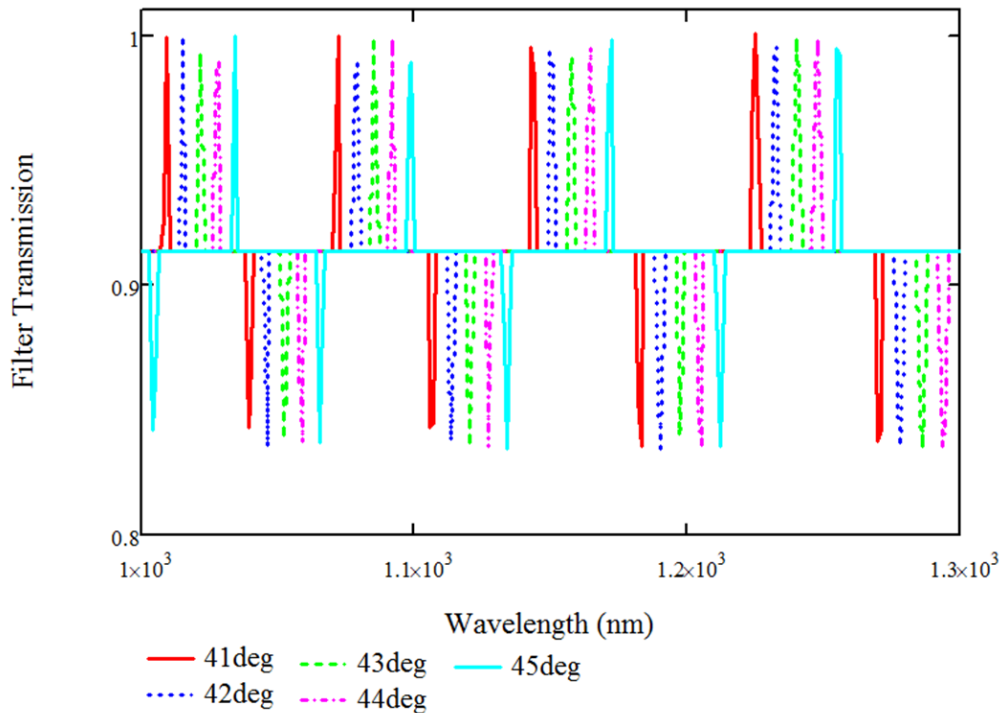
Figure 4-22: Transmission of a 4 mm BRF with rotational angles ϕ= 41°-45°.

127

The free spectral range of the filter $\Delta\lambda$ is represented in Equation (4.1.7) [15] and shown in Figure 4-23 across a range of filter thicknesses, set at a wavelength $\lambda=1220$ *nm*.

$$\Delta\lambda = \frac{\lambda^2 \sin\theta}{\Delta nd \sin^2(\beta(\varphi))} \tag{4.1.7}$$
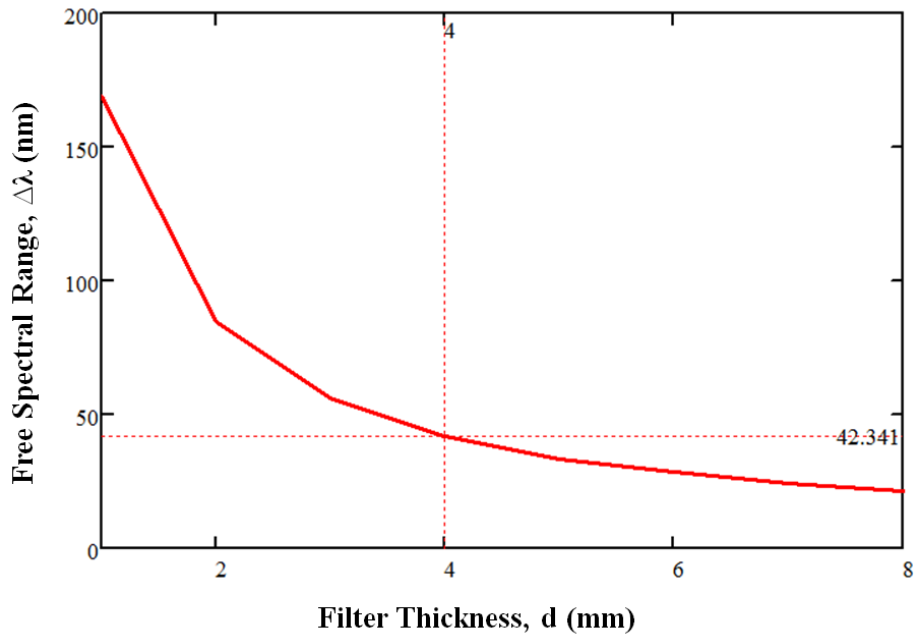
Figure 4-23: Free spectral range capability over a range of filter thicknesses, indicating $\Delta\lambda=42nm$ for a 4 mm thick BRF at a tuning angle $\varphi=41°$.

The SDL device using the MBE grown semiconductor material *AsN2527* designed to operate at 1220 nm, shall be used as an example to present the results obtained using these wavelength tuning and selection techniques. Figure 4-24 (a) shows a free-running wavelength spectrum obtained from an optical spectrum analyser (OSA), whilst insertion of the BRF into the laser cavity enabled the spectral narrowing to obtain 1213 nm, as shown in (b).
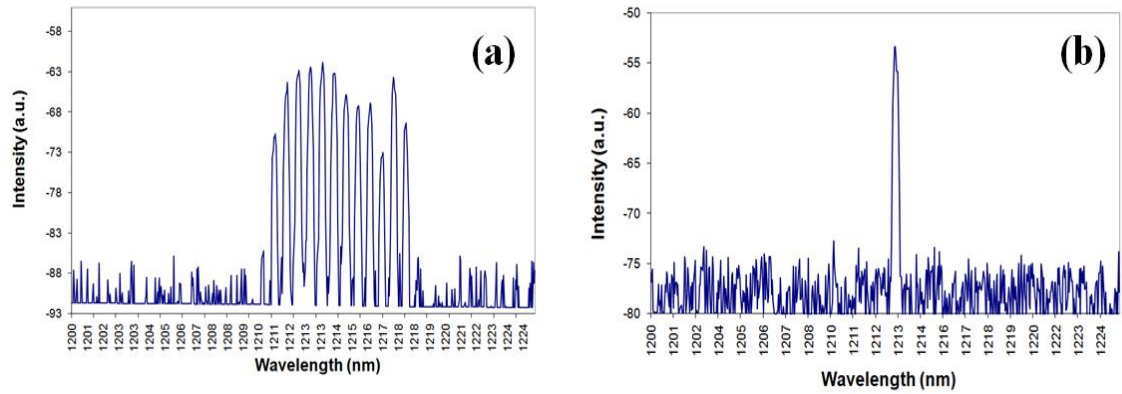
Figure 4-24: (a) Spectrum of a free-running AsN2527 1220 nm SDL, and (b) BRF selection of 1213 nm output wavelength.

The BRF was rotated to select wavelengths with the results shown in Figure 4-25, where the wavelength interval, $\Delta\lambda$ between two consecutive peaks was ~2 nm. This step-like selection of wavelengths is due to the plane-plane diamond heatspreader acting as an etalon within the cavity. The wavelength interval is found through the relationship $\Delta\lambda = \lambda^2/2nL$ where the $\lambda=1220$ nm, the refractive index $n=2.42$ and the thickness is ~200 μm resulting in a calculated value of 1.54 nm.

A suggested method to allow continuous wavelength tuning has been proposed by Maclean *et al.* [16], in which a wedged anti-reflection coated diamond heatspreader had been bonded to the semiconductor sample. However, this method has not been employed in this research work.
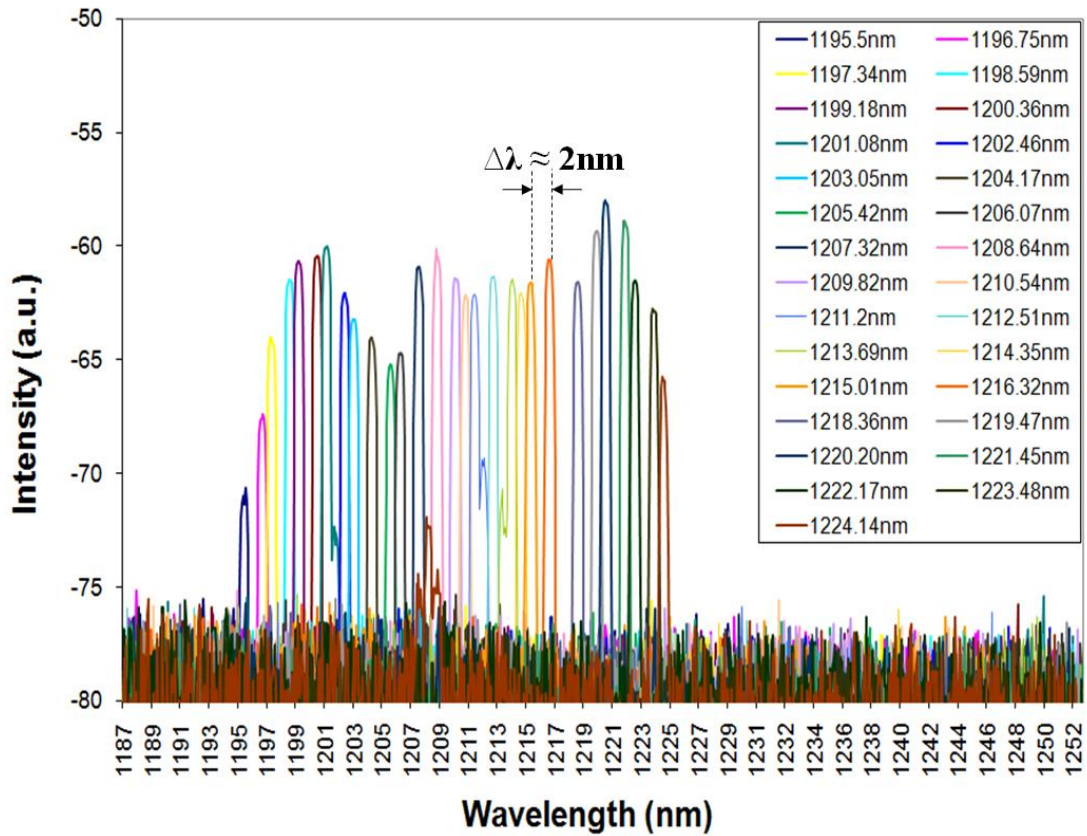
Figure 4-25: Wavelength tuning spectra, from 1195.5 nm to 1223.48 nm, indicated is the peak-to-peak wavelength separation Δλ≈2nm.

The results presented in Figure 4-26 provide the wavelength coverage with respect to output powers achieved, for three output coupler transmissions 1%, 2% and 3.5%. The average wavelength covered for this device ~27 nm.
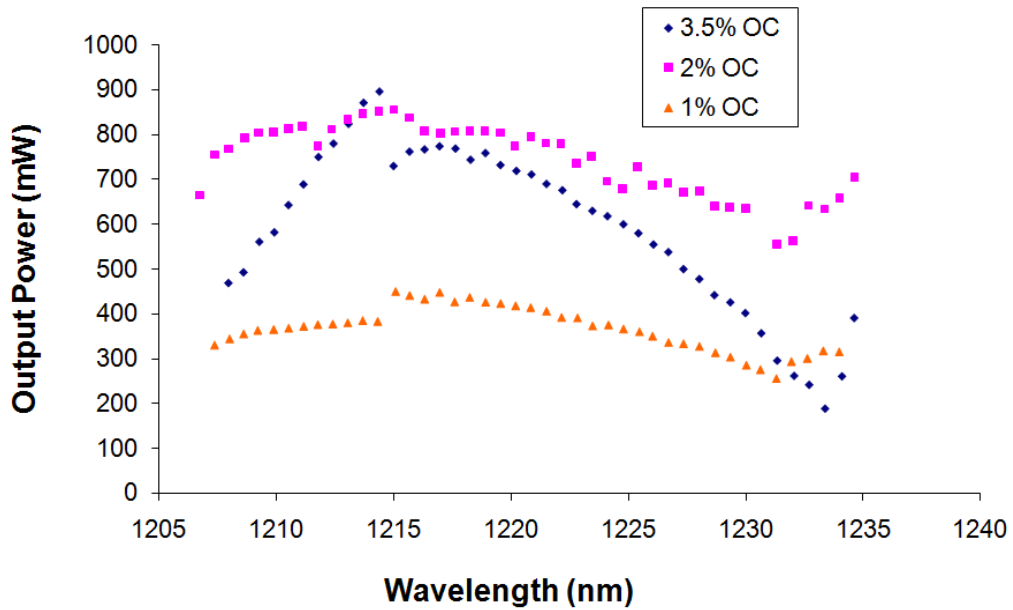
Figure 4-26: Wavelength tuning results for the *AsN2527* 1220 nm SDL, for output coupler transmissions 1%, 2% and 3.5%.

Cumulatively, SDL devices based on GaInNAs gain material have encompassed ~1170 nm to ~1340 nm, as shown in Figure 4-27.
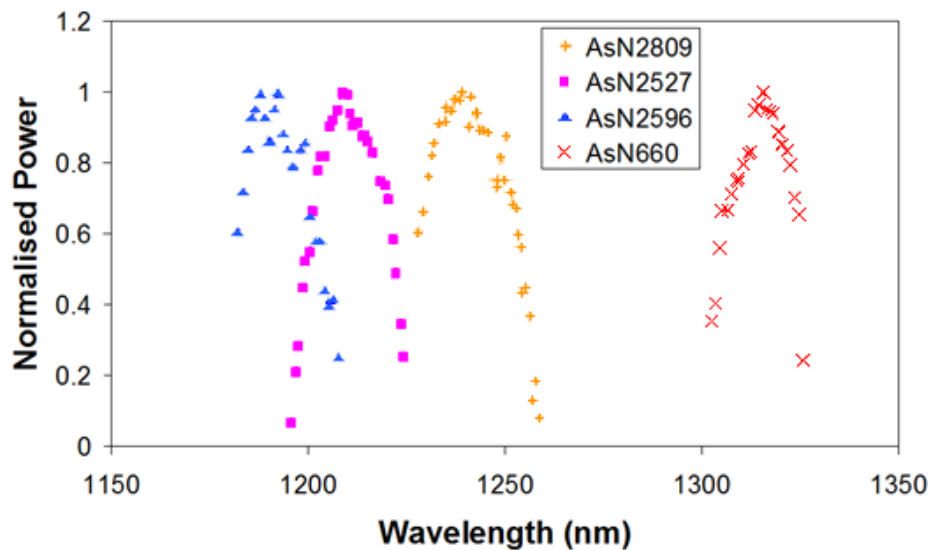
Figure 4-27: Wavelength tuning ranges for SDL devices *AsN2596* (1190 nm), *AsN2527* (1220 nm), *AsN2809* (1230 nm) and *AsN660* (1300 nm).

In a wider context the applications requiring lasers operating in these wavelength regimes span a variety of disciplines. Included are astronomy for frequency doubled 1180 nm in laser guide star applications [17], 1200 nm lasers for spectroscopy [18]

and gasoline octane detection [19], 1220 nm – 1240 nm lasers are required for tissue welding applications [20] and 1300 nm – 1340 nm of the O-band region for telecommunications [21].

4.4 Thermal Resistance Evaluation of an 1190 nm SDL

Using the techniques described in the previous sections, the 1190 nm SDL was assessed across a range of cooling temperatures from 5°C to 50°C. The data gathered was used to provide a measurement for the thermal resistance of the SDL. In Chapter 3, the importance and the techniques of thermal management were discussed, with the heatspreader approach providing the most effective way to dissipate heat within the device. The experimental methods described here vary the temperature cooling conditions of the device over a range of input powers, whilst maintaining the same pump spot size. The thermal resistance evaluation uses the variation response of the output based on thermal effects.

The mode radius onto the SDL chip was calculated to be ~40 µm. The pump beam was delivered by a fibre with a ~100 µm core diameter and optical elements of an 11 mm collimating lens followed by an 8 mm focusing lens, resulting in a pump spot radius of ~35 µm. This conforms to mode matching conditions, as described in Section 4.3.1.

The angle of the incident pump beam impacts the amount of reflected power at the air/diamond interface of the heatspreader. A more detailed mathematical description of reflectance and transmission of incident pump light at an oblique angle can be found through consulting MacLeod [22]. The expressions for these variables are shown in Equations (4.1.8) and (4.1.9).

$$R = \left(\frac{\eta_0 - \eta_1}{\eta_0 + \eta_1}\right)^2 \tag{4.1.8}$$

$$T = \frac{4\eta_0\eta_1}{(\eta_0 + \eta_1)^2} \tag{4.1.9}$$

The variables in these expressions for η_0 and η_1 are dependent upon the polarisation of the beam and can be substituted appropriately. The transverse electric (TE) or s-polarised light has $\eta_s = n_i \left(\sqrt{\dfrac{\varepsilon_0}{\mu_0}} \right) \cos \theta$ and the transverse magnetic (TM) or p-polarised light has $\eta_p = \dfrac{n_i \left(\sqrt{\dfrac{\varepsilon_0}{\mu_0}} \right)}{\cos \theta}$, with ε_0 and μ_0 the relative permittivity and permeability constants respectively. The refractive index term in these expressions n_i relates to the refractive index of the medium of the material, for example $n_0 = 1$ for air, and $n_1 = 2.432$ for the CVD diamond heatspreader.

Figure 4-28 shows the reflectance over a range of incident angles for the TE and TM response. The point at which the TM polarisation response falls to zero corresponds to Brewster's Angle (~70°). At a typical 45° incident pump angle the system experiences a ~18% reflectance.
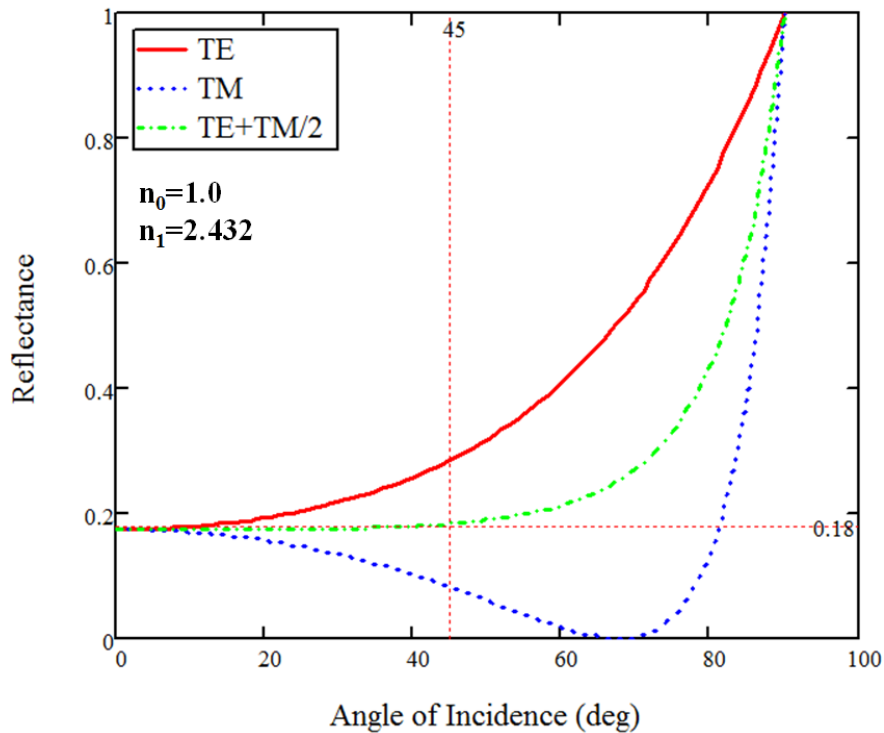
Figure 4-28: Reflectance of TE, TM and average TE+TM/2 of an incident beam from air, *n=1* to a CVD diamond heatspreader *n=2.432* over a range of incident angles.

Figure 4-29 are the power transfer curves obtained through measuring the output power across the range of temperatures. The increase in temperature adversely

affects the maximum achievable output powers, due to the different rates that the peak of the QW gain and the resonant-periodic-gain (RPG) shift with temperature. The misalignment between them can ultimately force the system to rollover.
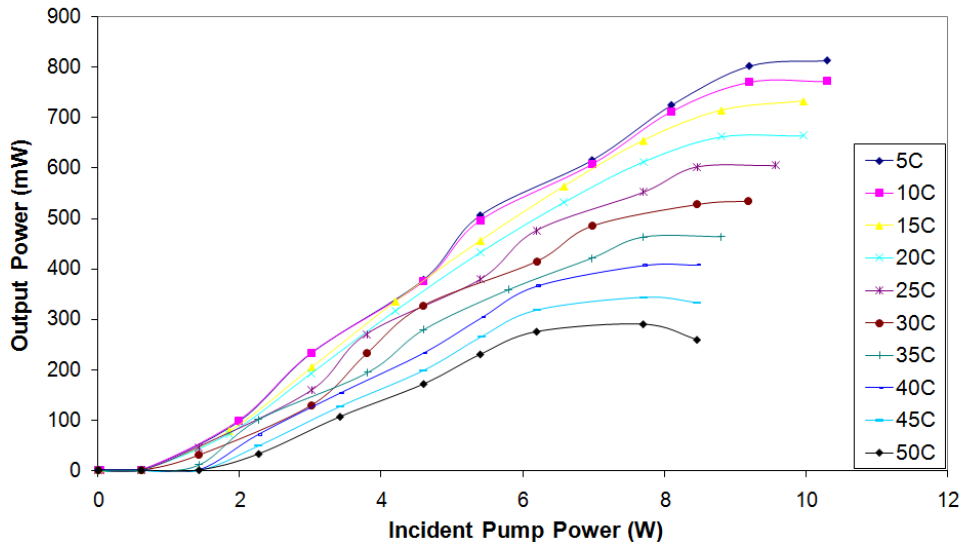
Figure 4-29: Power transfer curves ranging in temperature from 5°C to 50°C.

The relationship between the absorbed power P_{abs} and output power P_{out} is shown in Equation (4.2.0), where P_p is the incident pump power, $\varkappa_{abs}$ is the fraction of absorbed power and $R_{diamond}$ is the reflectance from the diamond heatspreader surface, taken to be ~18% based on the calculated values obtained above and verified in the analysis performed by Giet *et al.* [23].

$$P_{abs} = P_p(1 - R_{diamond})(1 - \varkappa_{abs}) - P_{out} \qquad (4.2.0)$$

 The spectral analysis of the device provided a means by which to equate the absorbed power P_{abs} with the change in wavelength, and is shown in Figure 4-30.
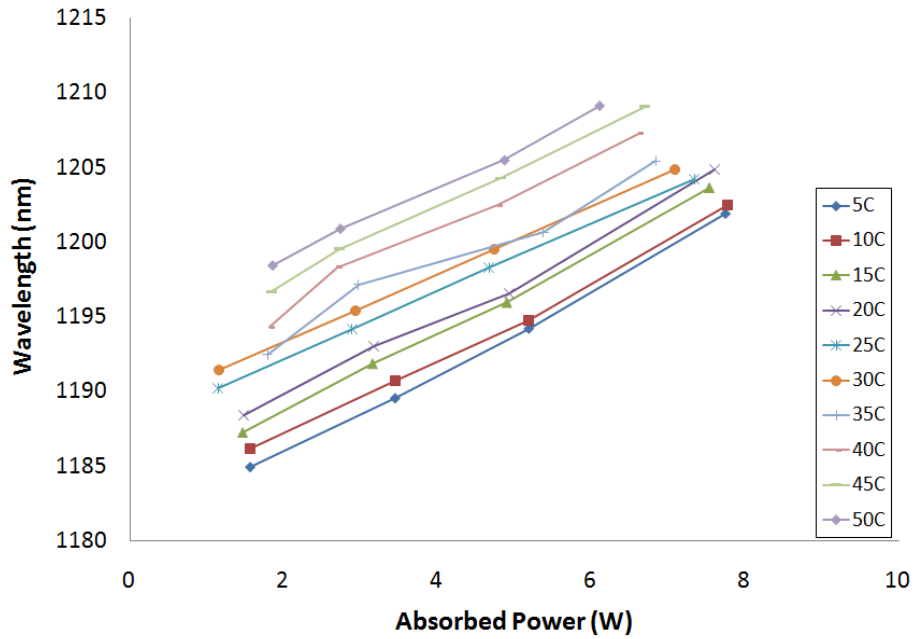
Figure 4-30: Wavelength variation with respect to the absorbed power across all temperatures.

The range of spectral wavelengths was red-shifted by ~0.2 nm/°C, which is evident in Figure 4-31. This shift lies in between the expected gain (0.3 nm/°C) and sub-cavity resonance (0.1 nm/°C) shifts due to temperature, thus their contributions may influence the spectral response of the device.
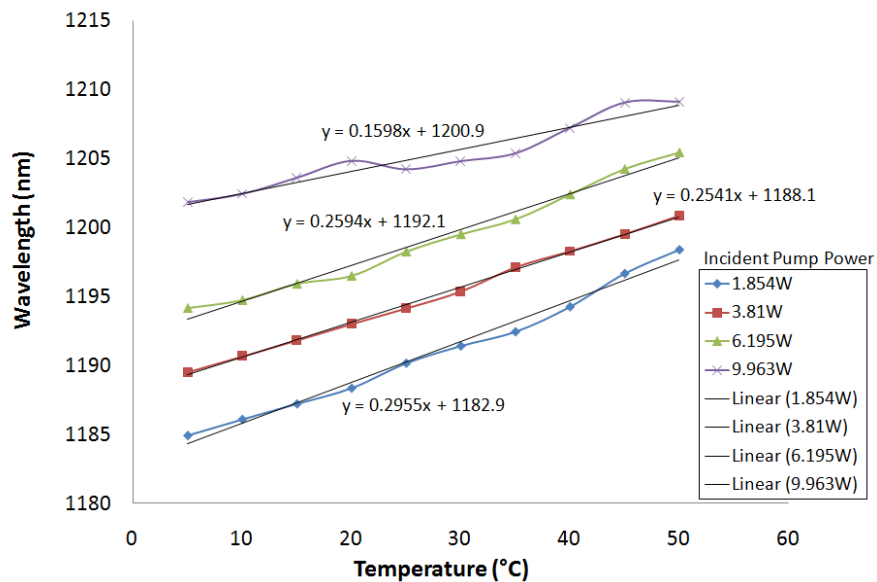
Figure 4-31: Wavelength variation across all temperatures at different incident pump powers.

135

The thermal resistance analysis was performed to take into consideration the output power changes due to temperature, as is clearly evident in Figure 4-31 showing a decrease by ~464 mW at the highest temperature 50°C with an incident pump power ~10 W. The absorbed power of the device shows a trend of decreasing, with increases to both temperature and the incident pump power, as shown in Figure 4-32.
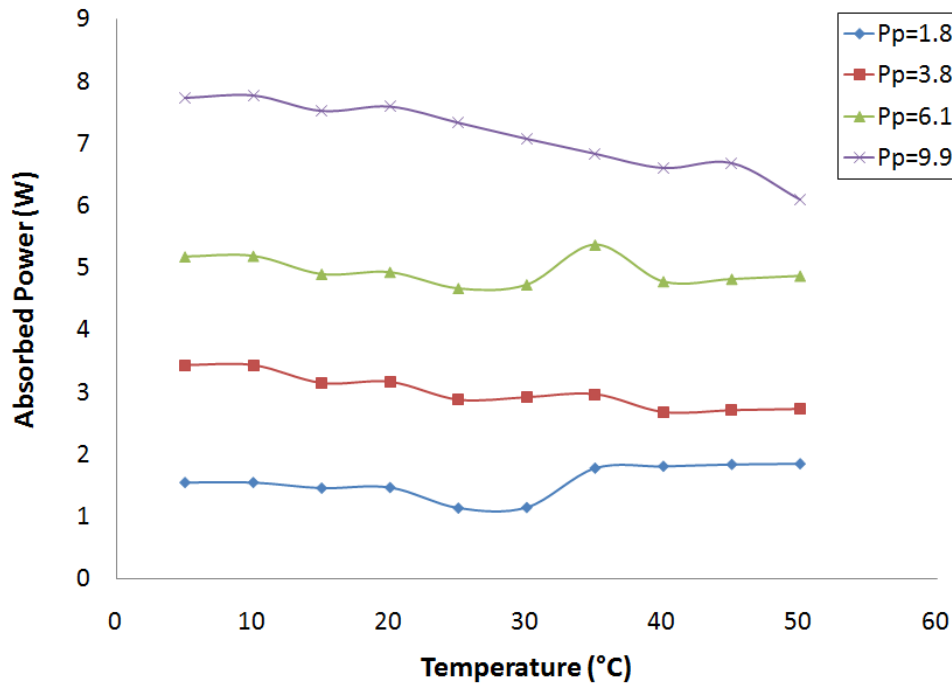
Figure 4-32: Absorbed power variation across the temperature range.

These variations are captured in Equation (4.2.1), in which the changes in wavelength variation are reduced by the absorbed power.

$$R_{th} = \frac{dT}{dP} = \left(\frac{dT}{d\lambda}\right)\left(\frac{d\lambda}{dP}\right)$$ (4.2.1)

The results using this equation show a thermal resistance R_{th} = 8.7 K/W.

A simulation of this type of device was performed using COMSOL Multiphysics[TM] software, using the conditions set out as part of the experimental design having a front pumped SDL with a diamond heatspreader. The results using a pump spot radius w_p = 40 μm, are shown in Figure 4-33.

136

Max:84.089

Radial Distance of Device (mm)
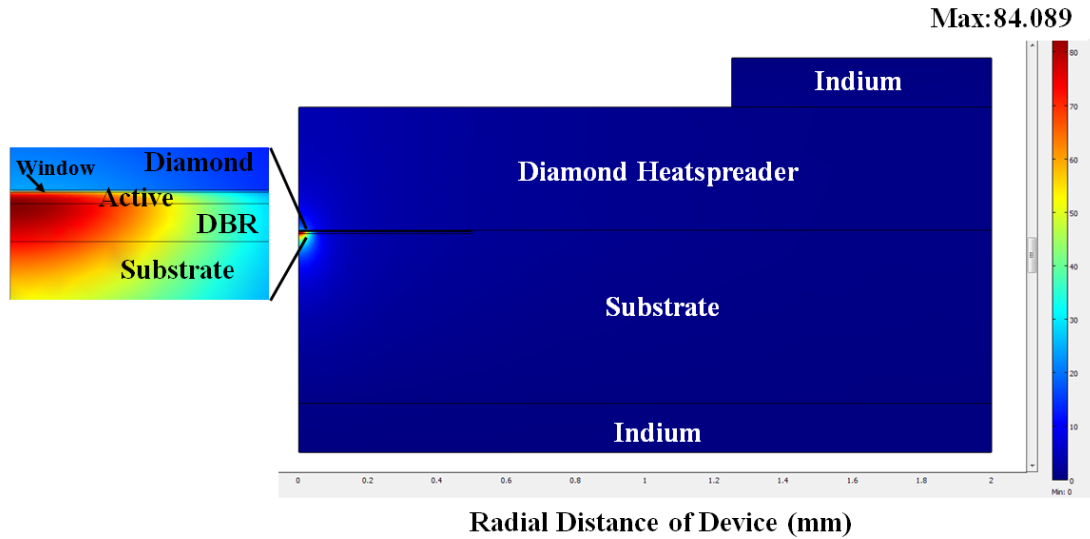
Figure 4-33: COMSOL Multiphysics^{TM} simulation results of the GaInNAs SDL, indicating a maximum temperature of 84.089°C.

The pump power in this simulation was 5W, and the average thermal resistance was calculated using Equation (4.2.2) [23].

$$R_{th\ ave} = \frac{\iiint_{V_a}(T(r,z)-T_{substrate})(P_p(r)dV}{\iiint_{V_a}P_p(r)dV} \qquad (4.2.2)$$

The result for the average thermal resistance was 9 K/W, and is in good agreement with the experimental data taking into account the accuracy of pump spot size onto the sample.

4.5 Conclusions

The characterisation and performance evaluations regarding GaInNAs SDL devices have been presented in this chapter. The results for GaInNAs/GaAs SDLs have achieved output powers > 2.5W, with a maximum slope efficiency of η_{diff} ~16% operating at room temperature (*T≈300K*). The beam quality with an M^2 < 2, demonstrates that these devices can attain near diffraction limited output beams. In a wider context, the spectral coverage of these SDLs extends from ~1170 nm up to ~1340 nm, which demonstrates their usefulness for a wide variety of applications. In the following chapter SDLs shall be applied as pump sources for a Tm-doped glass laser and in Raman amplification.

Implementations of the experimental techniques were carried out to measure the thermal resistance of the 1190 nm SDL. The result of 8.7 K/W was compared with that from simulation of ~9 K/W, in which the discrepancy was accounted for by the accuracy of beam size determinations.

References

[1]   W. J. Fan, S. T. Ng, S. F. Yoon, M. F. Li and T. C. Chong, "Effects of tensile strain in barrier on optical gain spectra of GaInNAs/GaAsN quantum wells," *Journal of Applied Physics,* vol. 93, pp. 5836-5838, (2003).

[2]   H. D. Sun, M. Hetterich, M. D. Dawson, A. Y. Egorov, D. Bernklau and H. Riechert, "Optical investigations of GaInNAs/GaAs multi-quantum wells with low nitrogen content," *Journal of Applied Physics,* vol. 92, pp. 1380 - 1385, (2002).

[3]   Y. P. Varshni, "Temperature dependence of the energy gap in semiconductors," *Physica,* vol. 34, pp. 149-154, (1967).

[4]   S. Giet, "Grating-controlled Infra-Red Vertical External Cavity Surface Emitting Lasers," PhD Thesis, Department of Physics, University of Strathclyde, Glasgow, (2008).

[5]   T. Y. Fan, A. Sanchez and W. E. DeFeo, "Scalable, end-pumped, diode-laser-pumped laser," *Optics Letters,* vol. 14, pp. 1057-1059, (1989).

[6]   T. Y. Fan and W. E. DeFeo, "Power Scaling of End-Pumped Lasers by Geometric Multiplexing," in *Advanced Solid State Lasers*, Salt Lake City, UT, USA, p. DPL10, (1990).

[7]   B. E. A. Saleh and M. C. Teich, "Matrix Optics", Chapter 1, pp. 1-39 in *Fundamentals of Photonics*, Second edition New York: John Wiley & Sons, (1991).

[8]   L. E. Hunziker, C. Ihli and D. S. Steingrube, "Miniaturization and Power Scaling of Fundamental Mode Optically Pumped Semiconductor Lasers," *IEEE Journal of Selected Topics in Quantum Electronics,* vol. 13, pp. 610-618, (2007).

[9]   M. Kuznetsov, "VECSEL Semiconductor Lasers: A Path to High-Power, Quality Beam and UV to IR Wavelength by Design", Chapter 1, pp. 1-71, O. G. Okhotnikov, Editor, *Semiconductor Disk Lasers Physics and Technology*. Wiley-VCH, (2010).

[10]   S. Calvez, J. E. Hastie, A. J. Kemp, N. Laurand and M. D. Dawson, "Thermal Management, Structure Design, and Integration Considerations for VECSELs," Chapter 2, pp. 73-117 in *Semiconductor Disk Lasers: Physics and Technology*, O. G. OKhotnikov, Editor, Wiley-VCH (2010).

[11]   S. L. Vetter, J. E. Hastie, V. M. Korpijarvi, J. Puustinen, M. Guina, O. Okhotnikov, S. Calvez and M. D. Dawson, "Short-wavelength GaInNAs/GaAs semiconductor disk lasers," *Electronics Letters,* vol. 44, pp. 1069-1070, (2008).

[12]   A. E. Siegman, "How to (Maybe) Measure Laser Beam Quality," Stanford University Tutorial, p. MQ1, (1998).

[13] W. Koechner, *Solid-State Laser Engineering*, 6th edition: Springer, (2006).

[14] D. R. Preuss and J. L. Gole, "Three-stage birefringent filter tuning smoothly over the visible region: theoretical treatment and experimental design," *Applied Optics,* vol. 19, pp. 702-710, (1980).

[15] S. Zhu, "Birefringent filter with tilted optic axis for tuning dye lasers: theory and design," *Applied Optics,* vol. 29, pp. 410-415, (1990).

[16] A. J. Maclean, A. J. Kemp, S. Calvez, S., J.-Y. Kim, T. Kim, M. D. Dawson and D. Burns, "Continuous Tuning and Efficient Intracavity Second-Harmonic Generation in a Semiconductor Disk Laser With an Intracavity Diamond Heatspreader," *IEEE Journal of Quantum Electronics,* vol. 44, pp. 216-225, (2008).

[17] C. A. Denman, P. D. Hillman, G. T. Moore, J. D. Drummond and J. M. Telle, "Continuous-wave sodium guidestar laser systems," in *Conference on Lasers and Electro-Optics, (CLEO).* p. 1 vol.1, (2004).

[18] A. Nevsky, U. Bressel, I. Ernsting, C. Eisele, M. Okhapkin, S. Schiller, A. Gubenko, D. Livshits, S. Mikhrin, I. Krestnikov and A. Kovsh, "A narrow-line-width external cavity quantum dot laser for high-resolution spectroscopy in the near-infrared and yellow spectral ranges," *Applied Physics B: Lasers and Optics,* vol. 92, pp. 501-507, (2008).

[19] J. J. Kelly, C. H. Barlow, T. M. Jinguji and J. B. Callis, "Prediction of gasoline octane numbers from near-infrared spectral features in the range 660-1215 nm," *Analytical Chemistry,* vol. 61, pp. 313-320, (1989).

[20] T. Jing, J. M. Evans, V. Petricevic, H. Ping-Pei and R. R. Alfano, "Tissue welding using near-infrared forsterite and cunyite tunable lasers," *IEEE Journal of Selected Topics in Quantum Electronics,* vol. 5, pp. 1103-1106, (1999).

[21] S. Young-Seok, Y. Fujimoto and M. Nakatsuka, "Optical amplification in the 1300nm telecommunications window in a Bi-doped silica fiber," in *Conference on Lasers and Electro-Optics, and Quantum Electronics and Laser Science Conference. CLEO/QELS*, pp. 1-2, (2006).

[22] H. A. MacLeod, *Thin-film Optical Filters*, Third edition Bristol and Philadelphia: Institute of Physics Publishing, (2001).

[23] S. Giet, A. J. Kemp, D. Burns, S. Calvez, M. D. Dawson, S. Suomalainen, A. Harkonen, M. Guina, O. Okhotnikov and M. Pessa, "Comparison of thermal management techniques for semiconductor disk lasers," *Proceedings of the SPIE Solid State Lasers XVII: Technology and Devices,* vol. 6871, pp. 687115-687115-10, (2008).

Chapter 5

Semiconductor Disk Laser Applied as a Pump Source

5.1 Introduction

The high optical power and good beam quality capability of SDL devices provides an attractive alternative in applications typically using bulky and expensive solid-state or gas lasers [1, 2]. In the present chapter the SDL shall be used as a pump source in two distinct material systems. The first involves bulk rare earth doped dielectrics, in the form of tellurite optical glasses and tungstate crystal material. These have been singly doped with thulium (Tm^{3+}) or co-doped with thulium and holmium (Tm^{3+},Ho^{3+}) providing laser emission wavelengths at ~2 μm. The second uses a single-mode silica fibre to produce Raman amplification in the region of 1.3 μm, an important wavelength for optical telecommunications networks.

5.2 Tm^{3+}(,Ho^{3+})-(co)doped Laser Systems

The demand for lasers operating with ~2 μm emission spans a wide range of disciplines. In the field of medicine, the water molecule experiences high absorption at that wavelength which has enabled lasers to be successfully applied in laser surgery [3-5]. Light Detection and Ranging (LIDAR) which is a remote sensing technology, has been used to monitor and detect trace gasses in the atmosphere [6]. NASA has a particular interest in 2 μm lasers for differential absorption LIDAR (DIAL) in the measurement of CO_2 concentrations in the atmosphere and wind velocities [7]. For free space optical communication networks, the useful eye safe wavelength of 2 μm has been used to broadcast across distances over 8 km using a pulsed laser [8]. Finally, material processing applications in the form of producing High Spatial Frequency Ripples (HSFR) on GaAs semiconductor material has been

demonstrated, with the long term goal of applying this to directional biological cell growth on laminar surfaces and for surface structuring of photovoltaic devices [9].

The supply of 2 μm lasers has generally been dominated by Tm-doped and Tm,Ho–co-doped dielectrics [10] including the recent development of a Tm-doped tellurite microsphere laser [11]. However, the European funded project *VERTIGO* (Versatile Two Micron Light Source) [12] has expanded the portfolio of 2 μm lasers to include GaSb-based optically pumped SDLs using a GaInAsSb/AlGaAsSb gain material system [13-16]. The highest output powers achieved have been ~5W in CW operation, cooled to -15°C [17] with the most recent results reporting a 200 kHz laser linewidth and 118 nm tuning range at 200mW CW output power [16].

The experimental work presented in this thesis has been performed in close collaboration with Professor Wilson Sibbett's group at St Andrews University, and in particular Dr. Flavio Fusari. Supply of their bulk materials; Tm^{3+}-doped and Tm^{3+},Ho^{3+}-co-doped tellurite glasses along with a Tm^{3+},Ho^{3+}-co-doped potassium yttrium tungstate ($Tm^{3+},Ho^{3+}:KY(WO_3)_4$) crystal has enabled the first demonstration of ~2 μm laser systems pumped by an SDL.

The optical glasses were produced at the University of Leeds, under the guidance of Professor Animesh Jha at the Institute of Material Research. The spectroscopic properties and laser development of KYW crystal has been previously reported for Tm^{3+}-doped [18] and Tm^{3+},Ho^{3+}-co-doped [19] laser systems.

5.2.1 Material Properties and Previous Results

Tellurium oxide, *TeO₂* optical glasses used throughout these experiments have been chosen due to their proven record in successful IR laser generation. They have exhibited low phonon energies [20] with a much improved solubility of the rare-earth dopants compared with other glasses such as silica and germanium [21]. There were two bulk glass samples that were used, having molar % compositions 75 TeO_2–10 ZnO–10 Na_2O-5 GeO_2 (TZNG) doped with 2wt% Tm_2O_3 and 80 TeO_2–10 ZnO–10 Na_2O (TZN) doped with 2wt% Tm_2O_3 and 0.2wt% Ho_2O_3. A more rigorous analysis

into the production of these glasses can be found by consulting the PhD thesis of F. Fusari [22]. The Tm^{3+},Ho^{3+}:KYW crystal material was grown using the *flux growth technique* in which the crystal materials were grown from flux in a platinum crucible using $K_2W_2O_7$ as the solvent [19]. The doping levels in the crystal were 0.014 wt% (*5 at.%*) Tm_2O_3 and 0.0011 wt% (*0.4 at.%*) Ho_2O_3.

Table 5.1: Summary of Tm(,Ho)-(co)doped laser material parameters.

| Dopants | Concentrations | | Host Material | Length |
	Tm^{3+} (wt%)	Ho^{3+} (wt%)		(All materials were Brewster Cut)
Thulium (Tm^{3+})	2	-	TZNG glass	5 mm
Thulium and Holmium (Tm^{3+},Ho^{3+})	2	0.2	TZN glass	4.5 mm
Thulium and Holmium (Tm^{3+},Ho^{3+})	0.014	0.0011	KYW crystal	1.5 mm

The absorption spectra of these samples have been obtained at the University of Leeds, using a Perkin Elmer Lambda 950 UV/VIS Spectrophotometer. Figure 5-1 shows the absorption coefficient spectrum for singly doped Tm^{3+} material and Figure 5-2 for co-doped Tm^{3+} and Ho^{3+} material.
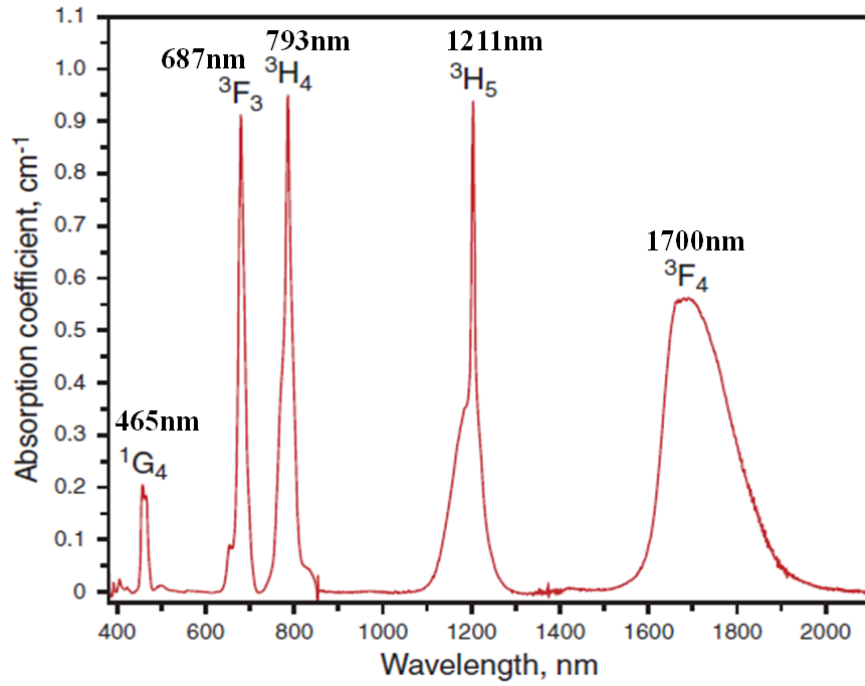
Figure 5-1: Absorption coefficient spectra for the Tm2%wt:TZNG bulk glass sample indicating the energy transitions and respective wavelengths [23].
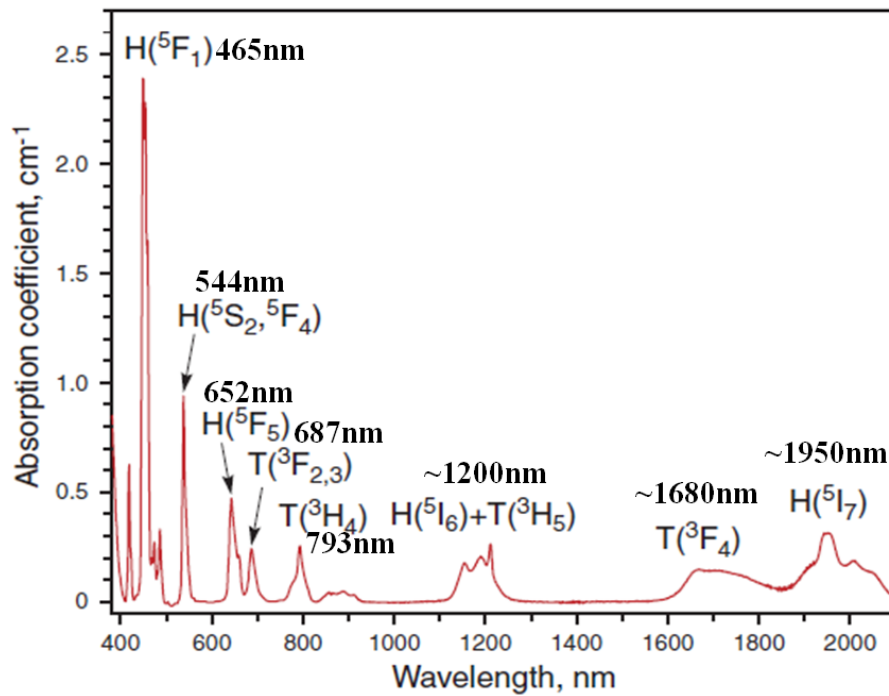
Figure 5-2: Absorption coefficient spectra for the Tm2%wt,Ho0.2%wt:TZN bulk glass sample [23].

The two absorption regions of interest here are 793 nm and ~1200 nm. Examining the energy transitions occurring within the material creates a clearer picture as to the

expected emission wavelengths from the system. These may also aid our understanding of comparable performance between one pumping regime and another, especially in terms of efficiency. Relying upon detailed spectroscopic studies made by Fusari *et al.* [24], Lagatsky *et al.* [19] and Richards *et al.* [23] using these material systems, allows us to infer the ~1200 nm pumping response predicated by the more widely used ~800 nm pumping regime.

In order to depict the complex nature of the energy transitions, energy level diagrams shall be used based upon those originally developed by G. H. Dieke [25]. Through the process of optical pumping, energy is transferred to the active ions through *ground state absorption* (GSA) and *excited state absorption* (ESA), the latter considered a parasitic process. Energy is then redistributed within the material producing energy transitions, with promotion to higher states and relaxation to lower energy levels. The presence of other ions gives an added complexity to the system, allowing energy to be transferred to neighbouring ions in *donor* and *acceptor* roles.

Turning our attention initially to GSA of $^3H_6 \rightarrow {}^3H_4$ 793 nm pumping, Figure 5-3 illustrates the transitions taking place within a singly-doped Tm^{3+} sample, such as the TZNG glass sample used in these experiments. The population of the $^3H_4$ energy level facilitates a process known as *upconversion* (UC), in which the relaxation $^3H_4 \rightarrow {}^3H_6$ transfers energy, enabling the $^1G_4$ energy level to be populated. As a consequence weak 480 nm fluorescence has been observed, through transition $^1G_4 \rightarrow {}^3H_6$ in the material, a demonstration of this blue 'glow' within the glass is shown in Figure 5-6. Another aspect to the ~800 nm pumping is the Cross Relaxation (CR), which takes place when the relaxation from $^3H_4$ serves to populate the $^3F_4$ lasing level whilst promoting a neighbouring Tm^{3+} ion (acceptor) transition from the ground state $^3H_6 \rightarrow {}^3F_4$. This process results in a 200% quantum efficiency [23], with output centred ~1800 nm.
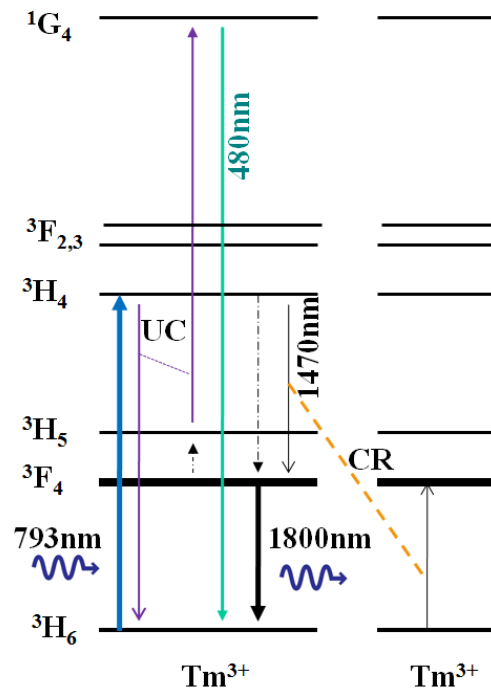
Figure 5-3: Tm³⁺ energy transitions from a 793 nm excitation source, with upconversion (UC) processes (*purple*), nonradiative decay (*black dashed*), cross-relaxation (CR) (*orange dashed*) and emission transitions of 480 nm, 1470 nm and 1800 nm.

The Tm^{3+}, Ho^{3+} co-doped materials, in the form of the TZN glass and KYW crystal, forms a more complex energy transition network in which the Tm^{3+} acts as a donor with the Ho^{3+} as acceptor. The energy transitions present through 793 nm pumping are illustrated in Figure 5-4. The many energy transfers (ET) and UC processes between the two ions serve to populate higher energy levels in Ho^{3+}. The UC from transition $^3H_4 \rightarrow {}^3H_6$ in Tm^{3+} enables ESA $^5I_6 \rightarrow {}^5F_3$ in Ho^{3+} to produce green ~550 nm fluorescence in the material, with ET processes populating the $^5I_7$ lasing level in Ho^{3+} allowing 1950 nm radiative emission.
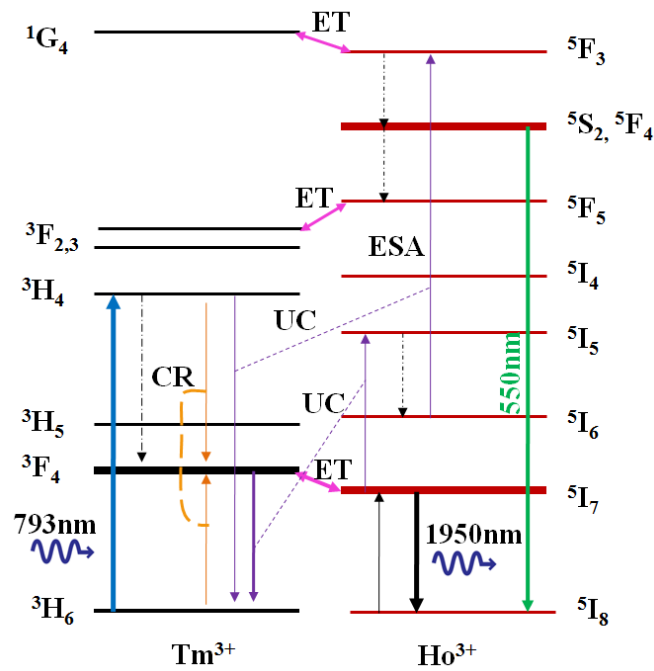
Figure 5-4: Tm³⁺ and Ho³⁺ energy transitions from a 793 nm excitation source, with cross-relaxation (CR) (*orange lines*), energy transfers (ET) between Tm³⁺ and Ho³⁺ (*pink arrows*), upconversion (UC) and excited-state absorption (ESA) (*purple lines*), nonradiative decay (*black dashed*) and emission transitions 550 nm and 1950 nm.

Previous results using a Ti:Sapphire laser as the pump source have been reported for the same tellurite glasses and tungstate crystal material used in the experimental work presented in this chapter. Table 5.2 results indicate the capability of these material systems, and shall be used as a comparison with the SDL ~1200 nm pumping results presented in Section 5.2.3.

Table 5.2: Results of ~800 nm pumped Tm³⁺-doped TZNG glass, Tm³⁺,Ho³⁺-codoped TZN glass, and Tm³⁺,Ho³⁺-codoped KYW crystal.

Laser System	Output Power (mW)	Central Wavelength (nm)	Optimum Output Coupler (%)	Slope Efficiency η (%)	Wavelength Tuning Range, $\Delta\lambda_{FWHM}$ (nm)	Reference
Tm³⁺:TZNG Glass (Tm 2 wt%)	124	1960	6.1	28.4	135	[24]
Tm³⁺,Ho³⁺:TZN Glass (Tm 2 wt%,Ho 0.2 wt%)	25	2020	0.8	9.5	80	[26]
Tm³⁺,Ho³⁺:KYW Crystal (Tm 5 at.%, Ho 0.4 at.%)	460	2056	1	44	190	[19]

In the case of the $^3H_6 \rightarrow {}^3H_5$ pumping scheme provided by the ~1200 nm SDL, the energy level transitions for Tm^{3+} are illustrated in Figure 5-5. Notably there is no ion-ion interaction taking place in this scenario, with ESA processes enabling fluorescence at ~480 nm in the material. With the upper state lifetime in $^3H_5$ found to be ~300 μs compared with 1.3 ms in the $^3F_4$ lasing level [26], laser emission ~1800 nm occurs through $^3F_4 \rightarrow {}^3H_6$.
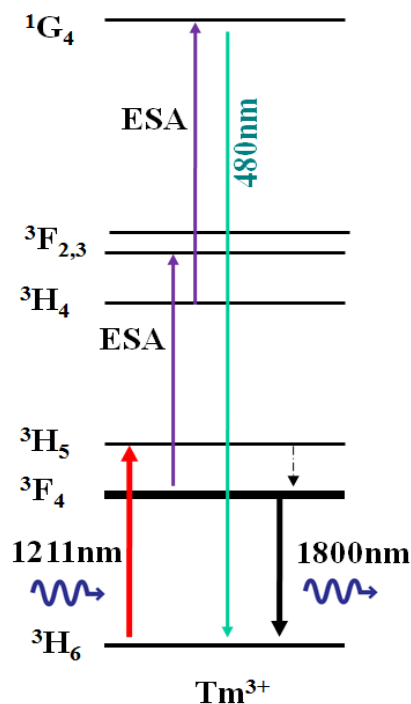
Figure 5-5: Tm^{3+} energy transitions using a 1211 nm excitation source, with excited-state absorption (ESA) (*purple lines*), and emission transitions of 480 nm and ~1800 nm.

The observance of blue fluorescence at ~450 nm as a result of UC, is shown in Figure 5-6 during ~1211 nm SDL pumping.
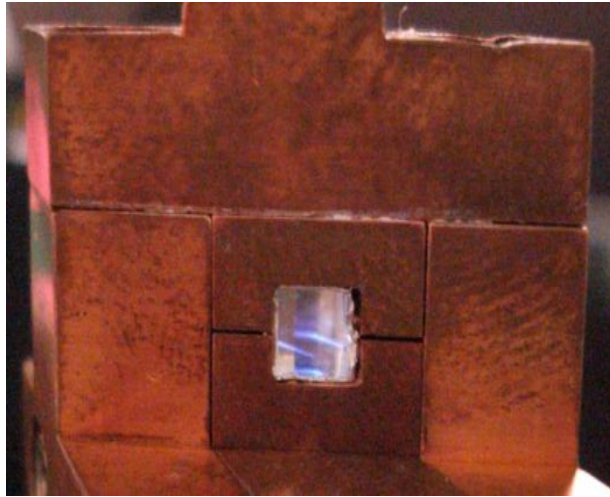
Figure 5-6: Tm³⁺:TZNG glass sample in a brass mount, with visible blue fluorescence due to upconversion along the incident pump radiation within the glass.

This scheme aims to promote more efficient lasing with an aim to reduce ESA by more closely targeting the 1200 nm absorption region of the material, in comparison to alternatively used ~1060 nm pumping, as referenced in Table 5.3. It may not achieve the same quantum efficiency expected with ~800 nm excitation; however it has the potential of a more simplistic and compact system, using the semiconductor thin disk approach.

Finally, the energy transitions for Tm^{3+} and Ho^{3+} codoped material pumped by ~1200 nm are illustrated in Figure 5-7. Similar to the singly doped Tm^{3+} material, ESA processes are present in both Tm^{3+} and Ho^{3+} enabling energy transitions to populate the Ho^{3+} $^5F_3$ level with consequential 550 nm fluorescence. More importantly the energy transfers from $^3F_4$ (Tm^{3+}) to the lasing level $^5I_7$ (Ho^{3+}) facilitates radiative emission at ~1950 nm.
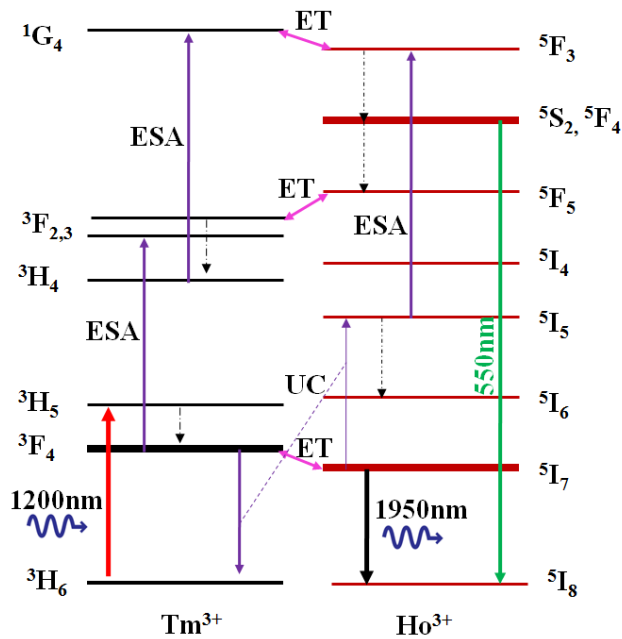
Figure 5-7: Tm³⁺ and Ho³⁺ energy transitions using a 1200 nm pumping scheme, with excited-state absorption (ESA) and upconversion (UC) processes (*purple*), energy transfers (ET) between Tm³⁺ and Ho³⁺ (*pink arrows*), nonradiative decay (*black dashed*), and emission transitions 550 nm and 1950 nm.

Scarce pump resources available to target the ~1200 nm absorption region in the material, presents a solution in the form of SDL devices with their flexible design and wavelength tunability. Table 5.3 provides a list of previous pump sources aimed at transitions into the $^3H_5$ level.

To date ~1200 nm pump sources have mainly used cascaded Raman fibre lasers as a means to generate laser emission at this wavelength. Three cascading fibre systems were used to ultimately produce the required ~2 μm laser output. In both examples given, ytterbium (Yb) doped fibre lasers are used to pump the silica-based fibres, exploiting the stimulated Raman scattering in the material. In this way a suitable stokes shifted frequency can serve as the output to pump the Tm(,Ho)-doped silica fibre laser. The available pump power had been up to 20W capability through use of a one-stage phosphosilicate-based Raman fibre at 1231 nm. The advantage to this method is the integration of an all-fibre based system. However, in the case of Tm(,Ho)-(co)doped bulk lasers, the Raman fibre laser would not provide the same

level of effectiveness, requiring efficient coupling out from the fibre laser and into the bulk material.

When pumping in the ~1200 nm regime, an area of most concern is that of ESA losses. However upconversion lasers exploit this process, which is considered detrimental to ~2 μm lasers, to produce lasers with blue emission based on transitions $^1G_4 \rightarrow ^3H_6$ in Tm-doped materials. Examples are given in Table 5.3, including the use of a Nd^{3+}:YAG laser as the pump source providing emission at 1123 nm, by implementing dichroic mirrors to suppress the 1064 nm laser line thereby targeting the upconversion in a blue Tm^{3+}:ZBLAN (ZrF_4-BaF_2-LaF_3-AlF_3-NaF) fibre laser.

The next closest alternative to 1200 nm has been to use more readily available ~1060 nm sources. An interesting array of methods has been employed, mainly involving dual pumping regimes such as 1064 nm with 795 nm or 645 nm. These systems are not targeting ~2 μm emission but aim for transitions at ~800 nm and 455 nm in the material, similarly in the case of 1123 nm pumping. For example, Brunet *et al.* [27] has capitalised on 455 nm laser emission using a Tm^{3+}:ZBLAN fibre laser, with dual pumping at 1064 nm and 645 nm. However, 1060 nm is in the tail absorption profile of the gain medium which may be acceptable for Tm^{3+}-doped fibres but may not be appropriate for bulk materials. Included amongst the 1060 nm pumping examples is a theoretical model, indicating the capability of 1060 nm pumping using an aluminosilicate fibre as the host to the thulium dopant, to increase the quantum efficiency of the system.

Finally, the 1050 nm diode laser examples provide by Jackson *et al.* [28] have been promising, with outputs measured at 1.74W with a slope efficiency of 51% for unidirectional pumping in the fibre, scaling to 4.77W when both fibre ends are pumped. In this system, as with those using 1060 nm and 1123 nm pump wavelengths, highlight the motivation to reduce ESA through the pursuit of ~1200 nm pump sources.

Table 5.3: Synopsis of previous pumping schemes of Tm^{3+}-doped and Tm^{3+},Ho^{3+}-codoped laser systems

Pump Scheme	Laser System	Results	Comments	Reference
~1200 nm Pumping				
Raman Fibre Laser: 1064 nm Yb-doped fibre laser 8.4 W CW pumping a 1km SMF with 3 cascading cavities using Fibre Bragg Gratings with reflectivity at the 1st stoke (1120 nm), 2nd stoke (1180 nm) and 3rd stoke (1212 nm) (output coupler 15% at 1212 nm).	Tm^{3+},Ho^{3+}-codoped silica fibre laser	Using 270cm long silica fibre, achieved P$_{out}$ =450 mW at 1970 nm, η_{slope}=31%, $\eta_{opt-opt}$=18%, Threshold P$_p$=1.12W	• Dopant levels were 9000 ppm wt Tm^{3+} ions and 1500 ppm wt Ho^{3+} ions • used fusion splicing to minimize losses • report negligible ESA using this pump scheme	[29]
Raman Fibre Laser: 1058 nm Yb-doped fibre laser 32W CW pumping a one-stage Raman phosphosilicate fibre of 50m length using built-in Fibre Bragg Gratings with reflectivity at the 1st stoke (1058 nm), 2nd stoke (1231 nm) and 3rd stoke (1956 nm) (output coupler at 1231 nm)	Tm^{3+}-doped aluminosilicate fibre laser	Using 50m length aluminosilicate fibre, P$_{out}$=7W at 1956 nm with 56% quantum efficiency with up to 20W 1231 nm pumping	• Dopants of silica fibre 4wt% Al$_2$O$_3$, 1.5wt% GeO$_2$, and 0.8wt% Tm$_2$O$_3$, • Achieved single mode output of 7W at 1956 nm • pumping using shorter wavelengths <1200nm in this absorption band ^{3}H$_5$, ESA prevents efficient lasing.	[30, 31]
~1123 nm Pumping				
Nd^{3+}:YAG pumped by 7-W 807 nm diode bar, dichroic mirrors used to suppress 1064 nm lasing, gain medium length 10 mm, up to 1.6W at 1123 nm achieved.	Tm^{3+}-doped fluorozirconate (ZBLAN) fibre laser	Targeting blue upconversion emission, using 2.2 m long ZBLAN fibre, P$_{out}$=~230mW at 481 nm, η_{slope}=18.5% (at 120mW output)	• Doping level was 1000 ppm Tm^{3+} ions, • Diode pump beam M^2~20,40 requiring beamshaper for input to Nd^{3+}:YAG, • Suppression of 1064nm, ~15 times higher than 1123 nm.	[32, 33]

Pump Scheme	Laser System	Results	Comments	Reference
~1060 nm Pumping				
Theoretical Modeling: 1060 nm pumping regime	Tm^{3+}-doped Silica-based alumina-doped Fibre Lasers	Targeting 810 nm emission of the $^3H_6 \rightarrow {}^3H_4$ transition, predicted P_{out}=2W using 5W 1060 nm pump, with >30nm tunability	• Disadvantages of fluoride fibres include low pump power damage threshold, hygroscopicity and difficulties with fabrication, • Alumina co-dopant provides a 4 times increased quantum efficiency compared to pure silica host	[34]
Dual Pumped: 1064 nm Nd:YAG laser + 795 nm Ti:Sapphire	Tm^{3+}-doped Tellurite single-mode fibre laser	7dB gain with gain slope of 1064 nm ~0.17 dB/mW	• Tellurite fibre preferred over fluorides due to extended gain to longer wavelengths (~1520nm) • Using 1064 nm pump, some ions removed from $^3F_4$ level, and signal ESA is reduced	[35]
Dual Pumped: 1064 nm + 645 nm	Tm^{3+}-doped ZBLAN fibre laser	Targeting 455 nm output, achieving P_{out} ~3 mW launching 104 mW 1064 nm and ~300 mW 645 nm.	• Dopant level was 1000 ppm Tm^{3+} ions • Transition $^1D_2 \rightarrow {}^3H_4$ provides 455 nm emission • 455 nm Pout and threshold strongly depend on 1064 nm pump power	[27]

Pump Scheme	Laser System	Results	Comments	Reference
~1050 nm Pumping				
Diode Lasers: 1050 nm pump source consisting of InGaAs QWs, with GaAs waveguides and AlGaAs cladding layers with TE polarisation	Tm^{3+}-doped Silica fibre laser	Using 3.3m length silica fibre, with unidirectional pumping achieved P_{out}=1.74W at 2.03 μm and η_{slope}=51%, scaling to P_{out}=4.77W with bi-directional pumping	• Doping level was 3 wt% Tm^{3+} ions, • High concentration of Tm^{3+} allows CR process to redirect excitation back to upper lasing level thereby limiting additional pump ESA losses.	[28]

Theoretical evaluations performed by Jackson *et al.* [36] based on Tm^{3+}-doped silica fibre lasers, have made direct comparisons between an ~800 nm pumping regime and that of ~1200 nm. Figure 5-8 (b) indicates improved slope efficiencies of ~55% using ~1200 nm pump wavelengths in comparison to the curves in (a) showing ~38% with ~790 nm pumping. This stark contrast has raised expectations for the provision of 1200 nm SDL pumping.
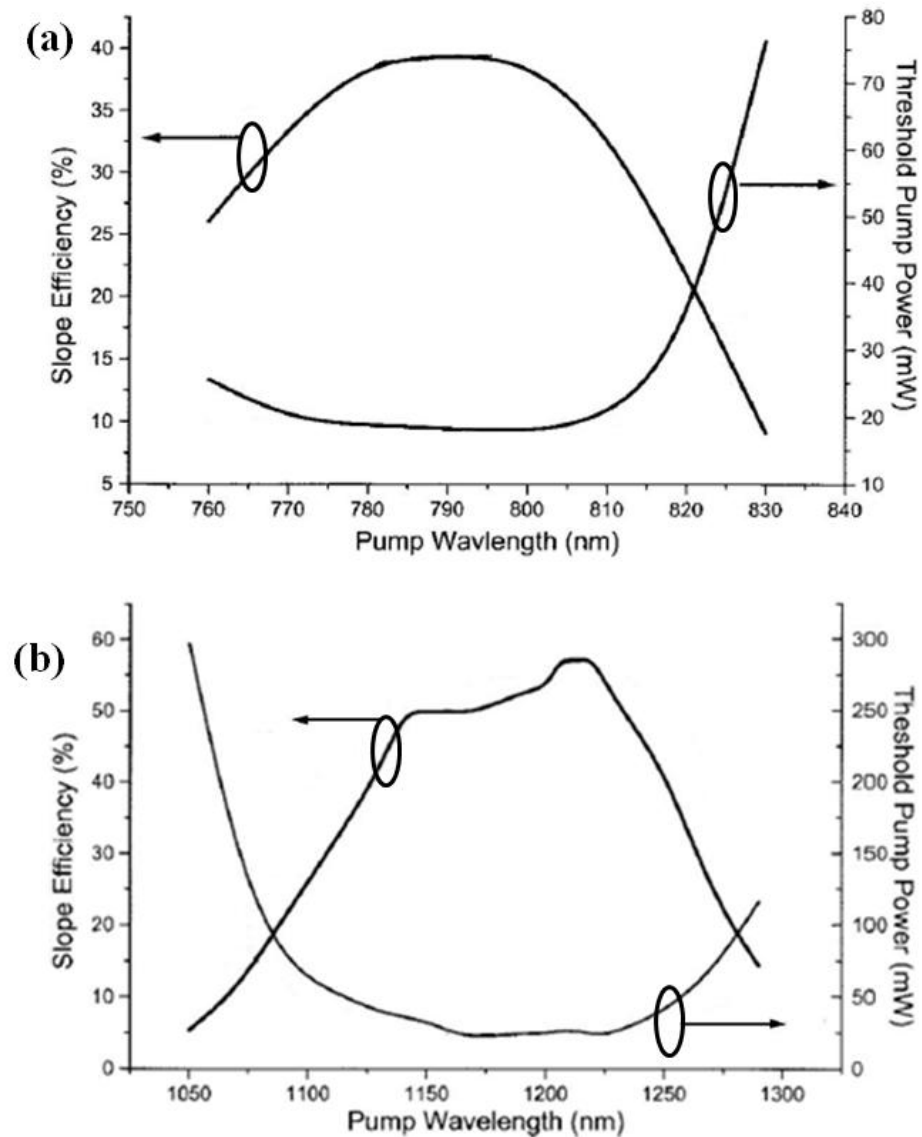
Figure 5-8: Calculated results for Tm^{3+}-doped silica fibres, showing the estimated slope efficiency and threshold pump power for (a) $^3F_4$ absorption band pumping and (b) $^3H_5$ absorption band pumping [36].

154

5.2.2 SDL Requirements for Use as a Pump Source

In order to fulfil its role as an excitation source for the Tm-doped and Tm,Ho-codoped laser systems, the SDL must adhere to some operational specifications. Importantly it must target the correct wavelength, be power scalable with good beam quality, maintain operational stability and be reasonably reliable such that the Tm laser system is not disadvantaged by the performance of its pump source. Many of the experimental techniques described in Chapter 4 used to evaluate the performance of the SDL such as wavelength tuning and M^2 measurements, have been used here.

The target power threshold for the Tm glass laser was found to be ~100 mW and ~50 mW for the Tm:KYW crystal laser, based on the previous ~800 nm pumping results [19]. The power transfer curves obtained for sample *AsN2527* the GaInNAs/GaNAs/GaAs 10 QW SDL, are shown in Figure 5-9. The maximum output power achieved was 1.35W, using a 2% power transmission output coupler (OC) and 650 mW with the inclusion of the birefringent filter tuned to ~1212 nm, as shown in Figure 5-10. These have provided a more than adequate level of threshold power for each of the doped dielectric systems.
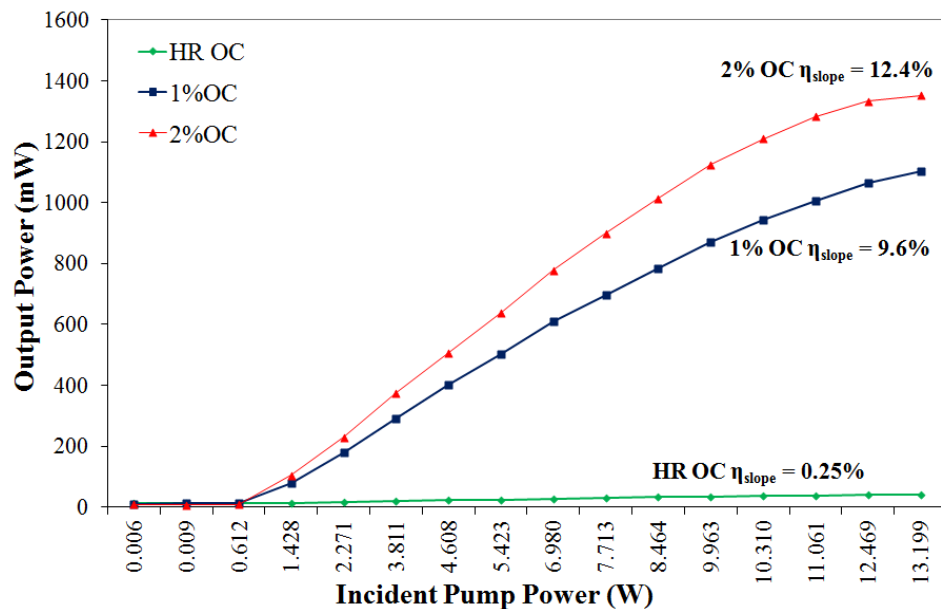
Figure 5-9: Power transfer curves of *AsN2527* 1220 nm SDL with Output Couplers (OC) High Reflectance (HR), 1% and 2% transmissions.

155
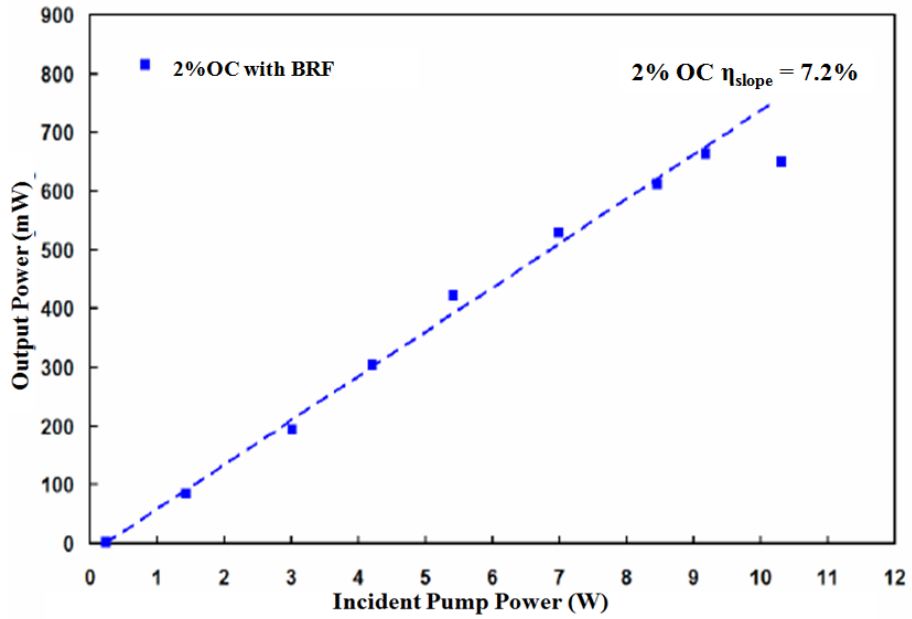
Figure 5-10: Power transfer results of the SDL with an intracavity birefringent filter (BRF), tuned to 1212 nm.

The wavelength coverage of this laser extended across ~23 nm at FWHM, as indicated in Figure 5-11. The provision to target the absorption region of ~1200 nm in the material systems has therefore been achieved.
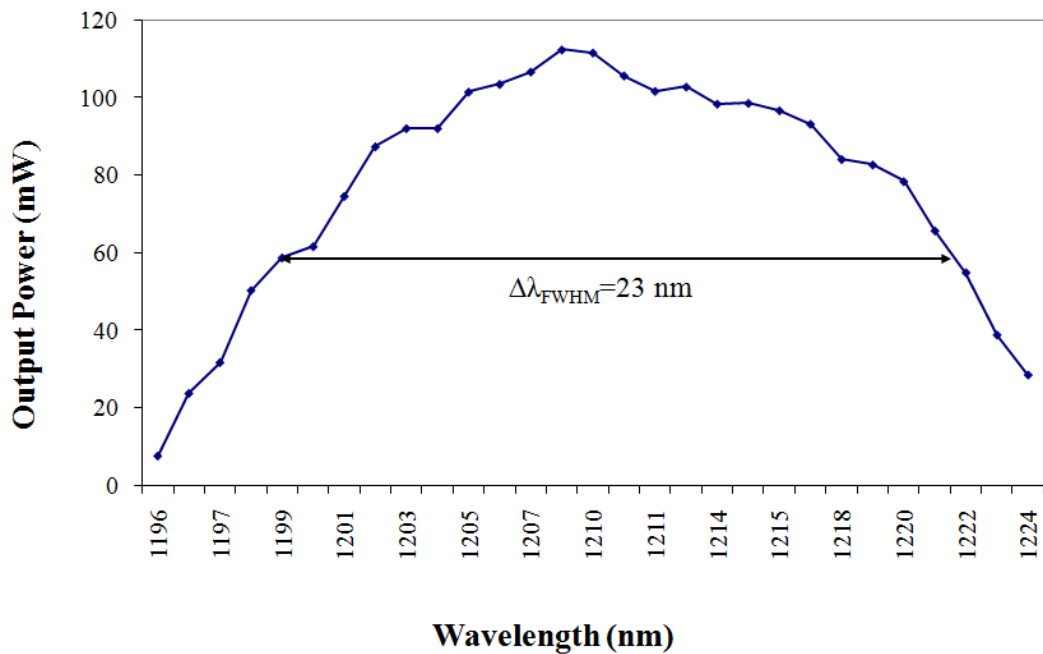
Figure 5-11: Wavelength tuning range for AsN2527 1220 nm SDL.

The M^2 measurement results, obtained using a scanning detector are given in Figure 5-12. An optimal M^2 was required, in order to allow the best performance from the Tm-doped laser system. Unlike the SDL, which may use a beam of low quality from the diode pump and transforms it into a higher quality output beam, the Tm-doped laser requires the best input in order to achieve reasonable gain, additionally a tighter focus into the gain medium.
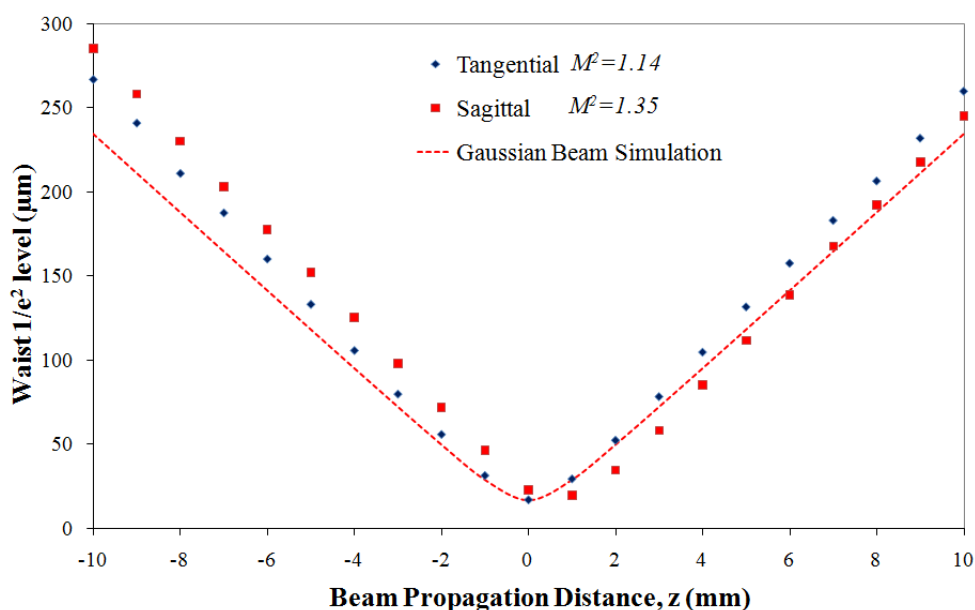
Figure 5-12: M^2 measurements for *AsN2527* 1220 nm SDL with cavity dimensions D1=59 mm and D2=225 mm.

It must be stated that these were optimal M^2 results, obtained during the characterisation of the ~1211 nm SDL pump source. During experimentation, the M^2 had been >2 as a consequence of higher operational output powers, which ultimately impacts upon the ~2 μm laser output.

5.2.3 Experimental Set-up

An illustration of the two V-folded laser cavities is provided in Figure 5-13. The thermal management of the SDL used water cooling, as explained previously in Chapter 3. The Tm(,Ho)-(co)doped glass and crystal samples were wrapped in indium foil and placed in a brass mount especially designed for these samples, and

shown in Figure 5-6. The materials were temperature controlled to ~15°C using a thermo-electric cooler, to optimise laser performance and minimise any opportunity for damage especially to the glass samples as a consequence of the optical pumping. Furthermore a chopper was positioned prior to the Tm(,Ho) laser cavity, indicated in Figure 5-13, to reduce by 50% the maximum power incident onto the glass/crystal. This served to suppress thermal lensing effects and prevent damage, particularly to the glass samples which were prone to cracking due to the high heat loads deposited in the material through optical pumping.
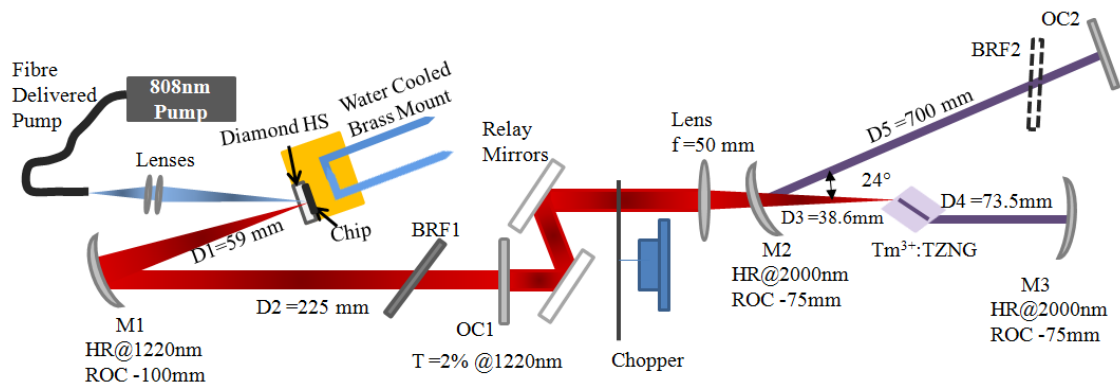
Figure 5-13: Schematic of the SDL pumping of the Tm-doped glass laser, using the Tm^{3+}:TZNG glass sample that was Brewster cut with length 5 mm.

The incident pump power measurements at ~1200 nm were taken immediately after the relay mirrors, incurring cumulative losses of approximately 10%. These mirrors were necessary to enable more control over the alignment of the beam into the Tm-doped gain medium. The recorded incident pump power and power values behind the glass/crystal provided the means to calculate the absorbed power, P_{abs} of the system, thereby allowing the *internal efficiency* of the system to be measured. The experimental set up illustrated in Figure 5-13 includes the Tm^{3+}:TZNG glass sample, however the material was swapped out for the Tm^{3+},Ho^{3+}:TZN glass and Tm^{3+},Ho^{3+}:KYW crystal samples over the course of experimentation with slight adjustments made to the ~2 μm cavity. However, no changes were made to the cavity of the SDL pump source throughout all experiments. It should also be noted that the performance of the SDL remained consistent throughout the period of its required operation, which was in the region of one month, providing a reliable and stable pump source.

5.2.4 Results and Discussion

The power transfer curves for all three laser systems are given in Figure 5-14, using the absorbed power results. There is a clear distinction between the results obtained for the glass lasers compared with those of the crystal, which is consistent with those obtained previously using the ~800 nm pumping regime. Much higher output powers were achieved in the KYW crystal of ~200 mW, as opposed to ~60 mW from the TZNG glass laser. Likewise the slope efficiencies (internal efficiencies) follow suit, with 34.8% obtained for KYW compared with 22.4% for the TZNG glass.
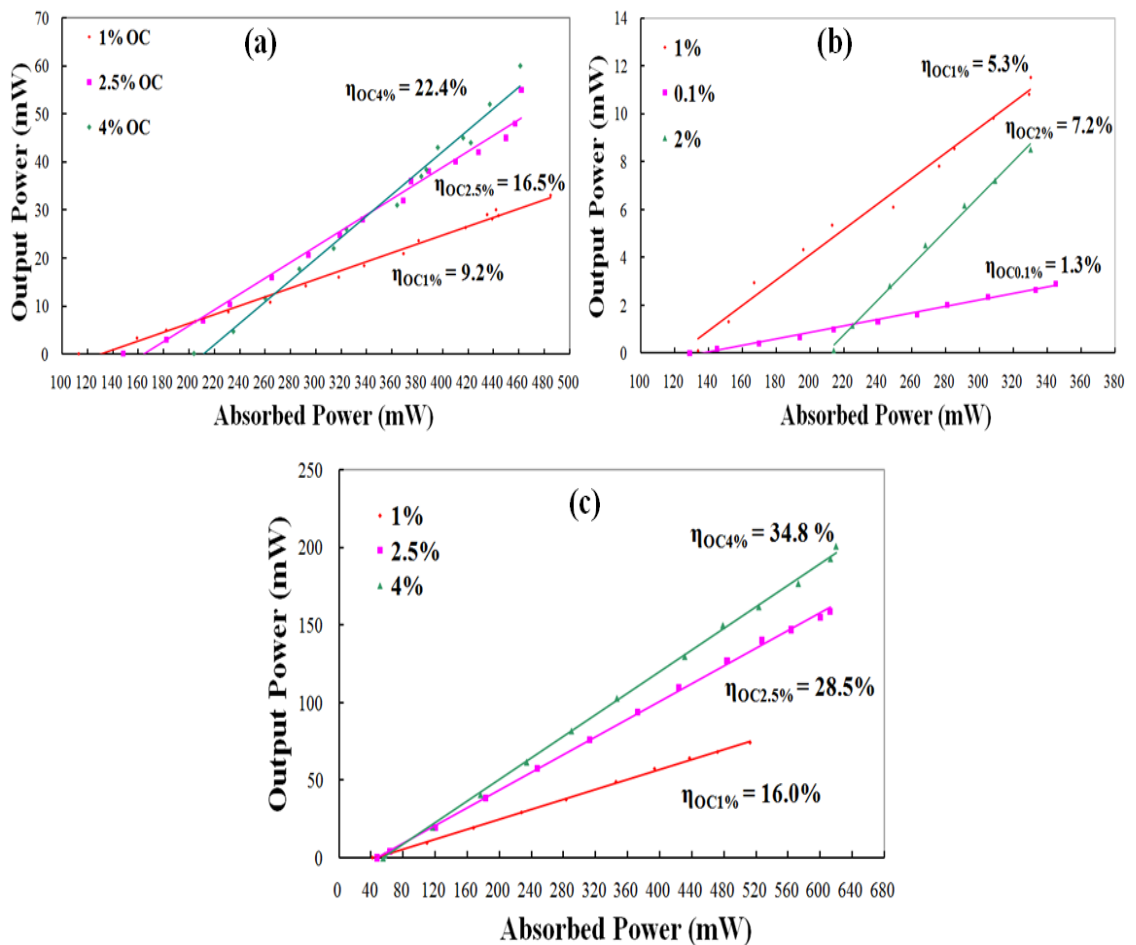
Figure 5-14: ~2 µm output power as a function of absorbed power results for (a) Tm³⁺:TZNG, (b) Tm³⁺,Ho³⁺:TZNG and (c) Tm³⁺,Ho³⁺:KYW.

Table 5.4 summarises the pump power thresholds and slope efficiencies for each of the output coupler transmission powers used in the set of experiments. These values

are of particular interest for the analysis on resonator losses. Major sources of loss in such a cavity include reflection losses at the surfaces of the Brewster cut glass/crystal and at the mirrors, as well as the intracavity birefringent filter *BRF2* (when included).

Table 5.4: Experimental results obtained of the lasing thresholds and slope efficiencies at the respective output coupler (OC) transmissions.

OC Transmission, T_{OC} (%)	Lasing Threshold (mW)	Slope Efficiency, η (%)
Tm^{3+}:TZNG		
1	149	9.2
2.5	198	16.5
4	277	22.4
Tm^{3+},Ho^{3+}:TZN		
0.1	170	1.3
1	186	5.3
2	289	7.2
Tm^{3+},Ho^{3+}:KYW		
1	42	16
2.5	48	28.5
4	57	34.8

Caird analysis [37] was performed on the results, to determine the resonator efficiency and losses for all three doped-dielectric systems. Equation (5.1.1) expresses the slope efficiency η obtained with the corresponding output coupler transmissions T_{OC} from Table 5.4 relating to the maximum possible slope efficiency η_0 and losses *L*.

$$\eta = \eta_0 \frac{T_{OC}}{T_{OC}+L} \tag{5.1.1}$$

Equation (5.1.1) has been re-organised and given in Equation (5.1.2). Plots of $\frac{1}{\eta}$ as a function of $\frac{1}{T_{OC}}$ have been generated and given in Figure 5-14, as a means to evaluate η_0 and *L*, with the best fit linear regression used again here.

$$\frac{1}{\eta} = \frac{1}{\eta_0} + \frac{L}{\eta_0}\left(\frac{1}{T_{OC}}\right) \tag{5.1.2}$$
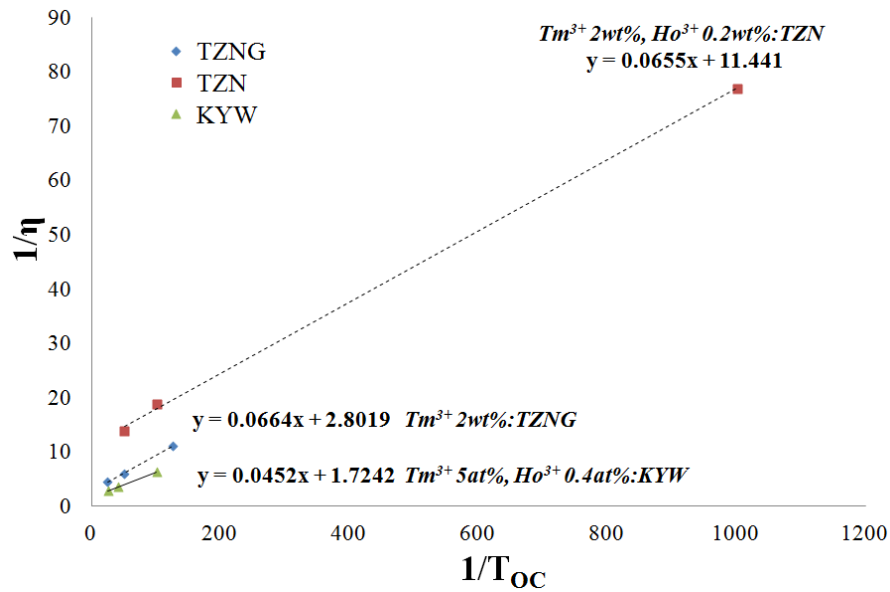
Figure 5-15: Caird analysis using inverse slope efficiencies as a function of the inverse of the output coupler transmission T_{OC}, results for Tm^{3+},Ho^{3+}:TZN, Tm^{3+}:TZNG and Tm^{3+},Ho^{3+}:KYW.

The results generated using the Caird approach have provided losses of 2.4% (TZNG), 0.6% (TZN) and 2.6% (KYW). Based on this analysis, the maximum attainable slope efficiencies were calculated to be 36%, 9% and 58% for TZNG, TZN and KYW respectively.

The insertion of a birefringent filter (BRF2) into the ~2 μm laser cavity, as illustrated in Figure 5-13, enabled wavelength tuning to be carried out for each of the lasers. The results of the tuning curves are shown in Figure 5-16 below, each obtained using a 1% output coupler. A noticeable 'dip' at ~1900 nm was observed in the wavelength tuning range results for the Tm^{3+},Ho^{3+}:KYW crystal laser, which happens to coincide with a decreased absorption cross-section and gain in the material at that wavelength [19].
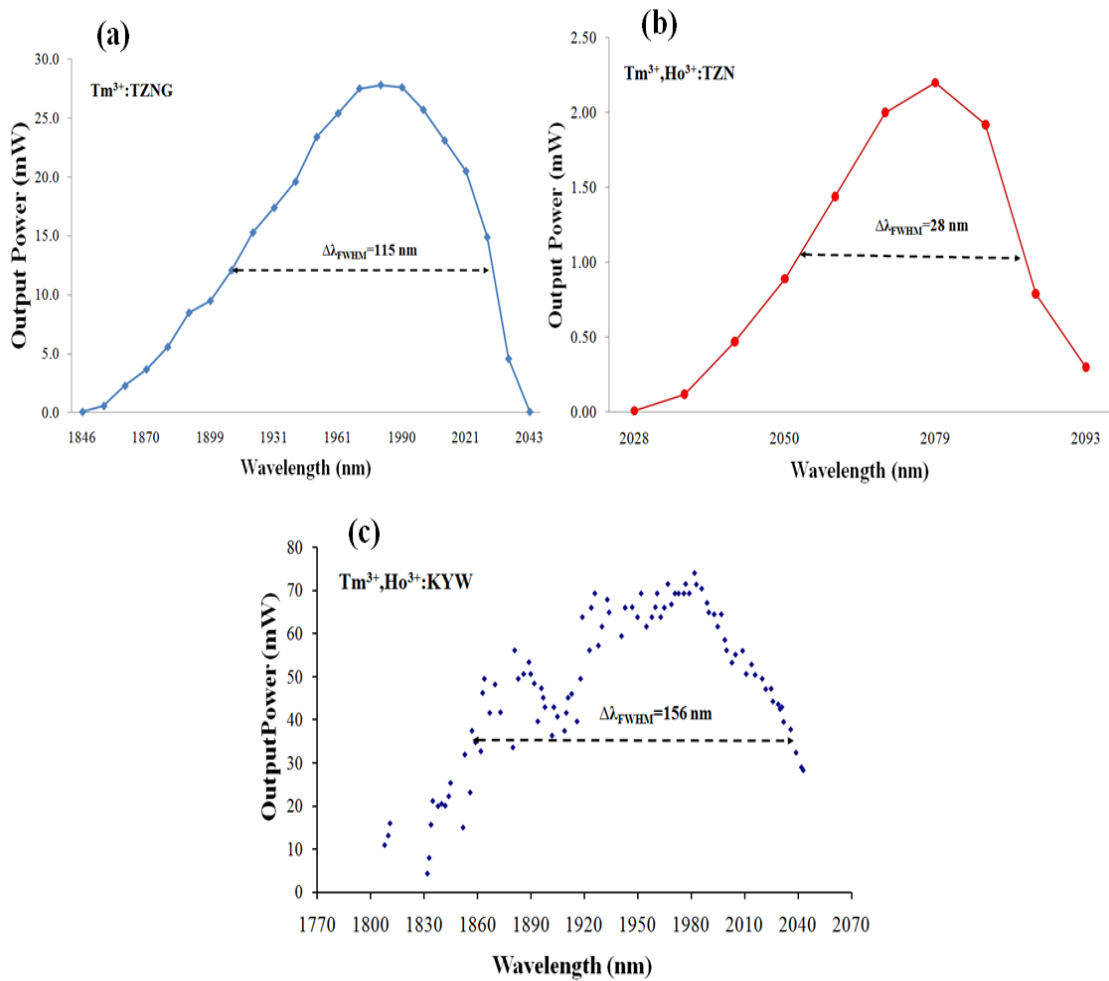
Figure 5-16: Wavelength tuning curve results using 1% output couplers (OC) for (a) Tm³⁺:TZNG glass, (b) Tm³⁺,Ho³⁺:TZN glass and (c) Tm³⁺,Ho³⁺:KYW crystal.

A synopsis of all ~1211 nm and ~800 nm pumping results are provided in Table 5.5, indicating TZNG as the best performing glass sample, whilst the crystal outperforms glass. As expected crystal is a more robust material, able to withstand higher pumping powers and higher concentrations of heat, with the glasses visibly showing signs of cracking during experiments.

Examining the results side-by-side between the two pumping schemes, highlights some similarities especially in terms of slope efficiencies and tuning ranges. The Ti:Sapphire pump source however, has been able to supply better beam quality at high powers, resulting in twice the maximum achievable output powers to those obtained through SDL pumping.

Table 5.5: Summary of results of ~1211 nm pumped Tm³⁺-doped TZNG and TZN glasses, and Tm³⁺,Ho³⁺-codoped KYW crystal compared with ~800 nm pumping.

Laser System	Max Output Power	Slope Efficiency,η	Δλ$_{FWHM}$	η$_0$	Loss
~1211 nm Pumping					
Tm³⁺:TZNG Glass (Tm 2 wt%)	60 mW at 1942 nm	22.4% using 4%OC	115 nm	36%	2.4%
Tm³⁺,Ho³⁺:TZN Glass (Tm 2 wt%, Ho 0.2 wt%)	12 mW at 1967 nm	7.2% using 2%OC	28 nm	8.7%	0.6%
Tm³⁺,Ho³⁺:KYW Crystal (Tm 5 at.%, Ho 0.4 at.%)	200 mW at 1963 nm	34.8% using 4%OC	156 nm	58%	2.6%
~800 nm Pumping					
Tm³⁺:TZNG Glass (Tm 2 wt%)	124 mW at 1960 nm	28.4% using 6.1% OC	135 nm	35%	1.5%
Tm³⁺,Ho³⁺:TZN Glass (Tm 2 wt%, Ho 0.2 wt%)	25 mW at 2020 nm	9.5% using 0.8% OC	80 nm	30%	0.9%
Tm³⁺,Ho³⁺:KYW Crystal (Tm 5 at.%, Ho 0.4 at.%)	460 mW at 2056 nm	44% using 1% OC	190 nm	61%	0.3%

The impact the pump beam M² parameter has on the beam profile inside the gain medium was estimated, based on evaluations by Augé *et al.* [38]. In Equation (5.1.3) the pump wavelength λ_p and the focused pump beam radius w_{p0} values were taken from experimental results relating to the Tm³⁺:TZNG glass sample expressed in [22] and listed in Table 5.6.

$$\omega_p^2(z) = \omega_{p0}^2(\lambda_p) + \left(\frac{M^2(z-z_0)\lambda_p}{\pi\omega_{p0}(\lambda_p)n}\right)^2 \tag{5.1.3}$$

Table 5.6: Parameters used in pump beam evaluation inside Tm:TZNG laser medium [22].

Parameter	Description	Value
n	Refractive Index	2
ω$_{p0}$ (λ$_p$=793 nm)	Pump beam radius for 793 nm pump wavelength	33 μm
ω$_{p0}$ (λ$_p$=1211 nm)	Pump beam radius for 1211 nm pump wavelength	25 μm
z$_0$	Offset distance inside the medium	2.5 mm

The 793 nm and 1211 nm pump wavelengths were compared, both using a near diffraction limited input beam of $M^2=1.2$ and a larger $M^2=3$ value. Based on these estimates, there is a larger divergence experienced in the 1211 nm beam compared with that of the 793 nm, as shown in Figure 5-17. This ultimately impacts on the mode matching capability and overall efficiencies of the ~2 μm, and thus may contribute to the disparity between results.
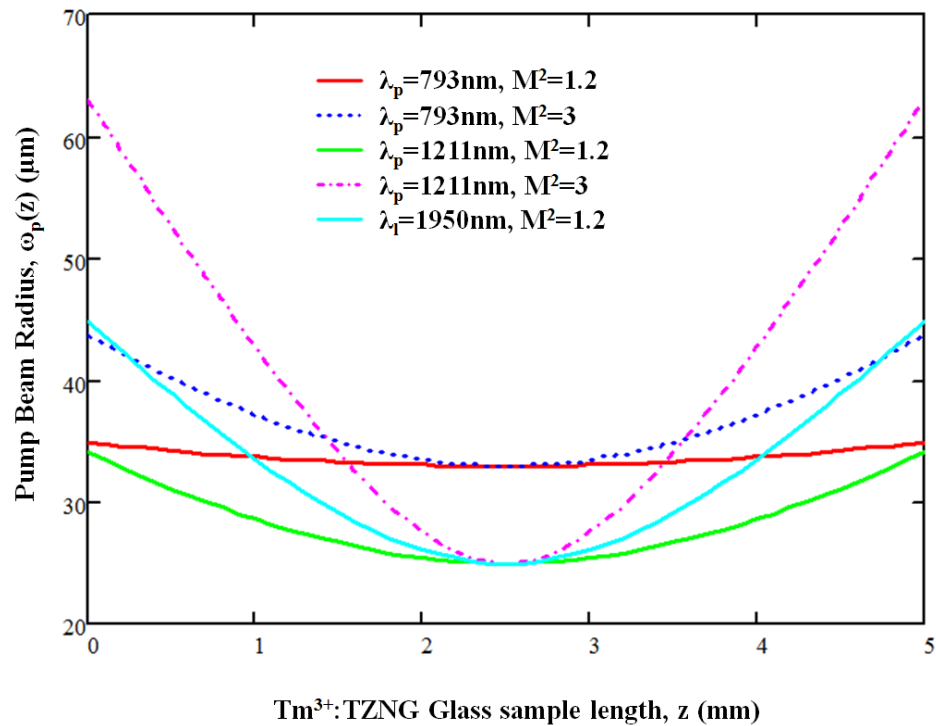
Figure 5-17: Comparison of 793 nm and 1211 nm pumping, with varying M^2 parameters showing the pump beam radii inside the Tm^{3+}:TZNG glass sample of length 5 mm. Included is the 1950 nm laser beam profile through the crystal with $M^2=1.2$.

Variation in results obtained for the ~800 nm pumping compared to ~1200 nm may also come from the differences in pump location within the material. The doping concentrations within the glasses may exhibit forms of inhomogeneity, having a knock on effect upon the consistency of performance.

It must be stressed that the SDL pump source offers an alternative and less complicated means to target excitation into the $^3H_5$ energy level, compared to the previously shown cascading Raman fibre lasers.

In the next section, the SDL shall again be used as a pump source, but to achieve fibre Raman amplification.

5.3 Raman Amplification in a Silica Fibre

Increasing demands for bandwidth across telecommunication networks creates an environment receptive to new opportunities which can build upon existing technologies. The existence of fibre optic communication links has been around since the late 1960's; having first established optical waveguide capability [39] to improvements of the fibre glass purity [40, 41] and finally implementing telecom networks across mainland US cities [42]. A major engineering achievement came in 1988 with the connection of Tuckerton, New Jersey to both Widemouth, England and Penmarche, France through the deployment of over 5,600 km of fibre optic cable called *TAT-8* [43]. Over such large distances, emerging technologies such as fibre optic amplifiers allowed the capability of boosting optical signals without the need for electro-optic regeneration of the signal in the form of repeaters. These amplifiers have proven most useful for wavelength division multiplexing (WDM) with the simultaneous amplification of multi-channel lightwave signals.

The most widely used method to amplify the signal has been Erbium-doped Fibre Amplifiers (EDFA) [44]. However, such a mature technology is coming close to its limit of development design, thus competition to continue expanding bandwidth comes in the form of Raman fibre amplifiers [45]. Benefits to this approach include; simplicity of amplifier architecture, since the signal amplification uses the transmission fibre itself; flexibility in signal wavelengths, as the Raman gain depends on the pump wavelength; low noise [46]; and larger gain bandwidths possible through use of multiple pump sources [47-49]. Table 5.7 provides a comparison of two available commercial systems of Raman Fibre Amplifier and EDFA in the conventional *C-band*. This band covers the telecommunications wavelength region 1530 − 1565 nm, which is referred to as the 'erbium window' [50] due to energy of photons in this band coinciding with the energy level of erbium ions.

Table 5.7: Data relating to commercially available Raman Fibre Amplifiers and EDFA [51].

System	Pump Power	Gain	Noise Figure
Raman Fibre Amplifier	500 mW typical	10dB typical	-1.0 dB typical
EDFA	35mW	>32dB (small signal gain at 1550 nm)	~5.5 dB (typical of ~3dBm input signal)

It is clear from Table 5.7 that in order to achieve Raman fibre amplification, high power laser sources are required. In addition it is evident the exclusive use of EDFAs in the C-band, provides further opportunities in fibre amplifier development within the O-band (1260 – 1360 nm) region. The focus of the work presented in this section is to demonstrate the application of an SDL designed for 1220 nm emission as the pump source of a 26.6 km length of single mode (SM) silica core fibre.

5.3.1 Raman Gain Principles and System Requirements

Stimulated Raman scattering in the material forms the foundation for Raman amplification. The incoming photon is either red-shifted (*Stokes shift*) or blue-shifted (*anti-Stokes shift*) through the interaction with the medium. In the case of the Stokes shift the final energy level of the molecule is lower than the incoming energy, with the opposite true for anti-Stokes. It is the *Stokes shift* that has relevance in these experiments, as the system aims to reach longer wavelengths around 1.3 µm. An illustration is given in Figure 5-17 of stimulated Raman scattering. The difference in the frequencies, between the pump and signal corresponds to the Stokes shift *(hv_p-hv_s)*.
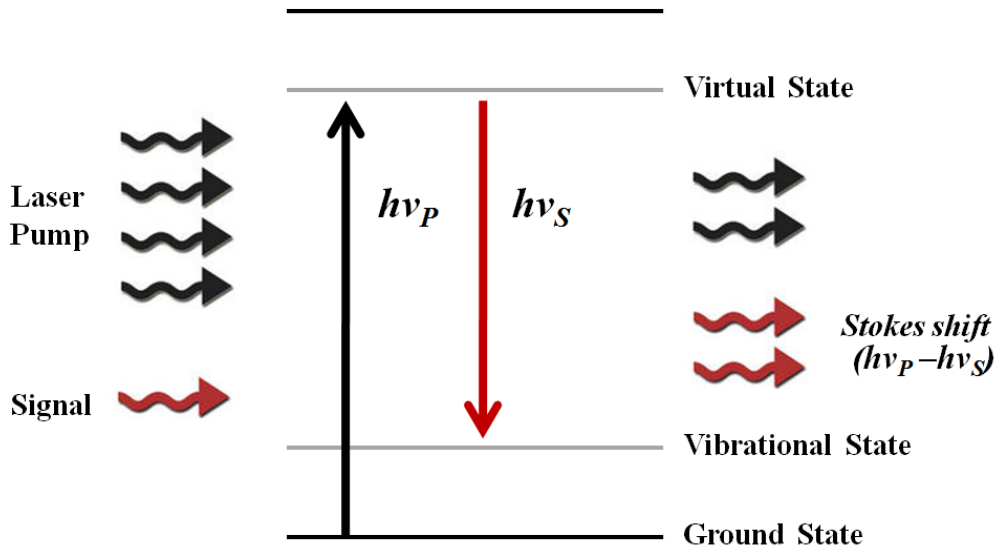
Figure 5-18: Schematic of the stimulated Raman scattering process.

An added advantage in using a silica fibre for Raman amplification has been the wealth of simulation and experimental studies available on this material [52-54]. As a basis for this study, the models used to describe the system comprise mainly those of Agrawal [55, 56] and Hollenbeck *et al.* [54].

Considering signal and pump beam co-propagation through the silica fibre, the power of the Raman scattered signal grows proportionally with the pump P_p and signal P_s power, as given in Equation (5.1.4). The variable γ_R corresponds to the probability of stimulating Raman scattering in the medium, with A_{eff} the effective core area in the fibre where $A_{eff}=\pi w^2$, in which w is the field mode radius.

$$\frac{dP_s}{dz} = \left(\frac{\gamma_R}{A_{eff}}\right) P_p P_s = g_R P_p P_s \tag{5.1.4}$$

The Raman gain coefficient g_R is a significant parameter, which has been often used to describe the Raman gain spectrum of the fibre system. In the analysis presented by Walrafen and Krishnan [57], they had proposed a set of Gaussian components to model the performance of the Raman spectrum of fused silica fibres. In their model, they have decomposed the spectrum into 13 Gaussians to describe the vibrational spectrum in the material. Extended use of this model was presented by Hollenbeck *et*

al. [54] in which the Raman response function and gain spectrum were successfully demonstrated. Using their methods Equation (5.1.5) evaluates the spectral response of the fibre output, where Γ_i corresponds to the Gaussian linewidths, A_i' the modal amplitudes, and $\omega_{v,i}$ relates to the vibrational frequencies. Values for these parameters were based on those from the Hollenbeck paper. The frequency ω is the difference associated with the pump and signal wavelengths, given $\omega = \left(\frac{1}{\lambda_p} - \frac{1}{\lambda_s}\right)$.

$$g_R = \sum_{i=1}^{13} \frac{A_i'}{2\omega_{v,i}} exp\left[\frac{(\omega - \omega_{v,i})^2}{\Gamma_i^2}\right] \tag{5.1.5}$$

A Mathcad programme developed by Dr. S. Calvez has been written based on this platform, and used to simulate the proposed system. Power transfers taking place in the material are depicted in Equations (5.1.6), (5.1.7) and (5.1.8), in which the power of forward travelling beams for the pump and signal are given as P^f_p and P^f_s respectively, whilst the backward direction for the signal is given P^b_s. As the pump is unidirectional, backward pump power has not been included in these calculations. Attenuation coefficients of the pump α_p and signal α_s, are wavelength dependent due to the response of the silica material.

$$t^f_p = -\alpha_p P^f_p - \left(\frac{\lambda_s g_R P^f_p \left(P^f_s + P^b_s\right)}{\lambda_p A_{eff}}\right) \tag{5.1.6}$$

$$t^f_s = -\alpha_s P^f_s + \left(\frac{g_R P^f_p P^f_s}{A_{eff}}\right) \tag{5.1.7}$$

$$t^b_s = \alpha_s P^b_s - \left(\frac{g_R P^f_p P^b_s}{A_{eff}}\right) \tag{5.1.8}$$

Figure 5-19 depicts the cross-section of the silica fibre, to illustrate the pump and signal beams travelling through a section of the fibre governed by the above equations.
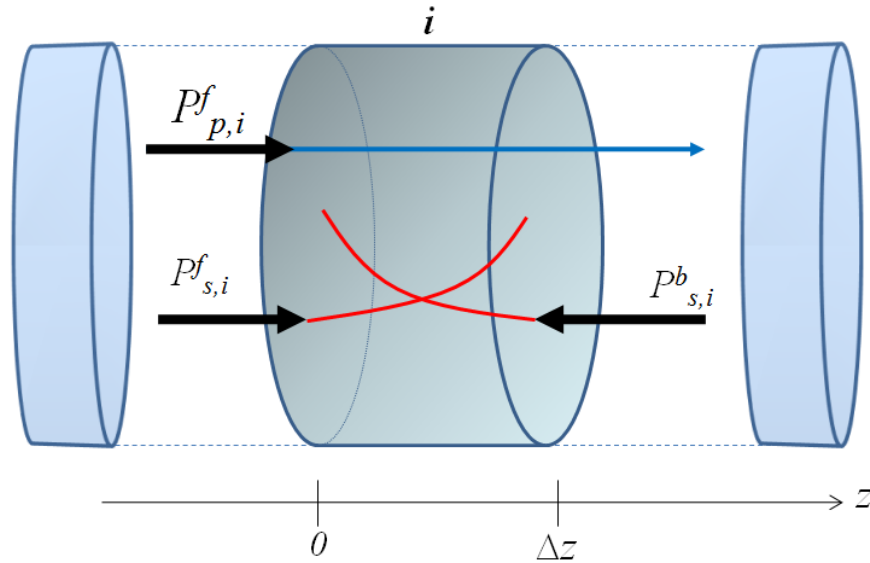
Figure 5-19: Schematic of the silica fibre in a section *i* over a distance Δ*z*, in which the forward pump power $P^f_{p,i}$ and the signal power in the forward direction $P^f_{s,i}$ and backwards direction $P^b_{s,i}$ are shown.

Parameters used in the evaluation are given in Table 5.8.

Table 5.8: Parameters used for calculating the Raman gain spectrum.

Parameter	Definition	Value
α_p, α_s	Attenuation coefficient at the pump, signal wavelength (1 dB/km)	1.2 dB/km
λ_p	Pump wavelength	1220 nm
λ_s	Signal wavelength	1289 nm
P_s	Signal power	1 μW
$A_{eff}(w=5\mu m)$	Effective mode area	78.5 μm^2

Using this model the simulated Raman gain spectrum is shown in Figure 5-20, spanning across wavlengths 1235 nm to 1350 nm.
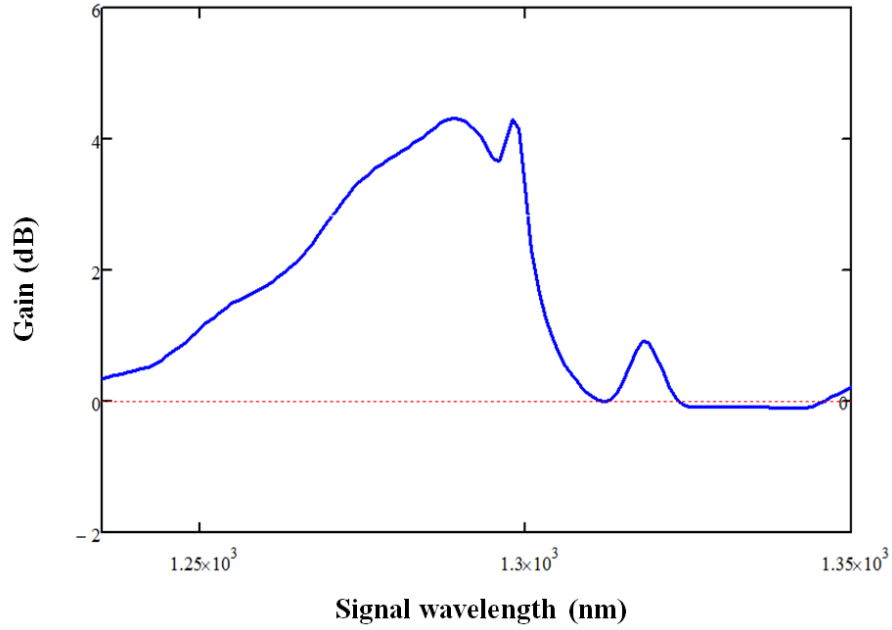
Figure 5-20: Simulated results of the Raman gain spectrum for the silica fibre pumped by a 1220 nm source.

In amorphous silica fibres the main peak of the Stokes shift occurs around 440 cm^{-1} (*13.2 THz*) [52]. Effectively the Raman gain spectrum experiences gain at a frequency ~13 THz below the pump frequency, therefore the use of the pump laser designed for 1220 nm operation expects to produce a Stokes shifted wavelength of between 1280 - 1320 nm [58].

Due to the pump absorption, there is an effective interaction length known as the *Raman effective length* given in Equation (5.1.9), which is dependent upon the attenuation coefficient of the fibre material at the pump wavelength α_p [56].

$$L_{eff} = \frac{\left(1 - exp(-\alpha_p L)\right)}{\alpha_p} \tag{5.1.9}$$

Using a solution of the small-signal power based on the expression given by Agrawal [56], an expression for the signal output power at the end of the fibre length $P_s(L)$ is given in Equation (5.2.0). The pump input at front facet of the fibre, at z=0 is $P_p(0)$ with the signal given as $P_s(0)$, with the attenuation at the signal wavelength given as α_s.

170

$$P_s(L) = P_s(0)exp\left[g_R P_p(0) L_{eff} - \alpha_s L\right] \tag{5.2.0}$$

Through differentiation of the exponential in the above expression, an estimation of the optimum length of the fibre can be made using Equation (5.2.1), using the attenuation coefficients for the pump α_p and signal α_s wavelengths given in Table 5.8.

$$L_{optimum} = \frac{ln\left(\frac{g_R}{\alpha_s}P_p(0)\right)}{\alpha_p} \tag{5.2.1}$$

Figure 5-21 gives an indication that the 26.6 km of silica fibre used in these experiments requires a minimum of ~450 mW to achieve any level of Raman amplification.
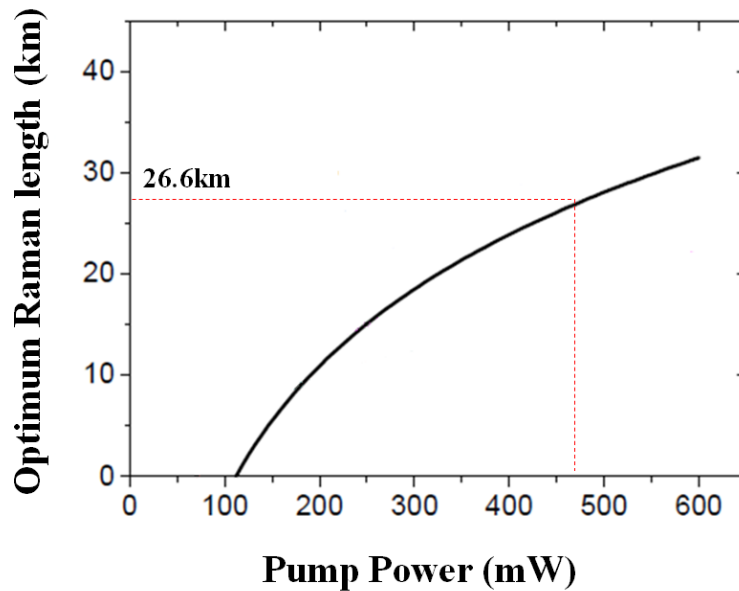
Figure 5-21: Optimum Raman fibre length as a function of pump power.

An important requirement of a Raman pump laser is stability, in terms of wavelength and power. Fluctuations in pump laser power can be transferred to the Raman gain response, likewise with such a strong dependency upon the pump wavelength any drift will ultimately impact on the gain spectrum. A measurement of the time-dependent performance of the SDL was carried out, which had formed part of the analysis of pumping of the $Tm^{3+}(,Ho^{3+})$-(co)doped laser systems but is valid since it pertains to the same SDL device, with the results presented in Figure 5-22 [59]. The

noise in the laser signal had exhibited a root-mean square deviation of 0.9% over a period of 24 seconds. During this measurement no special efforts were made to neither improve the mechanical stability nor apply electrical shielding, which implies possible improvements to the relative noise intensity (RIN) of the SDL.
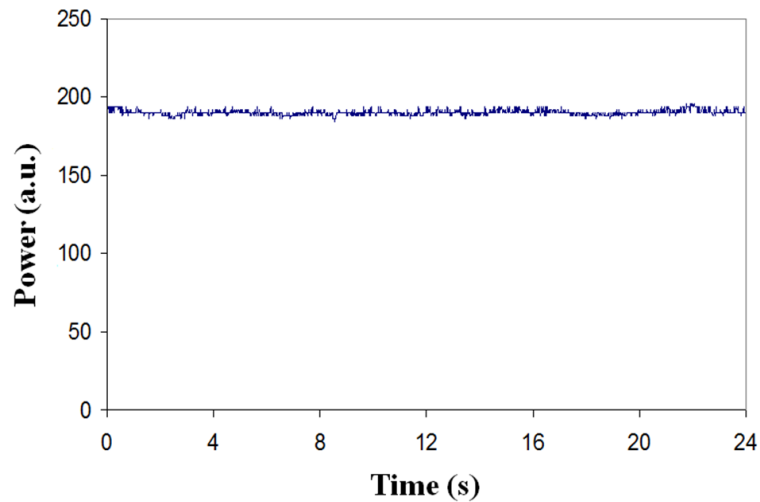
Figure 5-22: Time-dependent performance of 1220 nm SDL operating at full power [59].

5.3.2 Experimental Set-up
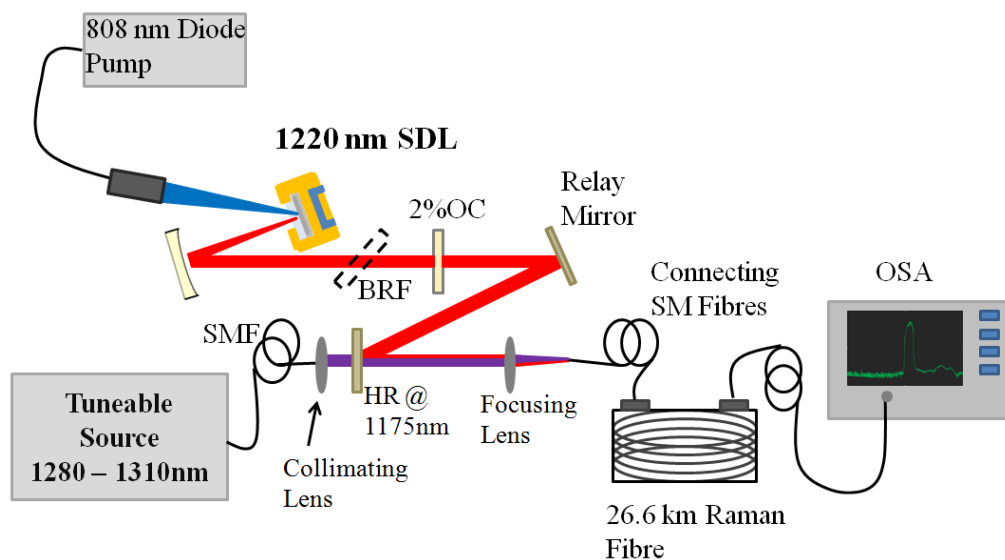
Figure 5-23: Raman amplification setup. The optically pumped V-cavity SDL uses a 2% output coupler (OC) and intracavity birefringent filter (BRF). The tuneable source and pump beams are coupled into a single mode fibre (SMF), which has been connected to the 26.6km Raman fibre with the output collected by the optical spectrum analyser (OSA).

The supply of the extensive 26.6 km length of silica fibre used in this experiment came from the Centre for Photonic Systems, Engineering Department, University of Cambridge. The fibre was completely enclosed within a sealed box, therefore two connecting SMF-28 fibres were needed to couple the pump and signal into the fibre, and output to the OSA.

The maximum coupling efficiency achieved into the first stage of SMF had been 42%, providing ~540mW input to the 26.6km Raman fibre from ~1.3W SDL pump power. A series of measurements were performed, in which the source was tuned across a range from 1270 nm to 1310 nm, with the spectral response recorded using the optical spectrum analyser (OSA).

The experiments conducted have been performed on the premise of the small-signal regime, with the tunable source input to the fibre typically no larger than 32dBm (*1.5mW*). In this respect the gain was determined by the pump power and fibre properties. Using the technique described by Agrawal [55] in which the on/off Raman gain G_A given in Equation (5.2.2), provides the amplifier signal gain distribution along the length of the fibre L.

$$G_A(\lambda_s) = \frac{P_S \text{ with pump on} - Noise \text{ with pump on}}{P_S \text{ with pump off} - Noise \text{ with pump off}} \approx \frac{P_S \text{ with pump on}}{P_S \text{ with pump off}} = \exp(g_R P_p L)$$

(5.2.2)

Through the course of processing the experimental data points, the inherent noise signal of the OSA was recorded and subsequently subtracted from each of the P_{out} measurements. This was carried out to ensure a more accurate representation of the Raman gain results.

5.3.3 Raman Gain Results

Figure 5-24 shows the response recorded by the OSA, clearly indicating the spectra of the 1216 nm SDL pump and the signal tuned to 1286 nm. The pump on/off technique was employed providing a means to measure the small signal Raman gain output from the Raman fibre.
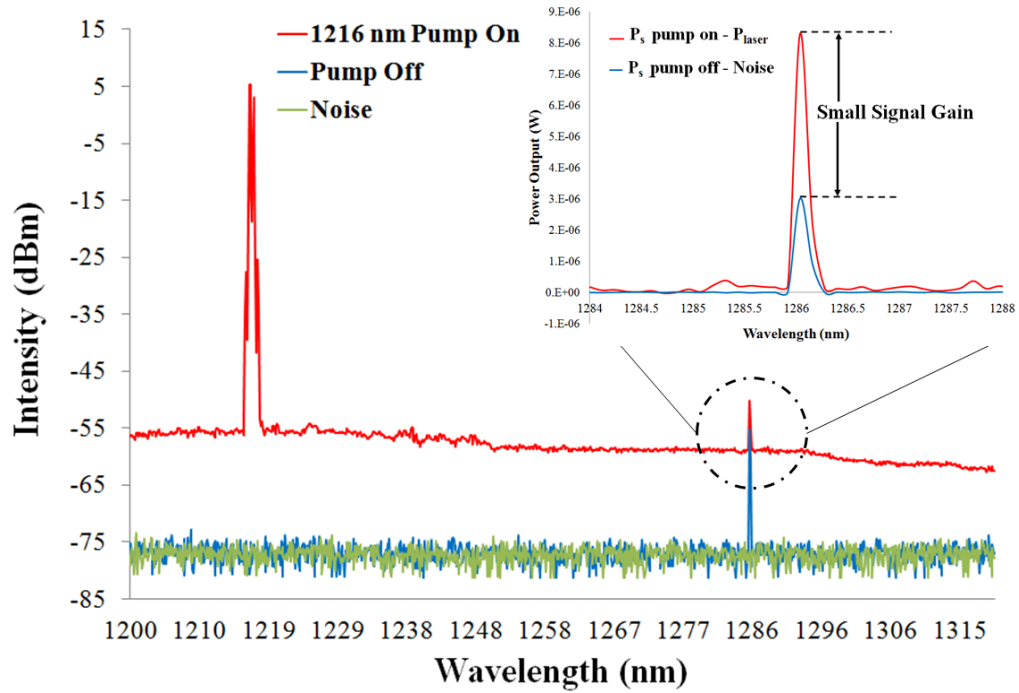
Figure 5-24: Spectra measured using the OSA with a resolution of 0.06 nm, showing the 1216 nm SDL pump, 1286 nm signal and noise level measured in the absence of both signal and pump. Inset is the result showing the small signal gain, found through the difference between the (P_s with pump on - $Pump_{laser}$) and (P_s with pump off- Noise).

Overall results are given in Figure 5-25, alongside the simulated Raman gain spectra. It was found that the filtered pump, with the SDL operating at 1216 nm, had provided the highest gain at 4.6dB compared with the free running system obtaining a maximum of 2.9dB. It is expected that the overall Raman on/off gain increases as the pump wavelength increases [60]
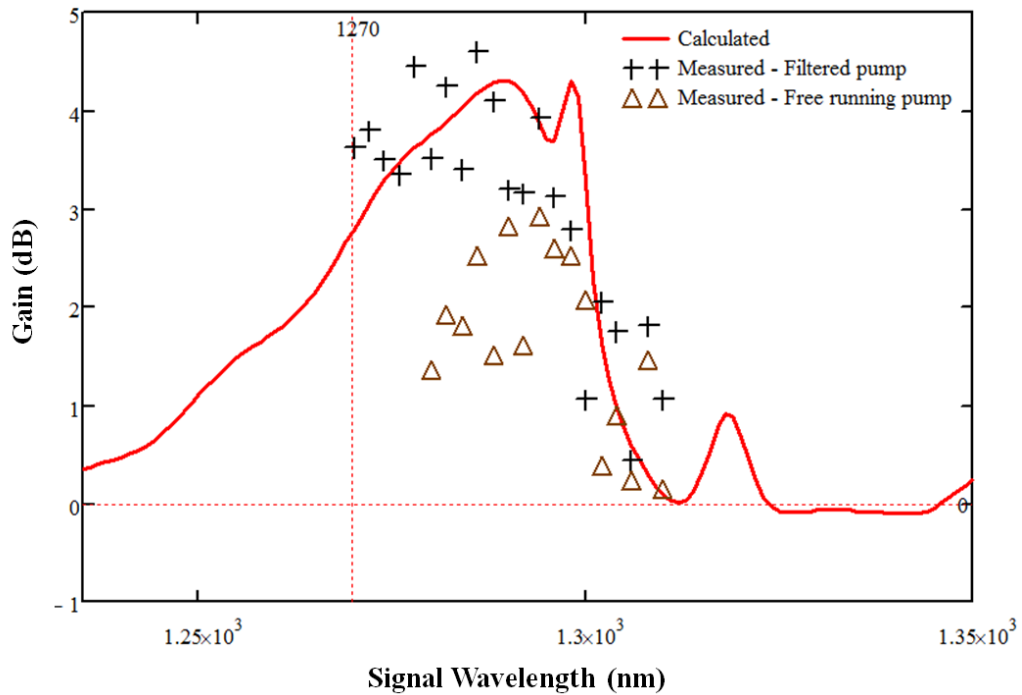
Figure 5-25: Empirical Raman gain results for free running pump (*brown triangles*) and filtered pump (*black crosses*) at 1216 nm pump wavelength, compared with simulated spectral gain results (*red solid line*) (*Programme Courtesy of Dr. S. Calvez*).

The broadened and diminished Raman gain profile of the free running results follow suit with the broadening of the pump laser linewidth through the fibre, as presented in Figures 5-26 and 5-27. It is expected that the free-running pump would ultimately provide better performance, since at increasing pump powers the filtered pump system would experience Stimulated Brillouin Scattering (SBS), with backscattering of light in the medium. This is a limitation for optical fibres, and usually avoided by broadening the laser spectrum (*free running*) above the width of the Brillouin line, which is typically 20-100 MHz in silica fibres [61]. It was proposed by Marconi *et al.* [62] that the addition of strain distributions along the fibre would act to solve the SBS problem, whilst allowing narrower pump laser linewidths.
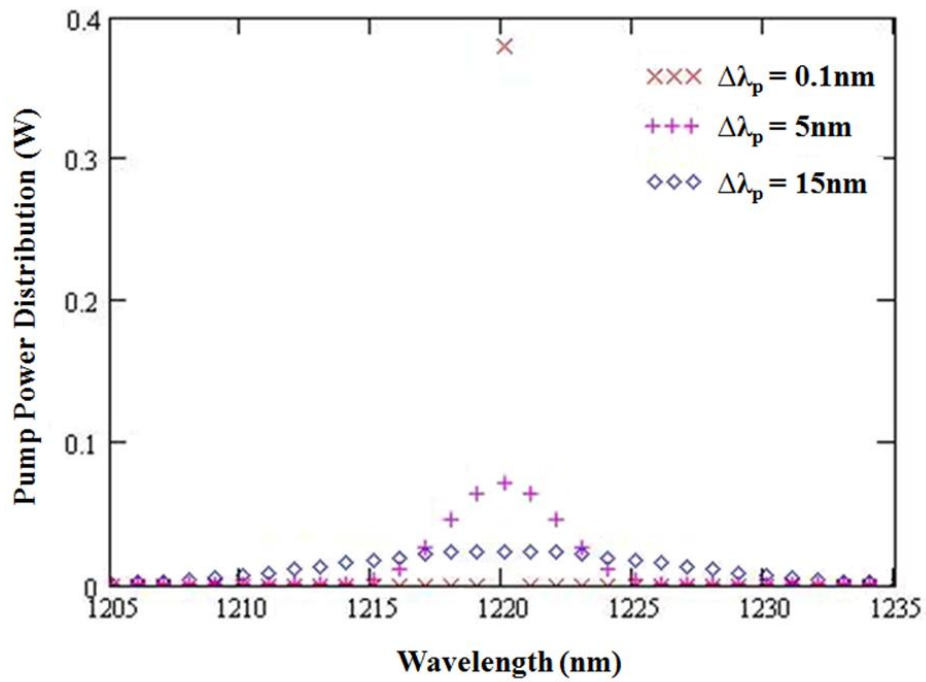
Figure 5-26: Simulation of 0.38 W Pump power with a variable Gaussian spectral distribution in the Raman fibre, across pump laser linewidths $\Delta\lambda_p$ = 0.1nm, 5 nm and 15nm (*Programme Courtesy of Dr. S. Calvez*).
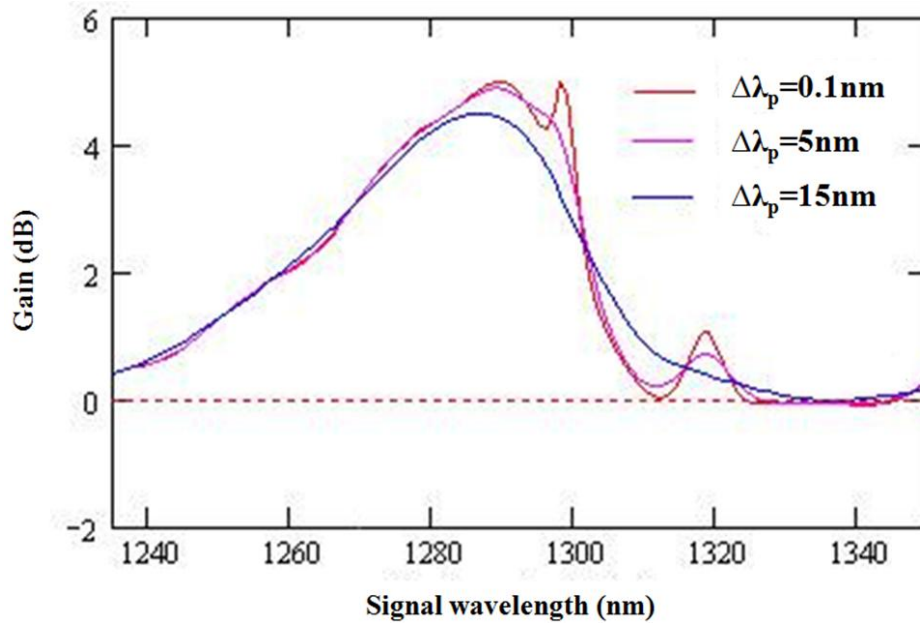
Figure 5-27: Simulation gain profile at the end of the Raman fibre, across pump laser linewidths $\Delta\lambda_p$ = 0.1nm, 5 nm and 15nm (*Programme Courtesy of Dr. S. Calvez*).

Large disparity between the two results may be accounted for by improvements to the overall set up during transitions between each set of measurements. Over the

period in which these measurements were taken, breakages occurred in the SMF and connectors, thus changing the continuity. However the trend of the results follows that of the simulation spectra, especially in the case of the filtered pump.

It should be noted that there were limits on the tunable source range, restricted to between 1250 – 1320 nm. In addition the HR mirror bandwidth had a cut-off wavelength at 1270 nm. These provide some explanation as to the distribution of measured results shown in Figure 5-25.

To improve upon these results, it would be prudent to control the polarisation orientation of the two inputs, which had not been done on the present system. It has been recognised that co-polarised beams would enable a more efficient and higher yielding gain result [55].

As a final note, parallel investigations performed by Chamorovskiy *et al.* [63] employing the same principles using 1.22 µm SDLs, have yielded higher Raman gain results due to better quality of laser gain material. Their results have confounded the successful employment of SDL pumping to achieve Raman amplification, and further in the development of fibre Raman lasers [64].

5.4 Conclusions

The motivation for this work has been to explore the potential for SDL devices, expanding functionality and exploiting the benefits from their flexible wavelength design and high output capability. This chapter has successfully demonstrated the novel approach to applying a ~1220 nm SDL as an excitation source. Slope efficiency results obtained in the ~2 µm rare earth doped dielectric laser systems have been on a par with those found using the ~800 nm Ti:Sapphire as the pump source. This creates an opportunity previously unseen in SDL applications. Further, the Raman amplification in a single-mode silica fibre has also opened up more potential uses for SDLs.

As a continuation of this theme, the application of a frequency doubled microchip SDL design shall be explored in the next chapter.

References

[1]   H. M. Pask, R. J. Carman, D. C. Hanna, A. C. Tropper, C. J. Mackechnie, P. R. Barber and J. M. Dawes, "Ytterbium-Doped Silica Fiber Lasers: Versatile Sources for the 1-1.2 um Region," *IEEE Journal of Selected Topics in Quantum Electronics,* vol. 1, pp. 2-13, (1995).

[2]   L. S. Meng, P. A. Roos and J. L. Carlsten, "High-efficiency continuous-wave Raman laser pumped by an injection-locked broad-area diode laser," *IEEE Journal of Quantum Electronics,* vol. 40, pp. 390-393, (2004).

[3]   E. Passacantilli, G. Anichini, C. P. Delfinis, J. Lenzi and A. Santoro,"Use of 2-μm Continuous-Wave Thulium Laser for Surgical Removal of a Tentorial Meningioma: Case Report," *Photomedicine and Laser Surgery,* vol. 29, pp. 437 - 440, (2011).

[4]   H. Ludwig, T. Kruschat, T. Knobloch, H. O. Teichmann, K. Rostasy and V. Rohde,"First experiences with a 2.0-μm near infrared laser system for neuroendoscopy," *Neurosurgical Review,* vol. 30, pp. 195-201, (2007).

[5]   S. J. Xia, J. Zhuo, X. W. Sun, B. M. Han, Y. Shao and Y. N. Zhang, "Thulium laser versus standard transurethral resection of the prostate: a randomized prospective trial," *European Urology,* vol. 53, pp. 382 - 389, (2007).

[6]   M. J. Vaughan, "Remote optical sensing by laser," pp. 1217-1295 in *Handbook of Optoelectronics (Two-Volume Set)*, Taylor & Francis, (2006).

[7]   U. N. Singh, J. Yu, M. Petros, S. Chen, M. J. Kavaya, B. Trieu, Y. Bai, P. Petzar, E. A. Modlin, G. Koch and J. Beyon, "Advances in high-energy solid-state 2-micron laser transmitter development for ground and airborne wind and CO_2 measurements," pp. 783202-18, in *Lidar Technologies, Techniques and Measurements for Atmospherc Remote Sensing VI*, Toulouse, France, (2010).

[8]   G. D. Wilkins, "Eye-Safe Free-Space Laser Communications," Wright Laboratory Avionics Directorate (1996).

[9]   M. Ramme, J. Choi, T. Anderson, I. Mingareev and M. Richardson, "Sub-micron machining of semiconductors: femtosecond surface ripples on GaAs by 2 um laser light," pp. 759004-8 in *Micromachining and Microfabrcation Process Technology XV*, San Francisco, California, USA, (2010).

[10]   A. Godard, "Infrared (2-12 um) solid-state laser sources: a review," *Comptes Rendus Physique,* vol. 8, pp. 1100-1128, (2007).

[11]   J. J. Wu, Q. Shibin, K.-G. Tiequn and N. Makoto Peyghambarian,"2 μm lasing from highly thulium doped tellurite glass microsphere," *Applied Physics Letters,* vol. 87, (2005).

[12]   VERTIGO. Available: http://www.2micron-laser.eu/

[13]   J.-M. Hopkins, A. J. Maclean, D. Burns, E. Riis, N. Schulz, M. Rattunde, C. Manz, K. Köhler and J. Wagner, "Tunable, Single-frequency, Diode-pumped 2.3μm VECSEL," *Optics Express,* vol. 15, pp. 8212-8217, (2007).

[14]   N. Schulz, M. Rattunde, C. Manz, K. Kohler, C. Wild and J. Wagner, "High power GaSb-based optically pumped VECSEL at 2.3 um," in *Conference on Lasers and Electro-Optics, 2006 and 2006 Quantum Electronics and Laser Science Conference. CLEO/QELS,* pp. 1-2, (2006).

[15]   N. Schulz, M. Rattunde, C. Manz, K. Kohler, C. Wild, J. Wagner, S. S. Beyertt, U. Brauch, T. Kubler and A. Giesen, "Optically pumped GaSb-based VECSEL emitting 0.6 W at 2.3 um," *IEEE Photonics Technology Letters,* vol. 18, pp. 1070-1072, (2006).

[16]   M. Rattunde, S. Kaspar, B. Rösener, T. Töpper, C. Manz, K. Köhler, O. Ambacher and J. Wagner,"Narrow linewidth 2um GaSb-based semiconductor disk laser," in *The European Conference on Lasers and Electro-Optics (CLEO/Europe)* p. CB6_4, (2011).

[17]   M. Rattunde, B. Rösener, N. Schulz, C. Manz, J.-M. Hopkins, D. Burns and J. Wagner, "Two-micron semiconductor disk lasers achieve higher powers", *Lasers & Sources.*(2008).

[18]   A. E. Troshin, V. E. Kisel, A. S. Yasukevich, N. V. Kuleshov, A. A. Pavlyuk, E. B. Dunina and A. A. Kornienko,"Spectroscopy and laser properties of Tm^{3+}:KY(WO$_4$)$_2$ crystal," *Applied Physics B: Lasers and Optics,* vol. 86, pp. 287-292, (2007).

[19]   A. Lagatsky, F. Fusari, S. Kurilchik, V. Kisel, A. Yasukevich, N. Kuleshov, A. Pavlyuk, C. Brown and W. Sibbett,"Optical spectroscopy and efficient continuous-wave operation near 2 μm for a Tm, Ho:KYW laser crystal," *Applied Physics B: Lasers and Optics,* vol. 97, pp. 321-326, (2009).

[20]   S. D. Jackson and A. Lauto,"Diode-pumped fiber lasers: A new clinical tool?," *Lasers in Surgery and Medicine,* vol. 30, pp. 184-190, (2002).

[21]   A. Jha, S. Shen, S. and M. Naftaly, "Structural origin of spectral broadening of 1.5-μm emission in Er^{3+}-doped tellurite glasses," *Physics Review B,* vol. 62, pp. 6215 - 6227, (2000).

[22]   F. Fusari, "Continuous Wave and Modelocked Femtosecond Novel Bulk Glass Lasers Operating Around 2000 nm," PhD Thesis, School of Physics and Astronomy, St Andrews University, St Andrews, (2011).

[23]   B. Richards, A. Jha, Y. Tsang, D. Binks, J. Lousteau, F. Fusari, A. Lagatsky, C. Brown and W. Sibbett,"Tellurite glass lasers operating close to 2μm," *Laser Physics Letters,* vol. 7, pp. 177-193, (2010).

[24]   F. Fusari, A. A. Lagatsky, B. Richards, A. Jha, W. Sibbett and C. T. Brown, "Spectroscopic and lasing performance of Tm^{3+}-doped bulk TZN and TZNG tellurite glasses operating around 1.9 um," *Optics Express,* vol. 16, pp. 19146-19151, (2008).

[25]   G. H. Dieke, "Spectra and Energy Levels of Rare Earth Ions in Crystals," *American Journal of Physics,* vol. 38, p. 399, (1970).

[26]   F. Fusari, "Continuous Wave and Modelocked Femtosecond Novel Bulk Glass Lasers Operating Around 2000 nm," PhD Thesis, School of Physics and Astronomy, St Andrews University, St Andrews, (2011).

[27]   F. Brunet, P. Laperle, R. Vallee, S. LaRochelle and L. Pujol, "Modeling of Tm-doped ZBLAN blue upconversion fiber lasers operating at 455 nm," in *Infrared Optical Fibers and Their Applications*, Boston, MA, USA, pp. 125-135, (1999).

[28]   S. D. Jackson, F. Bugge and G. Erbert,"High-power and highly efficient Tm^{3+}-doped silica fiber lasers pumped with diode lasers operating at 1150 nm," *Optics Letters,* vol. 32, pp. 2873-2875, (2007).

[29] A. Taniguchi, T. Kuwayama, A. Shirakawa, M. Musha, K.-i. Ueda and M. Prabhu,"1212 nm pumping of 2 μm Tm–Ho-codoped silica fiber laser," *Applied Physics Letters,* vol. 81, pp. 3723-3725, (2002).

[30] K. S. Kravtsov, I. A. Bufetov, O. I. Medvedkov, E. M. Dianov, M. V. Yashkov and A. N. Gur'yanov, "7-W single-mode thulium-doped fibre laser pumped at 1230 nm," *Quantum Electronics,* vol. 35, pp. 586-590, (2005).

[31] I. A. Bufetov, M. M. Bubnov, Y. V. Larionov, O. I. Medvedkov, S. A. Vasiliev, M. A. Melkoumov, A. A. Rybaltovsky, S. L. Semjonov, E. M. Dianov, A. N. Gur'yanov, V. F. Khopin, F. Durr, H. G. Limberger, R.-P. Salathe and M. Zeller,"Highly Efficient One- and Two-Cascade Raman Lasers Based on Phosphosilicate Fibers," *Laser Physics* vol. 13, pp. 234-239, (2003).

[32] R. Paschotta, N. Moore, W. A. Clarkson, A. C. Tropper, D. C., Hanna and G. Maze,"230 mW of blue light from a thulium-doped upconversion fiber laser," *IEEE Journal of Selected Topics in Quantum Electronics* vol. 3, pp. 1100-1102, (1997).

[33] S. G. Grubb, K. W. Bennett, R. S. Cannon and W. F. Humer,"CW room-temperature blue upconversion fibre laser," *Electronics Letters,* vol. 28, pp. 1243-1244, (1992).

[34] P. Peterka, I. Kasik, A. Dhar, B. Dussardier and W. Blanc,"Theoretical modeling of fiber laser at 810 nm based on thulium-doped silica fibers with enhanced $^3H_4$ level lifetime," *Optics Express,* vol. 19, pp. 2773-2781, (2011).

[35] L. N. Ng, E. R. Taylor and J. Nilsson, "795 nm and 1064 nm dual pump thulium-doped tellurite fibre for S-band amplification," *Electronics Letters,* vol. 38, pp. 1246-1247, (2002).

[36] S. D. Jackson and T. A. King, "Theoretical modeling of Tm-doped silica fiber lasers," *Journal of Lightwave Technology* vol. 17, pp. 948-956, (1999).

[37] J. Caird, L. DeShazer and J. Nella,"Characteristics of room-temperature 2.3-um laser emission from tm^{3+} in YAG and $YAlO_3$," *IEEE Journal of Quantum Electronics,* vol. 11, pp. 874-881, (1975).

[38] F. Auge, F. Druon, F. Balembois, P. Georges, A. Brun, F. Mougel, G. Aka and D. Vivien, D., "Theoretical and experimental investigations of a diode-pumped quasi-three-level laser: the Yb^{3+}-doped $Ca_4GdO(BO_3)_3$ (Yb:GdCOB) laser," *IEEE Journal of Quantum Electronics,* vol. 36, pp. 598-606, (2000).

[39] K. C. Kao and G. A. Hockham,"Dielectric-fibre surface waveguides for optical frequencies," *IEE Proceedings* vol. 113, pp. 1151-1158, (1966).

[40] R. D. Maurer and P. C. Schultz, "Fused Silica Optical Waveguide," USA Patent, (1972).

[41] D. B. Keck and P. C. Schultz, "Methods of Producing Optical Waveguide Fibers," USA Patent, (1973).

[42] D. R. Nicol, J. T. Harvey, V. Svoboda, F. A. Donaghy, C. H. Storey and K. R. Ballinger, "A 2 km Optical Fiber Communication Trial," *IEEE Transactions on Communications* vol. COM-26, pp. 1061-1067, (1978).

[43] Computer Business Review. *Fibre Optic TAT-8 Cable Goes into Service Across the Atlantic*. (1988) Available: http://www.cbronline.com/news/fibre_optic_tat_8_cable_goes_into_service_across_the_atlantic

[44]   E. Desurvire, Erbium-doped fiber amplifiers: principles and applications: John Wiley & Sons, Inc., (1994).

[45]   D. Z. Chen, T. J. Xia, G. Wellbrock, P. Mamyshev, S. Penticost, G. Grosso, A. Puc, P. Perrier and H. Fevrier, "New Field Trial Distance Record of 3040 km on Wide Reach WDM With 10 and 40 Gb/s Transmission Including OC-768 Traffic Without Regeneration," *Journal of Lightwave Technology,* vol. 25, pp. 28-37, (2007).

[46]   P. B. Hansen, L. Eskildsen, J. Stentz, T. A. Strasser, J. Judkins, J. J. DeMarco, R. Pedrazzani and D. J. DiGiovanni, "Rayleigh scattering limitations in distributed Raman pre-amplifiers," *IEEE Photonics Technology Letters,* vol. 10, pp. 159-161, (1998).

[47]   M. Yan, J. Chen, W. Jiang, J. Li, J. Chen and X. Li, "New design scheme for multiple-pump Raman fiber amplifiers using a simulated annealing algorithm," *Microwave and Optical Technology Letters,* vol. 30, pp. 434-436, (2001).

[48]   L. A. M. Saito, P. D. Taveira, P. B. Gaarde, K. De Souza and E. A. De Souza, "Multi-pump discrete Raman amplifier for CWDM system in the O-band," *Optical Fiber Technology,* vol. 14, pp. 294-298, (2008).

[49]   H. Kidorf, K. Rottwitt, M. Nissov, M. Ma and E. Rabarijaona,"Pump interactions in a 100-nm bandwidth Raman amplifier," *IEEE Photonics Technology Letters,* vol. 11, pp. 530-532, (1999).

[50]   D. Garthe, J. Ip, P. Colbourne, R. E. Epworth, W. S. Lee and A. Hadjifotiou, "Low-loss dispersion equaliser operable over the entire erbium window," *Electronics Letters,* vol. 32, pp. 371-373, (1996).

[51]   Amonics. Available: http://www.amonics.com/index.html

[52]   R. H. Stolen, C. Lee and R. K. Jain, "Development of the stimulated Raman spectrum in single-mode silica fibers," *Journal of the Optical Society of America B,* vol. 1, pp. 652-657, (1984).

[53]   R. H. Stolen, J. P. Gordon, W. J. Tomlinson and H. A. Haus,"Raman response function of silica-core fibers," *Journal of the Optical Society of America B,* vol. 6, pp. 1159-1166, (1989).

[54]   D. Hollenbeck and C. D. Cantrell,"Multiple-vibrational-mode model for fiber-optic Raman gain spectrum and response function," *Journal of the Optical Society of America B,* vol. 19, pp. 2886-2892, (2002).

[55]   G. P. Agrawal, "Theory of Raman Amplifiers," Chapter 2, pp. 33-97 in *Raman amplification in fiber optical communication systems*, C. Headley and G. P. Agrawal, Editors, Burlington, MA, USA: Elsevier Academic Press, (2005).

[56]   G. P. Agrawal, "Stimulated Raman Scattering," Chapter 8, pp. 298-346 in *Nonlinear Fiber Optics*, P. L. Kelley, I. P. Kaminow and G. P. Agrawal, Editors, Third edition San Diego: Academic Press, (2001).

[57]   G. E. Walrafen and P. N. Krishnan, "Model analysis of the Raman spectrum from fused silica optical fibers," *Applied Optics,* vol. 21, pp. 359-360, (1982).

[58]   A. M. Glass, D. J. DiGiovanni, T. A. Strasser, A. J. Stentz, R. E. Slusher, A. E. White, A. R. Kortan and B. J. Eggleton, "Advances in Fiber Optics," *Bell Labs Technical Journal,* vol. 5, pp. 168-187, (2002).

[59]   S. L. Vetter, L. J. McKnight, S. Calvez, M. D. Dawson, F. Fusari, A. A. Lagatsky, W. Sibbett, C. T. A. Brown, V.-M. Korpijärvi, M. D. Guina, B.

Richards, G. Jose and A. Jha, "GaInNAs semiconductor disk lasers as pump sources for Tm3+ (,Ho3+)-doped glass, crystal and fibre lasers " in *Proceedings of SPIE Solid State Lasers XVIII: Technology and Devices*, (2009).

[60]   N. R. Newbury, "Pump-Wavelength Dependence of Raman Gain in Single-Mode Optical Fiber," *Journal of Lightwave Technology,* vol. 21, pp. 3364-3373, (2003).

[61]   R. Paschotta, *Encyclopedia of Laser Physics and Technology* vol. A-M: Wiley-VCH, (2008).

[62]   J. D. Marconi, J. M. Chavez Boggio and H. L. Fragnito, "Narrow linewidth fibre-optical wavelength converter with strain suppression of SBS," *Electronics Letters,* vol. 40, pp. 1213-1214, (2004).

[63]   A. Chamorovskiy, J. Rautiainen, A. Rantamäki and O. G. Okhotnikov, "Low-noise Raman fiber amplifier pumped by semiconductor disk laser," *Optics Express,* vol. 19, pp. 6414-6419, (2011).

[64]   A. Chamorovskiy, J. Rautiainen, A. Rantamäki and O. G. Okhotnikov, "Raman Fiber Oscillators and Amplifiers Pumped by Semiconductor Disk Laser," *IEEE Journal of Quantum Electronics,* vol. 47, pp. 1201-1207, (2011).

Chapter 6

Towards a Microchip Frequency Doubled Semiconductor Disk Laser

6.1 Introduction

In this chapter the provision of frequency doubling an SDL device shall be merged with the concept of a microchip laser configuration. The benefits of a compact frequency doubled device include a system needing no alignment, which requires less packaging and has the potential to become a mobile product.

The nonlinear effect in producing the second harmonic has been a common technique to access the visible and UV spectral ranges, which have been difficult to obtain directly. In Section 6.2 the variety of research in frequency doubled SDLs shall be presented, which extends over a 12 year period. In light of the capability with regards to spectral coverage of the GaInNAs/GaAs SDLs presented throughout this thesis, the ~1180 nm SDL shall be used to target the yellow/orange (~590 nm) visible wavelength. Yellow/orange laser light has gained interest in recent years due to its application in the treatment of diabetic retinopathy [1-3] and to act as a sodium guide star in astronomy [4-7].

The experimental work presented in Section 6.3 explores a route towards a microchip configuration with the compact design of a double bond arrangement between the nonlinear crystal, the heatspreader and the semiconductor chip.

6.2 Frequency Doubling in SDLs

Accessing the visible spectrum has a significant importance for a wide range of applications, including medical [8-10], display for laser TV/projection [11, 12], astronomical [4] and spectroscopy [13]. The frequency doubling process, also known as second harmonic generation (SHG), has been a successful method over the last 50

years to produce lasers that operate in the UV and visible spectrum ranges. SDLs were a logical source for frequency doubling due to their versatility in accessing such a large range of wavelengths through careful choice of gain material and QW composition, as discussed previously in Chapter 2.

6.2.1 Prior Results of Frequency Doubled SDLs

The progress and variation of experimental work utilising frequency doubled SDLs is presented in Table 6.1. Typical cavity configurations which have been used are those represented in Figure 6-1.
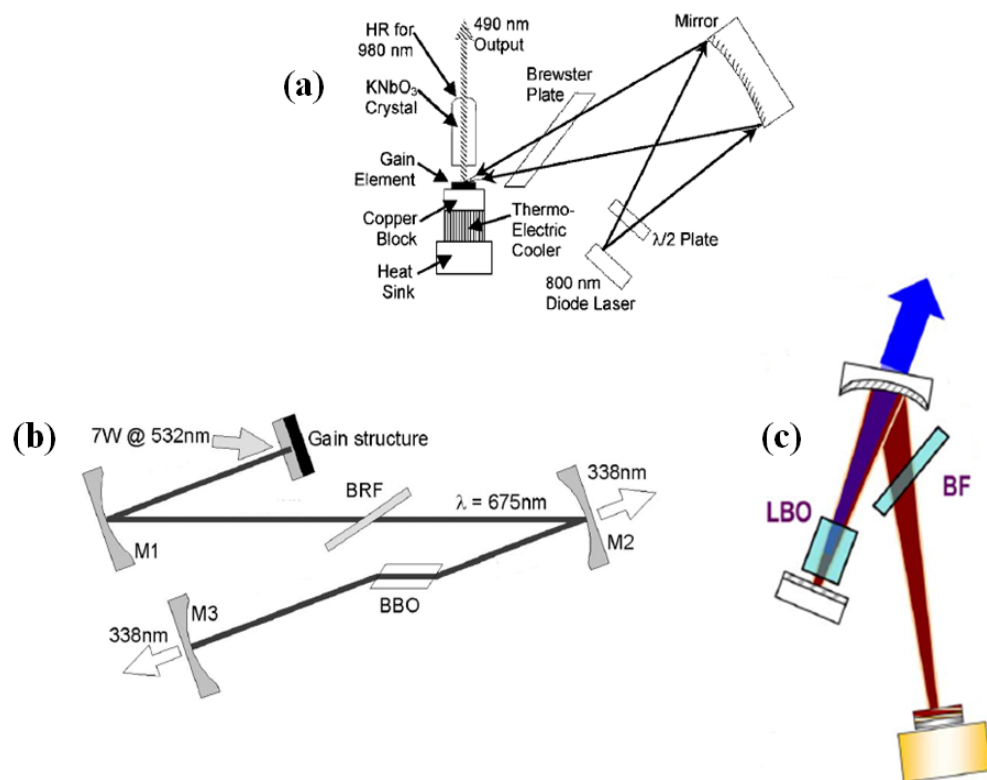
Figure 6-1: Cavity configurations for frequency doubled SDLs (a) incorporating a shaped SHG crystal [14], (b) 4-mirror (Z-cavity) [15] and (c) 3-mirror (V-Cavity) [16].

A majority of these devices have targeted the green (495 nm – 560 nm) visible region covering a diverse range of applications to include projection displays, bio-photonics, pump sources for other laser systems and micro-machining. The next

popular visible region has been blue (450 nm – 495 nm), which has also been applied to projection displays and bio-photonics, and also in data storage.

The wavelength range 560 nm – 635 nm (yellow/orange), which forms the focus of this work, is of particular interest for medical applications, specifically the treatment of retinal vascular disease [8]. These studies have shown, through use of a dye laser, the successful treatment for macular edema in diabetic retinopathy whereby micro-aneurisms were focally closed using the laser operating around 577 nm. This specific wavelength also has been used for dye and drug delivery in the presence of blood [17] as 577 nm is the peak absorption wavelength of haemoglobin. In the field of forensics, lasers operating in the visible spectrum are used to examine biological evidence. Coherent Inc. have developed in 2006 a product called TracER[TM], a portable forensics laser device weighing <1kg designed to operate with 6-8W green (542 nm), 3-5W yellow (577 nm) and 2W blue (460 nm) with a retail value between $41k and $48k [18].

Another application which has attracted considerable interest for yellow/orange laser development has been the *sodium guide star*, to aid astronomical telescopes with atmospheric corrections. The sodium atoms, which occur in the mesosphere at an altitude of ~90km, absorb at 589.2 nm and emit fluorescence at the same wavelength thus providing a signal from an artificial star that the telescope can analyse and implement adaptive optic corrections. The development of lasers operating at 1178 nm with the capability of narrow linewidth frequency doubled 589 nm at high output powers has been explored by Härkönen *et al.* [19], Holzlohner *et al.* [7] and Fallahi *et al.* [16].

The Gerster et al [20] approach to produce frequency doubled 610 nm used an intracavity LBO crystal with a thin disk GaAsSb/GaAs based SDL in a two mirror cavity configuration. The crystal and laser were cooled to -15°C, to achieve a maximum fundamental output power of 68 mW and 30 mW at the second harmonic. Similarly an InGaAs/GaAs thin disk device with an intracavity LBO crystal were used by Fallahi *et al.* [16] in a three mirror cavity configuration. The operating temperatures in these experiments were much higher at 15°C and 25°C, with output

powers of 8W at the fundamental 1175 nm and 5W at 585-589 nm. It becomes apparent that the choice in SDL gain material is key in the design of a high power, frequency doubled laser system. Demonstrations of yellow/orange frequency doubled SDLs based on GaInNAs/GaAs have been shown by Härkönen *et al.* [21], Korpijärvi *et al.* [22] and Leinonen *et al.* [23].

This frequency doubled SDL approach had been identified with commercial potential by two initial patents from Coherent, Inc in 1999. The first was from Caprara *et al.* [24] swiftly followed by Spinelli [25], both describing intracavity frequency doubled optically pumped SDLs. The market potential for laser TV and projection displays motivated patents from Novalux, Inc. in 2005 [26] for red, green and blue laser displays and in 2006 [27] for frequency stabilised external cavity lasers. This was closely followed by Samsung Electronics Co. Ltd. in 2007 with a patent from Kim [28] for an optically pumped SDL, whilst a colleague Cho [29] filed a patent the same year for mirror coated nonlinear crystals within an SDL for more efficient frequency doubling. In contrast an electrically pumped SDL targeting the green wavelength region was patented by Baier and Weichmann in 2008 [30]. All patents broadly encapsulate nonlinear medium; periodically-poled lithium niobate (PPLN), periodically-poled potassium titanyl phosphate (PPKTP), beta-barium borate (β-BBO), bismuth borate (BiBO), potassium titanyl phosphate (KTP) and lithium triborate (LBO).

Table 6.1: Frequency doubling using SDLs between 1999 and 2011.

Year	Nonlinear Crystal	SDL Gain	Wavelength Conversion	SHG Output Powers	Conversion Efficiencies	References
1999	$KNbO_3$	InGaAs/ GaAsP/GaAs	980nm to 490nm	5mW	1.5%	[14]
2000	$KNbO_3$	GaAs/AlGaAs	860nm to 430nm	11.6mW		[31]
2003	LBO	GaAsSb/GaAs	1220nm to 610nm	30mW		[20]
2003	PP KTP ($1x5x10mm^3$)	InGaAs/GaAsP/GaAs *	980nm to 480nm	42mW	1.3%	[32]
2005	BiBO (4mm length)	InGaAs/GaAs	1040nm to 520nm	0.7W	10%	[33]
2005	LBO (5mm length)	InGaAs/GaAs **	978nm to 489nm	6mW (P_{avg})		[34]
2005	MgO-doped PPLN (PPKTP)	InGaAs/GaAsP/GaAs *	1064nm to 532nm (920nm to 460nm)	34mW (20mW)		[35]
2006	$KNbO_3$	InGaAs/GaAs	1003nm to 501nm	62mW	0.6%	[36]
2006	BBO ($3x3x7\ mm^3$)	AlInGaP	675nm to 388nm	120mW		[37]
2006	BBO ($3x3x8\ mm^3$)	InGaAs/GaAsP/GaAs	1060nm to 535nm	7W	27%	[38]
2006	LBO	InGaAs	920nm to 460nm	2W	10%	[39]
2007	BiBO ($3x3x4mm^3$)	InGaAs/GaAs	1050nm to 529nm	220mW	52%	[40]
2007	LBO	InGaAs/GaAsP/GaAs	1160-1108nm to 580-554nm (1150nm to 575nm)	100mW (8.5W)		[41]
2007	LBO (5mm length)	InGaAs/GaAsP/GaAs	1064nm to 535nm*** (980nm to 488nm)	55W (15W)		[42]
2007	BBO (4 mm length)	GaInNAs/GaAs	1230nm to 615nm	172mW		[21]

Year	Nonlinear Crystal	SDL Gain	Wavelength Conversion	SHG Output Powers	Conversion Efficiencies	References
2008	LBO (3 x 3 x 15mm^3)	InGaAs/GaAs	977nm to 488nm	480mW	8.5%	[43]
2008	LBO (2x2x5mm^3)	InGaAs/GaAs	1080nm to 540nm	12mW	30%	[44]
2008	LBO (3x3x10mm^3)	InGaAs/GaAs	1175nm to 587nm	5W		[16]
2009	PPLN	InGaAs *	980nm to 490nm	250mW		[45]
2009	LBO (10mm length)	InGaAs/ GaAsP/GaAs	1178nm to 589nm	2W		[46]
2010	BBO (4mm length)	GaInNAs/GaNAs/GaAs	1180nm to 590nm	6.2W		[22]
2010	LBO (15mm length)	GaInNAs/GaNAs/GaAs	1180nm to 590nm	5.2W, 22°C (6.2W, 8°C)	15.5% (12.9%)	[23]
2011	BiBO (3x3x5mm^3)	InGaAs/GaAsP/GaAs	920nm to 460nm	1.61W	14.5%	[47]

*Electrically pumped SDL, **Modelocked SDL, ***Implemented 3 SDL chips*

A common theme to achieve these results has been to place the nonlinear crystal intracavity. The reason for this approach has been to capitalise on the high intracavity power densities of these devices, providing an efficient means to promote the second harmonic within the crystal [48]. In addition the short (*ns*) gain lifetime reduces *'green'* noise compared to doped dielectric versions [40, 49, 50].

6.2.2 Frequency Doubling in a Microchip SDL

The frequency doubling process occurs when the energy of an optical wave with frequency ω propagates through a nonlinear crystal, inducing an electric polarisation component oscillating at frequency 2ω. The polarisation effect has a significant contribution to the nonlinear optical process by the charges oscillating in the material due to the incident oscillating electric field and re-radiating, thereby adding to the field. The relationship between polarisation of a system and the strength of the electric field E [51] is expressed as a power series in Equation (6.1.1).

$$P = \epsilon_0 \chi_1 E + \epsilon_0 \chi_2 E^2 + \epsilon_0 \chi_3 E^3 + \cdots \qquad (6.1.1)$$

Within this equation the permittivity of free space is given as ϵ_0, and the first, second and third order susceptibilities χ_1, χ_2, χ_3 are proportionality constants to the system. Due to the small higher order susceptibilities (χ_2, χ_3) compared with χ_1, nonlinear optical effects come into play only for high energy fields, such as those experienced by an SDL intracavity. In the case of frequency doubling the nonlinear polarisation P_2 expression is given in Equation (6.1.2), where the electromagnetic wave is twice the frequency 2ω of the incident wave.

$$P_2 = 2\epsilon_0 \chi_2 EE^* + 2\epsilon_0 \chi_2 E^2 e^{-i2\omega t} + 2\epsilon_0 \chi_2 E^{*2} e^{-i2\omega t} \qquad (6.1.2)$$

The second-order nonlinear susceptibility χ_2, relates to the symmetry of the crystal. Conventional notation [51] [52] uses the tensor

$$d_{ijk} = \frac{1}{2}\chi_{ijk} \qquad (6.1.3)$$

to evaluate the susceptibility, where the *ijk* indices correspond to the permutation symmetry of the light waves inside the crystal structure. This tensor is also referred to as the *nonlinear coefficient*, and is used in describing the strength of the higher order nonlinear effect. In the case of a centrosymmetric crystal or one that possesses inversion symmetry, the nonlinear coefficient $d_{ijk}=0$ and there are no second-order nonlinearity effects. Thus only non-centrosymmetric crystals can be used to achieve frequency doubling, such as those listed in Table 6.1.

6.2.2.1 Phase Matching Conditions

Phase matching is an important aspect of frequency doubling but can be difficult to achieve due to dispersion in the crystal material. A general term for an electromagnetic wave in relation to the refractive index in the material and its angular frequency is expressed in Equation (6.1.4) as a propagation vector *k*.

$$k_\omega = \frac{n_\omega \omega}{c} , k_{2\omega} = \frac{n_{2\omega} 2\omega}{c}$$

(6.1.4)

The mismatch of the momentum associated with the electromagnetic waves is presented in Equation (6.1.5).

$$\Delta k = k_{2\omega} - 2k_\omega = \frac{2\omega}{c}(n_{2\omega} - n_\omega)$$

(6.1.5)

The phase matching condition occurs when $\Delta k = 0$, thus $n_{2\omega} = n_\omega$. However, due to dispersion usually $n_{2\omega} \neq n_\omega$. There are two types of phase matching that can be achieved for frequency doubling, *critical* and *non-critical*.

Angular phase matching or *critical phase matching* is achieved by a particular orientation of the uniaxial crystal with respect to the propagation direction of the incident beam. Equation (6.1.6) relates to the geometry for critical phase matching, as illustrated in Figure 6-2 with the index ellipsoid.

$$\frac{1}{n_e(\theta')^2} = \frac{\sin^2 \theta}{n_e^2} + \frac{\cos^2 \theta}{n_o^2}$$

(6.1.6)
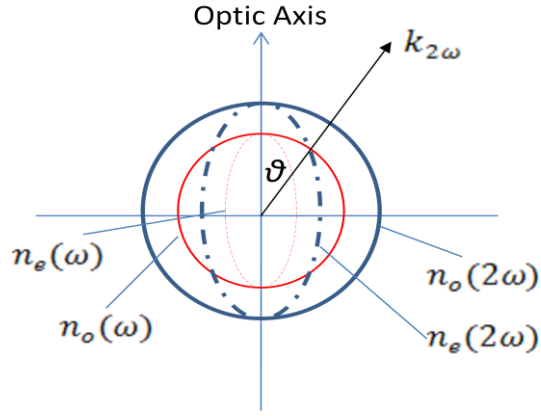
Figure 6-2: Refractive index ellipsoid indicating the ordinary and extraordinary indices for the fundamental, *ω* and doubled frequency, *2ω*. Included is the frequency doubled propagating wave vector, $k_{2\omega}$ and its phase matching angle *θ* with the optic axis.

In order to satisfy the phase matching condition, $\Delta k = 0$, the value of θ can be calculated under the conditions $n_e(\theta') = n_e$ for $\theta'=90°$ and $n_e(\theta') = n_o$ for $\theta'=0$. Therefore using Equation (6.2.0) and the conditions listed in Figure 6-3, an evaluation is performed in the case of a *negative type I* uniaxial crystal such as that of the chosen β-BBO. The fundamental frequency ω with an ordinary index produces frequency doubled 2ω and an extraordinary index. Through substitution of the correct variables, Equation (6.1.6) introduces the phase matching angle θ_m.

$$\frac{1}{n_o(\omega)^2} = \frac{\sin^2 \theta_m}{n_e(2\omega)^2} + \frac{\cos^2 \theta_m}{n_o(2\omega)^2} \tag{6.1.7}$$

Through substitution using the trigonometric relationship $\cos^2 \theta = 1 - \sin^2 \theta$ the Equation (6.1.7) reduces to Equation (6.1.8), resolving the phase matching angle.

$$\sin^2 \theta_m = \frac{n_o^{-2}(\omega) - n_o^{-2}(2\omega)}{n_e^{-2}(2\omega) - n_o^{-2}(2\omega)} \tag{6.1.8}$$

191

Type I   Type II

positive

$$n_e^1 \omega_1 + n_e^2 \omega_2 = n_o^3 \omega_3 \qquad\qquad n_o^1 \omega_1 + n_e^2 \omega_2 = n_o^3 \omega_3$$

$$n_e(\theta, \omega) = n_o(2\omega) \quad \text{(P. M.C.)} \quad n_o(2\omega) = \frac{1}{2}[n_o(\omega) + n_e(\theta, \omega)]$$

negative

$$n_o^1 \omega_1 + n_o^2 \omega_2 = n_e^3 \omega_3 \qquad\qquad n_e^1 \omega_1 + n_o^2 \omega_2 = n_e^3 \omega_3$$

$$n_e(\theta, 2\omega) = n_o(\omega) \quad \text{(P. M.C.)} \quad n_e(\theta, 2\omega) = \frac{1}{2}[n_o(\omega) + n_e(\theta, \omega)]$$

Figure 6-3: Uniaxial crystal phase-matching methods and phase matching conditions (P.M.C) for Type I and Type II crystals, for positive ($n_o < n_e$) and negative ($n_e < n_o$). The insert diagram shows an example of a negative Type I uniaxial crystal, indicating the phase matching angle, θ made with the optic axis, (O.A.).[51] [52]

An aspect associated with nonlinear crystals is something known as the *beam walk-off angle*. This angle is made between the ordinary and extraordinary beams that have the same phase velocity but travel in different directions, as illustrated in Figure 6-6. The angle ρ from the diagram can be formulated based on previous evaluations using the ordinary and extraordinary indices [52].

$$\tan \rho = \frac{1}{2}\left(\frac{(n_e^2 - n_o^2)\sin 2\theta}{n_e^2 \cos^2 \theta + n_o^2 \sin^2 \theta}\right) = \frac{n^2(\theta)}{2}\left(\frac{1}{n_o^2} - \frac{1}{n_e^2}\right)\sin 2\theta \qquad (6.1.9)$$

When the phase matching angle θ is 90° then the walk-off angle ρ is 0, this condition is referred to as *90° phase matching* or *non-critical phase matching* (NCPM). The usefulness of NCPM is prevalent in nonlinear crystals that have their refractive indices tuned through temperature control. An advantage to this is potentially high conversion efficiencies due to the fact that the beam can be much more tightly focussed into the crystal and beam alignment is not as critical. For other crystals that are not temperature sensitive, the walk-off angle has the potential to limit the conversion efficiency, since the orientation of the crystal must be precise to maximise nonlinear interaction within the crystal. The acceptance length l_{acc}, as

192

shown in Figure 6-4, is the point at which the frequency doubled beam deviates from the fundamental beam and they no longer overlap.
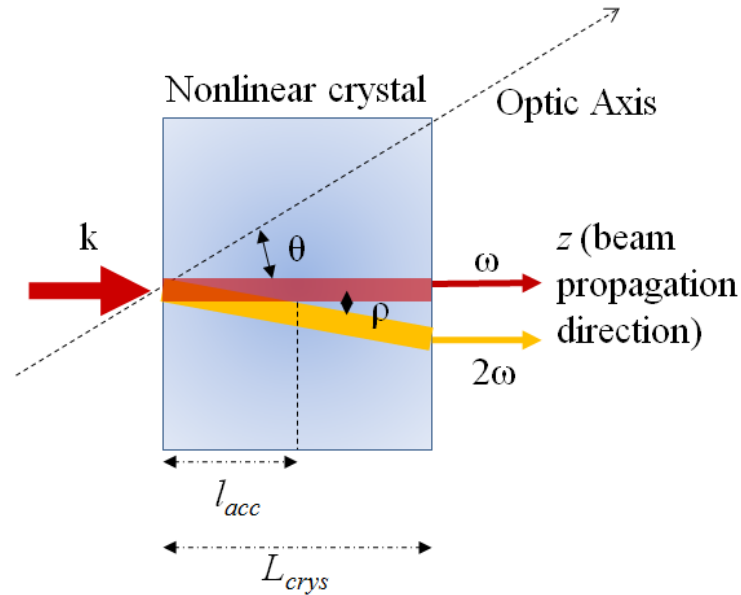
Figure 6-4: The beam walk-off angle ρ with respect to the phase matching angle θ and the optic axis in a nonlinear crystal, where the input *k* wavevector and fundamental frequency ω with frequency doubled 2ω outputs. The acceptance length, l_{acc} indicated is the length before the frequency doubled beam 'walks-off' the fundamental beam.

The length of the crystal is the space through which the fundamental beam interacts with the material to produce frequency doubled output. However, the fundamental and second harmonics travel at different speeds due to the wavelength dependent refraction through the material. The second harmonic will have reduced efficiency when it is out of phase with the fundamental. Therefore in order to achieve phase matching, the coherence length needs to have a phase difference of π between the two beams, i.e. when $\frac{\Delta k l}{2} = \pi$. The coherence length, l_c of the crystal at normal incidence is calculated using Equation (6.1.5) such that $l_c = \frac{\pi}{\Delta k}$ and is the distance at which the frequency doubled power is at its maximum. The second harmonic is suppressed when the crystal length $L_{crys}=ml_c$, where $m=2n+1$.

The intensity of the frequency doubled beam at a distance l inside the nonlinear crystal is described in Equation (6.2.0) [55]. The Δk is the same as in Equation (6.1.5), c and ε_0 are constants, n implies the refractive indices (which can be included

as n_o, n_o and n_e for a *type I negative* uniaxial crystal), d_{eff} is the effective nonlinear coefficient and the fundamental beam intensity is I_ω.

$$I_{2\omega} = \frac{2\omega^2 d_{eff}^2 l^2}{n^3 c^3 \varepsilon_0} I_\omega^2 \frac{\sin^2\left(\frac{\Delta kl}{2}\right)}{\left(\frac{\Delta kl}{2}\right)^2} \qquad (6.2.0)$$

Considering the fundamental input as a propagating Gaussian beam, having a radial intensity distribution, the waist size and its location in the crystal along with the divergence angle are important parameters to evaluate conversion. The relationship between intensity and power is shown in Equation (6.2.1) with ω_0 corresponding to the $1/e^2$ half width of the intensity beam.

$$I_\omega = \frac{P_\omega}{\pi \omega_0^2} \qquad (6.2.1)$$

The conversion efficiency [55] over the length of the crystal L_{crys} is given in equation (6.2.2).

$$\eta = \frac{2\omega^2 d_{eff}^2 L_{crys}^2}{n^3 c^3 \varepsilon_0} I_\omega \, \text{sinc}^2\left(\frac{\Delta k L_{crys}}{2}\right) \qquad (6.2.2)$$

In phase matching, the efficiency of nonlinear conversion is limited to a finite frequency spectrum of the interacting fundamental and second harmonic waves. The consequences in deviating from the phase matching condition at a fixed length of nonlinear crystal, is a reduction of the SHG power which is given in Equation (6.2.3) [56].

$$\frac{P_{2\omega}}{P_{2\omega}^{max}} = \text{sinc}^2\left(\frac{\Delta k L_{crys}}{2}\right) \qquad (6.2.3)$$

This deviation from the phase matching angle, $\Delta\theta = \theta - \theta_m$ is shown in Figure 6-5. The values used for the calculation refer to a β-BBO negative type I nonlinear crystal with a fundamental wavelength of 1180 nm, phase matching angle θ_m of 21.4°, using a crystal of length 2 mm, having refractive indices $n_o(\omega)=1.65$, $n_o(2\omega)=1.67$ and $n_e(2\omega)=1.55$ found using Equation (6.2.2). The full width at half maximum (FWHM) value of the $\Delta\theta$, acceptance angle using these parameters results in 0.3 mrad-cm,

which is comparable with ~0.7 mrad-cm for conversion from 1080 nm to 540 nm [57].
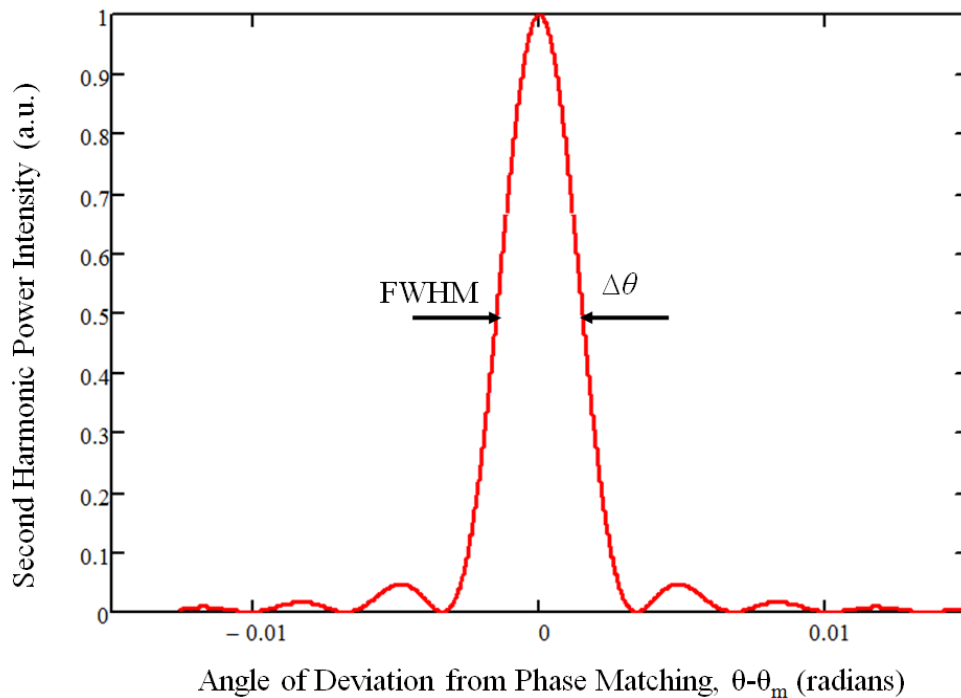
Figure 6-5: Second harmonic power as a function of the deviation from the phase matching angle.

6.2.2.2 Nonlinear Crystal Choice for a Microchip Laser

The selection of a nonlinear crystal is not a trivial matter, and is based on the performance constraints of the crystal for the required application. In this instance the requirement is for use in a frequency doubled *quasi-monolithic* SDL operating at the fundamental wavelength ~1180 nm. The crystal must therefore have transparency across both the fundamental and second harmonic wavelengths.

Due to the integration of the doubling crystal with the SDL in a double bond arrangement, this introduces the constraint on beam positioning within the crystal. The fundamental beam shall not be focussed into the centre of the crystal, but shall remain planar with roughly the same diameter as that of the mode size onto the SDL chip, as illustrated in Figure 6-8. The crystal must therefore have a low sensitivity to angular alignment.

The dimensions of the crystal are key, particularly the length which needs to be thin enough to allow for bonding to the diamond heatspreader, yet requires sufficient length to provide conversion from the infra-red to the yellow/orange. Therefore the crystal should have a large effective nonlinear coefficient to enable frequency doubling to take place over shorter distances. Microchip lasers such as those developed in St Andrews University by Sinclair *et al.* [53] have highlighted some issues with regards compact cavity configurations and SHG. One such issue refers to the stability of their plane-plane cavity, where thermal loads within the gain medium induced a thermal lens effect which acted to self-align the laser. In an SDL with the length of the gain region $< 2\mu m$, thermal lensing may have some contribution towards the cavity but it is the overall laser cavity length between the DBR mirror and external mirror which influences the laser mode size. The stability depends upon the radius of curvature of the external mirror, with any additional thermal lensing contributions. Therefore with the nonlinear crystal taking up a large proportion of the cavity, the length must be factored into the laser design. Drawing from the evaluations for optimal nonlinear crystal length developed by Smith [48], losses need to be kept to a minimum to provide high intracavity powers to enable good conversion efficiency. Therefore a low loss cavity requires a shorter length of nonlinear crystal.

Furthermore, the crystal does not have a separate temperature controller, but shall be at the temperature determined by the interface with the diamond heatspreader. In this respect the crystal should not be thermally sensitive, but should favour critical phase matching operation.

196

Table 6.2: Specifications for nonlinear crystals KNbO₃, LBO and β-BBO[54].

Nonlinear Crystal Material	KNbO$_3$	LBO	β-BBO
Crystal Type	Biaxial	Biaxial	Uniaxial
Phase Matching Type	I-CPM	I-CPM	I-CPM
Transparency Range (nm)	450 - 4500	160 - 2600	190 - 3500
Effective Nonlinear Coefficient, $d_{eff,}$ (pm/V) (θ,ϕ)	12.9 (θ =25.5, ϕ=90)	0.85 (θ =90, ϕ=4.1)	2.1 (θ =21.4, ϕ=0)
Acceptance Angle, $\Delta\theta$ (mrad/cm)	687.5	1136	974
Spectral Acceptance, $\Delta\lambda$ (nm/cm)	0.38	7.13	3
Walk-off Angle (mrad)	56	< 2.6	54
Temperature Acceptance, ΔT (°C/cm)	~0.6	5.2	51
Hygroscopic Susceptibility	Low	Low	Very Low

Table 6.2 provides a comparison between three of the nonlinear crystals for SHG operation at the 1180 nm fundamental wavelength. The KNbO$_3$ material has been typically used in non-critical phase matching conditions, which has benefits for not requiring angular precision, yet in this application temperature management of the crystal cannot be performed due to the cavity configuration. Added to this, the low hygroscopic property of the material may impede the bonding procedure to the heatspreader, thus making it an undesirable candidate for this application. The LBO crystal and β-BBO are close choices, with the LBO having a larger acceptance angle and smaller walk-off but a smaller effective nonlinear coefficient. As this is an important parameter for a thin enough crystal for bonding purposes as well as the lower hygroscopic property, the β-BBO crystal was chosen for use in the microchip SDL configuration.

6.2.2.3 Laser Cavity Configurations

The model developed by Kim *et al.* [58] for V-cavity configuration frequency doubled SDL, shall be adopted for use here. The inclusion of the BRF and the second harmonic generation crystal in combination with a CVD diamond heatspreader has been shown to introduce significant loss mechanisms into the cavity. A 7% reduction

in output power has been measured by Kim *et al.* [59], which conveys the importance in correct alignment of the birefringent sensitive elements in the cavity to achieve optimal output.
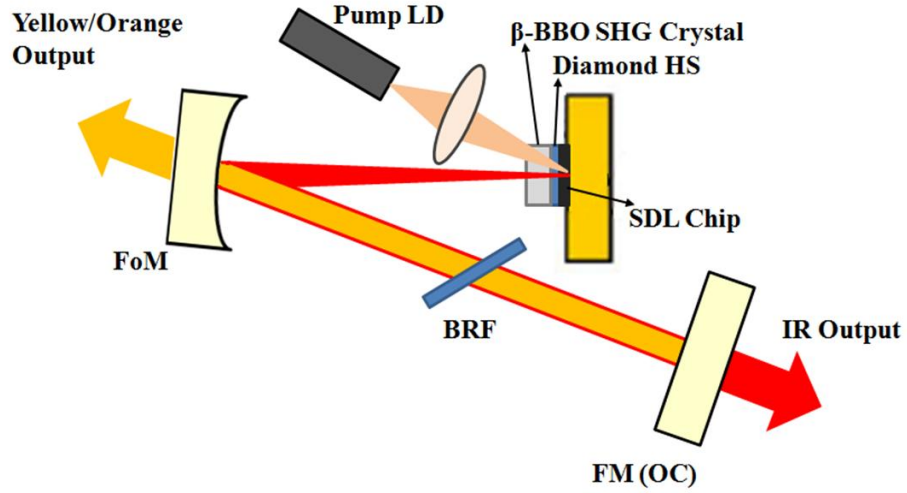

Figure 6-6: The V-cavity configuration based on Kim et al [60], adapted with the double bonded SDL chip, Diamond HS and β-BBO nonlinear crystal. Includes are the birefringent filter *BRF* between the folding mirror *FoM* and the output coupler/Flat mirror *FM (OC).*

The model calculates the second harmonic power P_{SHG} given in Equation (6.2.4) based on its mode size A_{shg} and nonlinear coupling coefficient K, which is expressed in Equation (6.2.5). The variables used in these equations are based on the system described above, where the mode size is close to that of the fundamental due to its proximity next to the SDL chip, the pump wavelength λ_p is 808 nm, the fundamental wavelength λ_l is 1180 nm, the length of the gain medium l_g is 2 μm, the pump threshold P_{th} is taken as 600 mW, the absorption efficiency η_{abs} and the confinement factor Γ use the values 0.66 and 2 respectively.

$$P_{SHG} = \frac{1}{4K}\left(-1 + \sqrt{1 + 4K\frac{\Gamma\eta_{abs}(P_p - P_{th})}{A_{shg}l_g\alpha_L}\frac{\lambda_p}{\lambda_l}}\right)^2 A_{shg} \qquad (6.2.4)$$

The variables used in the expression for the nonlinear coupling coefficient K for Equation (6.2.5) include the permeability μ_0 and permittivity ε_0 coefficients in free space, the speed of light c, the fundamental angular frequency ω_f, and associated crystal variables; the crystal length L_{crys}; effective nonlinear coefficient d_{eff}; ordinary

n_o and extraordinary n_e refractive indices; and the phase matching condition Δk from Equation (6.1.5).

$$K = 4\sqrt{\frac{\mu_0}{\varepsilon_0}}\frac{\omega_f^2 d_{eff}^2 L_{crys}^2}{n_o^2 n_e c^2}\,\text{sinc}^2\left(\frac{\Delta k L_{crys}}{2}\right) \qquad (6.2.5)$$
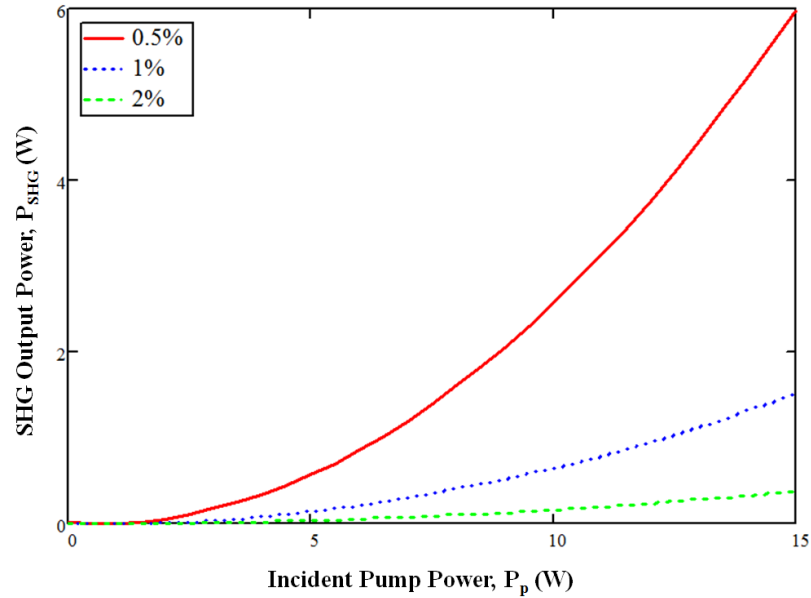
Figure 6-7: Simulated SHG output power for loss α_L values of 0.5%, 1% and 2%.

The mode diameter sizes within the region of the bonded components of the semiconductor chip, the diamond heatspreader and the β-BBO crystal are illustrated in Figure 6-8. The mode size within the nonlinear crystal was marginally larger at 78.7 µm compared with 77.5 µm incident onto the chip.
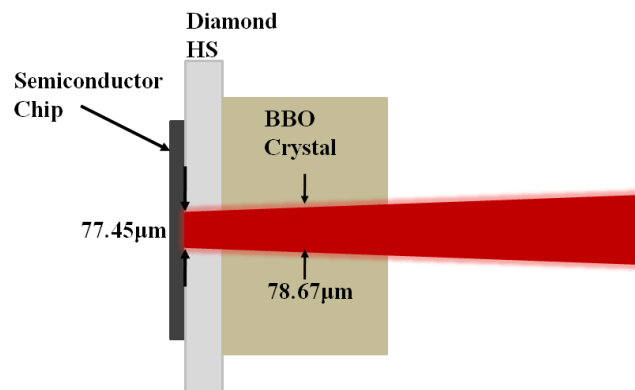
Figure 6-8: Beam incident onto the semiconductor chip, and at the centre of the BBO crystal, indicating the beam diameters.

With the conversion efficiency directly proportional to the fundamental intensity I_ω, as stated in Equation (6.2.2), the power density into the crystal is therefore an important factor for conversion. Using the relationship between the intensity and mode size from $I_\omega = \frac{P_\omega}{\pi \omega_o^2}$ the efficiency was calculated for a range of mode sizes as shown in Figure 6-9. The crystal length was kept at 2 mm with an effective nonlinear coefficient value for the negative type I β-BBO crystal of 2.1 pm/V. From this evaluation the mode radius of 40 μm inside the crystal for this V-cavity configuration, has an expected conversion efficiency >40%.
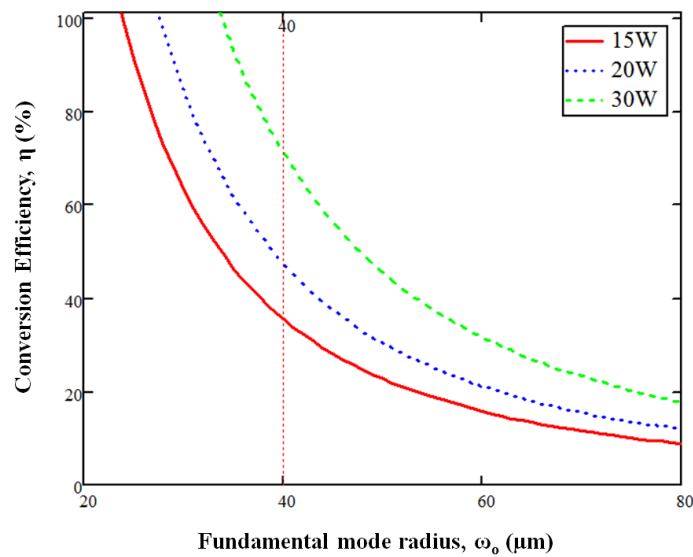

Figur 6-9: Theoretical conversion efficiencies across a range of fundamental mode radius sizes, for powers P_ω=15W, 20W and 30W.

In order to achieve higher efficiencies, reduced mode sizes with increased fundamental power would be necessary, which highlights the need to keep intracavity losses to a minimum. Furthermore the curved external mirror must be designed to allow a smaller mode size, whilst maintaining laser cavity stability.

Turning our attention to the microchip SDL, a possible configuration is illustrated in Figure 6-10. There are many variables to consider for this more complex cavity design. The inclusion of the microlens at the top surface of the nonlinear crystal introduces some limitation as to the focusing lengths of the beams within the compact cavity. This has been demonstrated by Laurand *et al.* [61] in studies using

microlensed microchip SDLs, in which their deposition technique limited the height h of the lens to that of ~0.75µm. Furthermore the mode matching conditions of the fundamental mode size and the pump beam spot radius onto the semiconductor chip should be $<2\omega_0$ for TEM_{00} output, above this higher order modes are allowed to oscillate. The pump beam conventionally is fibre delivered, thus mode matching relies on the selection of the pump delivery optics and focusing lens. In addition, the required specifications of coatings deposited onto the microlens should be anti-reflective at the pump wavelength of 808 nm, whilst highly reflective for the fundamental 1180 nm and provide sufficient output coupling of the 590 nm SHG light.
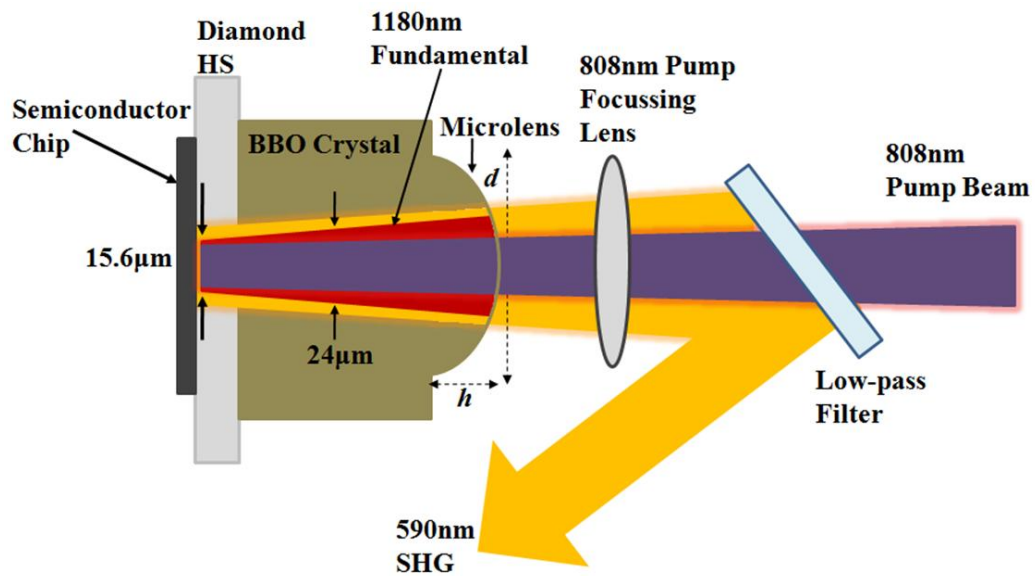
Figure 6-10: Microchip configuration indicating an 808nm pump beam (*purple*) at normal incidence focused onto the semiconductor chip, with the 1180 nm fundamental (*red*) within the micro-cavity and the 590 nm (*orange*) SHG output.

Laser stability for the microchip configuration, as presented in Figure 6-10, has the length of the cavity composed entirely of the heatspreader and the nonlinear crystal. As described in Chapter 4, the stability shows interdependency on the radius of curvature of the external mirror which is exhibited in the region of *zone I* in Figure 4-12, where $L_c < R_c$. Figure 6-11 illustrates the mode radius profiles for a range of microlens R_c values based on different lens diameters. These curves stem from the microlensed system [61, 62] evaluations using Equation (6.2.6) to determine the microlens radius of curvature and Equation (6.2.7) for the mode radius. For these

calculations, the microlens diameter is d with the height h limited to ~0.75 μm, the length of the cavity L_c and using the refractive index provided by the β-BBO crystal $n_o(\lambda_f)=1.652$ due to its contribution to a larger proportion of the cavity.

$$R_c = \frac{d^2 + 4h^2}{8h} \qquad (6.2.6)$$

$$\omega_0 = \sqrt{\left(\frac{L_c \lambda}{n\pi}\sqrt{\frac{nR_c}{L_c} - 1}\right)} \qquad (6.2.7)$$
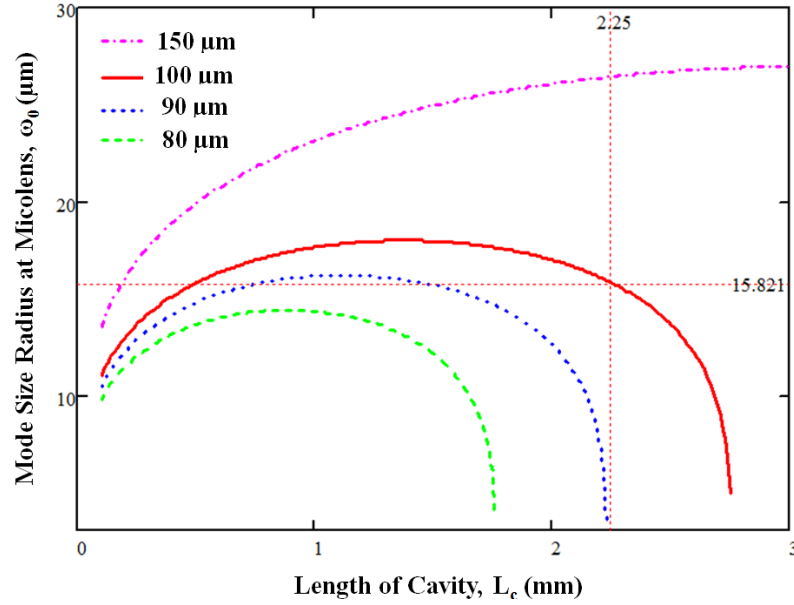
Figure 6-11: Microlens mode sizes with lens diameters d 150 μm, 100 μm, 90 μm and 80 μm over a range of cavity lengths for a frequency doubled microcavity SDL.

Based on these estimates, it is possible to obtain a mode size of ~16μm onto the SDL chip using the microlens approach for a cavity with a 2 mm long crystal and 250 μm diamond heatspreader. This enhances the prospect for higher conversion efficiencies within the nonlinear crystal. However such high powers concentrated into a smaller mode area may have consequences with regards higher thermal loads, which shall be explored in the next section.

6.2.2.4 Thermal Considerations of the Microchip

In solid state laser systems, thermal lensing has been known to distort the transverse mode and limit power scaling. However, in doped dielectric microchip lasers the thermal lensing can create a self alignment between the cavity and gain which

contributes to the overall success of such devices [53]. The thermal effects experienced in the frequency doubled microchip SDL may have an impact on the stability of the laser, in the same way that Magni [63] realised in solid-state laser design. Resonators experiencing a variable lens or thermal lens can operate in dynamic stability within certain cavity stability zones, and the mode spot size in the gain medium was insensitive to these lens variations. Due to the thermal sensitivity inherent in SDL operation, it is important to gauge the thermal response of the device, with the inclusion of the nonlinear crystal. Using finite element analysis the effect that the bonded β-BBO has on the thermal performance was explored. The parameters used for simulations are listed in Table 6.3.

Table 6.3: Finite element analysis parameters used in simulations

Symbol	Definition	Value
z_{window}	Window thickness	2.7×10^{-4} mm
z_{active}	Active region thickness	9.361×10^{-4} mm
z_{DBR}	DBR thickness	4.741×10^{-3} mm
z_{sub}	Substrate thickness	0.35 mm
z_{dia}	Diamond heatspreader thickness	0.25 mm
z_{BBO}	BBO nonlinear crystal thickness	2 mm
k_{window}	Window thermal conductivity	0.012 W/(mm.K)
k_{active}	Active region thermal conductivity	0.044 W/(mm.K)
k_{DBRz}	DBR axial thermal conductivity	0.0611 W/(mm.K)
k_{DBRr}	DBR radial thermal conductivity	0.0698 W/(mm.K)
k_{sub}	Substrate thermal conductivity	0.044 W/(mm.K)
k_{dia}	Diamond heatspreader thermal conductivity	2 W/(mm.K)
k_{BBO}	BBO nonlinear crystal thermal conductivity	0.0016 W/ (mm.K)
k_{indium}	Indium foil thermal conductivity	0.082 W/(mm.K)
α	Pump absorption coefficient in the gain	1430 mm^{-1}
P	Absorbed power contributing to heat	5 W
T_{sub}	Substrate temperature	0°C

The active region experiences a slight increase in temperature due to the bonded β-BBO crystal acting as a barrier for heat extraction, which is apparent in Figure 6-12 (b).
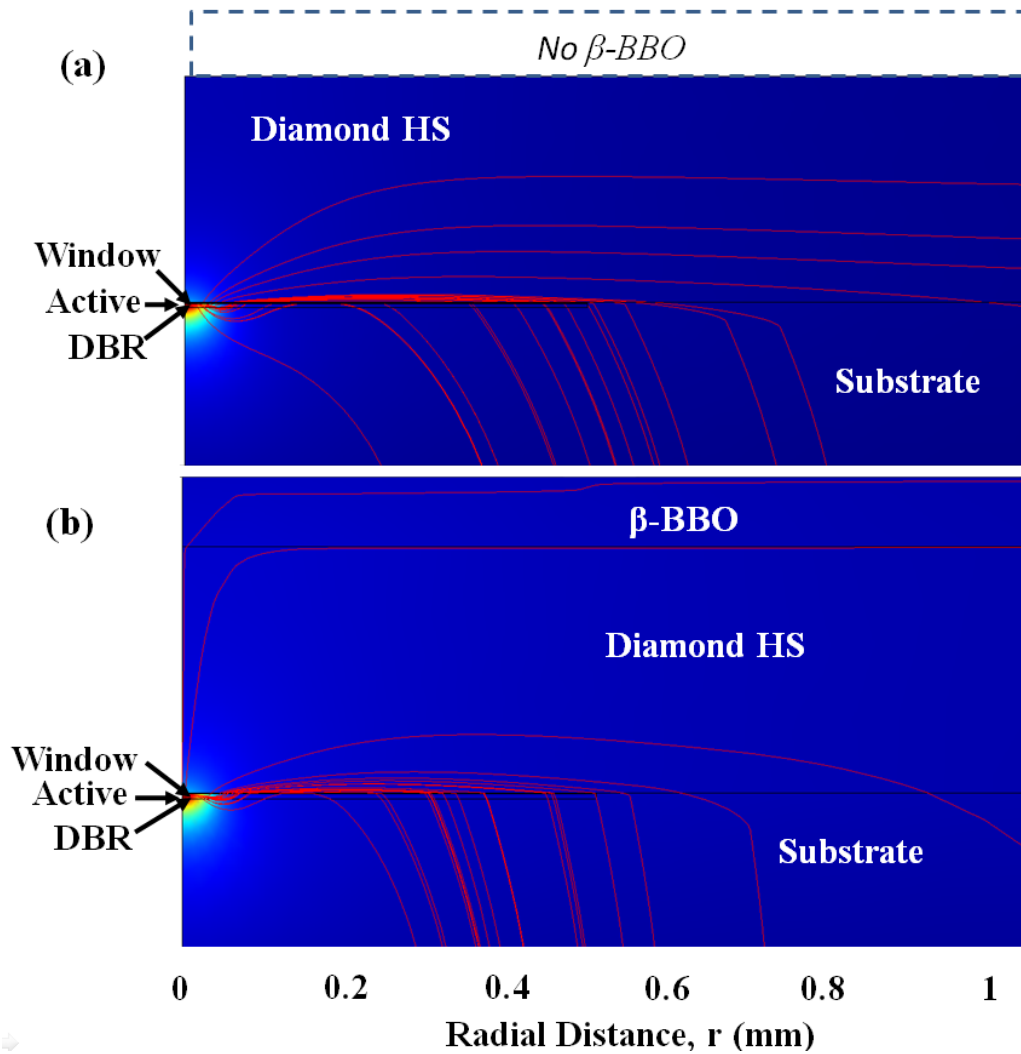
Figure 6-12: (a) Finite Element Analysis indicating the the heat flux paths (*red lines*) for the 1180 nm 10 QW GaInNAs/GaNAs/GaAs SDL with a diamond HS and pump spot radius w$_p$= 40 μm, (b) the same sample with the inclusion of the bonded β-BBO nonlinear crystal.

The increase in thermal resistance was found to be marginal at ~0.5 K/W between the two systems, as shown in Figure 6-13.
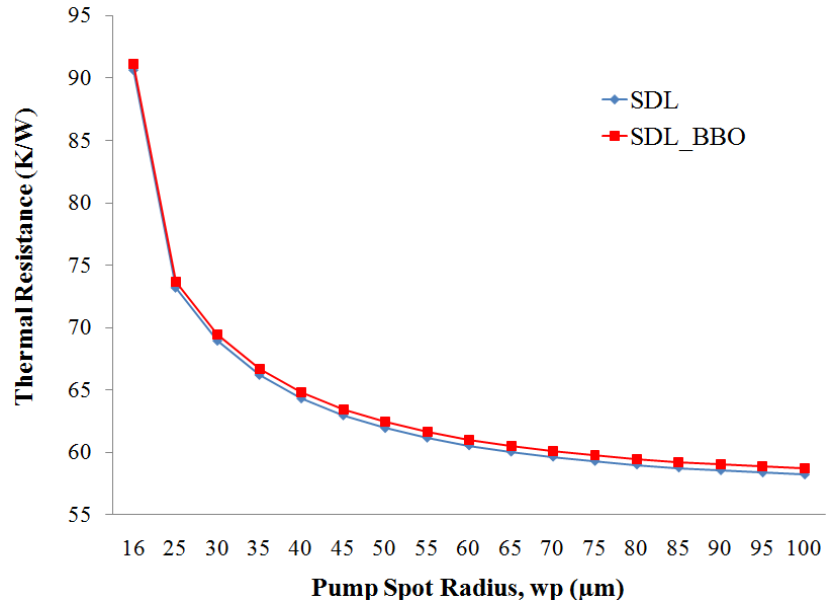
Figure 6-13: Thermal resistance comparison based on simulations of the 1180 nm GaInNAs SDL and the double bonded β-BBO SDL.

A thermal lens investigation was performed based on the above thermal simulations, to ascertain how much of a contribution this has to the stability of the microchip SDL, in terms of the microlens R_c. The axially averaged temperature change was used to convert to an equivalent optical path length using the thickness of the material, t and its thermo-optic coefficient $\frac{dn}{dT}$ used in Equation (6.2.8), where dT_{avg} is the axial average temperature and α is the thermal expansion coefficient of the material.

$$OL = \left[t + (\alpha dT_{avg}t)\right]\left[n + \frac{dn}{dT}dT_{avg}\right] \qquad (6.2.8)$$

The thermal lensing effects in most solid-state lasers manifest as refractive index changes and surface deformation to provide cavity stability [53]. The optical path length difference [64] [62] due to the thermo-optic effects in the SDL active region alters the point of overlap between the fundamental and second harmonic. The thermal focal length f_{th} relationship to the optical path length is expressed in Equation (6.2.9), where the optical path length at $r=0$ is $OL(0)$ and at a radial distance r is $OL(r)$.

$$OLD(r) = OL(0) - OL(r) = \frac{r^2}{4f_{th}} \qquad (6.2.9)$$

205

In an attempt to mode match the microcavity, the pump spot sizes were chosen to align with the calculated mode sizes using Equation (6.2.5). Given that the relationship of the focal length of the microlens with its radius of curvature R_c is $f=(nR_c/n-1)$ [62], the total focal length of the system has been formulated to account for the contribution of the thermal lens. Table 6.4 presents the results of the calculated microlens and simulated thermal focal lengths, which provides an initial indication that the thermal lens effect has a significant role in this application of a frequency doubled microlensed system. In light of these results, further analysis would be needed to assess how much of an impact this has on the system, with perhaps more accurate mode matching capability by factoring in thermal lens effects.

Table 6.4: Calculated results of ω_0 and f for a microlensed frequency doubled SDL, compared with simulated results using ω_p to obtain f_{th}, giving the total focal length of the system f_{total} (microlens height, h=0.75μm, diameters d=100μm, 150μm and 200μm for ω_0=16μm, 26.5μm and 32μm respectively).

Calculated Microlens Mode Radius, ω_0	Calculated microlens focal length, f	Pump mode radius, ω_p	Thermal lens focal length, f_{th}	Total focal length, f_{total} $\left(\frac{1}{f_{total}}=\frac{1}{f}+\frac{1}{f_{th}}\right)$[65]
16 μm	4.22 mm	16 μm	3.2 mm	1.8 mm
26.5 μm	9.5 mm	25 μm	4.6 mm	3.1 mm
32 μm	16.9 mm	30 μm	5.5 mm	4.2 mm

6.3 A Microchip Frequency Doubled SDL Operating in Yellow/Orange

Building upon the SDL microchip design, the following sections describe the construction and generation of yellow/orange laser light.

6.3.1 Double Bond: SDL Chip-Diamond Heatspreader-BBO Crystal

The bonding process was performed using the liquid capillary technique [66] as described in Chapter 3. Sample *AsN2906* was used with a GaInNAs/GaNAs/GaAs 10 QW material system, designed to operate around 1180 nm having been grown at ORC, Tampere, Finland. The semiconductor sample was cleaved to have dimensions

of approximately 3 mm^2, and bonded to a circular CVD diamond with diameter 4 mm and thickness ~250 μm. During this bonding procedure DI water was used to perform the bond. Due to the hygroscopic property of the nonlinear crystal β-BBO, methanol was used to perform the next stage of bonding to the crystal with dimensions 5x5x2mm^3. Figure 6-14 shows the bonded sample from three different perspectives, to illustrate the layering of the device and its dimensions. It is noticeable that the bond between the semiconductor and diamond heatspreader was a partial bond, with the fringes visible in the unbonded area as previously described in Chapter 3.
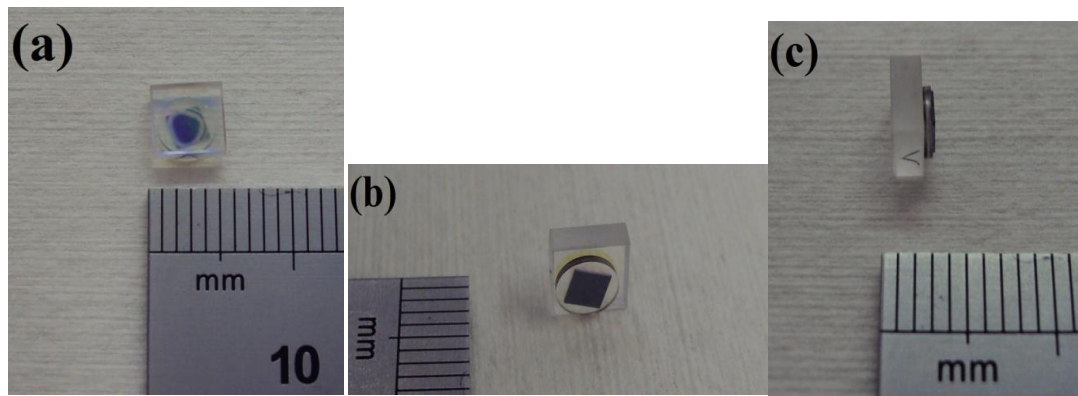
Figure 6-14: (a) Top view of the double bond between AsN2906 GaInNAs/GaAs semiconductor chip, diamond heatspreader and the β-BBO crystal, (b) back view of the device and (c) side view with the marked 'arrow' on the side indicating the AR@1180&590&808nm coating.

The bonded structure was placed into the water cooled copper mount, using the indium foil to aid thermal conduction. Orientation of the β-BBO crystal inside the mount was based upon markings provided by the supplier. A *dot* was placed on one edge of the crystal which corresponds to the surface which is parallel to the IR beam propagation plane. The crystal used in this experiment was cut with $\theta=21.3°$ and $\varphi=0°$ PM orientation.

The polarisation direction attributed to the fundamental beam of the SDL needs to be considered, to ultimately provide the best operation at the second harmonic. The beams must be orthogonal, in line with the type I second harmonic operation associated with the β-BBO uniaxial crystal. The semiconductor chip has intrinsic crystal birefringence associated with its growth axes, and in turn there is a QW gain

dichroism between the axes in the QW plane induced by elliptical pumping. Garnache *et al.* [67, 68] has explored this gain dichroism phenomenon in VCSEL and VECSEL devices. Notable observations were made into the effect of an elliptical pump spot onto the device due to the angled pump delivery method, which has also been adopted here. In the case of a circular pump spot incident onto the semiconductor chip, only one polarisation state is favoured. However, the elliptical spot allows any of the two polarisation states to be absorbed thereby increasing the associated gain.

6.3.2 Experimental Set-up

The laser was constructed as a three mirror cavity. The bonded structure had been placed in the water cooled copper mount and set up as shown in Figure 6-15 with a picture of the structure and folding mirror in Figure 6-16.
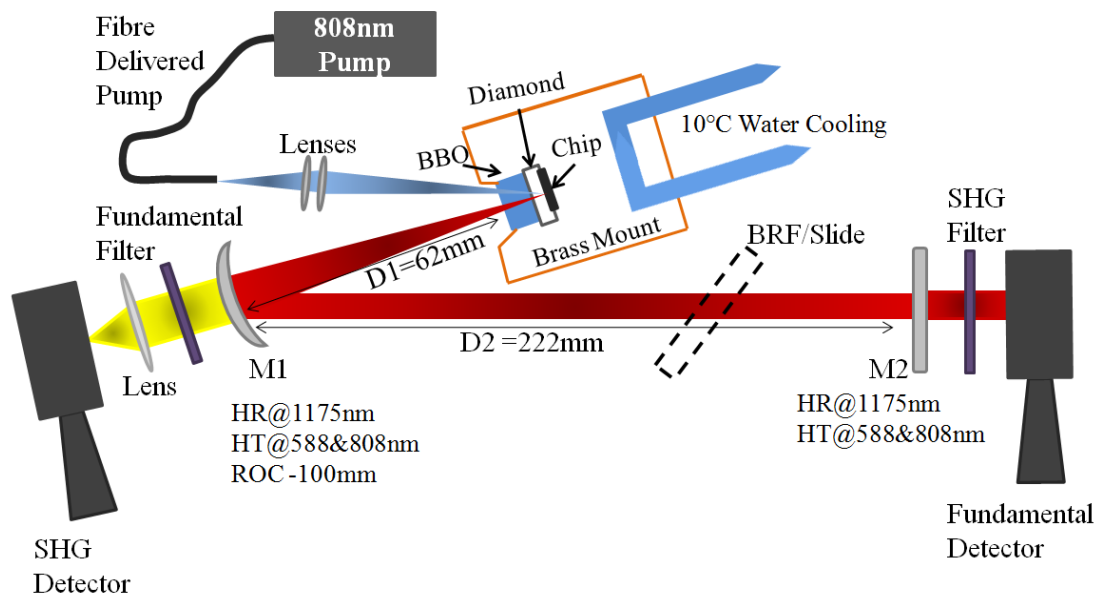

Figure 6-15: Schematic diagram of the SDL cavity consisting of an 808nm pump diode laser, the mounted double bonded chip-diamond-BBO structure, with HR cavity mirrors M1 and M2, and the birefringent filter *BRF* in the long arm of the cavity.
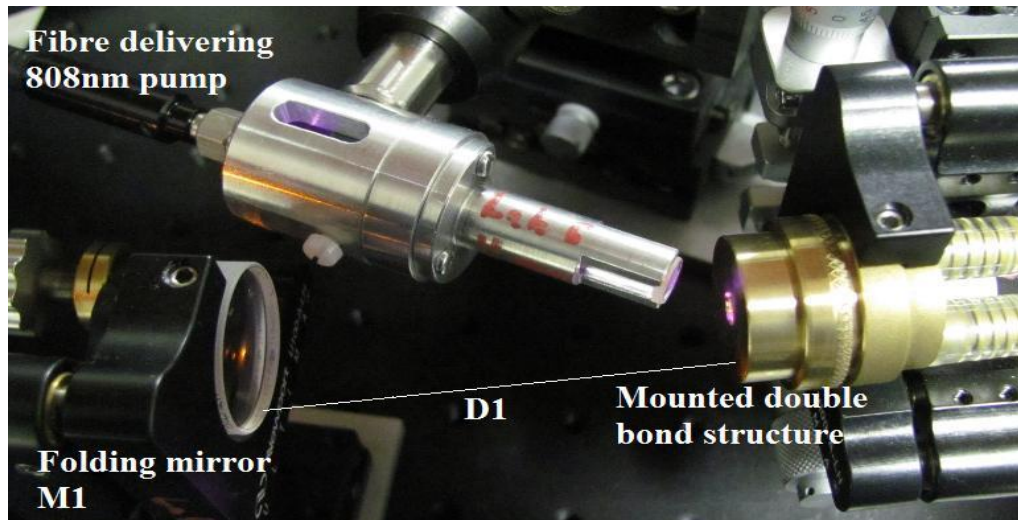
Figure 6-16: Picture of the 808 nm diode pump delivery through fibre and lenses, the mounted double bonded structure on the right and the folding mirror, M1 on the left.
(Photo courtesy of Dr. S. Calvez)

The SDL was optically pumped using a 50W 808 nm diode pump laser, delivered through a fibre with a 100 μm diameter core. The output from the fibre was collimated and focused with a pair of lenses, 14 mm and 11 mm respectively. The spot size radius of the pump was measured to be ~38 μm in air, which was aimed onto the surface of the semiconductor chip through both the β-BBO and Diamond heatspreader. The folding mirror, *M1* was placed at a distance *D1=62 mm* from the structure and the mirror *M2* placed *D2=222 mm* away, as indicated in Figure 6-13. The water cooling system was kept at a temperature of 10ºC to ensure the best performance at the fundamental wavelength as explained in Chapter 3. Notably no separate temperature control element was used for the nonlinear crystal.

During the course of experiments a 4 mm thick BRF, then separately a 1 mm thick uncoated slide were placed into the long arm of the cavity at Brewster's Angle, approximately 57° [69]. The uncoated slide provided a polarisation state discrimination element into the cavity, to select light with horizontal polarisation (i.e. state in the plane parallel to the optical table). The BRF was inserted to act as a wavelength selective element. These additional elements provided a platform to test the relationship between the fundamental and frequency doubled outputs. Consequently this also provides supporting data as to the effectiveness of the β-BBO crystal integrated as an SDL microchip device.

6.3.3 Results and Discussion
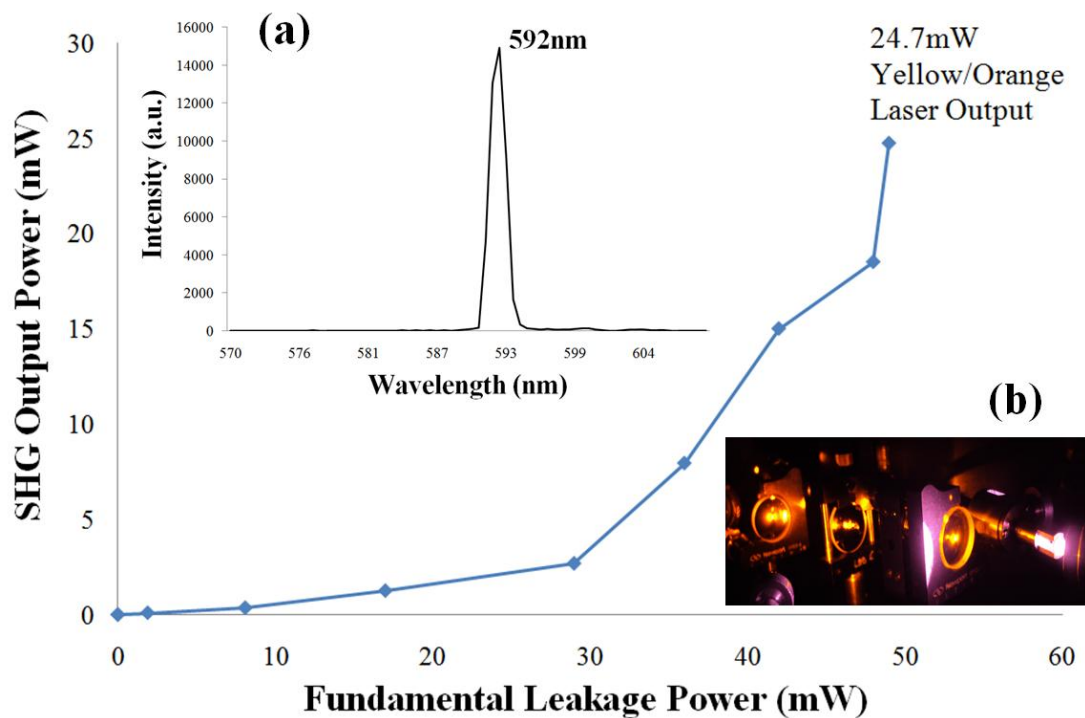
Figure 6-17: SHG output as a function of the Fundamental Leakage Power, inset (a) the SHG spectrum showing a peak at 592 nm and (b) photo of the yellow/orange laser output at the SDL folding mirror and immediately behind, focussing optics to the detector.

Figure 6-17 provides the free running output power of the microchip SDL operating at ~590 nm. Throughout the course of these experiments the distances between the cavity elements remained relatively stationary, with only slight modifications required for beam alignment.

The polarisation of the two signals was established using a *calcite Glan Thomson* polarising beamsplitter cube. The cube was 20 mm^3 in dimension in a manual rotational mount. The mode of operation of the cube splits a beam into two orthogonal polarised beams. Knowing the angle of the cube corresponding to horizontal and parallel polarisation directions can verify the polarised direction of the beams. The cube was placed at the output, external to the cavity, and rotated. Figure 6-18 presents the results for both the frequency doubled and fundamental outputs in

free running mode. The term free running refers to the laser output with no intracavity elements such as the BRF or uncoated slide.
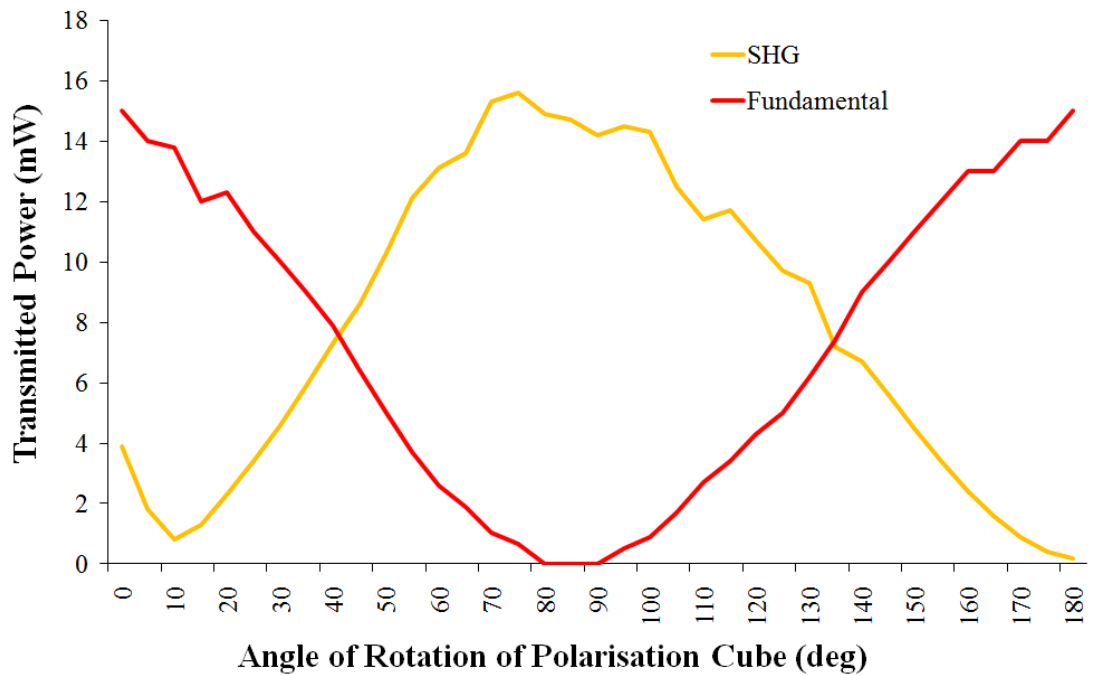
Figure 6-18: Graph of the transmitted powers of the fundamental and frequency doubled beams through 180° rotation of the polarisation cube.

It is apparent from the graph that the outputs have crossed polarisations as expected for this type I SHG.

The free running spectrum of the fundamental output was captured using an Agilent 86142B Optical Spectrum Analyser. The fundamental wavelength shift with increasing pump power is shown in Figure 6-19, using the power weighted averages of the fundamental beam spectra.
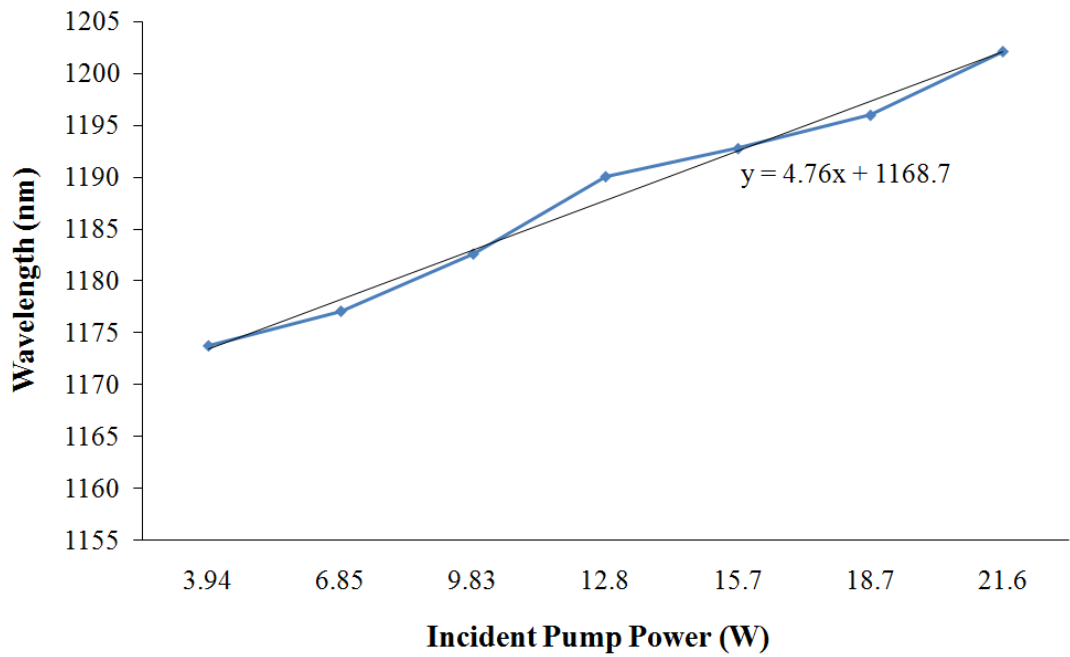
Figure 6-19: Wavelength shift with increasing incident pump power for free running fundamental output from the SDL.

The spectral output from the frequency doubled beam was captured using an Avantes Spectrum Analyser connected to the master input port, having a 1.5 nm resolution. A laptop having the associated software *Avasoft 7.3* installed was used to record the results. The frequency doubled signal was captured using a multi-mode fibre. To avoid saturation of the signal, the beam was offset with respect to the in-coupling fibre tip.

Wavelength tuning of the two outputs was performed through the insertion of the BRF approximately 80 mm from mirror *M2*, and rotated. The wavelength tuning spectra for the two beams is shown in Figure 6-20.
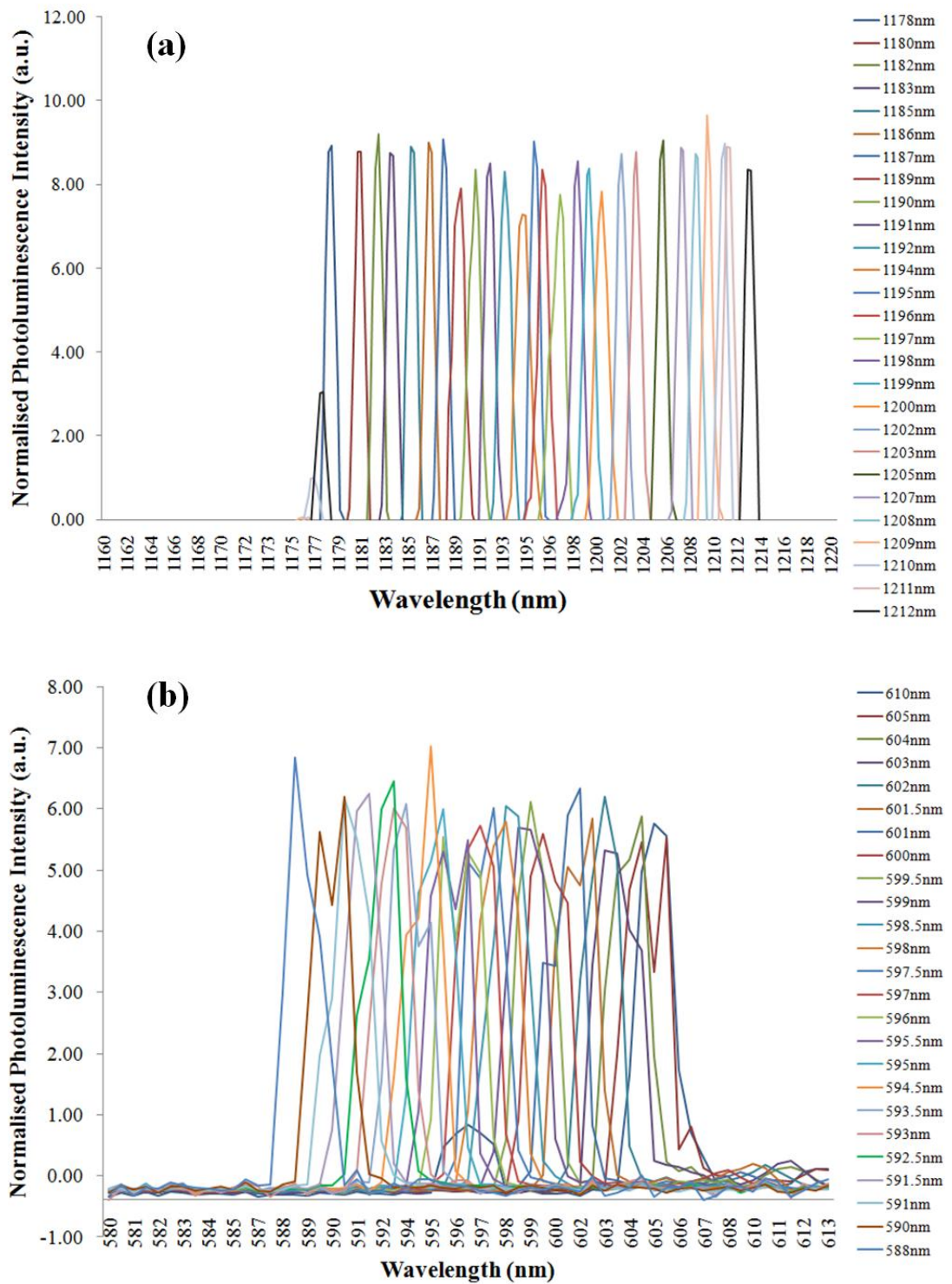
Figure 6-20: (a) Wavelength tuning spectra of the fundamental from 1178 nm to 1212 nm, (b) tuning spectra of the second harmonic from 588 nm to 610 nm.

The results are shown in the graph of Figure 6-21, spanning 34 nm wavelength tuning range. The fundamental *leakage* power was used as a measure of the increasing intracavity power. These results indicate a peak in power at 1209 nm for the frequency doubled output. This implies that the crystal was cut for preferred performance of 1209nm instead of 1180nm, with a calculated phase matching angle of θ = 21.1° at 1209 nm, instead of 21.4° for 1180 nm fundamental operation. The wavelength acceptance Δλ is calculated to be ≈ 6 nm from this data over a 0.2 cm (2 mm) crystal length, which is comparable to 3 nm/cm, with the specification information provided in Table 6.5, Section 6.2.3 for this β-BBO crystal.
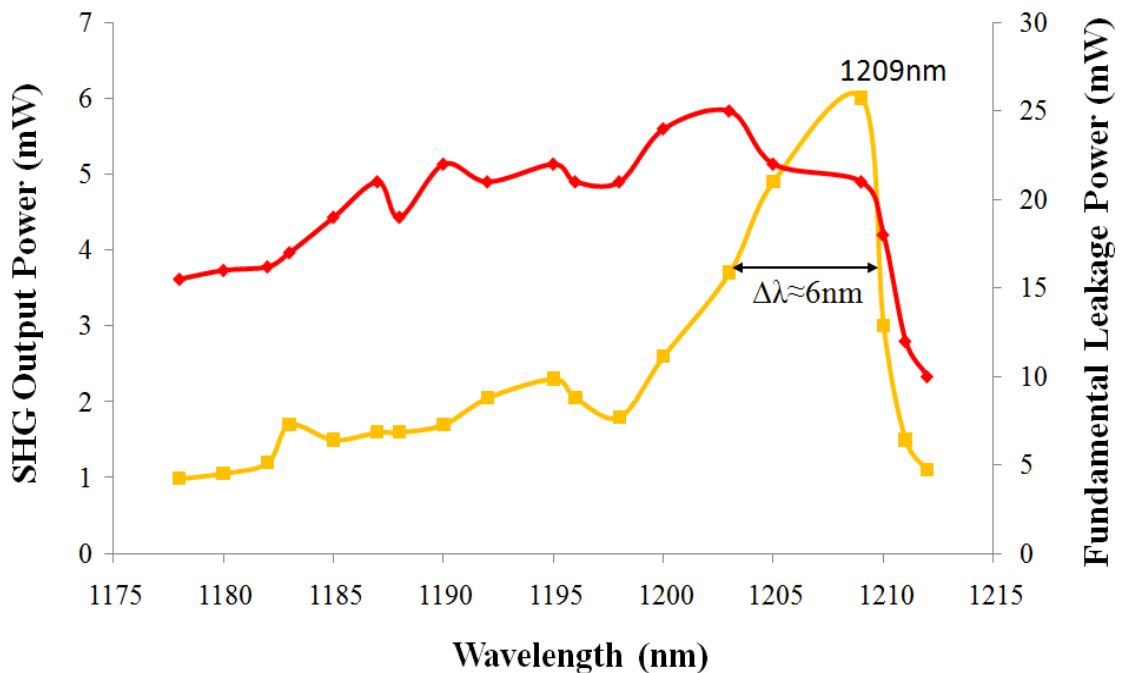
Figure 6-21: Graph of wavelength tuning using a 4 mm thick BRF.

The power transfer of the input pump power versus the outputs for both frequencies was performed in three cases; for a free running laser with no elements in the laser cavity, with an uncoated slide inserted at Brewster's Angle and finally with a BRF placed at Brewster's Angle and tuned to 1187nm.
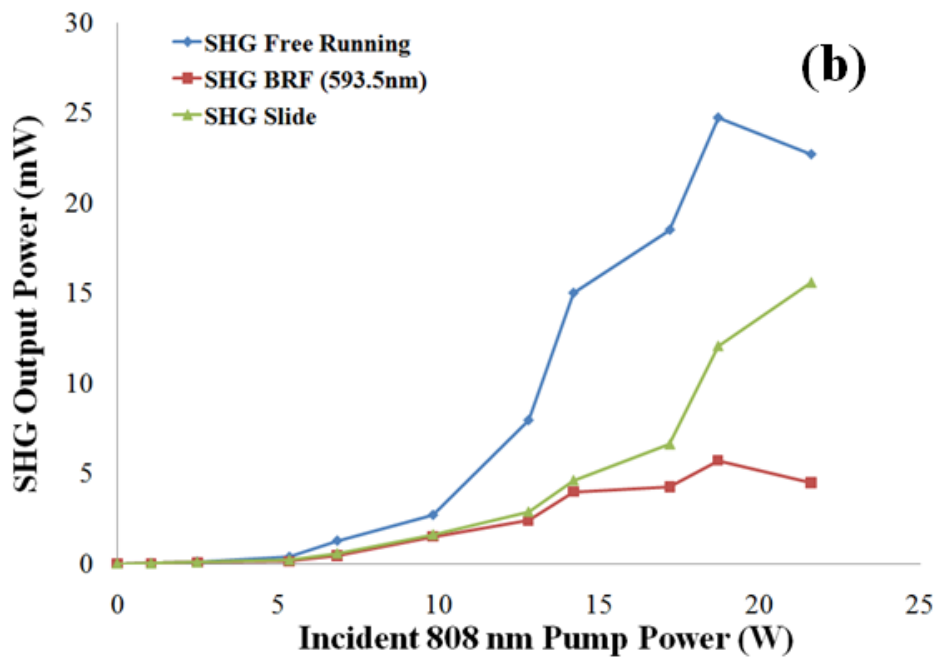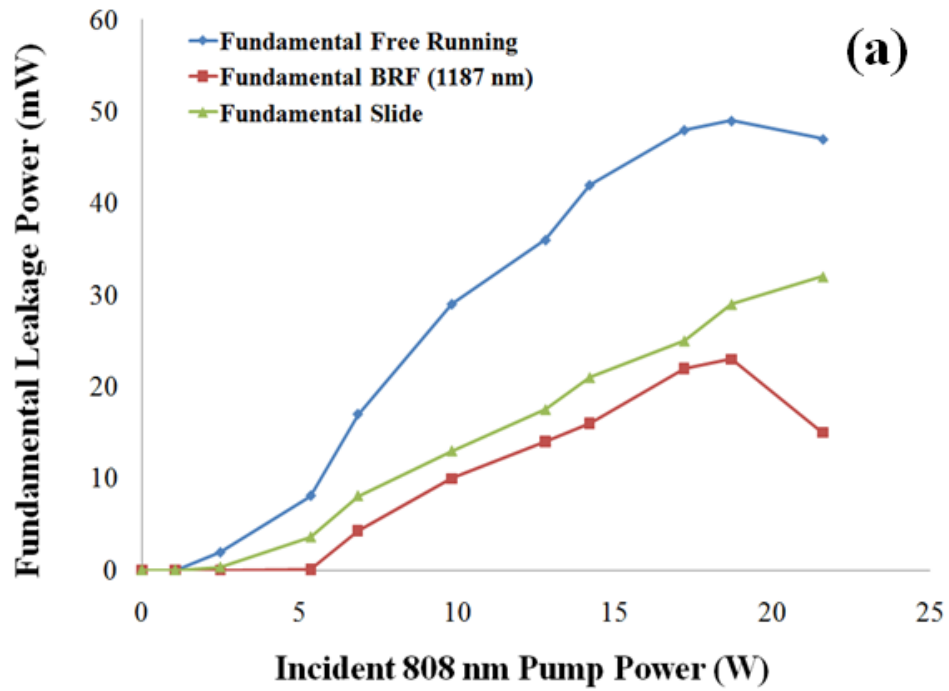
Figure 6-22: Power transfer curves for the (a) fundamental and (b) SHG, in free running mode, wavelength tuned using the BRF to 1187 nm (fundamental frequency) and with an uncoated slide.

On the assumption that the HR mirrors have a ~0.05% transmission, it is estimated that the intracavity power of the fundamental is ~19W, providing a maximum single-pass conversion efficiency to the second harmonic of ~0.07%. The inclusion of the

slide into the cavity reduces the fundamental output power by 35% and further reduction of 53% upon addition of the BRF. Thus inclusion of the BRF and slide add significant losses to the system, as shown in Table 6.5 with much higher threshold pump powers and lower slope efficiencies.

Table 6.5: Summary of Power Transfer Results for the Fundamental and SHG emissions

Operation	Max Output Power, P_{max}	Threshold Power, P_{th}	Slope Efficiency, η_{slope}
Fundamental			
Free Running	49 mW	2.5 W	0.3%
Slide Intracavity	32 mW	5.4 W	0.16%
BRF Intracavity	23 mW	6.9 W	0.15%
SHG			
Free Running	25 mW	6.9 W	0.2%
Slide Intracavity	16 mW	9.8 W	0.14%
BRF Intracavity	6 mW	9.8 W	0.05%

The relationship between the frequency doubled intensity and that of the fundamental beam was given in Equation (6.2.3), where $I_{2\omega}=\alpha I_{\omega}^{2}$ with α representing the beam propagation variable. Figure 6-23 shows a plot of the natural logarithm *ln* of the frequency doubled output power with respect to the fundamental output power, providing the relationship $ln(I_{2\omega})=ln(\sigma)+2ln(I_{\omega})$ on the assumption that the beam size remains constant. The power values are related to intensity through the expression in Equation (6.2.4), which shows an inverse relationship to the mode size of the beam.
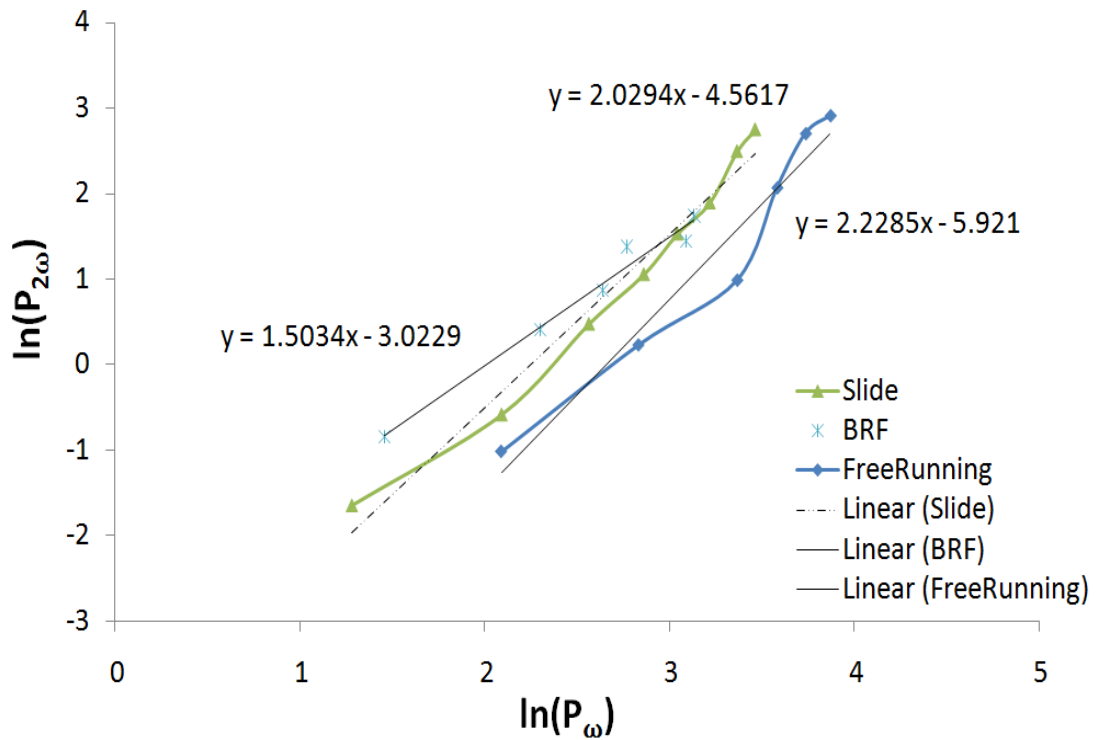
Figure 6-23: Graph of the relationship between the *ln(P_ω)* and *ln(P_2ω)* for the free running laser, an uncoated slide and a BRF tuned to 1187nm wavelength. The linear regression of this data provides the slope to evaluate *ln(I_2ω)=αln(I_ω)+ln(σ)*.

These results indicate that the relationship between the second harmonic intensity and that of the fundamental do not have the expected *squared* relationship as described in the equations. Instead the intensity adheres to that of Equation (6.3.0).

$$I_{2\omega} \propto I_\omega^\alpha \operatorname{sinc}^2\left(\frac{\Delta k L_{crys}}{2}\right) \qquad (6.3.0)$$

The variation in α is correlated to the changing mode size of the fundamental beam during multimode operation. The losses within the system from sources such as the intracavity element alignments, including their polarisation directions, may also contribute to mode size instabilities. Figure 6-24 shows the yellow/orange output beam reflected onto the optical bench divider. The beam shape may be attributed to the beam walk-off, which was relatively high at 54 mrads for a β-BBO doubling crystal. The 'tilting' effect may be attributed to wedged optics used within the laser cavity.

Figure 6-24: Picture of the yellow/orange frequency doubled output beam indicating a multimode profile.

The calculated external conversion efficiency of this system was found to be ~45%, based on Equation (6.2.5) and shown graphically in Figure 6-9 with a beam waist of 40µm, circulating fundamental power inside the cavity of 19 W and all HR mirrors at ~1180 nm. The maximum achievable conversion efficiency was ~0.1% with yellow output powers of ~25mW, obtaining a wavelength tuning range of ~22 nm. The disparity between calculated efficiency and empirical results highlight the improvements necessary in the fabrication and experimental set up, in order to achieve an optimum output. The solution will seek to improve conversion efficiency by selecting an SDL chip and nonlinear crystal that are better spectrally matched, in terms of gain control wavelength, emission linewidth, peak nonlinear conversion wavelength and acceptance bandwidth. Further, by ensuring that the laser operates in single lateral mode with low cavity losses. In addition, the true microchip configuration which eliminates the associated mirror reflections, but also creates a different mode of operation for the device, merits further investigation out-with the timeframe of this thesis.

6.4 Conclusions

The novelty of this research uses a GaInNAs/GaAs SDL in combination with a compact laser cavity design to produce yellow/orange laser output. The results have indicated the successful use of the double-bonded configuration, between the SDL chip, diamond heatspreader and nonlinear crystal, achieving ~25mW of yellow/orange laser light over a ~22 nm wavelength tuning range. Future prospects of such a device include the use of microlenses as described within this Chapter, with expected improvements to beam quality, yellow output powers and conversion efficiency.

References

[1]   H. Bi, X. Wang and M. Yuan "A clinical observation of krypton yellow laser photocoagulation for cystoid macular edema in nonproliferative diabetic retinopathy," *Chinese Journal of Ophthamology,* vol. 35, pp. 366 - 368, (1999).

[2]   D. R. Castillejos-Rios, K. Moffat and E. Yu "Dye yellow vs. argon green laser in panretinal photocoagulation for proliferative diabetic retinopathy: a comparison of minimum power requirements," *Canadian Journal of Ophthalmology,* vol. 27, pp. 243 - 244, (1992).

[3]   University of Malayasia, "A Randomised Control Trial Comparing the Effectiveness of Yellow 577 nm Laser to Conventional Green 532 nm Laser for Proliferative Diabetic Retinopathy", (2011) Available: http://clinicaltrialsfeeds.org/clinical-trials/show/NCT01044875

[4]   C. E. Max, K. Avicola, J. M. Brase, H. W. Friedman, H. D. Bissinger, J. Duff, D. T. Gavel, J. A. Horton, R. Kiefer, J. R. Morris, S. S. Olivier, R. W. Presta, D. A. Rapp, J. T. Salmon and K. E. Waltjen, "Design, layout, and early results of a feasibility experiment for sodium-layer laser-guide-star adaptive optics," *Journal of Optical Society of America A,* vol. 11, pp. 813 - 824, (1994).

[5]   D. M. Pennington, J. W. Dawson, A. Drobshoff, Z. Liao, S. Payne, D. Bonaccini, W. Hackenberg and L. Taylor, "Compact fiber laser approach to 589 nm laser guide stars," in *Conference on Lasers and Electro-Optics/International Quantum Electronics Conference and Photonic Applications Systems Technologies*, San Francisco, CA, USA, p. CFD1, (2004).

[6]   M. Duering, V. Kolev and B. Luther-Davies, "Generation of tuneable 589nm radiation as a Na guide star source using an optical parametric amplifier," *Optics Express,* vol. 17, pp. 437-446, (2009).

[7]   R. Holzlohner, S. Rochester, D. B. Calia, D. Budker, J. M. Higbie and W. Hackenberg, "Optimization of cw and Pulsed Sodium Guide Star Lasers," in

Adaptive Optics: Methods, Analysis and Applications (AO), San Jose, California, p. AOThB3P, (2009).

[8]   J. G. Cunha-Vaz and J. R. Faria Abreu,"The tunable dye laser in the management of retinal vascular disease," *International Ophthalmology,* vol. 12, pp. 193 - 196, (1988).

[9]   L. Brancaleon and H. Moseley, "Laser and Non-laser Light Sources for Photodynamic Therapy," *Lasers in Medical Science,* vol. 17, pp. 173 - 186, (2002).

[10]   N. S. Sadick and R. Weiss, "The utilization of a new yellow light laser (578nm) for the treatment of class I red telangiectasia of the lower extremities," *Journal of Dermatological Surgery,* vol. 28, pp. 21 - 25, (2002).

[11]   M. Jansen, G. P. Carey, R. Carico, R. Dato, A. M. Earman, M. J. Finander, G. Giaretta, S. Hallstein, H. Hofler, C. P. Kocot, S. Lim, J. Krueger, A. Mooradian, G. Niven, Y. Okuno, F. G. Patterson, A. Tandon and A. Umbrasas, "Visible Laser Sources for Projection Displays," *Proceedings of SPIE Projection Displays XII,* vol. 6489, pp. 648908-1 - 648908-6, (2007).

[12]   R. A. Hajjar, D. Kent and P. Malyak, "Laser displays using UV-excitable phosphors emitting visible colored light," US Patent 7474286, (2009).

[13]   W. Demtröder, Editor, *Laser Spectroscopy: Basic Concepts and Instrumentation*. Springer-Verlag, (2003).

[14]   T. D. Raymond, W. J. Alford, M. H. Crawford and A. A. Allerman, "Intracavity frequency doubling of a diode-pumped external-cavity surface-emitting semiconductor laser," *Optics Letters,* vol. 24, pp. 1127 - 1129, (1999).

[15]   J. E. Hastie, L. G. Morton, A. J. Kemp, M. D. Dawson, A. B. Krysa and J. S. Roberts, "Tunable ultraviolet output from an intracavity frequency-doubled red vertical-external-cavity surface-emitting laser," *Applied Physics Letters,* vol. 89, pp. 061114-3, (2006).

[16]   M. Fallahi, L. Fan, Y. Kaneda, C. Hessenius, J. Hader, H. Li, J. V. Moloney, B. Kunert, W. Stolz, S. W. Koch, J. Murray and R. Bedford,"5-W Yellow Laser by Intracavity Frequency Doubling of High-Power Vertical-External-Cavity Surface-Emitting Laser," *IEEE Photonics Technology Letters,* vol. 20, pp. 1700 - 1702, (2008).

[17]   B. Khoobehi, C. A. Char, G. A. Peyman and K. M. Schuele, "Study of the mechanisms of laser-induced release of liposome-encapsulated dye," *Lasers in Surgery and Medicine,* vol. 10, pp. 303-309, (1990).

[18]   Arrowhead Forensics. *Coherent TracER™ & TracER™ Compact*. Available: http://www.crime-scene.com/store/coherent_tracer.shtml

[19]   A. Härkönen, T. Leinonen, V.-M. Korpijärvi, J. Puustinen and M. Guina, "Multiple gain element GaInNAs disk laser generating narrow band (2.6 MHz) radiation at 1178 nm," in *The European Conference on Lasers and Electro-Optics (CLEO/Europe)*, Munich, Germany, p. CB_P15, (2011).

[20]   E. Gerster, I. Ecker, S. Lorch, C. Hahn, S. Menzel and P. Unger, "Orange-emitting frequency-doubled GaAsSb/GaAs semiconductor disk laser," *Journal of Applied Physics,* vol. 94, pp. 7397 - 7401, (2003).

[21]   A. Härkönen, J. Rautiainen, M. Guina, J. Konttinen, P. Tuomisto, L. Orsila, M. Pessa and O. G. Okhotnikov,"High power frequency doubled GaInNAs

semiconductor disk laser emitting at 615 nm," *Optics Express,* vol. 15, pp. 3224 - 3229, (2007).

[22]   V.-M. Korpijärvi, T. Leinonen, J. Puustinen, A. Härkönen and M. D. Guina, "11 W single gain-chip dilute nitride disk laser emitting around 1180 nm," *Optics Express,* vol. 18, pp. 25633-25641, (2010).

[23]   T. Leinonen, A. Harkonen, V.-M. Korpijarvi, M. Guina, R. J. Epstein, J. T. Murray and G. J. Fetzer, "High-power narrow-linewidth optically pumped dilute nitride disk laser with emission at 589 nm," Brussels, Belgium, pp. 772016-7, (2010).

[24]   A. Caprara, J. L. Chilla and L. A. Spinelli, "Intracavity Frequency-Converted Optically Pumped Semiconductor Laser," US Patent, (2000).

[25]   L. A. Spinelli, "Intracavity frequency-converted optically-pumped semiconductor laser," US Patent 6370168, (1999).

[26]   A. Mooradian, A. V. Shchegrov and J. P. Watson, "Projection Display Apparatus, System and Method," US Patent, (2005).

[27]   A. V. Shchegrov, "Frequency Stabalized Vertical Extended Cavity Surface Emitting Lasers," US Patent 7322704, (2006).

[28]   J.-Y. Kim, "High Efficiency Second Harmonic Generation Vertical External Cavity Surface Emitting Laser," US Patent, (2007).

[29]   S.-H. Cho, "Vertical external cavity surface emitting laser including second harmonic generation crystal having mirror surface " US Patent, (2007).

[30]   J. Baier and U. Weichmann, "Extended Cavity Semiconductor Laser Device With Increased Intensity" Netherlands Patent WO/2009/060365, (2009).

[31]   M. A. Holm, D. Burns, A. I. Ferguson and M. D. Dawson, "Single-frequency second-harmonic generation in a vertical external-cavity semiconductor laser," in *Conference on Lasers and Electro-Optics, (CLEO 2000).* pp. 440-441, (2000).

[32]   E. U. Rafailov, W. Sibbett, A. Mooradian, J. G. McInerney, H. Karlsson, S. Wang and F. Laurell,"Efficient frequency doubling of a vertical-extended-cavity surface-emitting laser diode by use of a periodically poled KTP crystal," *Optics Letters,* vol. 28, pp. 2091 - 2093, (2003).

[33]   S. Lutgen, M. Kuehnelt, U. Steegmueller, P. Brick, T. Albrecht, W. Reill, J. Luft, B. Kunert, S. Reinhard, K. VoIz and W. Stolz, "0.7W CW Output Power from a Green Semiconductor Disk Laser," *Conference on Lasers and Electro-Optics Europe,* p. 123, (2005).

[34]   O. Casel, D. Woll, M. A. Tremont, H. Fuchs, R. Wallenstein, E. Gerster, P. Unger, M. Zorn and M. Weyers, "Blue 489-nm picosecond pulses generated by intracavity frequency doubling in a passively mode-locked optically pumped semiconductor disk laser," *Applied Physics B: Lasers and Optics,* vol. 81, pp. 443 -446, (2005).

[35]   A. V. Shchegrov, J. P. Watson, D. Lee, A. Umbrasas, S. Hallstein, G. P. Carey, W. R. Hitchens, K. Scholz, B. D. Cantos, G. Niven, M. Jansen, J.-M. Pelaprat and A. Mooradian, A., "Development of compact blue-green lasers for projection display based on Novalux extended-cavity surface-emitting laser technology," *Proceedings of SPIE Vertical-Cavity Surface-Emitting Lasers IX,* vol. 5737, (2005).

[36]   M. Jacquemet, M. Domenech, J. Dion, M. Strassner, G. Lucas-Leclin, P. Georges, I. Sagnes and A. Garnache, "Single-frequency high-power

continuous-wave oscillation at 1003 nm of an optically pumped semiconductor laser " *Proceedings of SPIE: Semiconductor Lasers and Laser Dynamics II,* vol. 6184, (2006).

[37]   J. E. Hastie, L. G. Morton, A. J. Kemp, M. D. Dawson, A. B. Krysa and J. S. Roberts,"Tunable ultraviolet output from an intracavity frequency-doubled red vertical-external-cavity surface-emitting laser," *Applied Physics Letters,* vol. 89, pp. 06114-1 - 06114-3, (2006).

[38]   J. Lee, S. Lee, T. Kim and Y. Park, "7 W high-efficiency continuous-wave green light generation by intracavity frequency doubling of an end-pumped vertical external-cavity surface emitting semiconductor laser," *Applied Physics Letters,* vol. 89, pp. 241107-1 - 241107-3, (2006).

[39]   J.-Y. Kim, S. Cho, S.-J. Lim, J. Yoo, G. B. Kim, K.-S. Kim, J. Lee, S.-M. Lee, T. Kim and Y. Park, "Efficient blue lasers based on gain structure optimizing of vertical-external-cavity surface-emitting laser with second harmonic generation," *Journal of Applied Physics,* vol. 101, pp. 033103-1 - 033103-4, (2007).

[40]   R. Hartke, E. Heumann, G. Huber, M. Kuhnelt and U. Steegmuller, "Efficient green generation by intracavity frequency doubling of an optically pumped semiconductor disk laser," *Applied Physics B: Lasers and Optics,* vol. 87, pp. 95 - 99, (2007).

[41]   S. Hilbich, W. Seelert, V. Ostroumov, C. Kannengiesser, R. V. Elm, J. Mueller, E. Weiss, H. Zhou and J. Chilla, "New wavelengths in the yellow-orange range between 545 nm and 580 nm generated by an intracavity frequency-doubled optically pumped semiconductor laser," *Proceedings of SPIE Solid State Lasers XVI: Technology and Devices,* vol. 6451, (2007).

[42]   J. Chilla, Q.-Z. Shu, H. Zhou, E. Weiss, M. Reed and L. Spinelli,"Recent advances in optically pumped semiconductor lasers," *Proceedings of SPIE Solid State Lasers XVI: Technology and Devices,* vol. 6451, (2007).

[43]   S. Du, Y. Kaneda and M. Yarborough, "488 nm ultraviolate light generated by VECSEL and vcavity second-harmonic generation using lithium triborate," *Microwave and Optical Technology Letters,* vol. 50, pp. 2892-2894, (2008).

[44]   Y. Song, P. Zhang, X. Zhang, B. Yan, Y. Zhou, Y. Bi and Z. Zhang, "Intracavity frequency-doubled green vertical external cavity surface emitting laser," *Chinese Optics Letters,* vol. 6, pp. 271-273, (2008).

[45]   R. Van Leeuwen, J.-F. Seurin, G. Xu and C. Ghosh, "High Power Pulsed Intra-Cavity Frequency Doubled Vertical Extended Cavity Blue Laser Arrays," *Proceedings of SPIE Solid State Lasers XVIII: Technology and Devices,* vol. 7193, (2009).

[46]   Y. Kaneda, M. Fallahi, J. Hader, J. V. Moloney, S. W. Koch, B. Kunert and W. Stoltz, "Continuous-wave single-frequency 295 nm laser source by a frequency-quadrupled optically pumped semiconductor laser,"*Optics Express,* vol. 34, pp. 3511 - 3513, (2009).

[47]   A. Hein, F. Demaria, A. Kern, S. Menzel, F. Rinaldi, R. Rosch and P. Unger, "Efficient 460-nm Second-Harmonic Generation With Optically Pumped Semiconductor Disk Lasers," *IEEE Photonics Technology Letters,* vol. 23, pp. 179-181, (2011).

[48]   R. Smith, "Theory of intracavity optical second-harmonic generation," *IEEE Journal of Quantum Electronics,* vol. 6, pp. 215-223, (1970).

[49]   T. Baer, "Large-amplitude fluctuations due to longitudinal mode coupling in diode-pumped intracavity-doubled Nd:YAG lasers," *Journal of the Optical Society of America B,* vol. 3, pp. 1175-1180, (1986).

[50]   L. Fan, T.-C. Hsu, M. Fallahi, J. T. Murray, R. Bedford, Y. Kaneda, J. Hader. A. R. Zakharian, J. V. Moloney, S. W. Koch and W. Stolz,"Tunable watt-level blue-green vertical-external-cavity surface-emitting lasers by intracavity frequency doubling," *Applied Physics Letters,* vol. 88, p. 251117, (2006).

[51]   R. W. Boyd, *Nonlinear Optics*, 3rd edition: Elsevier Academic Press, (2008).

[52]   D. Meschede, Optics, Light and Lasers: The Practical Approach to Modern Aspects of Photonics and Laser Physics: Wiley-VCH, (2004).

[53]   B. D. Sinclair, "Frequency-doubled microchip lasers," *Optical Materials,* vol. 11, pp. 217-233, (1999).

[54]   A. Nebel, H. Frost, R. Beigang and R. Wallenstein, "Visible femtosecond pulses by second-harmonic generation of a cw mode-locked KTP optical parametric oscillator," *Applied Physics B: Lasers and Optics,* vol. 60, pp. 453-458, (1995).

[55]   W. Koechner, *Solid-State Laser Engineering*, 6th edition: Springer, (2006).

[56]   A. Yariv, "Introduction to Nonlinear Optics - Second-Harmonic Generation," Chapter 16, pp. 378 - 406, in *Quantum Electronics*, Third edition New York: John Wiley & Sons, (1989).

[57]   F.-T. Wu and W.-Z. Zhang, "Consideration of angular acceptance angle in BBO crystal on a highly efficient second harmonic generation," *Optics & Laser Technology,* vol. 30, pp. 189-192, (1998).

[58]   J.-Y. Kim and J. Shim, "An Analytical Model of the Intracavity Optical Second Harmonic Generation in a Vertical-External-Cavity Surface-Emitting Laser," *IEEE Journal of Quantum Electronics,* vol. 44, pp. 755-762, (2008).

[59]   J.-Y. Kim, J. Yoo, S. Cho, K.-S. Kim, G. B. Kim, J. Lee, S.-M. Lee, T. Kim and Y. Park, "Effect of the properties of an intracavity heat spreader on second harmonic generation in vertical-external-cavity surface-emitting laser," *Journal of Applied Physics,* vol. 101, pp. 073101-4, (2007).

[60]   K. Jun-Youn, L. Junho, C. Soohaeng, Y. Jaeryung, L. Sang-Moon, K. Ki-Sung, K. Gi Bum, H. Sung-Min, K. Taek and P. Yongjo,"Theory of Intracavity Optical Second Harmonic Generation in Vertical-external-cavity Surface-emitting Lasers (VECSELs)," in *19th Annual Meeting of the IEEE Lasers and Electro-Optics Society, LEOS 2006.*, pp. 472-473,(2006).

[61]   N. Laurand, C. L. Lee, E. Gu, J. E. Hastie, S. Calvez and M. D. Dawson, "Microlensed microchip VECSEL," *Optics Express,* vol. 15, pp. 9341-9346, (2007).

[62]   N. Laurand, C.-L. Lee, E. Gu, J. E. Hastie, A. J. Kemp, S. Calvez and M. D. Dawson, "Array-Format Microchip Semiconductor Disk Lasers," *IEEE Journal of Quantum Electronics,* vol. 44, pp. 1096-1103, (2008).

[63]   V. Magni, "Multielement stable resonators containing a variable lens," *Journal of the Optical Society of America A,* vol. 4, pp. 1962-1969, (1987).

[64]   C. Pfistner, R. Weber, H. P. Weber, S. Merazzi and R. Gruber, "Thermal beam distortions in end-pumped Nd:YAG, Nd:GSGG, and Nd:YLF rods," *IEEE Journal of Quantum Electronics,* vol. 30, pp. 1605-1615, (1994).

[65]   E. Hecht, "Geometrical Optics," Chapter 5, pp. 149 - 23 in *Optics*, E. Hecht, Editor, Fourth edition San Francisco: Addison Wesley, (2002).

[66]   Z. L. Liau, "Semiconductor wafer bonding via liquid capillarity," *Applied Physics Letters,* vol. 77, pp. 651 - 653, (2000).

[67]   A. Garnache, A. Ouvrard, L. Cerutti, D. Barat, A. Vicet, F. Genty, Y. Rouillard, D. Romanini and E. A. Cerda-Mendez, "2-2.7 um single frequency tunable Sb-based lasers operating in CW at RT: microcavity and external cavity VCSELs, DFB," Strasbourg, France, pp. 61840N-15, (2006).

[68]   A. Garnache, A. Bouchier, A. Ouvrard, L. Cerutti and E. Cerda-Mendez, "Gain, dichroism and quantum efficiency of Sb-based Quantum-Well VCSELs," in *European Conference on Lasers and Electro-Optics, 2007 and the International Quantum Electronics Conference. CLEOE-IQEC*, pp. 1-1, (2007).

[69]   E. Hecht, *Optics (4th Edition)*: Addison Wesley, (2001).

Chapter 7

Summary and Future Developments

7.1 Summary of Thesis

This thesis presented the multi-faceted design aspects of SDL devices with the aim of applying them in novel system configurations. Central to the design has been the GaInNAs gain material, providing the wavelength engineering capability for device emissions spanning ~1150 nm to ~1350 nm.

Due to the thermal sensitivity inherent to SDLs, special attention was given to the thermal management strategy and characterisation of the specific material system. Use of COMSOL Multiphysics^{TM} software enabled simulations across various platforms of material compositions and incumbent wavelength operation, as well as pumping regimes. Results using both GaInNAs and comparable InP-based devices have highlighted an improved thermal resistance performance using a heatspreader as opposed to the thin disk approach. Indications were also given of an improved thermal response with heatspreaders for pump spot radii below ~200 μm, above which thin disk SDL devices performed better, in either front or end pumping regimes. It was proposed that use of a double bonded thin disk SDL has the best potential effectiveness at heat removal, but may provide challenges in processing due to the physical dimensions of the semiconductor chip. Employing the intracavity diamond heatspreader thermal management technique, which was bonded directly to the semiconductor chip for all GaInNAs/Ga(N)As SDL devices, has enabled maximum achievable output powers in excess of 2.5W, with an external slope efficiency ~15% for a ~1220 nm emitting device.

The application of an SDL designed for emission ~1220 nm as a pump source was given in Chapter 5. In a collaborative effort with St Andrews University, the SDL was employed to pump Tm^{3+}-doped and Tm^{3+},Ho^{3+}-codoped tellurite glasses, as well as a Tm^{3+},Ho^{3+}-codoped tungstate crystal. The provision of an SDL designed for operation and tuning capability to target ~1200 nm absorption in the doped-dielectric

225

media, has resulted in internal slope efficiencies similar to those obtained from previous demonstrations using a ~800 nm Ti:Sapphire pump source. However, the ~2 μm emission output powers of the $Tm^{3+}(,Ho^{3+})$-(co)doped laser systems pumped by ~1200 nm SDL were about half those obtained by Ti:Sapphire pumping due to improved beam quality at high pump powers. As a first demonstration, this has shown the adaptability of SDLs and opened up a new opportunity to advance this technology. Additionally, the SDL has been demonstrated as a pump source alongside a tunable signal source, to achieve ~5dB gain in a ~26km single mode silica fibre. Raman amplification in fibres has significance in the advancement of optical telecommunication networks.

In Chapter 6 the foundations for a novel compact laser device operating in the visible spectral range have been explored. Initial operation had been based upon the standard V-cavity laser configuration, achieving ~25mW of yellow laser light with a tuning range of ~22 nm. However the conversion efficiency results had proven quite low, at ~0.1% with the main contributing factor identified to be the spectral mismatch between the gain and the nonlinear crystal, alongside the tendency to operate in multi-lateral mode regime. As a first proof of concept, this has demonstrated the capability of the double-bonded nonlinear crystal with diamond heatspreader and chip. True miniaturisation of the device would involve a monolithic structure, which has been examined through modeling techniques. The implementation of a microlens onto the nonlinear crystal has shown limitations as to the mode size onto the semiconductor chip. Adhering to the mode matching condition, a reduced pump spot size would concentrate the excitation beam into a smaller area with consequences to the thermal response of the device. Simulations were performed to measure thermal lensing effects, with results showing a significant contribution to the focal length of the system. Key indications provided by these models show great promise to this microchip SDL design, with further scope for improvements.

7.2 Future Development Work

Over the course of this PhD project there are a number of areas identified for future development which may be of interest. Three special topics are introduced below,

each focusing on specific aspects of the SDL device design and possible improvements to its performance.

7.2.1 Heatspreader Bonding Technique

The successful method for effective thermal management of SDLs has been demonstrated in Chapter 3, through the device bonding to a diamond heatspreader. Throughout the course of these experiments the cleaning and subsequent liquid capillary bonding method had frequently resulted in a partial bond. The clear disadvantages presented by the present technique include;

- a limitation of the device operating longevity with a higher probability of the device de-bonding, resulting in device failure;

- having a smaller bonded area requires careful targeting of the pump beam location onto the sample, with more time needed for manual alignment; and

- the process results are inconsistent, a reliable method that is repeatable would be a great benefit to the construction of the laser device.

The direct-bonding technique outlined in the PhD thesis of C. B. E. Gawith [1] draws parallels with the present methods using Van der Waals forces to bond two materials. However, chemical polishing and extensive cleaning were performed to fabricate LiNbO$_3$ waveguides. Immediate bonding occurred using a dry-surface method in which an inert gas completely dries the materials to help facilitate the bond. A key factor to the successful bond appears to lie in the thorough cleaning of the two surfaces. A patent presented in 1999 by Tong *et al.* [2], uses *periodic acid* as a cleaning agent to bond two semiconductor wafers together.

Another method is that of *compression bonding* [3] which may factor into commercial development of SDL devices (Solus-Technology Ltd [4], Samsung Advanced Institute of Technology [5]). A suitable force applied to bond the heatspreader and semiconductor chip might offer an alternative to liquid capillary bonding, but might require the correct apparatus to facilitate a successful bond without damaging the materials.

Taking inspiration from these previous methods may solve the partial bonding issue, by combining the use of a strong cleaning agent immediately followed by the dry-surface method or compression bonding. Further, these types of bonds may also prove sustainable whilst creating a more consistent assembly process.

7.2.2 Incorporation of Dielectric Mirrors into an SDL Design

Alternative arrangements to the DBR mirror in an SDL design were discussed in Chapter 2. Previous examples have been demonstrated in the use of dielectric mirrors implemented in VCSEL devices, forming part of the top mirror of the structure [6]. Similarly, dielectric mirror coatings onto the top surface of a diamond heatspreader bonded to an SDL chip gave proven results to facilitate microchip configurations [7]. The advantages to dielectric mirrors provide much higher reflectivity using fewer layers with low absorption properties. Typically these mirrors display poor thermal conductivity; however MgO/Si [8] and Al_2O_3/Si [9] have shown more promising results.

Exploring the possibilities presented by alternate mirror materials may improve upon existing semiconductor DBRs. The main challenges lie in the processing capability. Suitable materials with higher thermal conductivities to aid cooling of the device must use deposition methods which are compatible with the semiconductor materials used in laser production. Existing deposition methods include the following;

- thermal evaporation used for amorphous chalcogenide Sb-Se/Ge-S mirrors [10];
- pulsed laser deposition to produce ZnO/MgO DBRs, mainly focusing on UV and blue light emitting devices [11]
- RF magnetron sputtering in the creation of SiC/MgO DBRs [12], which may prove useful to aid in thermal extraction for an integrated SDL mirror.

These examples aim to highlight a previously unexplored area of potential development for SDL devices.

7.2.3 SHG Yellow Microchip SDL Laser

The initial concept of the yellow SDL microchip design has been demonstrated in Chapter 6. To further develop this device as it was intended there are many avenues to explore such as the already mentioned laser cavity, capitalising on the micro-lensed microchip concept as an adaptation of the work performed by Laurand *et al.* [13]. There are also opportunities to thin the nonlinear crystal, or perhaps try different geometries to more easily facilitate optical pumping. In terms of thermal management, miniaturising the device warrants other cooling methods other than the demonstrated water cooling. Ideally the heat extraction from the laser gain medium would be highly efficient, yet the energy may be channeled back into the device to perhaps optimise the efficiency of a temperature sensitive nonlinear crystal. Maintaining functionality of the laser, with single frequency output and broadly tunable, may require the incorporation of a filter or perhaps exploit the etalon function of the heatspreader as demonstrated by Lindberg *et al.* [14] and Laurain *et al.* [15]. Future prospects for such a device show great promise, not only applied to yellow laser output but paving the way for a selection of wavelength engineered devices capable of operation across the UV and wider visible spectrum.

It must be noted that this laser forms the platform for a recently awarded Entrepreneurial Fellowship by SU2P, with developmental work undertaken at both Stanford University and the University of Strathclyde. The project is scheduled to commence in the Autumn/Winter of 2011.

References

[1]   C. B. E. Gawith, "Novel Active Waveguide Devices in Direct-Bonded Structures," PhD Thesis, Faculty of Engineering and Applied Science Optoelectronics Research Centre, University of Southampton, Southampton, (2001).
[2]   Q.-Y. Tong, U. Goesele and L. Tong, "Method For The Cleaning And Direct Bonding Of Solids," US Patent 5915193, (1999).
[3]   S. Sato, "Chip compression-bonding apparatus and method," US Patent 5985064, (1999).
[4]   Solus-Technologies Ltd. Available: http://www.solus-technologies.com/

[5]   Samsung   Advanced   Institute   of   Technology.   Available: http://www.sait.samsung.co.kr/eng/about/e_index.jsp

[6]   P. Mackowiak and W. Nakwaski, "Some aspects of designing an efficient nitride VCSEL resonator," *Journal of Physics D: Applied Physics,* vol. 34, p. 954, (2001).

[7]   S. A. Smith, J.-M. Hopkins, J. E. Hastie, D. Burns, S. Calvez, M. D. Dawson, T. Jouhti, J. Kontinnen and M. Pessa, "Diamond-microchip GaInNAs vertical external-cavity surface-emitting laser operating CW at 1315 nm," *Electronics Letters,* vol. 40, pp. 935-936, (2004).

[8]   T. Baba, Y. Yogo, K. Suzuki, F. Koyama and K. Iga, "Near room temperature continuous wave lasing characteristics of GaInAsP/InP surface emitting laser," *Electronics Letters,* vol. 29, pp. 913-914, (1993).

[9]   S. Uchiyama, N. Yokouchi and T. Ninomiya, "Continuous-wave operation up to 36C of 1.3-um GaInAsP-InP vertical-cavity surface-emitting lasers," *IEEE Photonics Technology Letters,* vol. 9, pp. 141-142, (1997).

[10]   T. Kohoutek, J. Orava, T. Wagner, M. Hrdlicka, Mil. Vlcek and M. Frumar, "Preparation of dielectric mirrors from high-refractive index contrast amorphous chalcogenide films," *Journal of Physics and Chemistry of Solids,* vol. 69, pp. 2070-2074, (2008).

[11]   B. Huo, L. Hu, H. Zhang, Z. Zhao, Q. Fu and X. Chen, "ZnO/MgO distributed Bragg reflectors," *Optica Applicata* vol. 39, pp. 169 - 174, (2009).

[12]   M. S. K. Anuar, H. Soetedjo, A. M. Sharizal, S. M. Sufian, T. G. Boon, A. R. Saadah, Y. M. Razman and A. M. A. Fatah, "Development of SiC/MgO Distributed Bragg Reflector using RF Magnetron Sputtering Technique," in *IEEE International Conference on Semiconductor Electronics, ICSE '06.*, pp. 378-381, (2006).

[13]   N. Laurand, C. L. Lee, E. Gu, J. E. Hastie, S. Calvez and M. D. Dawson, "Microlensed microchip VECSEL," *Optics Express,* vol. 15, pp. 9341-9346, (2007).

[14]   H. Lindberg, A. Larsson and M. Strassner, "Single-frequency operation of a high-power, long-wavelength semiconductor disk laser," *Optics Letters,* vol. 30, pp. 2260-2262, (2005).

[15]   A. Laurain, M. Myara, G. Beaudoin, I. Sagnes and A. Garnache, "High power single-frequency   continuously-tunable   compact   extended-cavity semiconductor laser," *Optics Express,* vol. 17, pp. 9503-9508, (2009).

Appendix A

Publications and Conference Papers

Journal Publications

Short-wavelength GaInNAs/GaAs semiconductor disk lasers
<u>S. L. Vetter,</u> J. E. Hastie, V.-M. Korpijärvi, J. Puustinen, M. Guina, O. Okhotnikov, S. Calvez and M. D. Dawson, *Electronics Letters,* **vol. 44, pp. 1069-1070, (2008).**

Tunable laser operation of a Tm^{3+}-doped tellurite glass laser near 2 μm pumped by a 1211 nm semiconductor disk laser
F. Fusari, <u>S. Vetter,</u> A.A. Lagatsky, B. Richards, S. Calvez, A. Jha, M.D. Dawson, W. Sibbett and C.T.A. Brown, *Optical Materials,* **vol. 32, pp. 1007-1010, (2010).**

Thermal management of near-infrared semiconductor disk lasers with AlGaAs mirrors and lattice (mis)-matched active regions
<u>S. L.Vetter</u> and S. Calvez, *IEEE Journal of Quantum Electronics*, **JQE-132825-2011, Submitted (2011).**

Conference Papers and Presentations

Power scaling and tunability of 1150-1250nm GaInNAs/GaAs VECSELs
<u>S.L. Vetter</u>, J. Hastie, S. Calvez, M.D. Dawson, V.-M. Korpijärvi, J. Puustinen, M. Guina, O. Okhotnikov and M. Pessa. Presented at **Quantum Electronics and Photonics (QEP-18), Photon '08 Conference, Heriot-Watt University, Edinburgh (2008)**

Amplification characteristics of bismuth-doped silica fibres
<u>S. L. Vetter</u>, S. Calvez, M. D. Dawson, L. Bigot, I. Razdobreev, and G. Bouwmans Presented at **3rd EPS-QEOD EUROPHOTON CONFERENCE 31th August -5th September Paris, France (2008)**

1213nm semiconductor disk laser pumping of a Tm^{3+}doped tellurite glass laser
<u>S. Vetter</u>, S. Calvez, M.D. Dawson, F. Fusari, A. A. Lagatsky, W. Sibbett, C.T.A. Brown, V.-M. Korpijärvi, M. Guina, B. Richards, G. Jose and A. Jha, in **IEEE Lasers and Electro-Optics Society, LEOS 21st Annual Meeting, pp. 840-841 (2008)**.

GaInNAs semiconductor disk lasers as pump sources for Tm^{3+} (,Ho^{3+})-doped glass, crystal and fibre lasers
<u>S.L. Vetter</u>, L.J. McKnight, S. Calvez, M.D. Dawson, F. Fusari, A.A. Lagatsky, W. Sibbett, C.T.A. Brown, V.-M. Korpijärvi, M.D. Guina, B. Richards, G. Jose and A. Jha, in **Proceedings of SPIE Solid State Lasers XVIII: Technology and Devices, vol. 7193, pp.719317, (2009)**.

~1200-nm tunable fiber vertical-cavity surface-emitting laser
<u>S. L. Vetter,</u> N. Laurand, M.D. Dawson, S. Calvez and M. Guina, in **Proceedings of SPIE Solid State Lasers XIX: Technology and Devices, vol. 7578, pp. 75780Y, (2010)**.

Thermal managment of Semiconductor Disk Lasers with lattice-(mis)matched AlGaAs mirrors
<u>S. L. Vetter</u>, S. Calvez and M. D. Dawson, Presented at **4th EPS-QEOD EUROPHOTON CONFERENCE 29th August -3rd September Hamburg, Germany, TuP18, (2010)**

GaInNAs(Sb) for solid-state laser engineering
S. Calvez, in **13th International Conference on Transparent Optical Networks (ICTON), Mo.B6.2, pp. 1-4, (2011)**.

Appendix B

Glossary of Acronyms and Abbreviations

AlAs - Aluminium Arsenide

AlGaAs – Aluminium Gallium Arsenide

AlGaAsSb - Aluminium Gallium Arsenide Antimonide

AlInGaAs – Aluminium Indium Gallium Arsenide

AlInGaP - Aluminium Indium Gallium Phosphide

Al_2O_3 - Aluminium Oxide

at.% - Atomic Percentage

BAC – Band Anti-Crossing

$Ba(NO_3)_2$ – Barium Nitrate

β-BBO - Beta Barium Borate, $β-BaB_2O_4$

BiBO - Bismuth Borate, BiB_3O_6

Bi - Bismuth

BRF – Birefringent Filter

CB – Conduction Band

C-Band – Conventional-Band in telecom networks

cm – Centimetre, 10^{-2}m

CO_2 – Carbon Dioxide

CR – Cross Relaxation

Cr^{2+}:ZnSe – Chromium doped Zinc Selenide

CVD – Chemical Vapour Deposition

CW – Continuous Wave

dB - Decibel

DBR – Distributed Bragg Reflector

DI – De-ionised Water

DIAL – Differential Absorption LIDAR

DPSSL – Diode Pumped Solid-State Laser

DWELL – Dots-in-a-Well

Appendix B – Glossary of Acronyms and Abbreviations

dyn - Dyne

EDFA – Erbium Doped Fibre Amplifiers

Er – Erbium

ESA – Excited State Absorption

ET – Energy Transfer

eV – Electron Volt

FSR – Free Spectral Range

FWHM – Full Width at Half Maximum

Ga - Gallium

GaAs – Gallium Arsenide

GaInAs – Gallium Indium Arsenide

GaInAsSb - Gallium Indium Arsenide Antimonide

GaInNAs – Gallium Indium Nitrogen Arsenide

GaN – Gallium Nitride

GaNAs – Gallium Nitrogen Arsenide

Ge - Germanium

GSA – Ground State Absorption

hh – Heavy Hole

Ho^{3+} - Holmium ion

HR – High Reflectance

HT – High Transmission

HS – Heatspreader

HSFR – High Spatial Frequency Ripples

In - Indium

InGaAs - Indium Gallium Arsenide

InGaAsP – Indium Gallium Arsenide Phosphide

InP – Indium Phosphide

IR – Infrared

K - Kelvin

KDP - Potassium Dihydrogen Phosphate, KH_2PO_4

kg – Kilogramme, 10^3g

KGW - Potassium Gadolinium Tungstate, $KGd(WO_4)_2$

Appendix B – Glossary of Acronyms and Abbreviations

kHz – Kilohertz, 10^3Hz

km – Kilometre, 10^3m

KNbO$_3$ - Potassium Niobate, KNbO$_3$

KTP - Potassium Titanyl Phosphate, KTiOPO$_4$

KYW – Potassium Yttrium Tungstate, KY(WO$_3$)$_4$

LBO - Lithium Triborate, LiB$_3$O$_5$

LD – Laser Diode

LED – Light Emitting Diode

LGS – Lithium Gallium Sulphide, LiGaS$_2$

LIDAR – Light Detection and Ranging

LiNbO$_3$ – Lithium Niobate

lh – Light Hole

LiIO$_3$ - Lithium Iodate

MBE – Molecular Beam Epitaxy

MgO - Magnesium oxide

MHz – Megahertz, 10^6Hz

mm – Millimetre, 10^{-3}m

MMF – Multimode Fibre

MOCVD – Metalorganic Chemical Vapour Deposition

MOPA – Master Oscillator Power Amplifier

MQW – Multiple Quantum Well

mrad – Milliradian, 10^{-3}radian

mW – Milliwatt, 10^{-3} W

N – Nitrogen

NASA – National Aeronautical and Space Administration

NCPM – Non-Critical Phase Matching

Nd:YAG – Neodymium doped Yttrium Aluminium Garnet, Y$_3$Al$_5$O$_{12}$

Nd:YVO$_4$ – Neodymium doped Yttrium Orthovanadate

nm – Nanometre, 10^{-9}m

OA – Optical Axis

O-Band – Ordinary-band in telecom networks

OC – Output Coupler

Appendix B – Glossary of Acronyms and Abbreviations

OPA – Optical Parametric Amplifier

ORC – Optical Research Centre, Tampere, Finland

OSA - Optical Spectrum Analyser

$PbWO_4$ – Lead Tungstate

PL – Photoluminescence

pm – Picometre, 10^{-12}m

PPKTP - Periodically Poled Potassium Titanyl Phosphate, $KTiOPO_4$

PPLN - Periodically Poled Lithium Niobate, $LiNbO_3$

PPSLT - Periodically Poled Stoichiometric Lithium Tantalate

QCSE – Quantum Confined Stark Effect

QD – Quantum Dot

QW – Quantum Well

RF – Radio Frequency

RHEED – Reflection High Energy Electron Diffraction

RIN – Relative Intensity Noise

ROC – Radius of Curvature

RPG – Resonant Periodic Gain

RTA – Rapid Thermal Annealing

S – Sulfur

Sb - Antimonide

SBS – Stimulated Brillouin Scattering

SCL – Strain Compensating Layer

SDL – Semiconductor Disk Laser

Se - Selenium

SEM – Scanning Electron Microscope

SFM – Sum Frequency Mixing

SHG - Second Harmonic Generation

Si – Silicon

SiC – Silicon Carbide

SiO_2 – Silicon Dioxide

SMF – Single Mode Fibre

TD – Thin Disk

Appendix B – Glossary of Acronyms and Abbreviations

TE – Transverse Electric

THz – Terrahertz, 10^{12}Hz

TM – Transverse Magnetic

Tm^{3+} - Thulium ion

TV - Television

TZN - TeO_2– ZnO–Na_2O

TZNG - TeO_2– ZnO–Na_2O-GeO_2

UC - Upconversion

UV – Ultraviolet

μm – Micron, 10^{-6}m

μs – Microsecond, 10^{-6}s

V - Volt

VB – Valence Band

VCSEL – Vertical-Cavity Surface-Emitting Laser

VECSEL – Vertical External-Cavity Surface-Emitting Laser

VERTIGO – Versatile Two Micron Light Source

W – Watt

WDM –Wavelength Division Multiplexing

wt.% - Weight Percentage

Yb - Ytterbium

Yb:YAB – Ytterbium doped Yttrium Aluminium Tetraborate,$YAl_3(BO_3)_4$

ZBLAN - ZrF_4-BaF_2-LaF_3-AlF_3-NaF

ZnO – Zinc Oxide

ZrO_2 – Zirconium Dioxide, Zirconia